



HAL
open science

Dynamic and nonlinear properties of quantum dot lasers for photonic integrated circuits on silicon

Jianan Duan

► **To cite this version:**

Jianan Duan. Dynamic and nonlinear properties of quantum dot lasers for photonic integrated circuits on silicon. Optics / Photonic. Université Paris Saclay (COMUE), 2019. English. NNT : 2019SACLT050 . tel-02506422

HAL Id: tel-02506422

<https://pastel.hal.science/tel-02506422>

Submitted on 12 Mar 2020

HAL is a multi-disciplinary open access archive for the deposit and dissemination of scientific research documents, whether they are published or not. The documents may come from teaching and research institutions in France or abroad, or from public or private research centers.

L'archive ouverte pluridisciplinaire **HAL**, est destinée au dépôt et à la diffusion de documents scientifiques de niveau recherche, publiés ou non, émanant des établissements d'enseignement et de recherche français ou étrangers, des laboratoires publics ou privés.

Dynamic and nonlinear properties of quantum dot lasers for photonic integrated circuits on silicon

Thèse de doctorat de l'Université Paris-Saclay
préparée à Télécom Paris

École doctorale n°575 Electrical, Optical, Bio: PHYSICS AND ENGINEERING
(EOBE)

Spécialité de doctorat : Physique optoélectronique

Thèse présentée et soutenue à Palaiseau, le 28 Novembre 2019, par

JIANAN DUAN

Composition du Jury :

Marek Osiński Professeur, University of New Mexico, États-Unis	Rapporteur
Xavier Letartre Directeur de Recherche, CNRS (Institut des Nanotechnologies de Lyon), France	Rapporteur
Alexei Baranov Directeur de Recherche, CNRS (Institut d'Electronique et des Systèmes), France	Président
Johann-Peter Reithmaier Professeur, University of Kassel, Allemagne	Examineur
Béatrice Dagens Directrice de Recherche, CNRS (Centre de Nanosciences et de Nanotechnologies), France	Examineur
Cheng Wang Professeur assistant, ShanghaiTech University, Chine	Examineur
Frédéric Grillot Professeur, Institut polytechnique de Paris (Télécom Paris), France	Directeur de thèse

Acknowledgements

I would like to express my sincere gratitude to my PhD supervisor Prof. Frédéric Grillot for his excellent guidance and support throughout my PhD study. I truly appreciate all professional approach, tremendous scientific and technological knowledge he shared with me. I also thank him for supporting me on various international conferences that helped me to catch the most recent research topics and technology advances in industrial area.

I would like to thank Prof. John E. Bowers from University of California Santa Barbara, USA and Dr. Philip Poole from National Research Center, Canada for providing me high-quality laser samples which allowed me to achieve a rich variety of results sustaining the comprehension of underlying physics. I would also thank Prof. Cheng Wang from ShanghaiTech University, China for hosting me in his youthful and vigorous group for three months. In particular, his deep insights in optoelectronics granted me important guidance on my research work.

My special thanks to Dr. Heming Huang from Télécom Paris, France for tremendously supporting me to build up the experimental abilities and theoretical background.

I really appreciate the work of my collaborators: Dr. Justin C. Norman and Zeyu Zhang from University of California Santa Barbara, USA, Dr. Daehwan Jung from Korea Institute of Science and Technology, South Korea, Yueguang Zhou and Xingguang Wang from ShanghaiTech University, China, Prof. Kathy Lüdge and Felix Köster from Technische Universität Berlin, Germany, Dr. Zhenguo Lu from National Research Center, Canada and Bozhang Dong from Télécom Paris, France for helpful scientific discussions.

I would like to thank all the professors, all the colleagues and all the friends from Télécom Paris, France: Prof. Yves Jaouen, Prof. Cedric Wave, Prof. Mansoor Yousefi, Dr. Antonin Gallet, Dr. Louise Jumpertz, Dr. Jean-Maxime Sarraute, Olivier Spitz, Sandra Gomez, Dr. Wei Wei, Dr. Jinxin Du, Dr. Longguang Li, Dr. Pengwenlun Gu, Prof. Hao Cai, Dr. Mengying Ren, Dr. You Wang, Zepeng Liu, Dr. Mengdi Song, Dr. Wasyhun A. Gemechu and Jannik F. Ehlert who aided me in my work and life.

I also want to thank my undergraduate classmates from Huazhong University of Science and Technology, China, for their support and all the memorable moments we had together in France.

I acknowledge the China Scholarship Council and Campus France for funding my PhD work.

Finally, I deeply appreciate the persistent support and encouragement from my parents. My special thanks to my fiancée Jing Tian for her love, support as well as understanding.

Abstract

Silicon photonics have been introduced to overcome low efficiency and high energy consumption of telecom links using twisted pairs or coaxial cables. This technology provides novel functionality and high performance for applications in high speed communication systems, short reach optical interconnects, and the deployment of optical links from chip-to-chip, board-to-board or rack-to-rack (datacom). Silicon is known as a very efficient semiconductor material for waveguiding light in particular owing to the strong index contrast with silica. However, the indirect bandgap of silicon makes light emission from silicon inefficient, and other techniques such as wafer- or flip-chip bonding must be investigated if light emission is to be realized. The drawbacks of such heterogeneous integration concentrate on the high cost and the limited scalability. Lasers heterogeneously integrated on silicon are also more sensitive to optical reflections originating from the transition between passive/active interfaces. The best way to overcome these drawbacks is to move on to direct epitaxial growth of III-V materials on silicon for photonics integration. In this context, quantum dot lasers using semiconductor atoms as a gain medium are ideal because they enable smaller devices, amplification with large thermal stability and high tolerance to epitaxial defects. Ultra-low noise optical transmitters are required not only for the coherent systems but also for future chip-scale atomic clocks and radar related applications because of the sensitivity to the frequency noise and intensity noise can strongly affect the bit error rates. To this end, the first part of the thesis reports an intrinsic spectral linewidth as low as 80 kHz and a relative intensity noise less than - 150 dB/Hz in InAs/InP quantum dot lasers. In particular, it is shown that a small vertical coupling is more suitable for low intensity noise operation due to the suppression of the carrier noise in the excited state. The second part of the thesis investigates the dynamic and nonlinear properties of epitaxial quantum dot lasers on silicon. As mentioned above, lasers heterogeneously integrated on silicon are more sensitive to parasitic reflections. When combined with external optical feedback, the laser stability can be dramatically affected. As no on-chip optical isolators integrated with lasers and having sufficient isolation ratio exist, the development of feedback insensitive transmitters remains a major objective. This thesis presents an error-free transmission of an epitaxial quantum dot laser on silicon externally modulated at 10 Gb/s and subjected to 100 % optical feedback. Such

remarkable feedback insensitivity directly results from the near-zero linewidth enhancement factor, the large damping factor, the strong contrast between the ground state and excited states and a shorter carrier lifetime. These results pave the way for future high-performance photonics integrated circuits on silicon operating without optical isolators.

Keywords: semiconductor lasers, quantum dots, optical feedback, nonlinear dynamics, relative intensity noise, spectral linewidth

Table of contents

List of figures	xi
List of tables	xxi
1 Introduction	1
1.1 Needs for optical communication	1
1.2 Photonic integrated circuits	2
1.3 Development of quantum dot (QD) lasers	5
1.3.1 GaAs-based and InP-based QD lasers	5
1.3.2 Silicon-based QD lasers	7
1.4 Motivations of the dissertation	11
1.5 Organization of the dissertation	13
2 Fundamentals of quantum dot lasers	17
2.1 Electronic structure and carrier scattering processes	17
2.2 Gain broadening mechanisms	19
2.3 Linewidth enhancement factor	23
2.4 Dual states lasing emission	25
2.5 Relaxation oscillation frequency and damping factor	26
2.6 Summary	29
3 Noise properties of InAs/InP quantum dot distributed feedback lasers	31
3.1 Introduction to frequency noise and intensity noise	32
3.1.1 Frequency noise	32
3.1.2 Narrow linewidth single-mode lasers	33
3.1.3 Relative intensity noise	37
3.2 Theoretical investigation of the frequency noise and intensity noise	39
3.2.1 Quantum dot laser modal description	39
3.2.2 Effect of the carrier noise on the frequency noise and linewidth	43

3.2.3	Effect of the carrier noise on the relative intensity noise	46
3.3	Experimental analysis of spectral linewidth	51
3.3.1	InAs/InP QD DFB laser description	51
3.3.2	Linewidth measurement setup	55
3.3.3	Longitudinal spatial hole burning dependence of spectral linewidth	56
3.3.4	Temperature dependence of spectral linewidth	59
3.4	Experimental analysis of the relative intensity noise	62
3.4.1	RIN measurement setup	62
3.4.2	Analysis of the RIN properties	63
3.5	Summary	65
4	Epitaxial QD lasers on silicon: From advanced characterizations to dynamical properties	69
4.1	Investigated QD laser devices	70
4.1.1	Material growth and device fabrication	70
4.1.2	Light current characteristics and optical spectrum	72
4.2	Intensity noise properties	74
4.2.1	Effect of the p-doping on the relative intensity noise	74
4.2.2	Damping factor and relaxation oscillation frequency	77
4.2.3	Gain compression	80
4.3	Linewidth enhancement factor (α_H -factor)	82
4.3.1	Sub-threshold α_H -factor determination	83
4.3.2	Thermally insensitive determination of the α_H -factor	88
4.3.3	Above-threshold α_H -factor determination	93
4.4	Summary	98
5	Epitaxial QD lasers on silicon : Analysis of the reflection sensitivity	99
5.1	Introduction	99
5.1.1	Principle of optical feedback	99
5.1.2	Lang and Kobayashi equations	103
5.1.3	Light current characteristic with optical feedback	104
5.1.4	Phase shift with optical feedback	106
5.1.5	Bifurcation diagram representing the laser dynamics	109
5.1.6	Toward a feedback insensitive semiconductor laser	110
5.2	Experimental optical feedback apparatus	116
5.2.1	Coherent optical feedback setup	116
5.2.2	Incoherent optical feedback setup	117

5.2.3	High speed setup with optical feedback	118
5.3	Impact of the ES transition on feedback dynamics	118
5.3.1	Laser static characteristics	118
5.3.2	Maximum optical feedback tolerance	121
5.3.3	Dynamical routes	123
5.3.4	Impact of the ES-GS contrast	123
5.4	Effect of the p-doping on the reflection sensitivity	126
5.4.1	Coherent optical feedback	126
5.4.2	Incoherent optical feedback	131
5.4.3	High-speed experiments with optical feedback	132
5.5	Summary	136
6	Conclusions and perspectives	139
7	Résumé en Français	143
7.1	Introduction	143
7.2	Lasers à boîtes quantiques (QD) InAs/InP à rétroaction distribuée à faible bruit	144
7.3	Insensibilité aux réflexions optiques parasites dans les lasers à boîtes quantiques directement épitaxiés sur silicium	150
7.4	Conclusions et perspectives	155
	References	157
	Appendix A Publications	181
	Appendix B List of Acronyms	185

List of figures

1.1	Schematic representation of a WDM system with multiple wavelength channels. [26].	2
1.2	Component counts in a single PIC comparing PIC on native InP, monolithic silicon photonics and heterogeneous integration from [89].	3
1.3	Room-temperature photoluminescence comparison of single QW layer (a) and single QD layer (b) grown on GaAs versus silicon substrates [159]. . .	4
1.4	Evolution of the density of states for bulk material, quantum well and quantum dot, respectively, from [193].	5
1.5	Atomic force microscopy image of InAs QDashs grown on InP(100) substrate (left), QD grown on InP(100) substrate (middle) and QD grown on InP(311)B substrate (right) [6].	7
1.6	Threshold current density (a) and device lifetime (b) (either extrapolated or measured) for lasers on silicon operating in the continuous wave mode from [196].	8
1.7	(a) Cutaway schematic of DFB laser array on silicon showing the vertical layer structure, the output coupler and the etched gratings. (b) Optical spectra of a DFB laser array with different grating periods around their maximum output power levels before saturation at room temperature [278].	9
1.8	(a) Color-enhanced cross-sectional scanning electron microscopy (SEM) image of the whole epitaxial structure. (b) Optical spectra at various pump currents [297].	9
1.9	(a) Scanning electron micrograph of a microring device. (b) Power-current-voltage curves for a sub-milliamp threshold laser with inset illustration. (c) Optical spectra showing the lasing mode for various pump currents [271]. .	10
1.10	Schematic of the coherent detection.	11
2.1	Schematic of a QD laser electronic band structure of electrons and holes. . .	18

2.2	Photoluminescence spectrum as a function of temperature from a single InAs/GaAs dot from [16].	20
2.3	Simulated homogeneously broadened gain spectra for various carrier density from [290]. The arrow points to the direction of increasing carrier density.	21
2.4	Representation of the inhomogeneous broadening illustrating dots with different sizes which lead to energy state distribution from [15].	22
2.5	Schematic representations of how the inhomogeneous broadened gain spectrum of a QD laser is composed of contribution of dot groups with different emission energy [290].	23
2.6	Schematic of gain G and refractive index n profiles variation with the carrier density changes for QD and QW from [224].	25
2.7	(a) Integrated light-output power of a InAs/InP QD laser versus optical normalised pumping density with respect to the GS threshold intensity. (b) Room-temperature emission spectra under various pulsed optical excitation from [263].	26
2.8	Sketch of the modulation transfer function for increasing values of relaxation resonance frequency ω_R and damping factor γ . The relationship among the peak frequency ω_p , ω_R and the 3 dB down cutoff frequency ω_{3dB} are also illustrated in the sketch [41].	29
3.1	Frequency noise spectrum, illustrating contributions from both carrier and spontaneous emission noise [41].	32
3.2	(a) Schematics of the extended distributed Bragg reflector (E-DBR) laser, with SEM images of the transitions between the various sections of the laser, and ring resonator incorporated in the cavity to form the ring-assisted extended DBR(RAE-DBR) laser. (b) Frequency noise spectra for the E-DBR and RAE-DBR lasers [97].	34
3.3	(a) High-Q hybrid laser device schematics. Two-dimensional cross-section of the hybrid platform, with superimposed optical transverse mode profile. (b) Spectral linewidth of a single high-Q hybrid laser as a function of the offset pump current [227]	35
3.4	Extracted Lorentzian linewidths shown in marks. The simulated values are shown in solid lines: 20°C (blue), 40°C (purple), 60°C (orange), 80°C (red) [236].	36
3.5	Inversion factor as a function of photon energy for three currents [205].	37
3.6	Schematic of the relative intensity noise.	37

3.7	Plot of the Signal-to-Noise versus average photodiode current for thermal noise-limited, shot noise-limited, and three cases of RIN-limited detection in radar applications [45].	38
3.8	Schematic representation of the electronic structure and the corresponding carrier dynamics into the QD.	40
3.9	Carrier noise contribution to the FN at several bias currents. The solid line are with carrier noise while the dash-dot lines are not.	43
3.10	Contribution of the GS, the ES and the RS to the α_H -factor as a function of the normalized bias current.	45
3.11	(a) Calculated spectral linewidth as a function of the drive current for the AR/HR QD DFB laser. (b) Temperature dependence of the minimum linewidth at 155 mA.	45
3.12	Contribution of $F_{RS,ES,GS}$ to the RIN at bias currents of $1.5 \times I_{th}$, $2.5 \times I_{th}$ and $3.5 \times I_{th}$, respectively. The solid lines are with carrier noise while the dash-dot lines are not.	46
3.13	The bias current dependence of the damping factor and the resonance frequency of the RIN spectra including the $F_{RS,ES,GS}$	47
3.14	The RIN at 1 MHz with (solid line) and without (dash-dot line) carrier noise as a function of the normalized bias current.	48
3.15	Simulation of the RIN spectra at $1.5 \times I_{th}$ for the cases including the carrier noise sources $F_{RS,ES,GS}$, $F_{ES,GS}$, F_{GS} and without ($F_{RS,ES,GS} = 0$), respectively.	48
3.16	(a) Simulated RIN at 1 MHz as a function of the GS-ES separation (ΔE_{GS}^{ES}) for different photon numbers. (b) Illustration of GS-ES separation.	49
3.17	(a) The RIN at 1 MHz as a function of the relaxation time from ES to GS assuming a capture time $\tau_{ES}^{RS} = 2.17 \times \tau_{GS}^{ES}$ and a photon number of 2×10^5 . (b) Illustration of relaxation time.	50
3.18	(a) Calculated RIN at 1 MHz as a function of the bias current at 283 K, 293 K and 303 K, respectively. (b) RIN values as a function of temperature assuming a bias current of 160 mA.	50
3.19	(a) Schematic diagram of the InAs QD structure; (b) An atomic-force microscopy image of one QD layer ($1 \mu\text{m} \times 1 \mu\text{m}$) [213].	52
3.20	Cross section view of the DFB structure [213].	52
3.21	Light current curves measured for different temperature for AR/HR DFB laser (a) and AR/AR DFB laser (b).	53
3.22	Optical spectra measured at $2 \times I_{th}$ for AR/HR DFB laser (a) and AR/AR DFB laser (b).	54

3.23	The measured α_H -factor as a function of the lasing wavelength for the InAs/InP FP QD laser. The black dashed lines indicate the FP gain peak value (1545 nm) and DFB gain peak value (1520 nm).	54
3.24	Self-heterodyne interferometer used for the linewidth measurement. AOM: Acousto-Optic Modulator; PD: Photodiode; ESA: Electrical Spectrum Analyzer.	55
3.25	Normalized RF spectrum and the corresponding Voigt fitted spectrum.	57
3.26	Spectral linewidth fitted with a pseudo-Voigt profile as a function of the normalized drive current I/I_{th} , for AR/HR DFB laser (red) and AR/AR DFB laser (blue).	58
3.27	Simulated linewidth as a function of the bias current for different values of gain compression coefficient [218].	59
3.28	Spectral linewidth of the AR/HR DFB laser (a) and the QW DFB laser (b) as a function of the normalized bias current and measured at 283K, 293K and 303K, respectively. The black dashed lines indicate the minimum linewidth level at 283K and 303K.	60
3.29	Spectral linewidth of the AR/AR DFB laser as a function of the normalized bias current and measured at 293K, 303K and 313K, respectively.	61
3.30	Experimental setup used for investigating the RIN of QD lasers.	62
3.31	RIN spectra up to 10 GHz for QD lasers at various bias currents. The black lines indicate the curve fitting.	63
3.32	RIN at 100 MHz as a function of $(I/I_{th} - 1)$. The red line indicates the fitting of the dependence of $(I/I_{th} - 1)^{-3}$	64
3.33	The bias current dependence of the damping factor (a) and relaxation oscillation frequency (b).	65
3.34	Damping factor versus squared relaxation oscillation frequency.	66
4.1	Schematic description of the QD laser epi-layer structure.	70
4.2	(a) Atomic force microscope image of InAs QDs grown on a GaAs/Si template. Scale bar is 200 nm. (b) Photoluminescence spectrum of the full laser sample.	71
4.3	Cross-sectional scanning electron microscope image showing the facet of a fabricated FP QD laser on silicon.	72
4.4	Light-current characteristics of (a) undoped and (b) p-doped QD lasers as a function of temperature varying from 288 K to 308 K with a step of 5 K. The insets show corresponding optical spectra of ground state (GS) emission measured at $3 \times I_{th}$ at 293 K.	73

4.5	Optical spectral envelopes of (a) undoped and (b) p-doped QD lasers at $3 \times I_{th}$ as a function of temperature.	73
4.6	Light-current characteristics of the QD lasers under study.	74
4.7	RIN spectra up to 10 GHz for QD lasers A(a), B(b), C(c) and D(d), respectively.	75
4.8	Comparison of the relative intensity noise spectra between the undoped QD laser (Device A) and p-doped QD laser (Device B) biased at $3 \times I_{th}$ for (a) 293 K and (b) 303 K.	76
4.9	The measured damping factor (γ) as a function of the squared relaxation oscillation frequency (f_{RO}^2) both for QD (Device A) and QW lasers.	77
4.10	(a) The measured damping factor (γ) as a function of the squared relaxation oscillation frequency (f_{RO}^2) for the QD lasers under study. (b) The K -factor and inverse differential carrier lifetime (γ_0) versus the doping level.	78
4.11	The damping factor as a function of the squared relaxation oscillation frequency for (a) undoped and (b) p-doped QD laser device.	79
4.12	Illustration of gain saturation (a) versus gain compression (b) from [112].	80
4.13	The squared relaxation oscillation frequency (f_{RO}^2) versus the output power both for QD (Device A) and QW lasers.	81
4.14	(a) The squared relaxation oscillation frequency (f_{RO}^2) versus the output power (P) for the lasers under study. (b) The extracted gain compression as a function of doping level.	82
4.15	(a) Measured peak wavelength as a function of the duty cycle for different subthreshold bias currents. (b) Measured peak wavelength as a function of the bias current for two values of the duty cycle.	85
4.16	The α_H -factor as a function of the photon wavelength for the p-doped QD laser (293K). The black dotted line indicates the FP gain peak value (1295 nm). The inset indicates the corresponding net modal gain spectra for various subthreshold bias current conditions.	86
4.17	(a) Pulse width dependence of the measured α_H -factor at a fixed duty cycle of 0%. (b) Duty cycle dependence of the measured α_H -factor at a fixed pulse width of 0.1 μ s. Note that the linear curve-fitting (dashed lines) are for guiding eyes only.	86
4.18	The α_H -factor as a function of temperature for p-doped (red) and undoped (blue) QD lasers. The linear curve-fittings (dashed lines) are for guiding eyes only.	87
4.19	The α_H -factor as a function of the ridge waveguide width for p-doped (red) and undoped (blue) QD lasers (293K).	88

4.20	Experimental setup for measuring the α_H -factors.	89
4.21	Typical locking map of a laser diode, which includes Saddle-Node bifurcation, Hopf bifurcation and stable locking regime.	89
4.22	Measured optical spectra for the p-doped QD laser. The blue lines are for the free-running laser (i.e. without optical injection), and the red lines are for the laser that is injection-locked.	90
4.23	Wavelength variation of the measured net modal gain with detuning of the injected light from shorter to longer wavelength within the stable-locking range.	91
4.24	Wavelength dependence of the measured α_H -factor by ASE method and ASE IL method for (a) p-doped QD laser and (b) undoped QD laser. The black dotted lines indicate the FP gain peak value.	92
4.25	Voltage variation of the undoped laser as a function of the frequency detuning.	94
4.26	Optical spectra at different frequency detuning marked on Fig.4.25.	94
4.27	The effective α_H -factor measured as a function of the normalized bias current for p-doped (red) and undoped (blue) QD lasers (293K). The injection ratio is -2 dB.	95
4.28	The simulated α_H -factor as a function of the output power for the QW laser (a) and QD laser (b). Superimposed black stars in (b) correspond to experimental data from Fig.4.27.	96
5.1	Schematic illustration of a semiconductor laser under optical feedback	100
5.2	Schematic representation of the physical processes involved in a semiconductor laser under optical feedback.	101
5.3	Cartography of optical feedback regimes in a DFB QW laser from [255].	102
5.4	The comparison of the light current characteristics of a QD FP laser between the free-running operation and three different feedback ratio from [98]	105
5.5	Interaction between the external cavity modes M_i and the laser cavity modes N_i from [138].	105
5.6	Steady-state solutions with respect to parameter C . Solid and dashed lines are obtained for $C = 0.76$ and $C = 9.50$, respectively. The black circle corresponds to the single solution for $C < 1$ and white circles represent the various solutions for $C > 1$ from [200].	107
5.7	Carrier density variation as a function of the phase difference. Crossing points between solid and dashed sine waves give the locations of the modes. The red dot is the free-running mode [200].	107

5.8	Spectral linewidth as a function of the feedback strength. The markers represent different feedback phase conditions from [211].	108
5.9	(a) Numerical bifurcation diagram. Corresponding time trace for $\eta = 0.001$ (b), time trace for $\eta = 0.0027$ (c), time trace for $\eta = 0.0042$ (d), from [112].	109
5.10	Extrema of intensity as a function of bias current for a III-V laser integrated on silicon under free-running operation [230].	111
5.11	(a) Optical and (b) electrical spectra of the GS laser measured at $3 \times I_{th}$ without feedback (solitary) and for the maximal feedback strength. (c) Optical and (d) electrical spectra of the ES laser measured at $2.5 \times I_{th}$ without feedback (solitary) and for the maximal feedback strength [99].	112
5.12	Critical feedback level r_{crit} as a function of the effective α_H -factor for $\tau_{SRH} = 0.1, 0.5, 1$ and 5 ns, respectively.	115
5.13	Schematic representation of the setup for coherent optical feedback setup. .	116
5.14	Schematic representation of the setup for incoherent optical feedback setup.	117
5.15	External modulation transmission experiment with optical feedback apparatus. MZM: Mach-Zehnder modulator; SOA: semiconductor optical amplifier; SMF: 2 km long single mode fiber coil; VOA: variable optical attenuator. .	118
5.16	Light-current characteristics of laser #4. The red markers correspond to the optical spectra depicted in Fig.5.17.	119
5.17	Optical spectra measured for QD laser #4: (I) GS lasing, (II) GS-ES dual state lasing, (III) ES lasing. The bias conditions correspond to the red markers reported in Fig.5.16.	120
5.18	Spectral dependence of the α_H -Factor measured by amplified spontaneous emission (ASE) in QD lasers #2 and #3.	121
5.19	Optical and RF spectra for QD laser #2 (a,b) and #3 (c,d) operating in the free-running $r_{ext} = 0$ (black) condition and under $r_{ext} = 20\%$ optical feedback at $2 \times I_{th}$	122
5.20	Optical (first column) and RF (second column) spectra mappings of QD laser #3 measured at $2 \times$ ((a),(b)), $2.85 \times$ ((c),(d)) and $3.75 \times I_{th}^{GS}$ ((e),(f)) bias. The green lines mark the critical feedback levels (r_{crit}).	124
5.21	The critical feedback level r_{crit} for QD lasers #1, #2, #3, and #4 (with different ratio I_{th}^{ES}/I_{th}^{GS}) plotted as a function of the ratio of the bias current to the ES lasing threshold I/I_{th}^{ES}	125

5.22	(a) Optical and (c) RF spectral mappings of the p-doped QD laser on silicon as a function of the feedback strength at $3 \times I_{th}$; (b) Optical and (d) RF spectral mappings of the QW laser as a function of the feedback strength at $3 \times I_{th}$. The vertical axis is in logarithmic scale.	127
5.23	Critical feedback level (r_{crit}) as a function of the reflectivity. The black dotted lines indicate the lasers with facet reflectivity of cleave/99% and 60%/99%.	128
5.24	Optical spectra under free-running (red) and 20% (blue) of total reflection.	129
5.25	RF and optical spectra for the main longitudinal mode (gain peak) as a function of r_{ext} for the undoped laser at 293 K ((a), (e)) and 303 K ((c), (g)), as well as for the p-doped laser at 293 K ((b), (f)) and 303 K ((d), (h)). The bias current is fixed at $3 \times I_{th}$ for all subplots.	130
5.26	RF spectra in free-running and under 40% incoherent feedback for (a) undoped and (b) p-doped lasers.	132
5.27	BER plots for back-to-back (B2B) and after transmission (Trans.) with and without feedback (FB) for undoped device at (a) 293 K. (b) Eye diagram of the solitary laser and (c) with maximal feedback in B2B configuration. (d) Eye diagram of the solitary laser and (e) with maximal feedback after transmission. The maximal feedback level is at -8 dB and the bias current is fixed at $3 \times I_{th}$	133
5.28	BER plots for back-to-back (B2B) and after transmission (Trans.) with and without feedback (FB) for undoped device at (a) 303 K. (b) Eye diagram of the solitary laser and (c) with maximal feedback in B2B configuration. (d) Eye diagram of the solitary laser and (e) with maximal feedback after transmission. The maximal feedback level is at -8 dB and the bias current is fixed at $3 \times I_{th}$	133
5.29	BER plots for back-to-back (B2B) and after transmission (Trans.) with and without feedback (FB) for p-doped device at (a) 293 K. (b) Eye diagram of the solitary laser and (c) with maximal feedback in B2B configuration. (d) Eye diagram of the solitary laser and (e) with maximal feedback after transmission. The maximal feedback level is at -8 dB and the bias current is fixed at $3 \times I_{th}$	134

5.30	BER plots for back-to-back (B2B) and after transmission (Trans.) with and without feedback (FB) for p-doped device at (a) 303 K. (b) Eye diagram of the solitary laser and (c) with maximal feedback in B2B configuration. (d) Eye diagram of the solitary laser and (e) with maximal feedback after transmission. The maximal feedback level is at -8 dB and the bias current is fixed at $3 \times I_{th}$	134
5.31	B2B BER curves for solitary QW laser (red) and under 0.004% feedback (blue, eye-diagram in (b)). (c) eye-diagram of the laser under 0.4% feedback, above the critical level. The bias current is fixed at $3 \times I_{th}$	135
7.1	Schéma de principe de la dynamique des porteurs selon le modèle excitonique de relaxation en cascade.	145
7.2	(a) Contribution de $F_{RS,ES,GS}$ aux spectres de RIN à $1.5 \times I_{th}$, $2.5 \times I_{th}$, et $3.5 \times I_{th}$ respectivement; (b) Spectres de RIN à $1.5 \times I_{th}$ pour les cas comprenant $F_{RS,ES,GS}$, $F_{ES,GS}$, F_{GS} et sans bruit de porteurs $F_{RS,ES,GS} = 0$	147
7.3	(a) Contribution de $F_{RS,ES,GS}$ aux spectres de FN à $1.5 \times I_{th}$, $2.5 \times I_{th}$, et $3.5 \times I_{th}$ respectivement; (b) Largeur de raie spectrale calculée en fonction du courant normalisé.	147
7.4	(a) La structure du laser ; (b) Image MEB montrant une coupe transversale de la zone active du laser, le réseau de diffraction ainsi que les plans de boîtes quantiques.	148
7.5	Courbes courant-puissance et spectres optiques à 100 mA pour les lasers DFB InAs/InP AR/HR (a) et AR/AR (b). Les points rouges indiquent les mesures effectuées à $3 \times I_{th}$	148
7.6	(a) Largeur de raie en fonction du courant de pompe normalisé pour les lasers DFB AR/HR (en rouge) et AR/AR (en bleu). (b) Spectres de RIN mesuré à 95 mA pour le laser AR/AR.	149
7.7	(a) Illustration schématique de la structure épitaxiale du laser. (b) Spectre de photoluminescence de laser complet. L'encart montre une image au microscope à force atomique de boîtes quantiques InAs et la barre d'échelle est de 200 nm.	150
7.8	(a) La courbe courant-puissance du laser et le point rouge indique la mesure effectuée à $3 \times I_{th}$. (b) Le spectre optique mesuré à $3 \times I_{th}$	151
7.9	Schéma de la configuration expérimentale de retour optique externe.	151

-
- 7.10 (a) Spectres optique du laser hybride sur silicium mesurés à $3 \times I_{th}$ sans rétroaction (solitaire) et pour la force de rétroaction maximale (- 9 dB). (b) Cartographie des spectres électriques du laser hybride mesuré en fonction de r_{ext} 152
- 7.11 (a) Spectres optique du laser à boîtes quantiques sur silicium mesurés à $3 \times I_{th}$ sans rétroaction (solitaire) et pour la force de rétroaction maximale (- 7 dB). (b) Cartographie des spectres électriques du laser à boîtes quantiques mesuré en fonction de r_{ext} 153
- 7.12 (a) Les courbes BER en fonction de la puissance de réception par le détecteur pour le cas sans rétroaction et la force de rétroaction maximale après la transmission de 2 km. La ligne horizontale pointillée de couleur noire correspond à la limite conventionnelle sans erreur (BER = 10^{-9}). Diagramme de l'œil pour le cas sans rétroaction (b) et la force de rétroaction maximale (c). 154
- 7.13 (a) Les variations spectrales du facteur α_H sous-seuil pour le laser à boîtes quantiques et le laser à puit quantique. (b) Le facteur d'amortissement en fonction de la fréquence d'oscillation de relaxation au carré pour le laser à boîtes quantiques et le laser à puit quantique. 155

List of tables

1.1	Comparison of the price and wafer diameter for native substrate and silicon substrate from [196].	4
3.1	Material and optical parameters of the InAs/InP(311B) QD laser.	44
4.1	Static and dynamic characteristics of the undoped and p-doped QD lasers and QW laser.	76
5.1	Parameters of the InAs/GaAs QD lasers including from top to bottom, the ridge width, the threshold currents, the ES-to-GS lasing threshold ratio, the peak wavelength, and the GS-ES energy separation.	121

Chapter 1

Introduction

1.1 Needs for optical communication

Optical communication networks have been developed for years to make a global telecom networks which are structured in three main scales [107]. The first scale is the long haul networks, which connect continents with transpacific cables and transatlantic cables (several thousands kilometers). Second, the metropolitan networks connect countries and cities (several hundreds kilometers), which have a ring topology to efficiently connect regional, access and data center interconnects networks. Finally, the access networks connect individual endpoints to the local exchanges, while the interlinks are usually of a few kilometers. The C-band (1530-1565 nm) wavelength window is the preferred choice for long-haul optical communication since the optical fiber loss at 1550 nm is as low as 0.2 dB/km. Indeed, the low loss means that the signal needs to be amplified only every one hundred kilometers. Apart from the loss, another important parameter of the optical fiber is the chromatic dispersion, which leads to the broadening of the pulse light during the propagation. This dispersion is null at 1310 nm hence the O-band (1260-1360 nm) is suitable for short distances communication such as the up-streaming the data from the customer premises to the central office.

Over the years, data traffic increases at each scale especially the smartphones generate a large amount of data and 4 K videos need large bandwidth. However, due to the chromatic dispersion, the different modes in optical fiber don't propagate at the same speed and the signal can be distorted after certain distance. Therefore, the single mode laser is a preferable solution. In order to increase data traffic, the wavelength division multiplexing (WDM) technology needs to be introduced, which allows different data streams at different frequencies to be sent over a single optical fiber network and signals at WDM wavelengths are independent from each other [26]. As presented in Fig.1.1, multiple lasers can be simultaneously modulated, and then each modulated wavelength is multiplexed by a passive

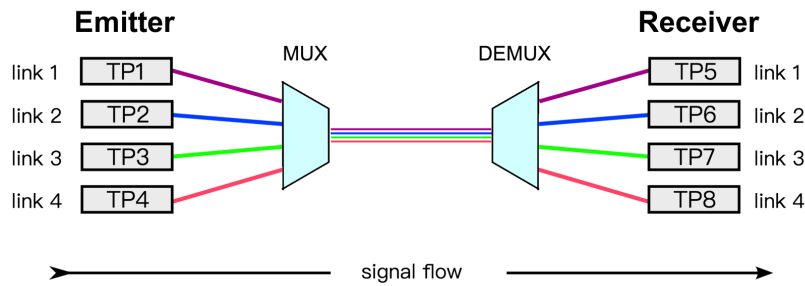


Fig. 1.1 Schematic representation of a WDM system with multiple wavelength channels. [26].

multiplexer. At the receiver side, wavelengths are demultiplexed and each wavelength is detected independently. As multiple lasers, modulators and filters are needed in the same WDM systems, photonic integrated circuits (PICs) are on demand since all components can be integrated on a single chip to ensure the cost-effective information transmission.

1.2 Photonic integrated circuits

Development of on-chip photonic integration brings many innovative perspectives, in particular, deployable gas and biomolecular sensing systems, compact laser-based radars for self-driving automobiles as well as energy efficient interconnects for datacom and telecom [197, 193, 89]. PICs based on InP provides high performance but the disadvantages are the high cost of InP wafers and the small size of the processed wafers [254, 130]. To address this issue, silicon photonics has been developed to make the PICs in high volume and lower cost [60, 261, 37, 17, 247]. Indeed, the building blocks that are available in the silicon photonic platform allow for the integration of a vast array of functionalities in a single circuit [246]. Over the past decades, silicon photonics have been introduced to overcome low efficiency and high energy consumption of metal wiring, in particular for high-speed communication systems, optical interconnects as well as board-to-board and chip-to-chip integrated circuits [8, 14, 147, 9, 36, 193].

Although silicon exhibits a strong index contrast with silica ($\Delta n \approx 2$) hence being an excellent candidate for an on-chip waveguide with strong light confinement, it can not provide efficient light emission due to its indirect bandgap nature. For instance, an electrically pumped germanium laser has been achieved with threshold current density of 300 kA/cm^2 which is much higher than what is observed in direct-gap III-V materials integrated with silicon [31]. More recently, a path towards lasing emission with pure germanium microdisk has also been proposed [58]. Despite that, to overcome this issue, many efforts have been devoted to

fabricate integrated light sources [36, 51, 116, 136, 137] either by considering heterogeneous integration of III-V semiconductor materials on silicon, or more easily through direct epitaxial onto silicon or even germanium [294, 114, 162]. The heterogeneous integration refers to III-V materials bonded to silicon-on-insulator (SOI) substrates [220]. Using this approach, many III-V semiconductor gain region such as GaAs and InP are bonded on a single silicon wafer in order to achieve optical transceivers. Fig.1.2 shows the historical evolution of PIC integration densities where the complexity of heterogeneous integration has grown fast and caught up with that of PIC on native InP substrate with over 400 photonic components on a single silicon substrate [288]. Nowadays, heterogeneous integration has been widely adopted by industry such as Juniper Networks, Hewlett Packard Enterprise and Intel [128, 148, 109].

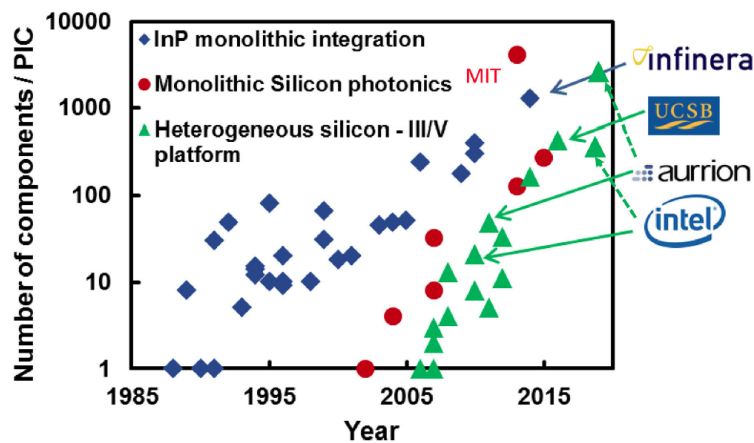


Fig. 1.2 Component counts in a single PIC comparing PIC on native InP, monolithic silicon photonics and heterogeneous integration from [89].

However, the drawbacks of heterogeneous integration consist in the high cost as well as the limited scalability. For heterogeneous integration, all III-V devices are firstly grown on a native substrate and then the whole device is bonded to silicon substrate while the native substrate is removed and discarded. Table 1.1 illustrates the comparison of the wafer cost and maximum size among native substrates and silicon substrate. As shown, compared with silicon wafer, the native substrates are not only orders of magnitude more expensive but also available at much smaller wafer sizes.

The only way to overcome the high costs of heterogeneous integration is to move on to direct epitaxial III-V materials on silicon process for photonics integration [156]. As shown in the Fig.1.2, recent advances in monolithic silicon complexity has comparable density to heterogeneous integration. The challenge of the epitaxial process is the mismatch between III-V material and silicon. For instance, the mismatch is 4 % between GaAs and silicon while

Table 1.1 Comparison of the price and wafer diameter for native substrate and silicon substrate from [196].

	InAs	InP	GaAs	SOI	silicon
Substrate cost (<i>dollar/cm²</i>)	18.25	4.55	1.65	1.30	0.20
Maximum size (cm)	7.6	15	20	45	45

it reaches 8 % between InP and silicon. Indeed, non-nitride III-V materials have larger lattice constants and higher coefficients of thermal expansion leading to high density of crystalline defects including primarily threading dislocations and antiphase domains. Fortunately, the defect density can be reduced by a few orders of magnitude attaining near native substrate level performance by means of careful optimization of growth conditions and utilization of dislocation filtering layers and techniques [156, 66, 114, 145]. Owing to the individual nature of quantum dots (QDs), QDs are more tolerant to epitaxial defects than their quantum well (QW) counterparts hence providing efficient stimulated emission despite in the presence of high-density defects [162, 115]. Fig.1.3 shows the comparison of room-temperature photoluminescence spectra from QW and QD structure grown on GaAs versus silicon. The intensity of the QW degraded by more than a factor of 10 when grown on silicon compared with grown on GaAs. However, the intensity of the QD on silicon is roughly 80% of the reference QD grown on GaAs with comparable linewidths, showing a good tolerance to epitaxial defects [159]. Consequently, QD lasers become the primary choice for monolithic integrated laser source on silicon.

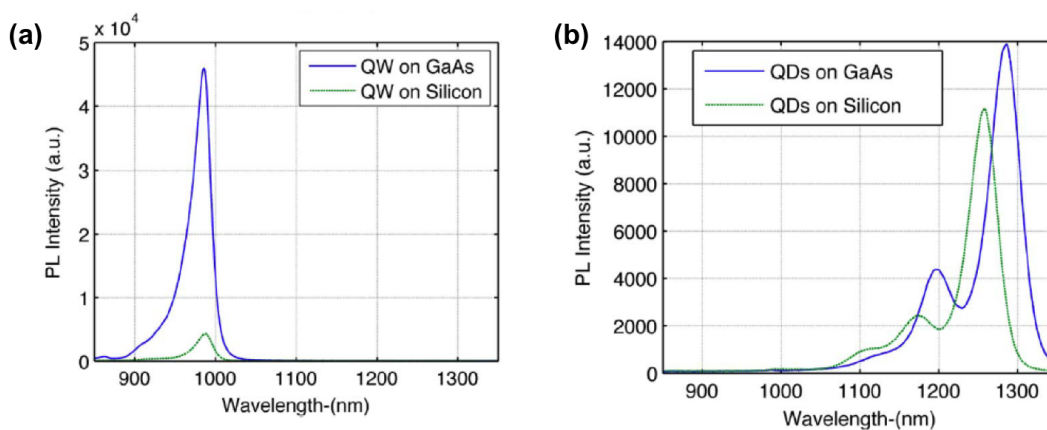


Fig. 1.3 Room-temperature photoluminescence comparison of single QW layer (a) and single QD layer (b) grown on GaAs versus silicon substrates [159].

1.3 Development of quantum dot (QD) lasers

1.3.1 GaAs-based and InP-based QD lasers

The semiconductor laser was at first demonstrated in 1960. Then, significant achievements have been reported including the room temperature and continuous wave lasing performance by using bulk heterostructure [135, 5]. Fig.1.4 displays the evolution of the density of states for bulk, QW as well as QD. As shown, in comparison with bulk material, the QW depends on using an ultra-thin film with a thickness of a few nanometer (nm) hence the carriers are confined in one dimension [260]. When one or more spatial dimensions of the nanocrystal approach the de Broglie wavelength of the carrier (~ 10 nm), the quantum confinement of electrical carriers occurs and leads to a quantification of the density of states. Thus, the continuous electron energy band of bulk semiconductor is split into discrete energy levels [49]. Owing to this discrete energy levels, the first QW laser is presented in 1975 exhibiting lower threshold current than that of bulk laser [260].

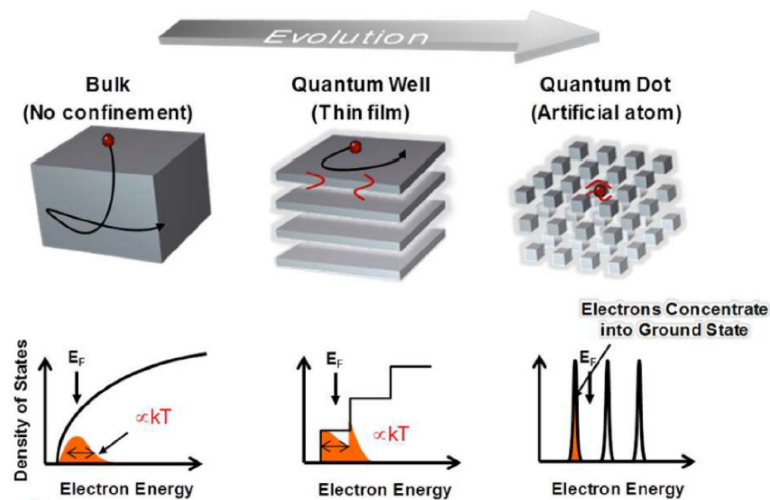


Fig. 1.4 Evolution of the density of states for bulk material, quantum well and quantum dot, respectively, from [193].

The formation of low dimensional nanostructures such as QD results from decreasing the three dimensional degree of freedom of carriers. Ideally, QD structure exhibits an atom-like density of states hence offering an ultimate carrier confinement as shown in Fig.1.4. The concept of QD laser has been firstly proposed in 1982 by Arakawa *et al.* [10] and demonstrated in 1994 by Kirstaedter *et al.* [126] with Mirin *et al.* in 1996 [183] showing the first clear evidence of the atom-like density of states. In the QDs, electrons and holes are three dimensionally confined into nanometer scale semiconductor crystals and the situation

is like an artificial atom. Compared to bulk and QW lasers, QD lasers have shown superior performances including low threshold current density [161], high temperature stability [182], high material gain and differential gain [22, 21].

However, it was quiet difficult to realize high-quality QDs. One initial approach used to obtain arrays of QDs was to apply patterned mesa-etched QWs grown by metal-organic chemical vapor deposit (MOCVD) or Molecular beam Epitaxy (MBE) [139, 184]. Etched QW layers not only produce radiative recombinations but also nonradiative defects which alter the material quality of the nanostructure matrix. Therefore, self-assembled QDs present their advantages such as uniformity, high density and high crystalline quality almost without dislocations, which are beneficial for high-quality QD lasers. The first report relating InAs/GaAs QD laser with self-assembled QDs operation at 77 K from a single QD layer was published in 1994 [126]. After that, great progresses had been made to achieve ultra-low threshold current density (26 A/cm^2) at room temperature [105, 161]. In order to increase the material gain, QD lasers with multiple stacks of dots are required [140]. Nevertheless, the increase of stacks number also accumulates the strain in each dot layer hence necessitating to use a thicker spacer in the structure to reduce the contribution to the gain and slow down the carrier dynamics [134]. The limit of the maximum number of dot layers is about $10 \sim 15$ for InAs/GaAs QD lasers [225].

InAs/GaAs QD lasers emitting in the O-band which exhibit both high thermal stability and low threshold current density that are both favorable to reduce the energy per bit consumption in the short-reach communication links [57]. On the other hand, InAs QDs grown on InP substrates are desired for quantum confined devices operating in the C-band. The first InAs/InP QD laser emitting at $1.84 \mu\text{m}$ at 77 K was reported in 1998 [259] and then room temperature operation was realized [194]. The first achievement of lasing at room temperature with a single QD layer on an InP substrate is published in 2007 [95]. In comparison with InAs/GaAs systems, the formation of nanostructures on InP is much more challenging than on the GaAs substrate because the lattice mismatch in InAs/InP (3%) is smaller than that in InAs/GaAs (7%) [71]. This small lattice mismatch along with the complex strain distribution lead to the formation of elongated dots named as quantum dash (QDash) instead of QD. QDash exhibits mixed characteristics in between QW and QD [277]. The QDashes are strongly anisotropic nanostructures and exhibit electronic properties rather close to quantum wires. A recent work demonstrates the importance of the dash orientation in the optical properties of the laser gain medium. Compared with QDash oriented parallel to the cavity axis, QDash perpendicular to the cavity shows the reduced linewidth enhancement factor (α_H -factor) hence the critical feedback level is found to be up-shifted by 11 dB [50]. The importance of α_H -factor and feedback resistance in semiconductor lasers will be discussed in

the following chapters. Thus, in order to fabricate the real InAs/InP QDs instead of QDash, the use of miscut InP(100) or InP(311)B misoriented substrates are required [122].

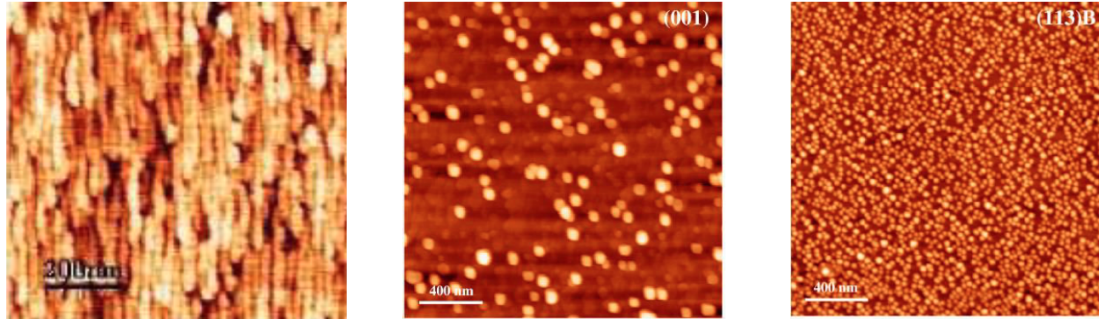


Fig. 1.5 Atomic force microscopy image of InAs QDashes grown on InP(100) substrate (left), QD grown on InP(100) substrate (middle) and QD grown on InP(311)B substrate (right) [6].

Fig.1.5 shows the atomic force microscopy (AFM) images of InAs/InP QDash, QD grown on InP(100) substrate and QD grown on InP(311)B substrate. The formation of QD or QDashes on InP(100) substrate is more complicated hence strongly depending on the growth conditions and on the thickness of the InAs layer. One of the major drawback for obtaining lasers with good performance is the low QD density on the order of $10^9 \sim 10^{10} \text{ cm}^{-2}$ provided by this kind of substrate [132]. By employing chemical beam epitaxy (CBE), an InAs/InGaAsP grating coupled external cavity QD lasers with an increased dot density of $3 \sim 6 \times 10^{10} \text{ cm}^{-2}$ has been reported [7]. As compared to InP(100) substrate, high indexed InP(311)B substrate provide higher nucleation point density which strongly reduces the surface migration effects and allows the formation of more symmetrical QDs in the planar direction. Moreover, a higher dot density of $5 \times 10^{10} \sim 10^{11} \text{ cm}^{-2}$ can be obtained [95, 44] as well as a smaller dispersion in size with dot sizes of 3 nm in high and 30 to 50 nm in wide have been reported [146]. However, due to the more complex technological process, applications of InAs/InP(311)B QD lasers are still limited with the industrial standards.

1.3.2 Silicon-based QD lasers

Since the lasers were the primary components in the silicon photonics platform, a lot of III-V/Si heteroepitaxy research has been focused on generating efficient lasers. The first laser ever reported on silicon was an AlGaAs double heterostructure laser with threshold current density of 10.8 kA/cm^2 and operating in pulsed mode at 77 K in 1984 [282]. In 2003, room temperature and continuous wave operation were achieved in a QW laser on silicon with threshold current density of 269 A/cm^2 along with a device lifetime of 4 h [79]. To the best of our knowledge, this is the record performance of epitaxial QW laser on silicon.

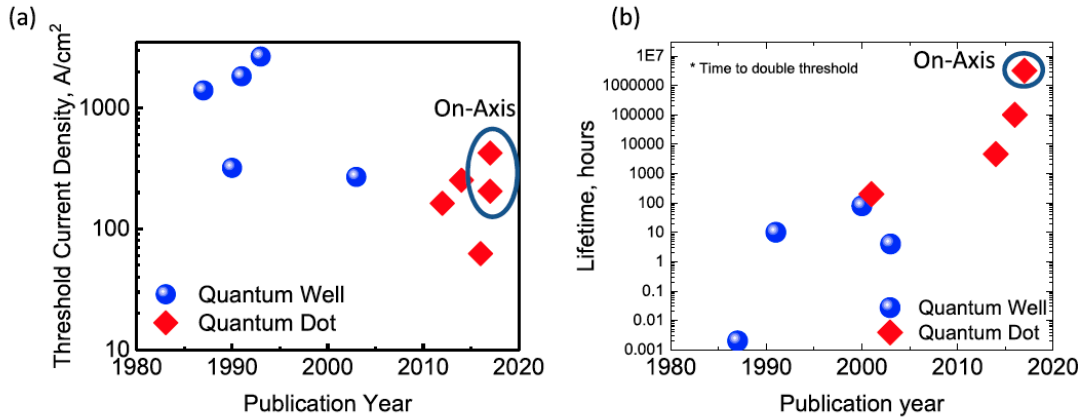


Fig. 1.6 Threshold current density (a) and device lifetime (b) (either extrapolated or measured) for lasers on silicon operating in the continuous wave mode from [196].

In the mean time, the first QD laser on silicon was grown in 1999 and lased under pulsed conditions at 80 K with a threshold current density of 3.85 kA/cm^2 [154]. In 2005, QD lasers on silicon were also being operated continuous wave and at room temperature with threshold current density of 1.5 kA/cm^2 [181]. In 2011, the first QD laser realized on a germanium substrate is presented with a low threshold current density of 55.2 A/cm^2 and under continuous-wave current drive at room temperature [162]. The advantage of using germanium substrate is that the lattice constant of GaAs was closely matched to germanium (0.08% mismatch). Since then, tremendous effort have been done to demonstrate the laser emission of InAs/GaAs QD lasers epitaxially grown on germanium-on-silicon substrate, offcut silicon substrate, and on-axis (001) silicon substrate [141, 36, 158]. In order to minimize the defect density, a lot of efforts have been devoted through the optimization of the buffer layer. The defect density has been reduced down to the order of $10^5 \sim 10^6 \text{ cm}^{-2}$, which is yet at least two orders of magnitude higher than that of QD laser on the native GaAs substrate [114, 115, 36]. Meanwhile, static performances of QD lasers on silicon have shown considerable improvements in terms of the threshold current density, the quantum efficiency, the high temperature operation as well as the aging lifetime. In 2016, the threshold current density as low as 62.5 A/cm^2 and extrapolated lifetimes $> 100\,000 \text{ h}$ have been reported in [36]. In 2017 and 2018, researchers at the University of California Santa Barbara have achieved QD lasers on silicon with threshold currents as low as 9.5 mA, single-facet output powers of 175 mW, ground state lasing up to $80 \text{ }^\circ\text{C}$, wall-plug-efficiencies as high as 38.4%, extrapolated lifetimes in excess of 10 000 000 h for aging at $35 \text{ }^\circ\text{C}$ and twice the threshold current density [115, 117, 116]. These high-quality lasers are used for investigating the

dynamical characteristics in chapter 4 and 5. Fig.1.6 shows the historical trends in threshold current density and device lifetime for QD lasers on silicon with the record values.

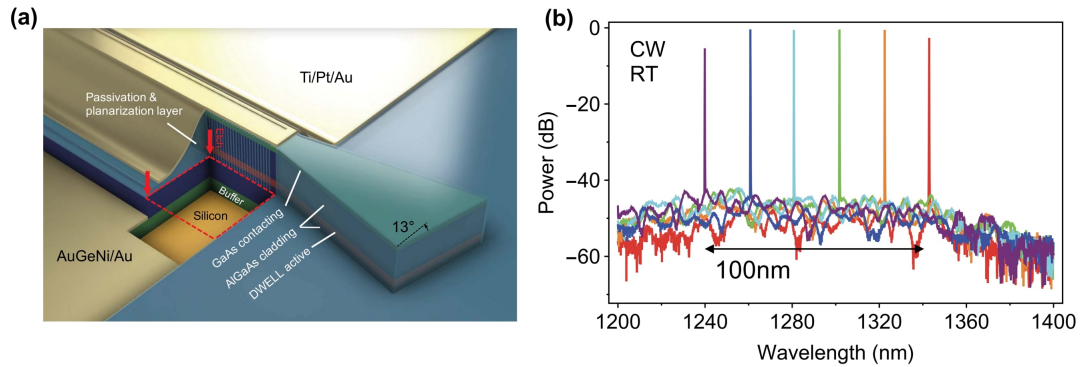


Fig. 1.7 (a) Cutaway schematic of DFB laser array on silicon showing the vertical layer structure, the output coupler and the etched gratings. (b) Optical spectra of a DFB laser array with different grating periods around their maximum output power levels before saturation at room temperature [278].

InAs/GaAs QD lasers on silicon based on Fabry-Perot (FP) cavity have been successfully achieved as aforementioned, which emit on multimodes. However, both optical communication and data center networks applications require single-mode laser sources, which are widely realized by distributed feedback (DFB) gratings. The first DFB QD lasers on silicon was successfully demonstrated by Wang *et al.* in 2018, showing a high side mode suppression ratio of 50 dB. Fig.1.7(a) displays the laser structure with the etched gratings. Besides, Fig.1.7(b) also shows the laser array compatible with WDM systems covering the full span of the O-band (100 nm) with a channel spacing of 20 nm [278].

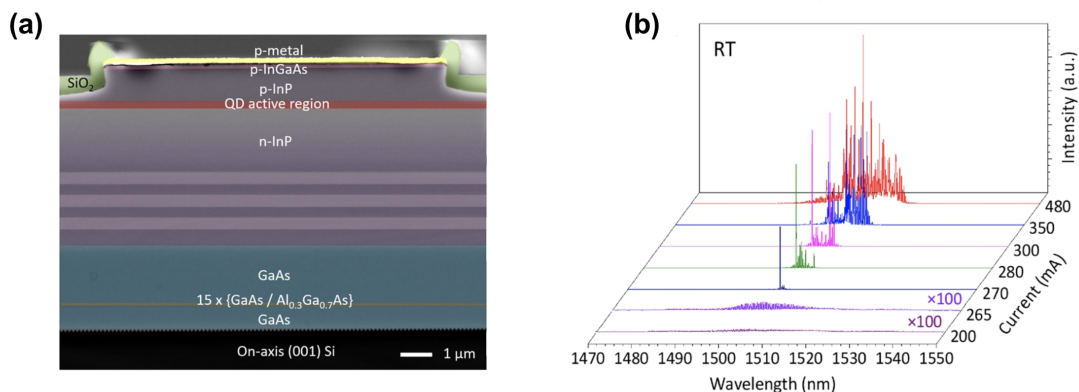


Fig. 1.8 (a) Color-enhanced cross-sectional scanning electron microscopy (SEM) image of the whole epitaxial structure. (b) Optical spectra at various pump currents [297].

Compared with InAs/GaAs QD lasers on silicon emitting in the O-band, the silicon-based C-band laser emission is also required for long haul communication. However, the fabrication of $1.5\ \mu\text{m}$ InAs/InP QD lasers directly grown on silicon is more challenging than that of $1.3\ \mu\text{m}$ InAs/GaAs QD lasers due to the lattice mismatch between InP and silicon is as large as about 8% and twice the mismatch between GaAs and silicon. This problem is circumvented through using V-grooved silicon substrate, which traps most twinned stacking faults in silicon but the defect density at the interface of the InP buffer layer is still as high as $10^9 \sim 10^{10}\text{cm}^{-2}$ [268, 145]. Despite these high defect density, Zhu *et al.* successfully demonstrated InAs/InP QD laser epitaxially grown on silicon with pulsed current pumping [297]. Fig.1.8(a) shows the complete structure of InAs/InP QD laser epitaxial on silicon and Fig.1.8(b) illustrates the optical spectra emitting at $1.5\ \mu\text{m}$ at various pump currents.

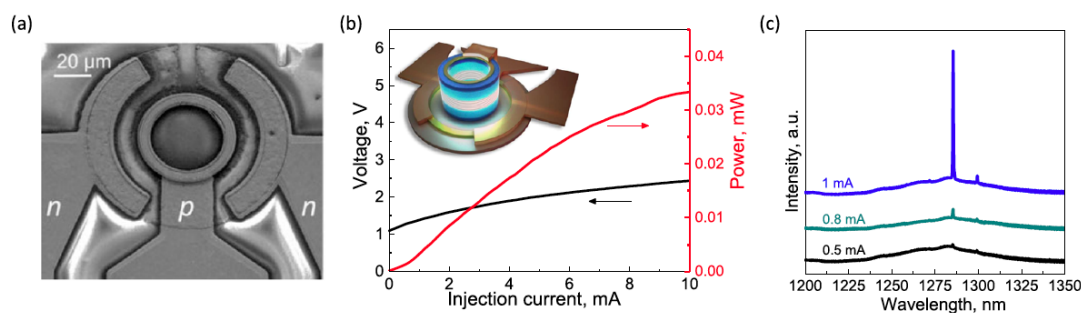


Fig. 1.9 (a) Scanning electron micrograph of a microring device. (b) Power-current-voltage curves for a sub-millamp threshold laser with inset illustration. (c) Optical spectra showing the lasing mode for various pump currents [271].

FP and DFB QD lasers on silicon typically have a footprint in the millimeter range. However, micro-disk as well as micro-ring lasers on silicon can reduce the laser footprint down to the micrometer range [269, 270, 267, 271], which are in favour of photonics integration. To this end, heterogeneous integration of QW micro-disk lasers on silicon have been achieved for optical interconnects [223, 83]. Using injection-locking scheme, the modulation bandwidth can be enhanced by involving distributed Bragg reflector master laser monolithically integrated with whistle-geometry micro-ring laser [239]. Recently, Wan *et al.* demonstrated record-small electrically pumped QD micro-ring lasers epitaxially grown on silicon substrates with continuous-wave lasing up to $100\ ^\circ\text{C}$ at $1.3\ \mu\text{m}$. Fig.1.9(a) shows the microring structure with a radius of $5\ \mu\text{m}$ and Fig.1.9(b) illustrates a submilliamp threshold of $0.6\ \text{mA}$ was achieved while the optical spectra are presented in Fig.1.9(c). These thresholds and footprints are orders of magnitude smaller than those previously reported lasers epitaxially grown on silicon.

1.4 Motivations of the dissertation

Based on the improved static performances of QD lasers, the dynamical characteristics of such lasers are drawing more and more attentions. The dynamic and nonlinear properties can directly determine the design of PIC systems. Therefore, the motivations and objectives of this thesis are concentrated on the following aspects:

First part of the thesis concentrates on InAs/InP QD lasers emitting at 1550 nm. With the growing requirement for transmission capacity in optical communication systems, coherent technology has been attracting more and more attention [124]. A coherent system is able to restore both the amplitude and phase information of optical signals, but remains very sensitive to the phase noise of both the transmitter and local oscillator [204]. Fig.1.10 shows the schematic of the coherent detection where a local oscillator mixes with the received signal to generate a product term. As a result, the received signal can be demodulated or frequency translated. In order to reduce the noise in the detection part, local oscillators with low phase noise are required.

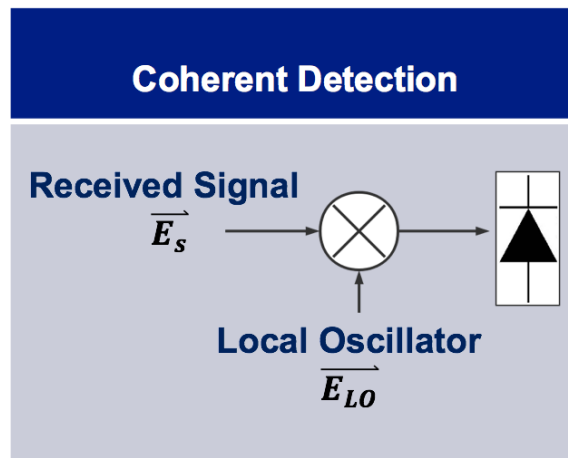


Fig. 1.10 Schematic of the coherent detection.

Indeed, although the frequency drift of the transmitter can be minimized, the carrier phase still fluctuates randomly because of the phase noise induced from the lasers. Therefore, a local oscillator with narrow spectral linewidth is a crucial requirement for realizing stable heterodyne detection. Over the past years, the fast digital signal processing (DSP) technology has been successfully implemented in the fibre transmission system and semiconductor lasers are nowadays used as local oscillators in coherent detection systems. Narrow linewidth lasers are especially important for new systems which use higher-order modulation formats. For instance, at 40 Gbit/s, the laser linewidth must be in the range of 240 kHz, 120 kHz, and 1

kHz for 16PSK, 16QAM, and 64QAM, respectively [235]. Apart from the high performance coherent communications systems, ultra-low noise semiconductor lasers are required for a wide range of applications including optical atomic clock [190], frequency synthesis [240], spectroscopy [245] as well as distributed sensing systems [65]. All these applications require oscillators with low frequency noise (FN) and relative intensity noise (RIN). This last point degrades the signal-to-noise ratio (SNR) and increases the bit-error rate of optical signals hence setting a limit of a high-speed communication system [41, 196]. A low RIN floor across the operating range is usually required to achieve a large SNR. System limitations due to poor SNR can be compensated by increasing the bias current of the laser source but at the price of a larger energy consumption. In radar related applications, the intensity noise of the laser is also of first importance since it is expected to be closed to that of the shot noise over a bandwidth ranging up to 20 GHz [46]. Although commercial solid-state lasers and fiber lasers have high performance, semiconductor lasers are still competitive in terms of size, power efficiency and cost. To meet these goals, QDs remain even more promising candidates owing to the ultimate carrier confinement and the low population inversion factor. For instance, Su *et al.* reported an InAs/GaAs QD laser with a linewidth around 500 kHz [46]. Lu *et al.* demonstrated a linewidth of less than 150 kHz in an InAs/InP QD laser [165] and a linewidth reduction from a few MHz to less than 200 kHz in an InAs/InP QD coherent comb laser by an external cavity self-injection feedback locking system [164]. Researchers at the University of Kassel, Germany and Technion—Israel Institute of Technology, Israel have made great progress in QD lasers linewidth reduction. For instance, Becker *et al.* reported a 1.2 mm long narrow linewidth InAs/InP QD laser with intrinsic linewidth of 110 kHz [18]. Very recently, Septon *et al.* further decreased the intrinsic linewidth down to 30 kHz with a 1.5 mm longer cavity [236]. As for the RIN, prior works have experimentally shown a RIN level as low as -160 dB/Hz on both InAs/GaAs and InAs/InP QD lasers [142, 32], whereas it was found slightly higher e.g. from -140 dB/Hz to -150 dB/Hz in QD lasers directly grown on silicon [149, 157].

Second part of the thesis focus on InAs/GaAs QD lasers directly grown on silicon. In PICs, unintentional reflections originating from various possible interfaces (active/passive transitions, waveguide crossings, regrowth interfaces unterminated fibers, etc.) can induce unwanted feedback effects to the laser. Most semiconductor lasers are relatively sensitive to optical reflections hence requiring the inclusion of an optical isolator to completely suppress the optical feedback. For instance, hybrid semiconductor lasers made with several passive and active interfaces/transitions between the III-V material and silicon can suffer from multiple internal reflections which when combined with external ones can become highly problematic for the laser stability [230]. However, up to now, no integrated isolator has been demonstrated

that provides strong isolation and negligible insertion loss, hence rendering the demonstration of feedback-insensitive lasers of paramount importance. The linewidth enhancement factor (α_H -factor) is known as one of the most important parameters of QD lasers, hence driving, for instance, the spectral linewidth and the sensitivity to optical injection or optical feedback [98]. At the system level, a large α_H -factor also results in a frequency chirping under direct modulation, hence limiting the maximum data rate and transmission distance over a dispersive fiber [129]. Apart from the α_H -factor, other dynamical and nonlinear features such as damping factor, relaxation frequency and gain compression are also worth investigating because of their strong importance for high-speed and reflection insensitivity performance [108]. In this context, InAs/GaAs QD lasers using nanostructures as gain media display a strong potential for cost reduction [57]. For instance, a recent work has reported on an InAs/GaAs QD laser transmitter integrated on silicon substrate without optical isolator for core I/O applications. An error-free transmission was successfully demonstrated at 25 Gbps using a pseudo random binary sequence (PRBS) pattern of $2^7 - 1$ [185]. Overall, QD lasers are more stable against optical feedback as opposed to their bulk or QW counterparts because of their quasi-class A behavior originated from the large damping [167]. The critical feedback level associated to the undamping of the relaxation oscillations and leading to the so-called chaotic state (e.g. coherence collapse) usually takes place at a higher feedback level [199]. Although prior works showed that this large feedback resistance depends on the type of QDs [155, 167] and the carrier dynamics through for instance the doping concentration [207], no study has reported on a total insensitivity down to a testbed environment. In this thesis, we will investigate the reflection sensitivity of QD lasers on silicon.

1.5 Organization of the dissertation

Based on the aforementioned motivations, this dissertation is organized as follows:

Chapter 2 reminds the fundamentals of QD lasers including the electronic structure and carrier scattering processes, the gain broadening mechanisms, the α_H -factor as well as the relaxation oscillations and damping. These fundamentals constitute a substrate for the understanding of the various experimental and theoretical investigations conducted throughout the thesis.

Chapter 3 investigate both experimentally and theoretically the FN, spectral linewidth and RIN characteristics of InAs/InP QD DFB lasers realized at the National Research Council of Canada. The simulations are analysed through a rate equation model taking into account both the spontaneous emission and carrier contributions. Results show that the carrier noise in the GS and the ES significantly increase the amplitude of the RIN, while the contribution

of the carrier noise in the RS remains negligible. In addition, it is demonstrated that the ES carrier noise contribution can be suppressed by considering QD lasers with a larger GS-ES energy separation, hence leading to a substantial reduction of the RIN. Simulations also point out that the carrier noise does not contribute that much to the FN which is determinant for narrow spectral linewidth operation as compared to what exists in QW or bulk lasers. Owing to the low inversion factor, experimental results show the potential of QDs as a gain medium for narrow spectral linewidth lasers. Using a DFB laser with asymmetric facet coatings, a spectral linewidth of 160 kHz (80 kHz intrinsic) is demonstrated. The temperature insensitive behavior between 283K and 303K agrees well with simulation. Symmetric anti-reflection facet coatings are also used to reduce the longitudinal spatial hole burning and make the spectral linewidth rather independent of the drive current. Nevertheless, a linewidth rebroadening is observed at higher temperature, which may be attributed to the spectral hole burning and to the variations of the α_H -factor with the temperature and bias current. Furthermore, the RIN of the symmetric DFB laser is experimentally discussed. An low RIN of less than -150 dB/Hz is measured in the range of 8 to 10 GHz. Both relaxation oscillation frequency and damping factor are also extracted from the curve fitting of the RIN spectrum.

Chapter 4 describes the effect of p-doping on the RIN properties and subsequently on the modulation properties of epitaxial InAs/GaAs QD lasers on silicon fabricated at University of California, Santa Barbara, USA. The measured RIN level is found very stable with temperature with a minimum value of -150 dB/Hz due to the low threading dislocations density and the p-modulation doped GaAs barrier layer in the active region. The dynamical features extracted from the RIN spectra show that p-doping between 0 and 30 holes/dot strongly modifies the modulation properties and gain nonlinearities through increased internal losses in the active region and thereby hindering the maximum achievable bandwidth. Moreover, we report on an ultra-low α_H -factor of 0.13 that is rather independent of the temperature range (288 K–308 K). Above the laser threshold, the α_H -factor does not increase extensively with the bias current. The below-threshold α_H -factor result was obtained from the amplified spontaneous emission (ASE), extracting the net modal gain change and longitudinal mode wavelength shift with the variation of the subthreshold current. Although this method has been used for years, it is known that it can possibly underestimate its value when thermal effects are not properly eliminated. Thus, we also performed the α_H -factor with a thermally insensitive method that relies on the evaluation of the gain and wavelength changes of the suppressed side modes by optical injection locking. Given that the method is thermally insensitive, the results show values of α_H -factor as low as 0.15, resulting from the low threading dislocation density and high material gain of the active region. Such results also confirm our initial measurements conducted with the ASE.

Chapter 5 systematically investigates the influence of optical feedback in epitaxial InAs/GaAs QD lasers on silicon. The boundaries associated to the onset of the critical feedback level corresponding to the first Hopf bifurcation are extracted at different bias conditions with respect to the onset of the first ES transition. Results show that QD lasers directly grown on silicon are much more resistant to optical feedback than QW lasers. However, results also unveil that the onset of the critical feedback level strongly depends on the ES-to-GS ratio, hence a figure of merit showing that a small ratio of the ES-to-GS lasing thresholds is not beneficial for maintaining a high degree of stability. Furthermore, the impact of the p-doping on the high-speed performance subjected to optical feedback is also discussed. Results show that quantum dot laser with p-doping exhibits reduced thermal sensitivity and intensity noise. Moreover, experiments show that these epitaxial QD lasers on silicon exhibit a very high degree of resistance to both incoherent and coherent optical feedback. 10 Gbps penalty-free transmissions are demonstrated under external modulation and for different temperatures. This feedback insensitivity results from the low α_H -factor, the high damping, the absence of off-resonance emission states and the shorter carrier lifetime.

Finally, chapter 6 gives a general conclusion and the perspectives to this thesis.

Chapter 2

Fundamentals of quantum dot lasers

This chapter will introduce the fundamental of quantum dot (QD) lasers. First, the electronic structure and carrier scattering processes including the capture and relaxation processes are presented. Second, the gain broadening mechanisms, the linewidth enhancement factor and dual states lasing emission feature are demonstrated. In the end, the dynamical properties in terms of relaxation oscillation frequency and damping factor are also introduced.

2.1 Electronic structure and carrier scattering processes

Fig.2.1 shows an illustration of the electronic structure in a QD laser. As shown, schematically, the active region of a QD laser contains a three-dimensional separate confinement heterostructure (SCH or barrier), a two-dimensional carrier reservoir (RS or roughly corresponding to the wetting layer) and dots spatially confined in three dimensions. In semiconductor physics, the discretization of the carrier mobility is achieved when the crystal dimension becomes lower or equal than the de Broglie wavelength of carriers. To this end, it is shown that the critical diameter D_{min} of discretization is defined as a function of the material band offset ΔE_c as follows [24]:

$$D_{min} = \frac{\pi \hbar}{\sqrt{2m_e^* \Delta E_c}} \quad (2.1)$$

where m_e^* the electron effective mass, $\hbar = h/2\pi$ the reduced Plank constant. Regarding the self-assembled QDs, the typical critical diameter value is 3 to 5 nm which is of the same order of magnitude of the dot dimension. Thus, the electronic structure of QD laser can be approximately displayed as a three-dimensional potential well with discretized energy levels.

In the QD laser structure, carriers are usually treated as quasi-free particles within the SCH and the RS. The densities of states for the SCH (per volume) and that for the RS (per

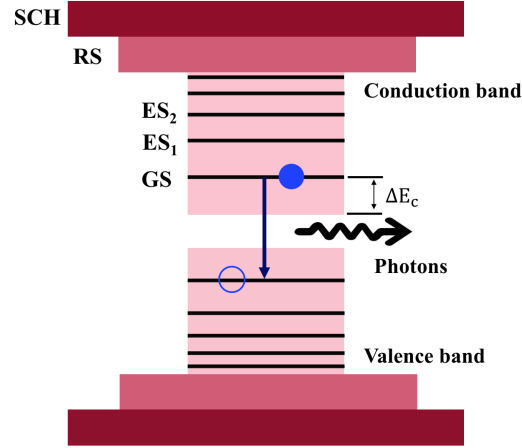


Fig. 2.1 Schematic of a QD laser electronic band structure of electrons and holes.

area) are respectively expressed as [67]:

$$\rho_{SCH} = 2 \left[2 \frac{m_{SCH}^*}{\hbar^2} \pi k_B T \right]^{3/2} \quad (2.2)$$

$$\rho_{RS} = \frac{m_{RS}^*}{\pi \hbar^2} k_B T \quad (2.3)$$

with m_e^* being the effective mass of either electrons or holes. It is noted that equations 2.2 and 2.3 are valid both for electrons from conduction band (CB) and holes from valence band (VB). The quasi-continuum carrier reservoir incorporating the localized energy states of the dots lead to smaller energy separations and thus states overlapping at higher energies. At lower energies, the discrete states are separated by a few tens of meV in the conduction band while such separation is smaller in the valence band because of the heavier effective hole masses [43].

Due to the Coulomb interaction, electrons and holes in the semiconductor active are bounded into excitons (electron-hole pairs). The Bohr radius of the exciton is defined as the distance between the electron and the hole within an exciton and is of a few nanometers [198]. Assuming the exciton approximation, semi-empirical QD laser model will be presented in Chapter 3. This model is simplified because it reduces half of the rate equations regarding the carrier populations. It is based on the configuration that the active region includes only one QD ensemble incorporating a two-fold degenerate ground state (GS) as well as a four-fold degenerate excited state (ES). This configuration has successfully reproduced noise properties as well as modulation dynamics of QD lasers [275, 272]. However, the excitonic approach has some limitations in predicting nonlinear behaviors such as the impact of p-doping on the

dynamical properties of QD lasers. In this case, the electrons and holes need to be considered respectively [226].

In a QD laser, once the current injection generates charge carriers in the SCH layer and then carriers transport across the SCH and reach the carrier reservoir for the localized QD states. The carrier transportation time through the SCH can be of several picoseconds (1 ~5 ps) depending on the thickness of the SCH [238]. The carrier dynamics in QD is mainly driven by two processes: the carrier capture and the carrier relaxation. The carrier capture process is that the subsequent carrier capture from the RS to the ES of dots. In the dots, carriers relax from high energetic ES levels down to the GS level, where the stimulated emission will take place owing to the recombination between electrons and holes. Moreover, carrier can also be directly captured from the RS to the GS level, which contributes to accelerate the carrier dynamics. This direct capture plays an important role on the dual-state lasing operation from which GS and ES can emit simultaneously [263].

The carrier capture and relaxation processes are supported mainly by Coulomb interaction induced carrier-carrier scattering (Auger process) as well as longitudinal optical (LO) phonon-carrier scattering [169]. The carrier scattering depends on the carrier density. At low carrier density, the interaction between carrier and LO phonons can offer the efficient scattering channels. While at high carrier density, carrier-carrier scattering from the RS into the dots is the dominant [191]. In addition, the relaxation time as low as 1 ps has been identified which is faster than the capture time [191].

2.2 Gain broadening mechanisms

In a real self-assembled QD laser, both homogeneous and inhomogeneous gain broadening mechanisms occur simultaneously. On the one hand, the homogeneous broadening is inversely proportional to the polarization dephasing time (T_2), which corresponds to the decay time of the optical polarization associated with an interband transition [232]. In the quasi-equilibrium carrier system, the dephasing time can be considered as a time constant, which is simply twice the total carrier scattering time [84]. The full width at half maximum (FWHM) of homogeneous broadening for a confined QD state can be expressed as [192]:

$$2\hbar\Gamma_{hom} = \frac{2\hbar}{T_2} = \hbar \left(\frac{1}{\tau_{hh}} + \frac{1}{\tau_{he}} + \frac{1}{\tau_{ee}} + \frac{1}{\tau_{eh}} \right) + \hbar \frac{1}{\tau_{phon}} + \hbar \frac{1}{\tau_{recom}} \quad (2.4)$$

where the first term represents the contribution of the Auger scattering process among electrons and holes (hh,he,ee,eh). The second term is due to the carrier-phonon interaction and carrier-carrier scatterings. The last term is attributed to the radiative recombination.

The homogeneous broadening is strongly temperature-dependent. Fig.2.2 shows the photoluminescence (PL) spectra as a function of temperature of a single InAs/GaAs QD. The PL spectrum broadens with the increase of the temperature from 2 K to 300 K hence the homogeneous broadening increases from a few micro-eV to a few meV [16].

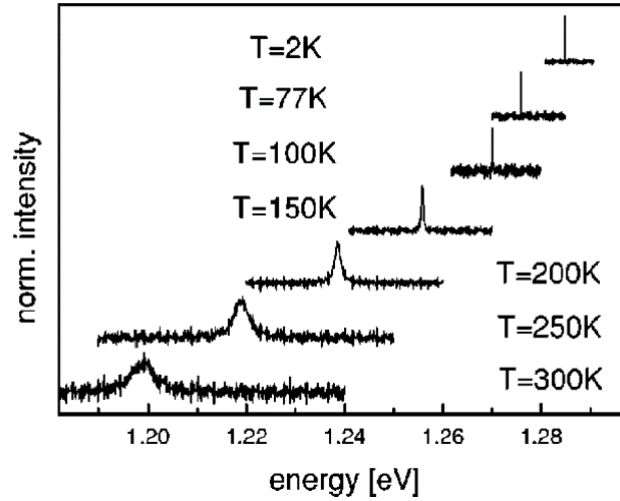


Fig. 2.2 Photoluminescence spectrum as a function of temperature from a single InAs/GaAs dot from [16].

In order to simulate the homogeneous broadening of QD active region, we start from solving the equation of motion for the electron-hole polarization amplitude $p_{\alpha\beta}$ is [38]:

$$\frac{dp_{\alpha\beta}}{dt} = i\omega_{\alpha\beta}p_{\alpha\beta} - i\Omega_{\alpha\beta}(n_{\alpha}^e + n_{\beta}^h - 1) + S_{\alpha\beta}^{c-p} + S_{\alpha\beta}^{c-c} \quad (2.5)$$

with $\omega_{\alpha\beta}$ and $\Omega_{\alpha\beta}$ are the renormalized transition and Rabi frequencies. n_{α}^e and n_{β}^h are the electron and hole populations in states α and β . $S_{\alpha\beta}^{c-p}$ and $S_{\alpha\beta}^{c-c}$ are the dephasing contributions from carrier-phonon and carrier-carrier scattering. And then the homogeneously broadened gain spectrum can be expressed as [290]:

$$G_M(\omega) = -\frac{\omega}{\epsilon_0 n c V E(\omega)} \text{Im} \left(\sum_{\alpha\beta} \mu_{\alpha\beta} p_{\alpha\beta} \right) \quad (2.6)$$

with ϵ_0 is the permittivity, c is the speed of light in vacuum, n is the refractive index, $E(\omega)$ is the laser electric field amplitude with ω the angular frequency, V is the volume of active region and $\mu_{\alpha\beta}$ is the dipole matrix element [38].

Fig.2.3 shows the simulated homogeneously broadened spectra with the increase of carrier density. The nonzero gain bandwidth is due to the carrier scattering mechanism (see

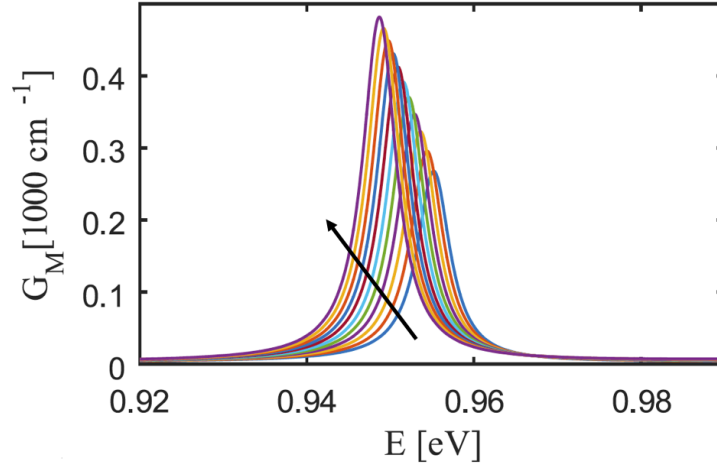


Fig. 2.3 Simulated homogeneously broadened gain spectra for various carrier density from [290]. The arrow points to the direction of increasing carrier density.

Eq.2.4) that results in a finite life time of carriers at certain energy state. This finite life time is translated to FWHM of ~ 5 meV in the homogeneously broadened gain spectrum. Furthermore, the red-shifted emission energy with the carrier density is due to bandgap renormalization from Coulomb interaction between discrete QD states and the RS [40, 231].

On the other hand, the self-assembled process of QD formation in crystal growth leads to nonuniformity in the QD size distribution. Fig.2.4 shows that QDs with dot size variation translates to an inhomogeneously broadened gain spectrum through the fluctuations in energy levels in QDs [15].

In order to simulate the inhomogeneous broadening, a statistical average over a range of band-gap energy ε to indicate the presence of inhomogeneous broadening due to QD size fluctuations has been performed as follows:

$$G_M^{inh}(\omega) = \int_{-\infty}^{+\infty} d\varepsilon \frac{1}{\sqrt{2\pi}\Delta_{inh}} \exp\left[-\left(\frac{\varepsilon - \varepsilon_g}{\sqrt{2}\Delta_{inh}}\right)^2\right] G_M(\omega) \quad (2.7)$$

with ε_g is the InAs bandgap energy and Δ_{inh} is an inhomogeneous broadening width by assuming a weighting described by a normal distribution. Fig.2.5 illustrates the inhomogeneously broadened gain spectrum which is the weighted sum of homogeneously broadened spectra of QD with different sizes [290]. This statistical broadening yields a highly symmetric and Gaussian-shape gain spectrum while the homogeneous broadening is rather in a shape of Lorentzian. As shown, the homogeneous QD group with highest dot density contribute to the peak gain. Owing to the small homogeneous gain bandwidth, QD groups more than 10 meV detuned from the gain peak hardly affect the peak gain despite their significant population.

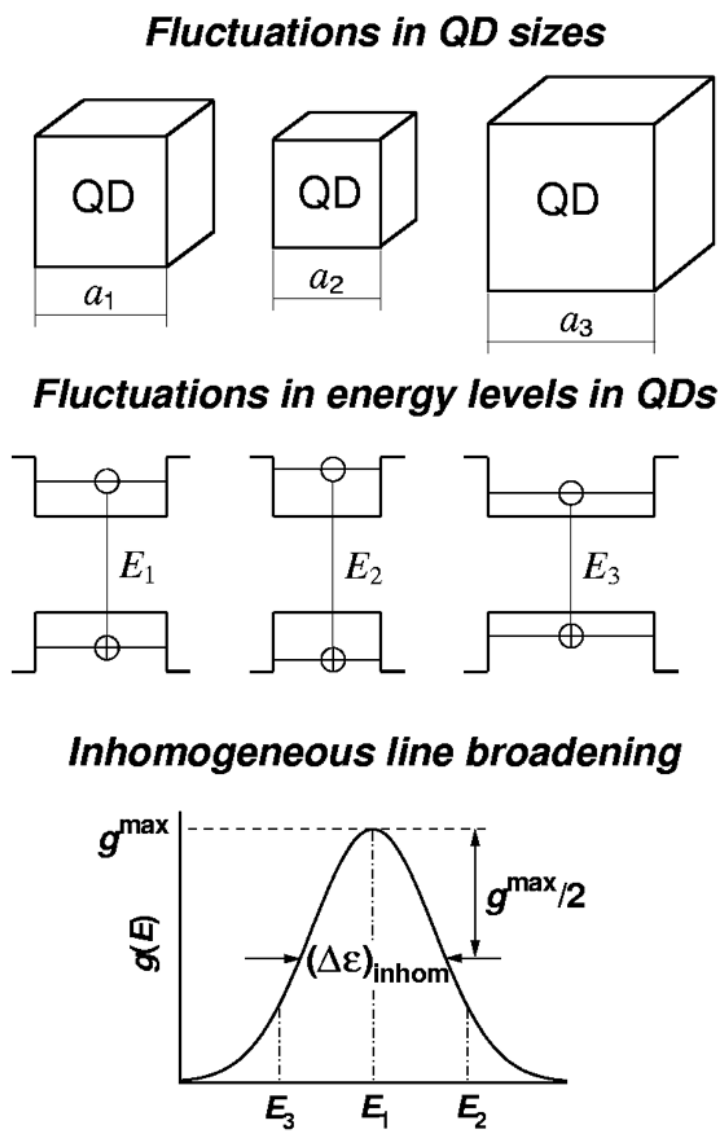


Fig. 2.4 Representation of the inhomogeneous broadening illustrating dots with different sizes which lead to energy state distribution from [15].

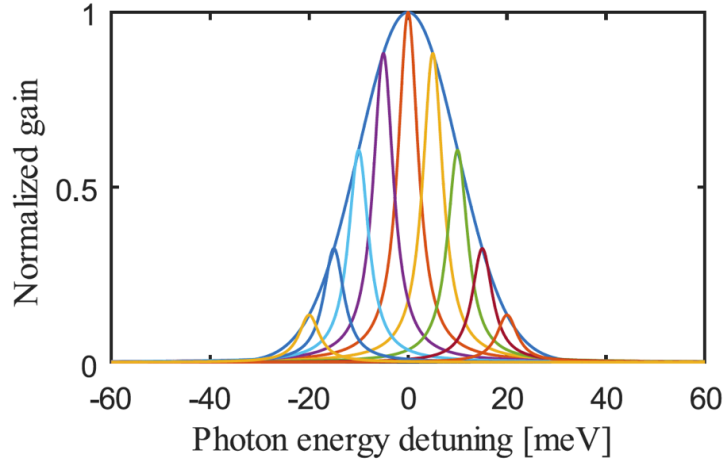


Fig. 2.5 Schematic representations of how the inhomogeneous broadened gain spectrum of a QD laser is composed of contribution of dot groups with different emission energy [290].

The inhomogeneous broadening provides additional tunability to the gain spectrum which is favorable for broad bandwidth applications such as amplifiers, tunable lasers as well as mode-locked lasers [163]. However, a smaller inhomogeneous broadening is desirable for single-mode lasing with low threshold and high feedback resistance QD lasers since off-resonance dots will still capture charge carriers and result in unclamped spontaneous emission [195]. Up to now, the narrowest inhomogeneous broadening as low as 24 meV at room temperature has been measured from the photoluminescence spectrum [118].

2.3 Linewidth enhancement factor

In semiconductor lasers, the laser field and the gain medium are coupled by the gain and the carrier induced refractive index via the Kramers-Kronig relations, or equivalently by the complex optical susceptibility. The linewidth enhancement factor (α_H -factor) typically describes the coupling between the carrier induced variation of real and imaginary parts of susceptibility [206]. In order to theoretical investigate the α_H -factor, it is necessary to solve microscopic equations including the contributions from the kinetic energies, the many-body Coulomb interactions, the electric-dipole interaction between the carriers and the laser field, the carrier-phonon interactions as well as the effects of the injection current [39]. The macroscopic polarization P can be expressed as the sum of the microscopic polarizations p_α

related to all interband transitions:

$$P = \frac{1}{V} \sum_{\alpha} \mu_{\alpha} p_{\alpha} \quad (2.8)$$

Assuming the gain medium isotropic, the complex optical susceptibility can be written as:

$$\chi = \frac{1}{\epsilon_0 n^2} \frac{P}{E} \quad (2.9)$$

The material gain is related to the imaginary part of the susceptibility (see Eq.2.17) while the carrier induced refractive index is connected with the real part of the susceptibility as follows:

$$\delta n = -\frac{\omega}{\epsilon_0 n c V E(\omega)} \text{Re}(P(\omega)) \quad (2.10)$$

From Eq.2.7 and Eq.2.10, the α_H -factor can be further reformed as the coupling between the gain and the refractive index [290]:

$$\alpha_H = -\frac{\frac{\partial \text{Re}(\chi)}{\partial N}}{\frac{\partial \text{Im}(\chi)}{\partial N}} = -\frac{\frac{d(\delta n)_{inh}}{dN}}{\frac{d(G_M)_{inh}}{dN}} \quad (2.11)$$

with N is the carrier density. In semiconductor lasers, the α_H -factor is a key parameter to characterize the dynamical properties such as: the spectral linewidth, the sensitivity to optical feedback, the nonlinear dynamics under optical injection and four-wave mixing generation [98]. Fig.2.6 describes the comparison of material gain (G) and refractive index (n) versus the lasing photon energy for QD and QW lasers. For QW, the zero point of the refractive index is dislocated from the gain peak both for low and high carrier density hence resulting in a nonzero α_H -factor. QW lasers usually exhibit α_H -factor in a range from 2 to 5 [41]. In contrast, for a QD ensemble with symmetric gain, the differential refractive index change is exactly zero at the lasing photon-energy both for low and high carrier density. Thus, the zero α_H -factor can be obtained when the QD lasers have a symmetric gain.

However in literature, the α_H -factor value in QD lasers varies from near-zero up to more than 10 [47]. This non-zero α_H -factor results from the large inhomogeneous broadening, the off-resonant states and the free carrier plasma. Indeed, with the increase of the injection current, the lower energy states are saturated and the carrier filling into the higher energy levels which significantly change the symmetry of the gain spectrum and enhance the α_H -factor value [189, 47, 180]. The measurement techniques of α_H -factor can be classified into three types: The first one relies on analysing the optical spectrum including the optical linewidth spectrum [90] and amplified spontaneous emission (ASE) spectrum [80]. The

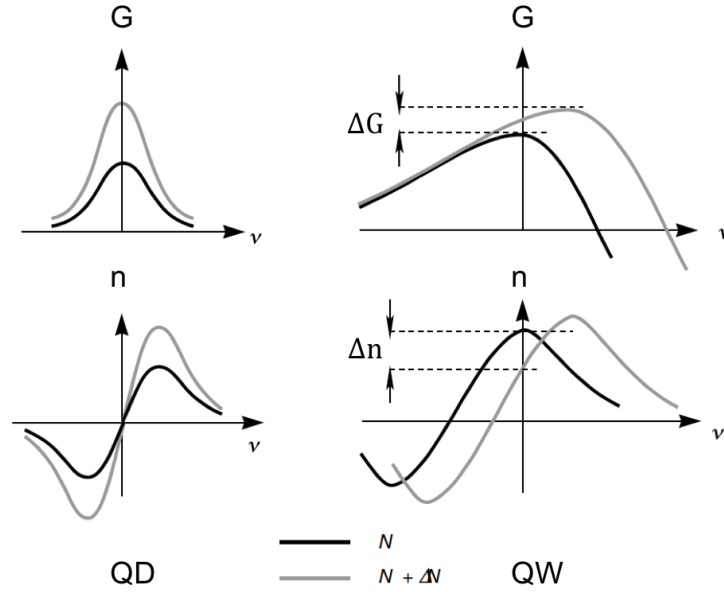


Fig. 2.6 Schematic of gain G and refractive index n profiles variation with the carrier density changes for QD and QW from [224].

second one depends on the high-frequency modulation including the FM/AM method [81, 216] and the Fiber Transfer Function method [48]. The last one focus on the external optical control including the optical injection [106], the optical feedback [287] and the four-wave mixing methods [151]. In chapter 4, the α_H -factor in QD lasers is analysed not only from the standard ASE method but also from a thermally insensitive method analyzing the residual side-mode dynamics under optical injection locking.

2.4 Dual states lasing emission

QD lasers can emit simultaneously from the ground state (GS) and the first excited state (ES) [266]. These dual states lasing emissions have attracted interests considering their potential application for terahertz, millimeter wave generation and optical sensing [94, 33, 68]. Fig.2.7(a) shows that for some values of the pump power, the GS lasing and ES lasing simultaneously coexist in an InAs/InP QD lasers [263]. Fig.2.7(b) shows the corresponding emission spectra as a function of the energy for different values of the pump power normalised with respect to the GS threshold value (P_{th}). The laser emission appears on the GS at 0.82 eV (1.51 μm) for $1.07 \times P_{th}$. Then, when the pump power reaches $1.45 \times P_{th}$, we observe the occurrence of a second emission centered at 0.86 eV (1.44 μm) and corresponding to

the appearance of the ES. It is also noted that at high pump power, the ES lasing dominates and the GS emission intensity is diminished, which is not shown in the Fig.2.7(b) [13]. The dual emission has been theoretically and experimentally investigated by different research groups both for InAs/InP QD laser and for InAs/GaAs QD laser [244, 172, 212, 222, 221]. The origin of the dual states lasing emission has been explained by the finite GS relaxation time using a cascade relaxation model which brings the GS emission to a constant value after the ES threshold [173].

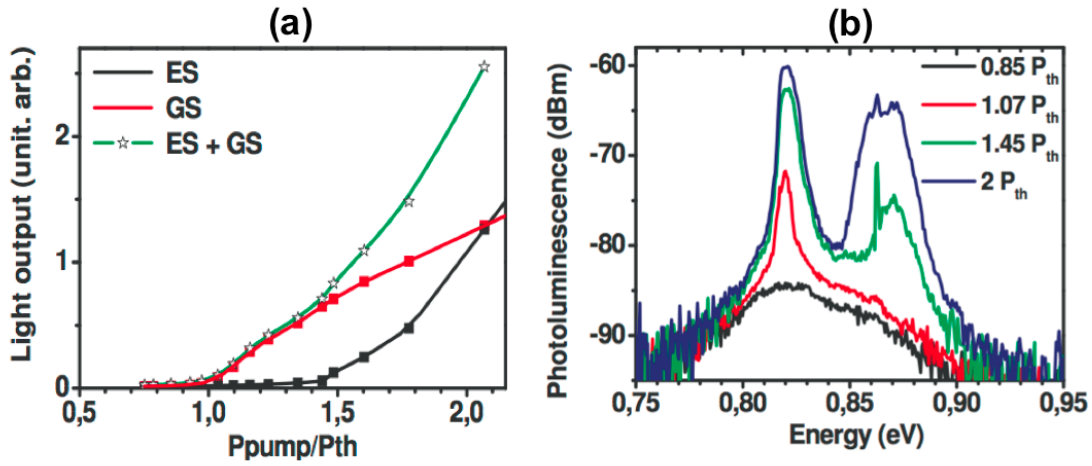


Fig. 2.7 (a) Integrated light-output power of a InAs/InP QD laser versus optical normalised pumping density with respect to the GS threshold intensity. (b) Room-temperature emission spectra under various pulsed optical excitation from [263].

2.5 Relaxation oscillation frequency and damping factor

In a semiconductor laser, the lasing field $\tilde{E}(t)$ can be expressed as a function of carrier density $N(t)$ [257]:

$$\frac{d\tilde{E}(t)}{dt} = \left\{ \frac{1}{2}(1 + i\alpha_H) \left[\Gamma G_N(N(t) - N_{tr}) - \frac{1}{\tau_p} \right] + i\omega \right\} \tilde{E}(t) \quad (2.12)$$

with Γ is the confinement factor, τ_p is the photon lifetime, G_N is the linear gain and N_{tr} is transparency carrier intensity. Furthermore, the lasing field can be expressed as $\tilde{E}(t) = A(t)\exp(i\omega t + i\phi(t))$. By separating the real part and the imaginary part of Eq.2.12, the rate

equations for the amplitude $A(t)$, the phase $\phi(t)$ and the carrier density $N(t)$ are given by:

$$\frac{dA(t)}{dt} = \frac{1}{2} \left[\Gamma G_N (N(t) - N_{tr}) - \frac{1}{\tau_p} \right] A(t) \quad (2.13)$$

$$\frac{d\phi(t)}{dt} = \frac{\alpha_H}{2} \left[\Gamma G_N (N(t) - N_{tr}) - \frac{1}{\tau_p} \right] \quad (2.14)$$

$$\frac{dN(t)}{dt} = \frac{\eta_i I}{qV} - \frac{N(t)}{\tau_c} - G_N [N(t) - N_{tr}] A^2(t) \quad (2.15)$$

with η_i is the injection efficiency, I is the injection current, q is the electron charge, τ_c is the carrier lifetime. The steady-state solutions of A_s , ϕ_s and N_s of Eq.2.13 to Eq.2.15 are indicated as:

$$A_s^2 = \frac{\eta_i I / qV - N_s / \tau_c}{G_N (N_s - N_{th})} \quad (2.16)$$

$$\phi_s = 0 (\omega_s = \omega) \quad (2.17)$$

$$N_s = N_{tr} + \frac{1}{\Gamma G_N \tau_p} = N_{th} \quad (2.18)$$

N_{th} is the threshold carrier density. Now, we introduce a small perturbations in the steady-state solutions :

$$A(t) = A_s + \delta A(t) \quad (2.19)$$

$$\phi(t) = (\omega_s - \omega_0)t + \delta \phi(t) \quad (2.20)$$

$$N(t) = N_s + \delta N(t) \quad (2.21)$$

By injecting Eq.2.16 to Eq.2.21 into Eq.2.13 to Eq.2.15, we can get the rate equations with perturbations:

$$\frac{d\delta A(t)}{dt} = \frac{1}{2} \Gamma G_N A_s \delta N(t) \quad (2.22)$$

$$\frac{d\delta \phi(t)}{dt} = \frac{\alpha_H}{2} \Gamma G_N \delta N(t) \quad (2.23)$$

$$\frac{d\delta N(t)}{dt} = -\frac{2A_s}{\Gamma \tau_p} \delta A(t) - \frac{1}{\tau_c} \delta N(t) - G_N A_s^2 \delta N(t) \quad (2.24)$$

Rearranging Eq.2.22 to Eq.2.24, we can get the following matrix:

$$\begin{bmatrix} \frac{d\delta A(t)}{dt} \\ \frac{d\delta \phi(t)}{dt} \\ \frac{d\delta N(t)}{dt} \end{bmatrix} \begin{bmatrix} 0 & 0 & \frac{1}{2} \Gamma G_N A_s \\ 0 & 0 & \frac{\alpha_H}{2} \Gamma G_N \\ -\frac{2A_s}{\Gamma \tau_p} & 0 & -\frac{1}{\tau_c} - G_N A_s^2 \end{bmatrix} \begin{bmatrix} \delta A(t) \\ \delta \phi(t) \\ \delta N(t) \end{bmatrix} = M_J \begin{bmatrix} \delta A(t) \\ \delta \phi(t) \\ \delta N(t) \end{bmatrix} \quad (2.25)$$

The solutions of Eq.2.22 to Eq.2.24 can be obtained from the eigenvalues ξ of the Jacobian Matrix M_J . The characteristics equation solving the ξ is:

$$|M_J - \lambda I| = -\xi \left[\xi^2 + \left(\frac{1}{\tau_c} + G_N A_s^2 \right) \xi + \frac{G_N A_s^2}{\tau_p} \right] = 0 \quad (2.26)$$

where the trivial solution is $\xi = 0$, and other two solutions are:

$$\xi = -\frac{1}{2} \left(\frac{1}{\tau_c} + G_N A_s^2 \right) \pm \sqrt{\frac{1}{4} \left(\frac{1}{\tau_c} + G_N A_s^2 \right)^2 - \frac{G_N A_s^2}{\tau_p}} \quad (2.27)$$

The laser classification will be introduced in Chapter 5, where semiconductor lasers (Class B laser) satisfy the relation $\tau_p \ll \tau_c$. Therefore, the term inside the square root is negative and the solution becomes complex with:

$$\xi = -\frac{1}{2} \left(\frac{1}{\tau_c} + G_N A_s^2 \right) \pm i \sqrt{\frac{G_N A_s^2}{\tau_p} - \frac{1}{4} \left(\frac{1}{\tau_c} + G_N A_s^2 \right)^2} = \xi_{Re} + i \xi_{Im} \quad (2.28)$$

The real part ξ_{Re} and the imaginary part ξ_{Im} represent the relaxation oscillation frequency f_{RO} and the damping factor γ , respectively, such as :

$$f_{RO} = \frac{1}{2\pi} \sqrt{\frac{G_N A_s^2}{\tau_p}} \quad (2.29)$$

$$\gamma = \frac{1}{2} \left(\frac{1}{\tau_c} + G_N A_s^2 \right) \quad (2.30)$$

From the Eq.2.29 and Eq.2.30, when the bias current increases, the steady-state field amplitude A_s increases and results in the increase of the f_{RO} and γ . The f_{RO} and γ can be obtained from the small signal modulation response or the relative intensity noise spectrum (RIN). Fig.2.8 shows the small signal modulation response spectrum with the increase of the bias current. The amplitude of the resonant peak is found at $\sim (\omega_{RO}/\gamma)^2$ while the relationship among the peak frequency ω_p , ω_R and the 3 dB down cutoff frequency ω_{3dB} are also illustrated.

It is worth noting that the modulation dynamics of QD lasers is strongly limited by the large damping rate compared with QW lasers, which is due to the carrier capture and relaxation processes as well as the Pauli blocking effect [168]. Moreover, the relaxation oscillation frequency and 3 dB modulation bandwidth are reduced result from the large inhomogeneous broadening and the high gain compression effects [41]. The record modulation bandwidths

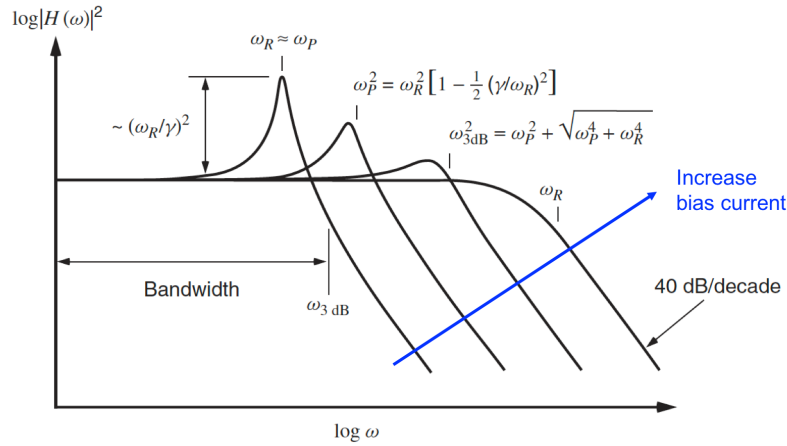


Fig. 2.8 Sketch of the modulation transfer function for increasing values of relaxation resonance frequency ω_R and damping factor γ . The relationship among the peak frequency ω_p , ω_R and the 3 dB down cutoff frequency ω_{3dB} are also illustrated in the sketch [41].

of 17.5 GHz have been achieved with InAs/InP QD laser in 2018 at University of Kassel result from the reduced size inhomogeneity and a high dot density [1]. In Chapter 3 and 4, both relaxation oscillation frequency and damping factor are extracted from the relative intensity noise spectrum and will be discussed later on.

2.6 Summary

This chapter has introduced the fundamental features of QD lasers including the electronic structure, the carrier dynamics, the gain broadening mechanisms, the linewidth broadening factor, dual states lasing emission as well as the relaxation oscillation frequency and damping factor. All these elements are helpful for understanding the results presented in the following chapters.

Chapter 3

Noise properties of InAs/InP quantum dot distributed feedback lasers

In semiconductor lasers, quantum fluctuations associated with the lasing process are known to alter both the intensity and the phase of the optical field, hence resulting in frequency and intensity noises [211]. This chapter will at first highlight the importance of low frequency noise (FN) for narrow linewidth operation applications, as well as the recent state of the art of narrow linewidth semiconductor lasers. Apart from the FN, the optical sources with low relative intensity noise (RIN) are highly desired not only for optical communication system, but also for radar related applications.

Second, we numerically investigate the FN and RIN of quantum dot (QD) lasers through a rate equation model, taking into account both the spontaneous emission and carrier contributions. The FN of QD lasers is investigated by including the phase of the electric field in the rate equation model. Indeed, it is known that carrier fluctuations provide an additional mechanism of phase fluctuations due to the coupling between the carrier density and the refractive index through the linewidth enhancement factor (α_H -factor) [41]. The carrier noise is actually found to have little impact on the FN of QD lasers, thus being negligible for the investigation of the spectral linewidth. On the other hand, numerical results also show that the carrier noise in the ground state (GS) and excited state (ES) significantly enhances the RIN, while that in the carrier reservoir (RS) does not play a role. In addition, simulations point out that a large GS-ES energy separation is much more favorable for low intensity noise operation. In other words, a small vertical coupling is always more suitable for RIN reduction due to the reduced contribution from the carrier noise in the ES. This last statement also proves that the inclusion of the ES contribution is definitely of vital importance for getting an accurate description of the QD laser intensity noise. Moreover, simulations also

unveil that both FN and RIN of QD lasers are rather temperature independent, which is of prime importance for the development of power efficient light sources.

In the end, we experimentally investigated the spectral linewidth and RIN of InAs/InP QD distributed feedback (DFB) lasers emitting at $1.52 \mu\text{m}$. Owing to a low inversion factor and a low α_H -factor, a narrow spectral linewidth of 160 kHz (80 kHz intrinsic linewidth) with a low sensitivity to temperature is demonstrated. When using anti-reflection coatings on both facets, narrow linewidth operation is extended to high powers, believed to be due to a reduction in the longitudinal spatial hole burning. Furthermore, a low RIN of less than -150 dB/Hz is measured in the 8-10 GHz range. Moreover, both relaxation oscillation frequency and damping factor are also extracted from the curve fitting of the RIN spectrum.

3.1 Introduction to frequency noise and intensity noise

3.1.1 Frequency noise

The FN in semiconductor lasers is contributed from low-frequency flicker noise, the spontaneous emission noise, and the carrier generation and recombination noise. The flicker noise arises from the current source, the thermal fluctuations, and the internal electrical noise. The remaining noise sources are white noise and govern the intrinsic spectral linewidth of the laser. Fig.3.1 shows the contribution of spontaneous emission noise and carrier noise to the FN spectrum.

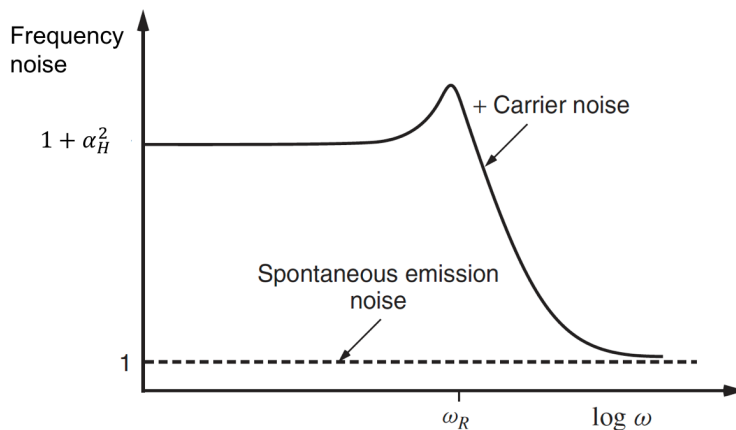


Fig. 3.1 Frequency noise spectrum, illustrating contributions from both carrier and spontaneous emission noise [41].

As shown, the FN spectrum above the resonance frequency (ω_R) arising from the spontaneous emission noise determines the Schawlow-Townes linewidth, and the full width at half

maximum (FWHM) is expressed as $\Delta\nu_{ST} = 2\pi FN(\omega \gg \omega_R)$. However, the FN spectrum below the ω_R is determined not only by the spontaneous emission but also by the carrier fluctuations through the α_H -factor with the quantity of $(1 + \alpha_H^2)$, hence the total optical linewidth is given by $\Delta\nu = 2\pi FN(\omega \ll \omega_R)$. These two linewidths are linked by:

$$\Delta\nu = \Delta\nu_{ST}(1 + \alpha_H^2) \quad (3.1)$$

3.1.2 Narrow linewidth single-mode lasers

Narrow linewidth semiconductor lasers are required for a wide range of applications, including high performance coherent communications systems [204], optical atomic clock [190], frequency synthesis [240], spectroscopy [245], as well as distributed sensing systems [65]. Aside from the linewidth, such lasers must also be single-frequency, energy efficient, and monolithically integrable [127]. To meet these goals, semiconductor distributed feedback lasers with strained quantum well (QW) layers have been touted to be very reliable single wavelength sources [150, 249]. However, most QW DFB lasers made with simple grating designs usually exhibit spectral linewidths of a few MHz [119, 150]. The first reason of such broad spectral linewidth in semiconductor lasers consists in the non-zero α_H -factor. Second, the laser's coherence time (τ_{coh}) is intimately linked with the laser linewidth through the relation:

$$\Delta\nu = \frac{1}{\pi\tau_{coh}} = \frac{c}{\pi L_{coh}} \quad (3.2)$$

with L_{coh} the coherence length, c the vacuum velocity of light. The linewidth can not become zero since the τ_{coh} can not be infinite. Third, the short optical cavity and weak internal feedback lead to a low Q -factor, which is the ratio of the energy stored by a cavity to the power lost.

Thus, in order to reach kHz spectral linewidth, continuous efforts have been made to decrease the spontaneous emission rate into the lasing mode or to increase the Q -factor and hence the number of photons stored in the cavity. Therefore, different designs of single-mode devices have been proposed to achieve narrow linewidths in the order of 100 kHz or below, such as external cavity [177], phase-shifted and chirped grating [292, 201], discrete mode DFB lasers [121], and fiber lasers [215]. The objective of this thesis is to achieve narrow linewidths with compact devices made without artificial parts.

The spectral linewidth of semiconductor lasers is expressed by the modified Schawlow-Townes expression [286]:

$$\Delta\nu = \frac{\Gamma g_{th} v_g^2 \alpha_m h\nu}{4\pi P_0} n_{sp} (1 + \alpha_H^2) \quad (3.3)$$

where $\Gamma_{g_{th}}$ is the modal gain at threshold, α_m the mirror loss, $h\nu$ the photon energy, P_0 the optical output power, n_{sp} the population inversion factor and v_g is the group velocity. From Eq.3.3, we can reduce the linewidth not only by decreasing the α_m or α_H -factor, but also by increasing the P_0 . The α_m can be expressed as:

$$\alpha_m = \frac{1}{2L} \ln\left(\frac{1}{R_1 R_2}\right) \quad (3.4)$$

where L is the cavity length, R_1 and R_2 are the facet reflectivity. By means of increasing the cavity length or the facet reflectivity, the spectral linewidth can be reduced. Fig.3.2 demonstrates a fully integrated extended distributed Bragg reflector (DBR) laser with ~ 1 kHz linewidth, as well as a ring-assisted DBR laser with less than 500 Hz linewidth [285, 97].

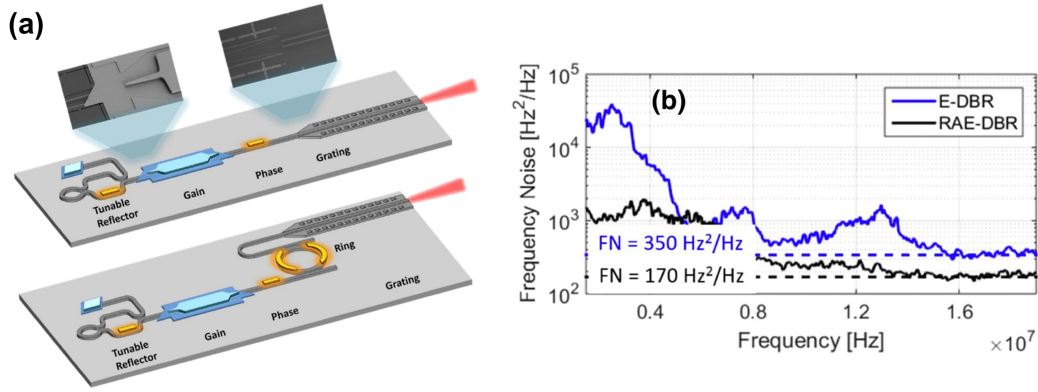


Fig. 3.2 (a) Schematics of the extended distributed Bragg reflector (E-DBR) laser, with SEM images of the transitions between the various sections of the laser, and ring resonator incorporated in the cavity to form the ring-assisted extended DBR(RAE-DBR) laser. (b) Frequency noise spectra for the E-DBR and RAE-DBR lasers [97].

On the other hand, the total quality factor (Q -factor), internal quality factor (Q_i -factor) and external quality factor (Q_{ext} -factor) can be defined as [63]:

$$Q = 2\pi\nu\tau_p = \frac{2\pi\nu}{v_g(\alpha_i + \alpha_m)} \quad (3.5)$$

$$Q_i = \frac{2\pi\nu}{v_g\alpha_i} \quad (3.6)$$

$$Q_{ext} = \frac{2\pi\nu}{v_g\alpha_m} \quad (3.7)$$

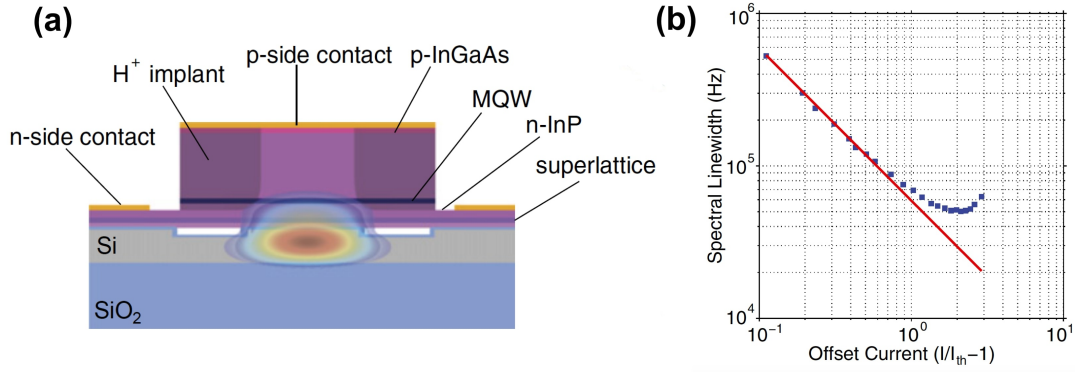


Fig. 3.3 (a) High-Q hybrid laser device schematics. Two-dimensional cross-section of the hybrid platform, with superimposed optical transverse mode profile. (b) Spectral linewidth of a single high-Q hybrid laser as a function of the offset pump current [227]

with τ_p the photon lifetime, ν the laser frequency and α_i the material loss. The three quality factors are linked by:

$$\frac{1}{Q} = \frac{1}{Q_i} + \frac{1}{Q_{ext}} \quad (3.8)$$

In Eq.3.3, the modal gain $\Gamma_{g_{th}} = \alpha_i + \alpha_m$ is replaced with its expression as a function of total quality factor $\frac{2\pi\nu}{v_g Q}$, mirror losses α_m by $\frac{2\pi\nu}{v_g Q_{ext}}$ as well as the optical output power P_0 by $\eta_d(I - I_{th})$, with η_d the differential efficiency and I_{th} the threshold current. Therefore, the definition of the spectral linewidth is then equivalently reexpressed in terms of quality factor by [63]:

$$\Delta\nu = \frac{\pi h \nu^3}{Q Q_{ext} \eta_d (I - I_{th})} n_{sp} (1 + \alpha_H^2) \quad (3.9)$$

From Eq.3.9, the spectral linewidth can be reduced by increasing the Q -factor through the increase of the τ_p and the decrease of the losses α_i and α_m (see Eq.3.5). In particular, one recent solution was obtained from a proper modal engineering of a DFB laser, in which light is generated in the III-V material and stored into the low-loss silicon material. As such, Fig.3.3(a) shows the structure of the high- Q hybrid laser using modal engineering to concentrate light in silicon, which unveils spectral linewidths five times smaller than any other semiconductor lasers, as illustrated in Fig.3.3(b) [227, 228]. A similar design has been proposed by Gallet *et al.* and high photon lifetime of 103 ps has been extracted [64].

Although these aforementioned techniques can satisfy ultra-narrow linewidth and power requirements, they require either more complex technologies or remain significantly bulky, with poorer mechanical stability as opposed to standard DFB lasers which can be manufactured in large numbers and at low cost. Additional breakthroughs can be achieved by using a

gain medium made with self-assembled QDs from which the shape of the density of states as well as the carrier confinement do substantially improve the laser performance [46, 57]. Spectral linewidths between 100 and 500 kHz have been reported for both InAs/GaAs and InAs/InP QD lasers [243, 165, 55, 18]. Very recently, the record intrinsic spectral linewidth as low as 30 kHz at 20 °C and less than 80 kHz at 80 °C have been demonstrated in an InAs/InP QD DFB laser as shown in the Fig.3.4 [236].

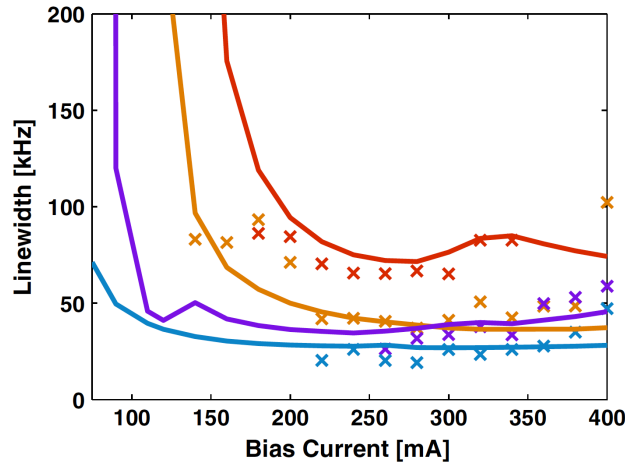


Fig. 3.4 Extracted Lorentzian linewidths shown in marks. The simulated values are shown in solid lines: 20°C (blue), 40°C (purple), 60°C (orange), 80°C (red) [236].

From Eq.3.3 and Eq.3.9, the α_H -factor appears as an additional mechanism of phase fluctuations responsible for the much broader linewidth in semiconductor lasers [274]. Therefore, narrow linewidth lasers should a priori be designed to minimize the effect of the α_H -factor. On the other hand, the need to pump the semiconductor to optical transparency creates a minimum carrier density and current at threshold. The inversion factor n_{sp} in Eq.3.3 and Eq.3.9 accounts for this minimum carrier density in the laser, applying a penalty for incomplete inversion. The n_{sp} is given by [41]:

$$n_{sp} = \frac{1}{1 - \exp(E_{21} - \Delta E_F / \kappa_B T)} \quad (3.10)$$

where E_{21} and ΔE_F are the energy separation between the bands and between their corresponding quasi-Fermi levels, respectively. In QW lasers, n_{sp} is typically in the range from 1.5 to 2.5, while it is much lower in QDs with a value of about 1 owing to the smaller number of activated states required to reach the transparency [205].

Fig.3.5 shows that the inversion factor in QD lasers converges towards 1 regardless of the bias current. Therefore, it will be shown later on that the quantity $n_{sp} \times (1 + \alpha_H^2)$ may be

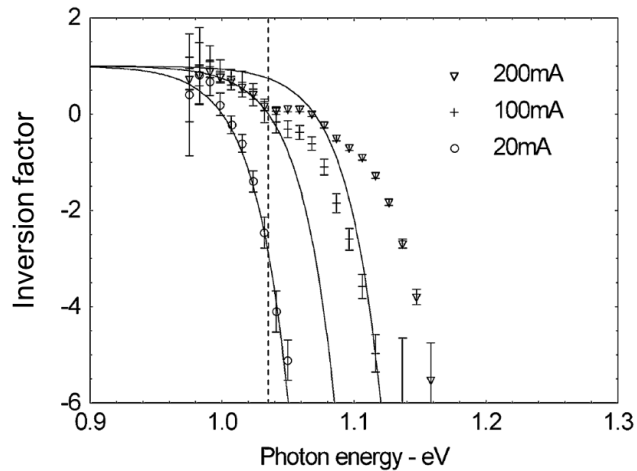


Fig. 3.5 Inversion factor as a function of photon energy for three currents [205].

used as the figure of merit of narrow linewidth operation rather than the sole α_H -factor [119]. For example, this quantity was found as low as 1.4 in InAs/InP QD laser, which is smaller than that of the QW laser with a value of 30 [46, 55].

3.1.3 Relative intensity noise

The relative intensity noise (RIN) of semiconductor lasers degrades the signal-to-noise ratio (SNR) and increases the bit-error rate of optical signals hence setting a limit of a high-speed communication system [41]. System limitations due to poor SNR can be compensated by increasing the bias current of the laser source but at the price of a larger energy consumption.

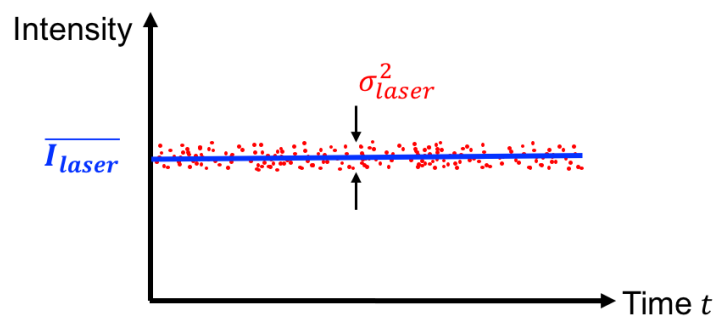


Fig. 3.6 Schematic of the relative intensity noise.

Thus, optical sources with low RIN are highly desired to carry broadband data with low bit error rate [41, 196]. The RIN mainly stems from intrinsic optical phase and frequency fluctuations caused by spontaneous emission as well as the carrier noise, describing the

fluctuations in the optical power of a laser [56]. As shown in the Fig.3.6, for a given intensity emitted by the laser $I_{laser}(t) = \overline{I_{laser}} + i(t)$, the RIN of the laser is defined as [41]:

$$RIN = \frac{\overline{i^2}}{I_{laser}^2} = \frac{\sigma_{laser}^2}{I_{laser}^2} \quad (3.11)$$

with $\overline{I_{laser}}$ the average flux intensity, $i(t)$ the temporal fluctuations of the emitted signal and σ_{laser}^2 the variance of the laser noise. For the frequencies below the resonance frequency (ω_R), the RIN can be reexpressed as:

$$RIN(dB/Hz) = \frac{4R_{sp}\gamma_{ae}^2}{\omega_R^4 SpV} \quad (3.12)$$

with R_{sp} the spontaneous emission factor, γ_{ae} the carrier damping rate, V the active region volume and Sp the energy flux in dB.

In radar related applications, Fig.3.7 shows the Signal-to-Noise as a function of the average photodiode current for thermal noise-limited, shot noise-limited, and three cases of RIN-limited detection. It is requested the laser's intensity noise to be drastically limited by the shot noise over a bandwidth ranging up to 20 GHz [45].

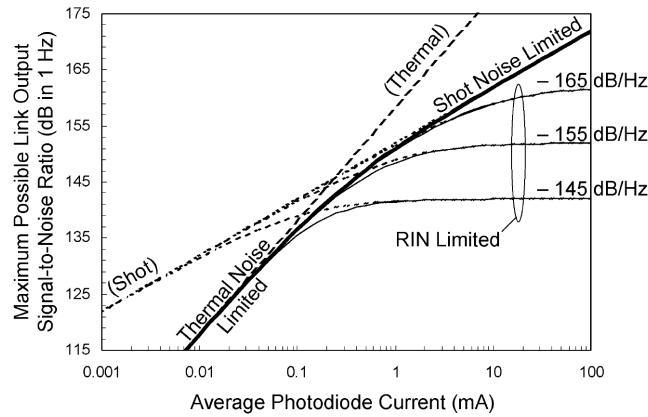


Fig. 3.7 Plot of the Signal-to-Noise versus average photodiode current for thermal noise-limited, shot noise-limited, and three cases of RIN-limited detection in radar applications [45].

As for QD lasers, a RIN level as low as -160 dB/Hz was experimentally measured with InAs/GaAs and InAs/InP QD devices [142, 32]. On the other hand, a QD comb laser with a RIN level ranging from -120 to -145 dB/Hz in the 0.1-10 GHz frequency band was also proposed for applications in wavelength-division multiplexing and passive optical networks [133]. More recently, it was shown that a QD laser epitaxially grown on silicon exhibits

a RIN from -140 dB/Hz to -150 dB/Hz while that directly grown on germanium is found higher at -120 dB/Hz [157, 149, 296]. Finally, another work unveiled that the RIN of a QD laser emitting on the pure ES emission is more suppressed than that of the GS one [152]. As opposed to the large number of theoretical studies reporting on the high-speed properties of QD lasers [166, 110, 69, 61, 59], literatures are not that abundant for the investigation of the intensity noise. In fact, most of them are not even sufficient because they usually do not consider the carrier noise in the model [209] or only take into account the carrier noise originating from the GS level [85]. Thus, in the next section, we semi-analytically investigate the FN and RIN of QD lasers through the inclusion of the carrier noise originating from both lasing and non-lasing states. This work is also supported by previous studies which unveiled that the strong negative correlations arising between carrier and photon noises can not be neglected for studying the dynamics of semiconductor lasers [178, 19, 170].

3.2 Theoretical investigation of the frequency noise and intensity noise

3.2.1 Quantum dot laser modal description

The three-level rate equations model is based on the QD electronics structure illustrated in Fig.3.8. This numerical model holds under the assumption that the active region consists of only one QD ensemble, thus the consideration of dot size dispersion through the inhomogeneous broadening of the gain profile is not taken into account in the model.

As discussed before, electrons and holes are regarded as neutral excitons that are directly injected from the electrodes into the two dimensional carrier RS meaning that the carrier dynamics in the three dimensional separate confinement heterostructure (barrier) layers is not considered in the model. As shown in Fig.3.8, the carriers are captured from the RS into the QD region which consists of a four-fold degenerate ES as well as a two-fold degenerate GS. The corpuscular rate equations describing carrier and photon dynamics are expressed as:

$$\frac{dN_{RS}}{dt} = \frac{I}{q} + \frac{N_{ES}}{\tau_{RS}^{ES}} - \frac{N_{RS}}{\tau_{ES}^{RS}}(1 - \rho_{ES}) - \frac{N_{RS}}{\tau_{RS}^{spon}} + F_{RS} \quad (3.13)$$

$$\frac{dN_{ES}}{dt} = \left(\frac{N_{RS}}{\tau_{ES}^{RS}} + \frac{N_{GS}}{\tau_{ES}^{GS}} \right) (1 - \rho_{ES}) - \frac{N_{ES}}{\tau_{GS}^{ES}}(1 - \rho_{GS}) - \frac{N_{ES}}{\tau_{RS}^{ES}} - \frac{N_{ES}}{\tau_{ES}^{spon}} + F_{ES} \quad (3.14)$$

$$\frac{dN_{GS}}{dt} = \frac{N_{ES}}{\tau_{GS}^{ES}}(1 - \rho_{GS}) - \frac{N_{GS}}{\tau_{ES}^{GS}}(1 - \rho_{ES}) - \Gamma_p \nu_g g_{GS} S_{GS} - \frac{N_{GS}}{\tau_{GS}^{spon}} + F_{GS} \quad (3.15)$$

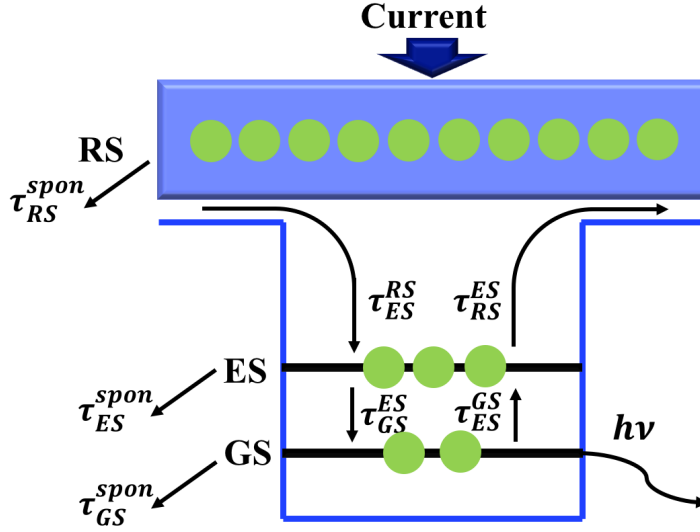


Fig. 3.8 Schematic representation of the electronic structure and the corresponding carrier dynamics into the QD.

$$\frac{dS_{GS}}{dt} = \left(\Gamma_p v_g g_{GS} - \frac{1}{\tau_p} \right) S_{GS} + \beta_{sp} \frac{N_{GS}}{\tau_{GS}^{spon}} + F_S \quad (3.16)$$

where I is the bias current, q is the elementary charge, and $N_{RS,ES,GS}$ are the carrier populations in the RS, ES, and GS, respectively. Only stimulated emission originating from the GS level is considered hence S_{GS} accounts for the photon number in the the GS level. In Eq.3.13 - Eq.3.16, the carriers are first captured from the RS into the ES with capture time τ_{ES}^{RS} , then relax from the ES down to the GS with a relaxation time τ_{GS}^{ES} . Owing to the thermalization, carriers are reemitted from the GS to ES with an escape time τ_{ES}^{GS} , and from the ES to the RS with an escape time τ_{RS}^{ES} . In addition, carriers also recombine spontaneously with spontaneous emission times $\tau_{RS,ES,GS}^{spon}$. Lastly, let us stress that Γ_p is the optical confinement factor, τ_p the photon lifetime, v_g the group velocity and β_{sp} the spontaneous emission factor. In order to retrieve the FN, the differential equation describing the phase dynamics of the electric field ϕ is also given by:

$$\frac{d\phi}{dt} = \frac{1}{2} \Gamma_p v_g (g_{GS} \alpha_{GS} + g_{ES} \kappa_{ES} + g_{RS} \kappa_{RS}) + F_\phi \quad (3.17)$$

where α_{GS} is the GS contribution to the α_H -factor. The $g_{RS,ES,GS}$ are the material gain of each state expressed as [273]:

$$g_{GS} = \frac{a_{GS}}{1 + \xi \frac{S}{V_S}} \frac{N_B}{V_B} (2\rho_{GS} - 1) \quad (3.18)$$

$$g_{ES} = a_{ES} \frac{N_B}{V_B} (2\rho_{ES} - 1) \quad (3.19)$$

$$g_{RS} = a_{RS} \frac{D_{RS}}{V_{RS}} (2\rho_{RS} - 1) \quad (3.20)$$

where $a_{RS,ES,GS}$ the differential gain, ξ the gain compression factor, V_S the volume of the laser field inside the cavity, N_B the total number of dots, V_B the volume of the active region, D_{RS} the total number of states in the RS and V_{RS} the volume of the RS [173]. $\rho_{GS,ES,RS}$ are the carrier occupation probabilities in the GS, the ES, and the RS, which are given by $\rho_{GS} = \frac{N_{GS}}{2N_B}$, $\rho_{ES} = \frac{N_{ES}}{4N_B}$, $\rho_{RS} = \frac{N_{RS}}{D_{RS}}$, respectively. $\kappa_{ES,RS}$ are coefficients linked to the ES and RS contributions, respectively and defined as:

$$\kappa_{ES,RS} = \frac{E_{GS}}{E_{ES,RS}} \left[\frac{\hbar}{(E_{ES,RS} - E_{GS})T_2} + \frac{(E_{ES,RS} - E_{GS})T_2}{\hbar} \right]^{-1} \quad (3.21)$$

with $E_{GS,ES,RS}$ state energies and T_2 the polarization dephasing time. Last but not least, it is worth noting that this model only considers the stimulated emission from the GS transition.

Modeling the RIN is conducted through the inclusion of the Langevin noise sources characterizing both the carrier and the spontaneous emission noises [211]. Here, $F_{RS,ES,GS}$, F_S , and F_ϕ are the carrier, photon, and phase noise sources respectively. The Langevin noise sources disturb the laser away from its steady-state condition. The expectation values of all Langevin noise terms are zero due to their white noise nature. Furthermore, the correlation strength of two Langevin noise sources is such as $\langle F_i(t)F_j(t') \rangle = U_{ij}\delta(t-t')$, where indexes i, j refer to RS, ES, GS, S and ϕ with U_{ij} the diffusion coefficient between two noise sources which are delta-correlated. Following the approach developed in [41] and using the steady-state solutions from 3.13 - 3.17, the diffusion coefficients are found to be expressed such as:

$$U_{RSRS} = 2 \times \left[\frac{N_{RS}}{\tau_{ES}^{RS}} (1 - \rho_{ES}) + \frac{N_{RS}}{\tau_{RS}^{spon}} \right] \quad (3.22)$$

$$U_{ESES} = 2 \times \left[\frac{N_{RS}}{\tau_{ES}^{RS}} + \frac{N_{GS}}{\tau_{ES}^{GS}} \right] (1 - \rho_{ES}) \quad (3.23)$$

$$U_{GSGS} = 2 \times \left[\frac{N_{ES}}{\tau_{GS}^{ES}} (1 - \rho_{GS}) - \Gamma_p v_g g_{GS} S_{GS} + \beta_{sp} \frac{N_{GS}}{\tau_{GS}^{spon}} S_{GS} \right] \quad (3.24)$$

$$U_{SS} = 2 \times \beta_{sp} \frac{N_{GS}}{\tau_{GS}^{spon}} S_{GS} \quad (3.25)$$

$$U_{\phi\phi} = \frac{1}{2S_{GS}} \beta_{sp} \frac{N_{GS}}{\tau_{GS}^{spon}} \quad (3.26)$$

$$U_{RSES} = - \left[\frac{N_{RS}}{\tau_{ES}^{RS}} (1 - \rho_{ES}) + \frac{N_{ES}}{\tau_{RS}^{ES}} \right] \quad (3.27)$$

$$U_{ESGS} = - \left[\frac{N_{GS}}{\tau_{ES}^{GS}} (1 - \rho_{ES}) + \frac{N_{ES}}{\tau_{GS}^{ES}} (1 - \rho_{GS}) \right] \quad (3.28)$$

$$U_{GSS} = - \left[2\beta_{sp} \frac{N_{GS}}{\tau_{GS}^{GS}} S_{GS} - \Gamma_p v_g g_{GS} S_{GS} \right] \quad (3.29)$$

$$U_{RS\phi} = U_{ES\phi} = U_{GS\phi} = U_{S\phi} = 0 \quad (3.30)$$

Through a small signal analysis, we linearize the rate equations 3.13 - 3.17, and yield:

$$\begin{bmatrix} \gamma_{11} + j\omega & -\gamma_{12} & 0 & 0 & 0 \\ -\gamma_{21} & \gamma_{22} + j\omega & -\gamma_{23} & 0 & 0 \\ 0 & -\gamma_{32} & \gamma_{33} + j\omega & -\gamma_{34} & 0 \\ 0 & 0 & -\gamma_{43} & \gamma_{44} + j\omega & 0 \\ -\gamma_{51} & -\gamma_{52} & -\gamma_{53} & -\gamma_{54} & j\omega \end{bmatrix} \times \begin{bmatrix} \delta N_{RS} \\ \delta N_{ES} \\ \delta N_{GS} \\ \delta S_{GS} \\ \delta \phi \end{bmatrix} = \begin{bmatrix} F_{RS} \\ F_{ES} \\ F_{GS} \\ F_S \\ F_\phi \end{bmatrix} \quad (3.31)$$

with

$$\begin{aligned} \gamma_{11} &= \frac{1 - \rho_{ES}}{\tau_{ES}^{RS}} + \frac{1}{\tau_{RS}^{spon}}; \gamma_{12} = \frac{1}{\tau_{RS}^{ES}} + \frac{1}{4N_B} \frac{N_{RS}}{\tau_{ES}^{RS}}; \\ \gamma_{21} &= \frac{1 - \rho_{ES}}{\tau_{ES}^{RS}}; \gamma_{23} = \frac{1 - \rho_{ES}}{\tau_{ES}^{GS}} + \frac{1}{2N_B} \frac{N_{ES}}{\tau_{GS}^{ES}}; \\ \gamma_{22} &= \frac{1 - \rho_{GS}}{\tau_{GS}^{ES}} + \frac{1}{\tau_{RS}^{ES}} + \frac{1}{\tau_{ES}^{spon}} + \frac{1}{4N_B} \left(\frac{N_{RS}}{\tau_{ES}^{RS}} + \frac{N_{GS}}{\tau_{ES}^{GS}} \right); \\ \gamma_{32} &= \frac{1 - \rho_{GS}}{\tau_{GS}^{ES}} + \frac{1}{4N_B} \frac{N_{GS}}{\tau_{ES}^{GS}}; \\ \gamma_{33} &= \frac{1 - \rho_{ES}}{\tau_{GS}^{GS}} + \frac{1}{\tau_{GS}^{spon}} + \frac{1}{2N_B} \frac{N_{ES}}{\tau_{GS}^{ES}} + \Gamma_p v_g a_{GS} S_{GS}; \\ \gamma_{34} &= -\Gamma_p v_g g_{GS} + \Gamma_p v_g a_p S_{GS}; \\ \gamma_{43} &= \Gamma_p v_g a_{GS} S_{GS} + \frac{\beta_{sp}}{\tau_{GS}^{spon}}; \\ \gamma_{44} &= \frac{1}{\tau_p} - \Gamma_p v_g g_{GS} + \Gamma_p v_g a_p S_{GS}; \\ \gamma_{51} &= \Gamma_p v_g a_{RS} \kappa_{RS}; \gamma_{52} = \frac{1}{4} \Gamma_p v_g a_{ES} \kappa_{ES}; \\ \gamma_{53} &= \frac{1}{2} \Gamma_p v_g a_{GS} \alpha_{GS}; \gamma_{54} = -\frac{1}{2} \Gamma_p v_g a_p \alpha_{GS}; \end{aligned} \quad (3.32)$$

where $a_{RS,ES,GS}$ are the differential gains with respect to the carrier density while a_p takes into account the fact that the gain is compressed at high photon densities such as $dg_{GS} = a_{GS}dN_{GS} - a_p dS_{GS}$. Following Cramer's rule, the FN of QD laser is calculated by :

$$FN(\omega) = \left| \frac{j\omega\delta\phi(\omega)^2}{2\pi} \right| \quad (3.33)$$

with $\delta\phi(\omega)$ being the phase fluctuation. And the RIN of the QD laser emitting on the GS transition is then expressed as follows:

$$RIN(\omega) = \frac{|\delta S_{GS}(\omega)|^2}{S_{GS}^2} \quad (3.34)$$

with $\delta S_{GS}(\omega)$ being the photon number variation in the frequency domain and S_{GS} being the average photon number. The laser under study is based on the InAs/InP(311B) QD structure. All material and optical parameters are listed in Table 3.1, unless stated otherwise [275]. The threshold current (I_{th}) is found of 48 mA in this QD laser.

3.2.2 Effect of the carrier noise on the frequency noise and linewidth

The FN is at first performed and the Fig.3.9 illustrates that the carrier noise has little contribution to the FN except at the resonance frequency (f_{RO}), where the peak is slightly enhanced.

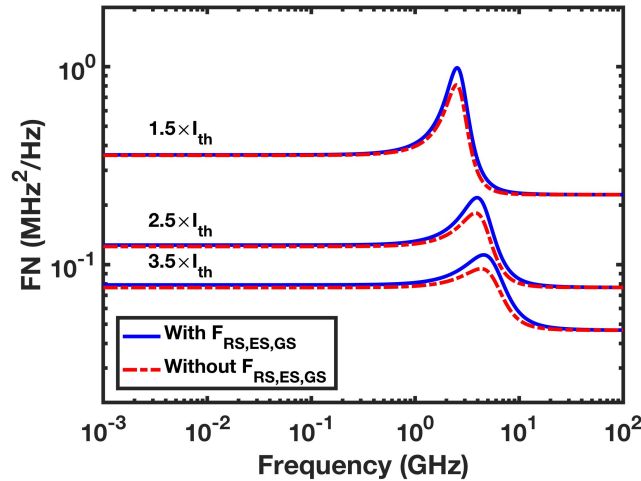


Fig. 3.9 Carrier noise contribution to the FN at several bias currents. The solid line are with carrier noise while the dash-dot lines are not.

Table 3.1 Material and optical parameters of the InAs/InP(311B) QD laser.

Symbol	Description	Value
E_{RS}	RS transition energy	0.97 eV
E_{ES}	ES transition energy	0.87 eV
E_{GS}	GS transition energy	0.82 eV
τ_{ES}^{RS}	RS to ES capture time	6.3 ps
τ_{GS}^{ES}	ES to GS relaxation time	2.9 ps
τ_{RS}^{ES}	ES to RS escape time	2.7 ns
τ_{ES}^{GS}	GS to ES escape time	10.4 ps
τ_{RS}^{spon}	RS spontaneous emission time	0.5 ns
τ_{ES}^{spon}	ES spontaneous emission time	0.5 ns
τ_{GS}^{spon}	GS spontaneous emission time	1.2 ns
τ_p	Photon lifetime	4.1 ps
T_2	Polarization dephasing time	0.1 ps
β_{sp}	Spontaneous emission factor	1×10^{-4}
a_{GS}	GS Differential gain	$5.0 \times 10^{-15} \text{ cm}^2$
a_{ES}	ES Differential gain	$10 \times 10^{-15} \text{ cm}^2$
a_{RS}	RS Differential gain	$2.5 \times 10^{-15} \text{ cm}^2$
ξ	Gain compression factor	$2.0 \times 10^{-16} \text{ cm}^3$
Γ_p	Optical confinement factor	0.06
α_{GS}	GS contribution to α_H -factor	0.5
N_B	Total dot number	1×10^7
D_{RS}	Total RS state number	4.8×10^6
V_B	Active region volume	$5 \times 10^{-11} \text{ cm}^3$
V_{RS}	RS region volume	$1 \times 10^{-11} \text{ cm}^3$
κ_{ES}	ES contribution coefficient	0.122
κ_{RS}	RS contribution coefficient	0.037

This is understandable because the high-frequency part of the FN is determined solely by the spontaneous emission of the GS whereas the low-frequency contribution is essentially governed by both the spontaneous emission and the α_H -factor of the QD laser [91]. As a conclusion, Fig.3.9 suggests that the neglect of the distributed carrier noise in the GS, ES and RS is a proper approximation for both FN and spectral linewidth investigations [275].

From the FN spectra, the α_H -factor of the QD laser can be extracted according to Eq.3.1 as depicted in Fig.3.10 [275]. The red squares present the α_H -factor including the contribution of all populations in the GS, ES and RS. It is found that the α_H -factor increases with the bias current from 0.76 at $1.2 \times I_{th}$ to 0.86 at $4.2 \times I_{th}$. Blue circles point out that the population in the RS has a negligible contribution to the α_H -factor. On the contrary, the contribution of the

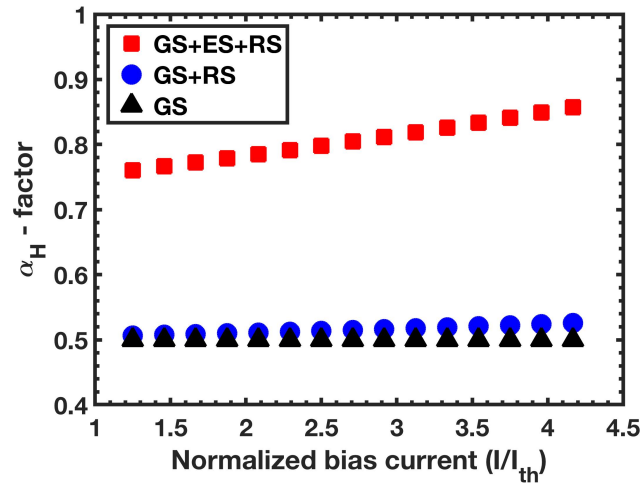


Fig. 3.10 Contribution of the GS, the ES and the RS to the α_H -factor as a function of the normalized bias current.

population in the ES to the α_H -factor is more than 34% at $1.2 \times I_{th}$ hence the population in the ES and GS dominate the contribution to the α_H -factor.

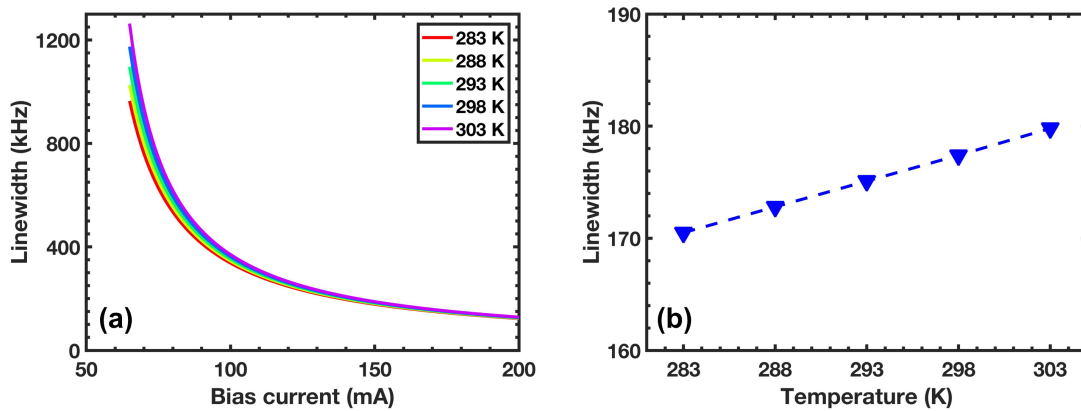


Fig. 3.11 (a) Calculated spectral linewidth as a function of the drive current for the AR/HR QD DFB laser. (b) Temperature dependence of the minimum linewidth at 155 mA.

Fig.3.11(a) presents the evolution of the calculated spectral linewidth as a function of the bias current between 283 K and 303 K. The corresponding experimental results will present in the next section. Overall, the simulation well reproduces the experimental results except the slope difference and the linewidth rebroadening. The latter can not be predicted because of the various assumptions made in the model. Indeed, flicker noise, gain compression and spatial hole burning are not taken into account at this stage [218]. Nevertheless, considering the same temperature range, numerical simulation shows a very good agreement with the

experiments while the Fig.3.11(b) confirms that the minimum linewidth is rather insensitive to the operating temperature. For a bias current of 155 mA, the calculated spectral linewidth increases from 170.5 kHz ($I/I_{th} = 3.4$) at 283K to 175.1 kHz ($I/I_{th} = 3.2$) at 293K, and 179.8 kHz ($I/I_{th} = 3.1$) at 303 K which is in agreement with the measured values. The simulation also confirms that the spectral linewidth of QD lasers is rather insensitive to the temperature range depicted hereinafter.

3.2.3 Effect of the carrier noise on the relative intensity noise

The effect of the carrier noise on the RIN is then performed. Fig.3.12 presents the RIN of the QD laser calculated for bias currents of $1.5 \times I_{th}$, $2.5 \times I_{th}$ and $3.5 \times I_{th}$, respectively. The RIN is almost constant at low frequencies below 1.0 GHz, and exhibits a peak at the resonance frequency of the QD laser. Above the resonance, the RIN decreases at high frequency. It has to be remarked that the partition noise arising from the random division of reflected and transmitted photons at the cavity facets is not included in the calculations, which leads to a noise floor in the high frequency part of the RIN spectrum [41]. At a higher bias current, the RIN decreases in the whole spectral range due to the larger damping factor and the peak shifts towards a higher frequency along with a reduced peak amplitude.

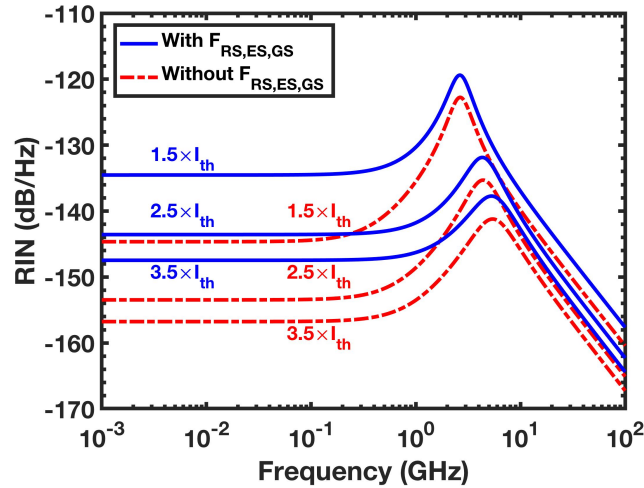


Fig. 3.12 Contribution of $F_{RS,ES,GS}$ to the RIN at bias currents of $1.5 \times I_{th}$, $2.5 \times I_{th}$ and $3.5 \times I_{th}$, respectively. The solid lines are with carrier noise while the dash-dot lines are not.

Fig.3.13 depicts the bias current dependence of the damping factor and the resonance frequency of the RIN spectra including the $F_{RS,ES,GS}$. At a higher bias current, both the damping factor and the resonance frequency are increased which is in agreement with

Fig.3.12 showing that the resonance frequency peak scales up with the bias current while its amplitude is reduced.

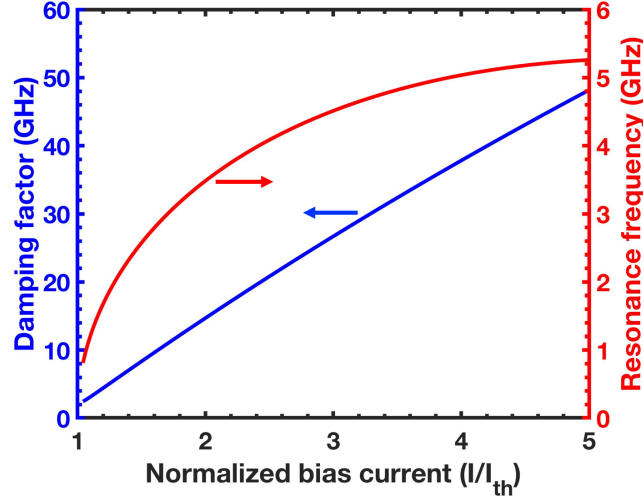


Fig. 3.13 The bias current dependence of the damping factor and the resonance frequency of the RIN spectra including the $F_{RS,ES,GS}$.

Surprisingly, the RIN including the carrier noise (solid curves) $F_{RS,ES,GS}$ has a significant difference in comparison to that without $F_{RS,ES,GS}$ (dash-dot curves), especially at low frequencies (< 1.0 GHz). For example, the low-frequency RIN (extracted at 1.0 MHz) at $1.5 \times I_{th}$ increases from -144 dB/Hz to -134 dB/Hz when the carrier noise is included. Fig.3.14 further shows that this discrepancy of 10 dB becomes even slightly larger at a higher bias current. In contrast, this difference in QW lasers is only less than 4 dB based on our simulations (not shown).

In order to clarify the contribution of the carrier noise of each state to the laser intensity noise, Fig.3.15 plots the RIN spectra at $1.5 \times I_{th}$ for the cases with $F_{RS,ES,GS}$ (solid line), $F_{ES,GS}$ (dash line), F_{GS} (dot line) and without $F_{RS,ES,GS}$ (dash-dot line), respectively. It is found that both F_{GS} and F_{ES} dominate the carrier noise contribution, while F_{RS} remains perfectly negligible. In addition, F_{GS} enhances the RIN amplitude over the whole frequency range, while F_{ES} only increases the RIN at frequencies below the resonance frequency. As performed in [3], it was shown that the carrier noise sources can affect the intensity fluctuations in a QW laser. Therefore, in case of QD lasers, these simulations prove that the inclusion of the carrier noise originating from both GS and ES is of first importance for investigating the RIN characteristics while that of the RS does not really play a role.

Since the carrier noise in the GS and ES has a dominant contribution to the RIN, it is possible to reduce the intensity noise by changing the GS-ES energy separation ΔE_{GS}^{ES} . As the threshold current changes with ΔE_{GS}^{ES} , the photon density is fixed in the simulations rather

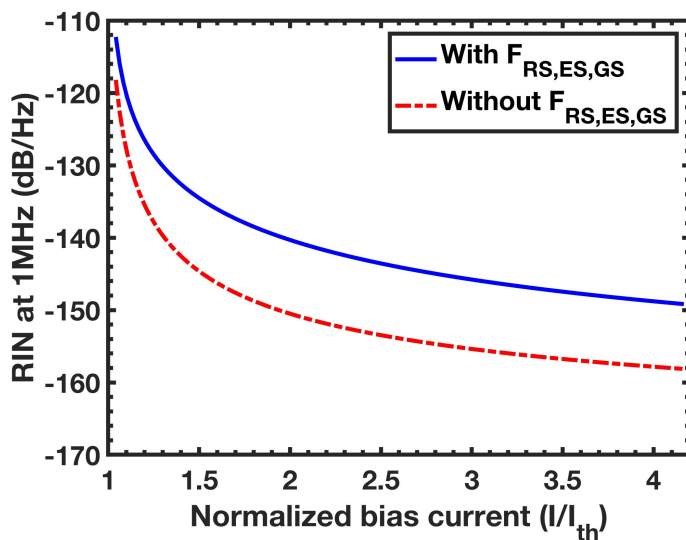


Fig. 3.14 The RIN at 1 MHz with (solid line) and without (dash-dot line) carrier noise as a function of the normalized bias current.

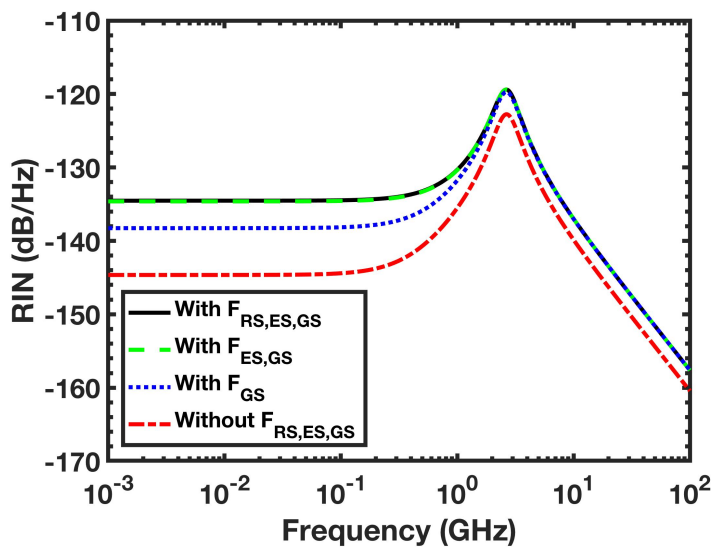


Fig. 3.15 Simulation of the RIN spectra at $1.5 \times I_{th}$ for the cases including the carrier noise sources $F_{RS,ES,GS}$, $F_{ES,GS}$, F_{GS} and without ($F_{RS,ES,GS} = 0$), respectively.

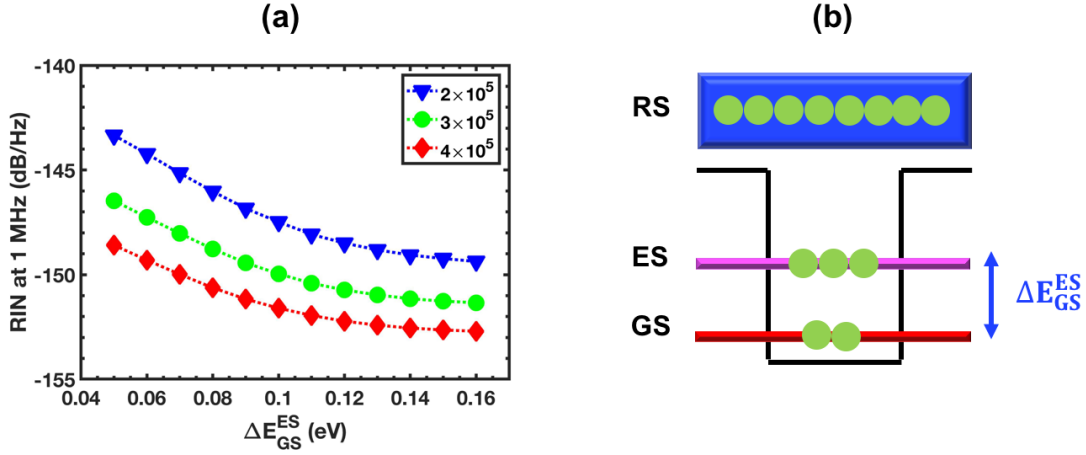


Fig. 3.16 (a) Simulated RIN at 1 MHz as a function of the GS-ES separation (ΔE_{GS}^{ES}) for different photon numbers. (b) Illustration of GS-ES separation.

than the bias current. Fig.3.16(a) depicts the RIN at 1 MHz as a function of ΔE_{GS}^{ES} for different photon numbers of 2×10^5 , 3×10^5 and 4×10^5 , respectively. Fig.3.16(b) is the illustration of GS-ES separation. The GS-RS energy separation is kept at $\Delta E_{GS}^{RS} = 3 \times \Delta E_{GS}^{ES}$ while the carrier capture and relaxation times are fixed (see Table 3.1) since the carrier scattering rates are weakly dependent on the energy separation [233]. It is shown that increasing the GS-ES energy separation reduces the RIN of the QD laser. For a lasing photon number of 2×10^5 , the RIN is found to decrease from -143 dB/Hz for $\Delta E_{GS}^{ES} = 0.05$ eV down to -149 dB/Hz for $\Delta E_{GS}^{ES} = 0.16$ eV hence corresponding to a reduction by as much as 6 dB. On the other hand, the amplitude also decreases at higher photon numbers due to the larger damping factor. However, further increase of ΔE_{GS}^{ES} will slowly reduce the RIN value since the contribution of carrier noise in the ES can be minimized by ΔE_{GS}^{ES} while that in the GS relies more on the inherent material property. Therefore, by further increasing the GS-ES energy level interval, e.g., by using smaller dots, and more QD layers in the active region, further improvements of the RIN performance is expected [1]. In conclusion, a small vertical coupling between the GS and the ES is in favor of low intensity noise operation because of the reduced carrier noise contribution from the ES. This proves that the inclusion of the ES contribution is required for getting a much better accurate description of the QD laser intensity noise.

The impact of the relaxation time on the RIN properties is also investigated. Fig.3.17(a) shows the calculated RIN at 1 MHz as a function of the relaxation time assuming a capture time from RS to ES such as $\tau_{ES}^{RS} = 2.17 \times \tau_{GS}^{ES}$ and a photon number of 2×10^5 . Fig.3.17(b) is the illustration of relaxation time. It is found that the RIN decreases rapidly with the increase of the relaxation time in particular below 10 ps because the carrier noise in the ES level has

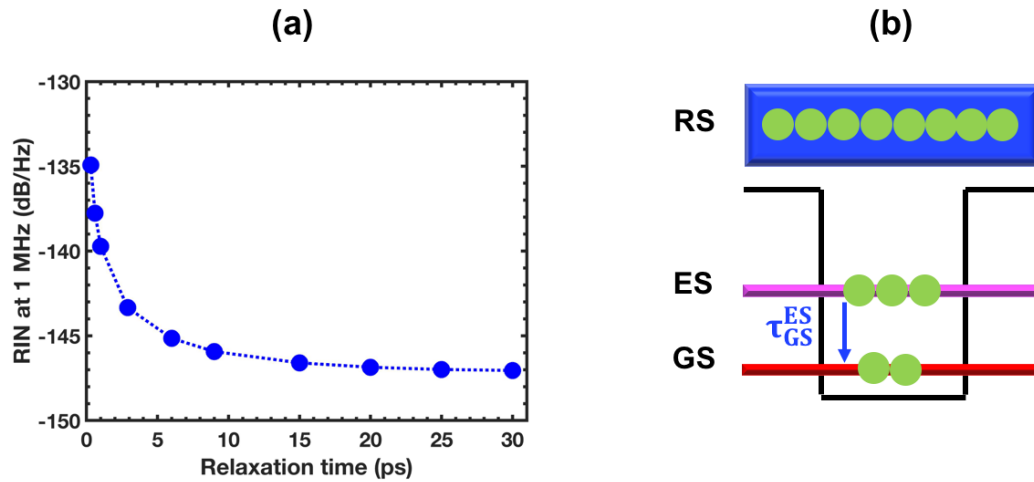


Fig. 3.17 (a) The RIN at 1 MHz as a function of the relaxation time from ES to GS assuming a capture time $\tau_{ES}^{RS} = 2.17 \times \tau_{GS}^{ES}$ and a photon number of 2×10^5 . (b) Illustration of relaxation time.

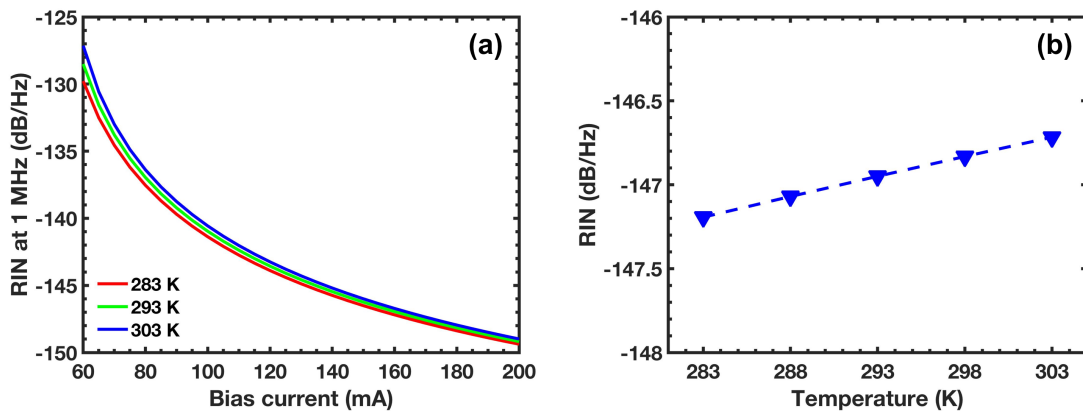


Fig. 3.18 (a) Calculated RIN at 1 MHz as a function of the bias current at 283 K, 293 K and 303 K, respectively. (b) RIN values as a function of temperature assuming a bias current of 160 mA.

less impact on the GS (see Eq.3.28). Beyond 10 ps, the RIN is found rather insensitive to the relaxation time. In addition, the RIN of QD lasers is expected to be reduced for longer photon lifetime, which is the same as in QW lasers [41, 111]. The increase of the photon lifetime can be achieved either by enlarging the cavity length, increasing the power reflectivities, or by reducing the internal loss. However, to reproduce the above relations in the simulations, further improvements of the current numerical model are required to take into account the impact of such modifications on the spontaneous emission factor [111] and the spatial hole burning effects [41], which is in the latter of paramount importance for distributed feedback lasers [229].

The effect of the temperature on the RIN of QD lasers is now investigated. Fig.3.18(a) presents the evolution of the calculated low-frequency RIN (at 1 MHz) as a function of the bias current between 283 K and 303 K. The RIN is at first drastically reduced near the threshold and a further decrease is achieved at high bias currents owing to the strong damping factor. For a bias current of 160 mA, Fig.3.18(b) also shows that the value of the RIN increases from - 147.2 dB/Hz at 283 K to - 147 dB/Hz at 293 K, and -146.7 dB/Hz at 303 K with a variation of 0.5 dB/Hz over the temperature range of 20 K. These results demonstrate the RIN of QD lasers is pretty stable over temperature variations.

3.3 Experimental analysis of spectral linewidth

3.3.1 InAs/InP QD DFB laser description

Fig.3.19(a) shows the schematic diagram of the InAs/InP DFB laser. The QD lasers under study were grown by chemical beam epitaxy (CBE) on a (100) oriented n-type InP substrate. The undoped active region of the laser consisted of 5 stacked layers of InAs QDs with 30 nm $\text{In}_{0.816}\text{Ga}_{0.184}\text{As}_{0.392}\text{P}_{0.608}$ (1.15Q) barriers. The QDs were tuned to operate in the desirable operation wavelength range by using a QD double cap growth procedure and a GaP sublayer [213]. Growing the dots on a thin GaP layer allows a high dot density to be obtained and improved layer uniformity when stacking multiple layers of dots, providing maximum gain. Photoluminescence (PL) from a 5 QD layer test structure grown just before the laser had a FWHM of 36.5 meV at 4 K which broadened to 60 meV at 300 K, indicating good dot size uniformity. This active layer was embedded in a 350 nm thick 1.15Q waveguiding core, providing both carrier and optical confinement. Fig.3.19(b) shows an atomic-force microscopy (AFM) image of one QD layer. An average dot density of approximately $4 \times 10^{10} \text{ cm}^{-2}$ per layer was obtained according to AFM measurements on uncapped stacked dot samples.

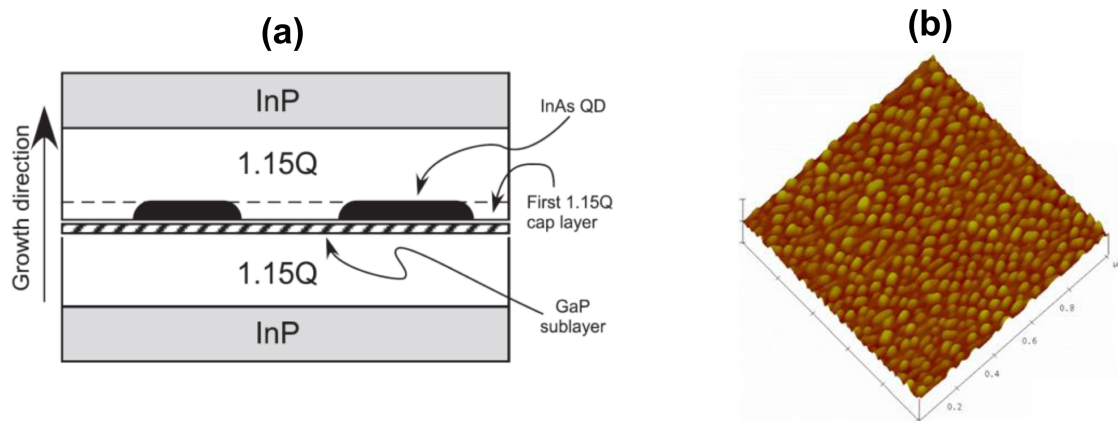


Fig. 3.19 (a) Schematic diagram of the InAs QD structure; (b) An atomic-force microscopy image of one QD layer ($1 \mu\text{m} \times 1 \mu\text{m}$) [213].

Following the growth of the QD active core, the wafer was removed to pattern the grating region. This was performed using a HeCd laser to holographically expose an optical resist with a uniform grating pattern across the whole wafer, followed by wet chemical etching.

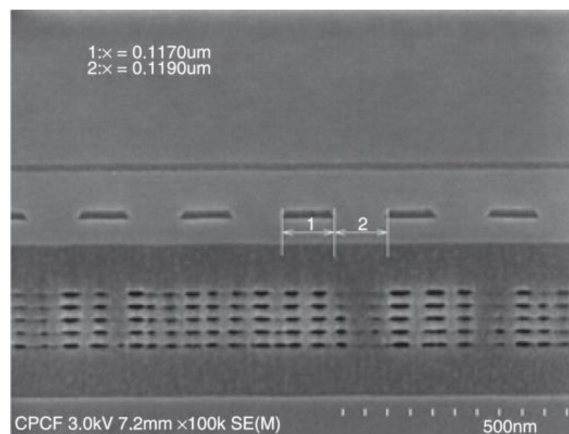


Fig. 3.20 Cross section view of the DFB structure [213].

Fig.3.20 shows the cross-sectional scanning of completed laser structure and the floating grating. After the patterning of the grating, the p-type InP cladding and InGaAs contact layers were regrown using metal-organic chemical vapor deposition (MOCVD). The wafer was photoluminescence (PL) mapped before and after regrowth by MOCVD and no change was observed in the PL emission wavelength, indicating the high material quality of both growth steps [86]. Single lateral mode ridge waveguide lasers were fabricated with a stripe width of $3 \mu\text{m}$ and a cavity length of 1mm . Both facets were coated to modify the reflectivity

of the laser cavity. One laser used a very low reflectivity antireflection coating (AR) on both facets ($<0.01\%$) to remove the effects of the termination phase of the grating at the cleaved facets [34], this laser is referred to as the AR/AR design. The other laser used asymmetric facet coatings, the output facet having a 2% reflectivity while the rear facet having a reflectivity of 62%, which is referred to as the AR/HR design. The AR/HR design is much more sensitive to the grating phase at the facets and since the grating used was uniform, i.e. there were no phase shifts introduced, this meant that different devices were observed lasing on the short wavelength side of the DFB stopband, the long wavelength side, and both sides simultaneously. For the AR/AR design, all the laser devices emitted on the short wavelength side of the stopband for all drive currents, a consequence of spatial hole burning in a symmetric device with a uniform grating [34]. The devices under study in this work emitted only at a single wavelength.

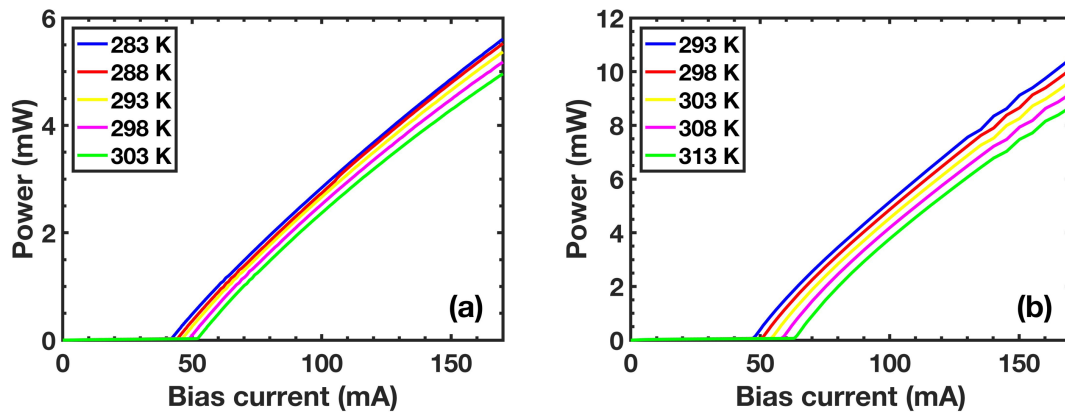


Fig. 3.21 Light current curves measured for different temperature for AR/HR DFB laser (a) and AR/AR DFB laser (b).

Fig.3.21 represents the light current characteristics of the QD DFB lasers for different temperatures. For AR/HR laser, the threshold current (I_{th}) is increased from 42 mA at 283 K to 52 mA at 303 K. While for AR/AR laser, the I_{th} increases from 47.5 mA at 293 K to 63 mA at 313 K for AR/AR laser.

Fig.3.22 shows the single-mode lasing spectra for both devices (at 100 mA), which exhibit lasing wavelengths at $1.52 \mu\text{m}$ and side mode suppression ratios (SMSR) of at least 50 dB over the whole current range. Fabry-Perot (FP) ripples are observed outside the grating stopband in the AR/HR device, while those disappear in the AR/AR device owing to the smaller facet reflectivities. The grating coupling constant κ was measured to be 10 cm^{-1} determining from the laser spectra just below threshold, leading to a value for κL of 1, with L being the length of the laser cavity [123, 28].

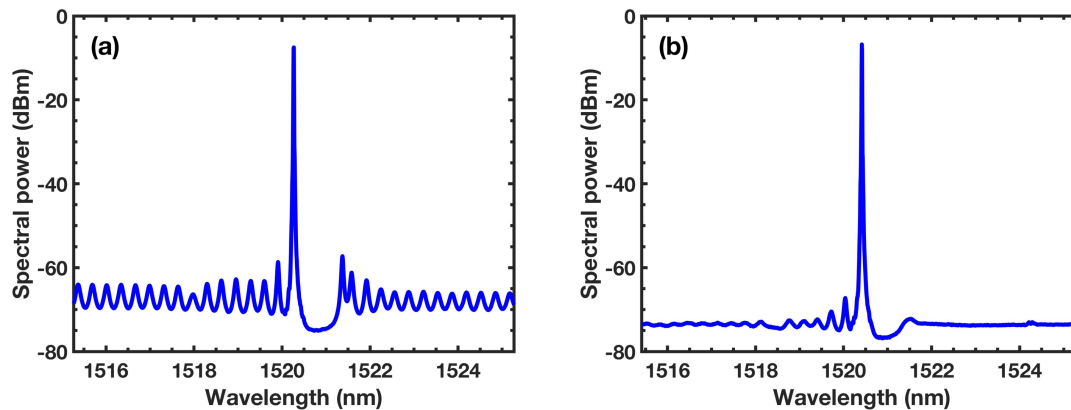


Fig. 3.22 Optical spectra measured at $2 \times I_{th}$ for AR/HR DFB laser (a) and AR/AR DFB laser (b).

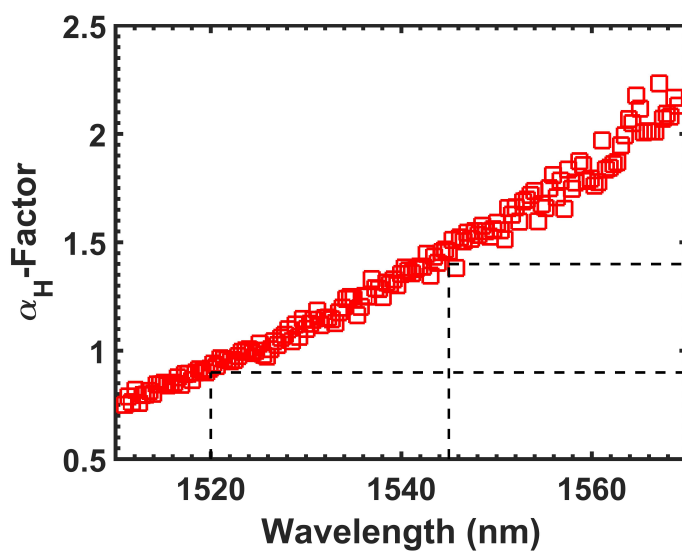


Fig. 3.23 The measured α_H -factor as a function of the lasing wavelength for the InAs/InP FP QD laser. The black dashed lines indicate the FP gain peak value (1545 nm) and DFB gain peak value (1520 nm).

The material α_H -factor is extracted from the amplified spontaneous emission (ASE) [103]. To do so, a FP cavity made with the same semiconductor material is considered because the ASE method is not easily applicable to DFB lasers for which the grating makes the gain extraction more complicated. The experimental procedure for retrieving the α_H -factor is fully detailed elsewhere [103]. Fig.3.23 depicts the measured α_H -factor as a function of the lasing wavelength. Values ranging from 0.7 to 2.2 are obtained over a span of 50 nm. At the FP gain peak (1545 nm), a relatively low value of 1.4 is obtained. Note that the α_H -factor quoted in Fig.3.23 is only valid for the FP laser which has no longitudinal spatial hole burning (LSHB). As such, it can not be used for analyzing the α_H -factor of DFB lasers except at low drive currents (i.e. not too far from the threshold) where the LSHB remains small.

3.3.2 Linewidth measurement setup

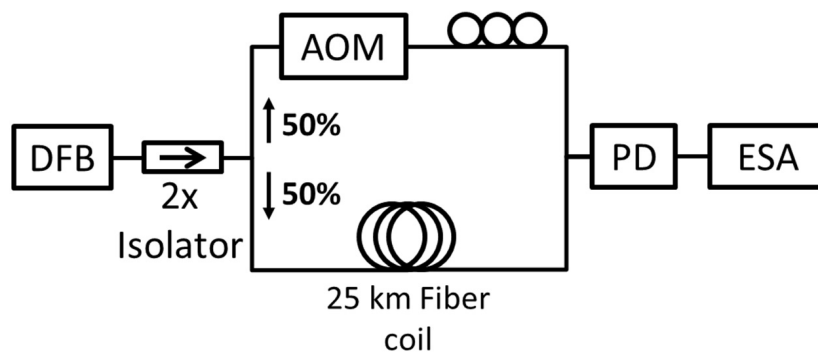


Fig. 3.24 Self-heterodyne interferometer used for the linewidth measurement. AOM: Acousto-Optic Modulator; PD: Photodiode; ESA: Electrical Spectrum Analyzer.

Fig.3.24 shows the self-heterodyne interferometric apparatus used to measure the spectral linewidth [202]. Once the laser emission is launched into the fiber interferometer, part of the signal is sent to a 100 MHz frequency-shifted acousto-optic modulator (AOM) while the other part propagates through a 25 km fiber coil. Such relatively long fiber length provides a sufficient time delay than the laser's coherence time. For example, according to Eq.3.2, a coherence length of 1 km is obtained if the laser exhibits a linewidth of 100 kHz. For sufficiently long delays, the superimposed beams are essentially uncorrelated and the output spectrum becomes a simple self-convolution of the laser output spectrum, from which the laser linewidth is easily retrieved. The polarization controller is used to match the polarizations in the two arms. At the output of the interferometer, the resulting beat note centered at the AOM frequency is recorded with the photodiode (PD) and sent to the electrical spectrum analyzer (ESA). Two optical isolators, of more than 60 dB isolation, were

used to eliminate reflected light. The intrinsic spectral linewidth has a Lorentzian shape, however, due to the Gaussian shape filter in the electrical spectrum analyzer (ESA) and the residual electrical noise from the power supply as well as thermal fluctuations, the linewidth is rather in the shape of a Voigt function, which is defined as the convolution of a Gaussian function and a Lorentzian function. In this work, the retrieval procedure is simplified by using a normalized pseudo-Voigt function f_V such as [253]:

$$f_V = (1 - \eta)f_G(x, \gamma_G) + \eta f_L(x, \gamma_L) \quad (3.35)$$

where f_G and f_L are the normalized Gaussian and Lorentzian functions represented as:

$$f_G(x, \gamma_G) = (1/\pi^{1/2}\gamma_G)\exp(-x^2/\gamma_G^2) \quad (3.36)$$

$$f_L(x, \gamma_L) = (1/\pi\gamma_L)(1 + x^2/\gamma_L^2)^{-1} \quad (3.37)$$

with γ_G and γ_L are related to the full-width at half maximum (FWHM) of the Gaussian and Lorentzian functions respectively, and η is the mixing parameter. In the experiments, the captured radio-frequency(RF) spectrum is the spectral aliasing of both the negative and the positive sides of the full spectral range, hence the output of the ESA is the convolution of two parts, which must be taken into account to retrieve the original spectral linewidth. As such, the FWHM linewidths from the Gaussian and Lorentzian parts can be expressed as:

$$\Gamma_G = 2\sqrt{\ln 2}\gamma_G \quad (3.38)$$

$$\Gamma_L = 2\gamma_L \quad (3.39)$$

The FWHM of the pseudo-Voigt profile can be defined as [253]:

$$\Gamma_V = (\Gamma_G^5 + 2.69269\Gamma_G^4\Gamma_L + 2.42843\Gamma_G^3\Gamma_L^2 + 4.47163\Gamma_G^2\Gamma_L^3 + 0.07842\Gamma_G\Gamma_L^4 + \Gamma_L^5)^{1/5} \quad (3.40)$$

For example, Fig.3.25 displays one experimental normalized radio-frequency (RF) spectrum (blue) as well as the corresponding Voigt fitted spectrum (red). The full width at half maximum extracted from the Voigt profile (red) leads to a minimum spectral line of 300 kHz which transforms into an intrinsic linewidth as low as 110 kHz with a Lorentzian fitting.

3.3.3 Longitudinal spatial hole burning dependence of spectral linewidth

Fig.3.26 illustrates the spectral linewidths fitted with the pseudo-Voigt profile as a function of the normalized drive current I/I_{th} , for the AR/HR (red) and the AR/AR lasers (blue). For the

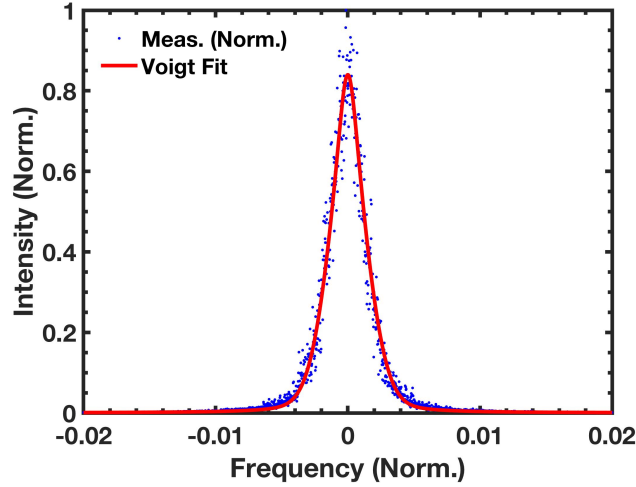


Fig. 3.25 Normalized RF spectrum and the corresponding Voigt fitted spectrum.

AR/HR DFB laser, a minimum linewidth of 160 kHz is reached at $I/I_{th} = 1.7$ with a fitted intrinsic Lorentzian linewidth as low as 80 kHz. Note that similar results are obtained with a pure Voigt profile. From Eq.3.3, the threshold gain is calculated by taking into account the loss induced by the grating that is about 6 cm^{-1} , which contributes to a modal gain at threshold of about 19 cm^{-1} . Then, the physical quantity $n_{sp} \times (1 + \alpha_H^2)$ is estimated to be about 1.4 at 1 mW output power leading to an inversion factor n_{sp} below the unity (assuming $\alpha_{H,DFB} \approx \alpha_{H,FP} = 0.9$ at threshold current at 1520 nm) which is in agreement with other values reported for QD lasers [205]. In this work, the $n_{sp} \times (1 + \alpha_H^2)$ is found much smaller than that reported for an InAs/GaAs QD DFB laser with a spectral linewidth of 800 kHz at 1 mW output power [46].

Although from Eq.3.3 narrow linewidth is obtained by increasing the laser power, Fig.3.26 also shows that the minimum achievable linewidth can be actually limited by a linewidth rebroadening. The rebroadening refers to an increase of the linewidth with increasing bias current at high output power levels. For instance, the spectral linewidth of the AR/HR DFB laser rebroadens up to 600 kHz at $I/I_{th} = 4.4$. In fact, the linewidth rebroadening occurs in any semiconductor lasers due to thermal effects, mode instability [203], longitudinal spatial hole burning (LSHB) [248] and gain compression [2, 70]. The first three of these effects are related to the device structure and can be minimized or eliminated by optimizing the laser design. For instance, a low grating coupling coefficient can reduce the effects of the spatial nonlinearities and so the spectral linewidth. Controlling the optical field distribution along the cavity through the facet coatings is also a way of eliminating the linewidth rebroadening, which will be shown later. As for the gain compression, it is fundamentally related to the timescales for the carrier equilibrium dynamics in the semiconductor gain media and is

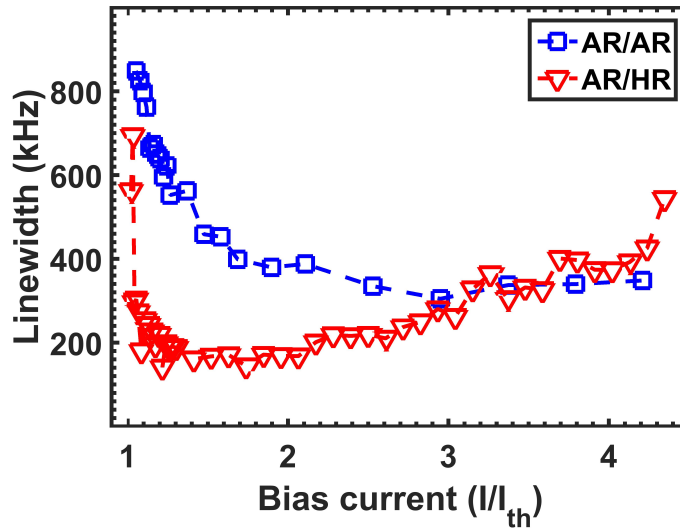


Fig. 3.26 Spectral linewidth fitted with a pseudo-Voigt profile as a function of the normalized drive current I/I_{th} , for AR/HR DFB laser (red) and AR/AR DFB laser (blue).

usually enhanced in QD gain media. Fig.3.27 depicts the simulated linewidth as a function of the bias current for different values of gain compression coefficient. Therefore, as compared to QW lasers, the re-broadening can be actually more pronounced in QD lasers because of the increased scattering rates with the injected current and larger gain nonlinearities [218, 179].

As for the AR/AR DFB laser depicted in Fig.3.26 (blue) the minimum linewidth is at 300 kHz with a fitted intrinsic Lorentzian linewidth as low as 110 kHz. By comparison with the AR/HR DFB laser, the spectral linewidth is now rather independent of the drive current without any re-broadening at the power levels investigated. Since both the gain medium and cavity parameters (length, ridge width, etc.) are identical for the AR/HR and AR/AR devices, the difference in behavior must be associated with the different optical field distribution along the cavity for the two devices, and hence different degrees of LSHB which is known to impact linewidth [34, 283]. For the AR/AR device the field distribution is always symmetric about the centre of the cavity [283] and weak due to the small value of κL , but for the AR/HR case it is highly asymmetric [264], enhancing the LSHB. Lastly, although the AR/HR structure shows a narrower linewidth, random facet phase effects are problematic for practical applications since every laser may exhibit different spectral characteristics, including linewidth. This is avoided by using AR coatings on both facets as long as the AR coating reflectivity is low enough, typically $<0.01\%$ [120, 72].

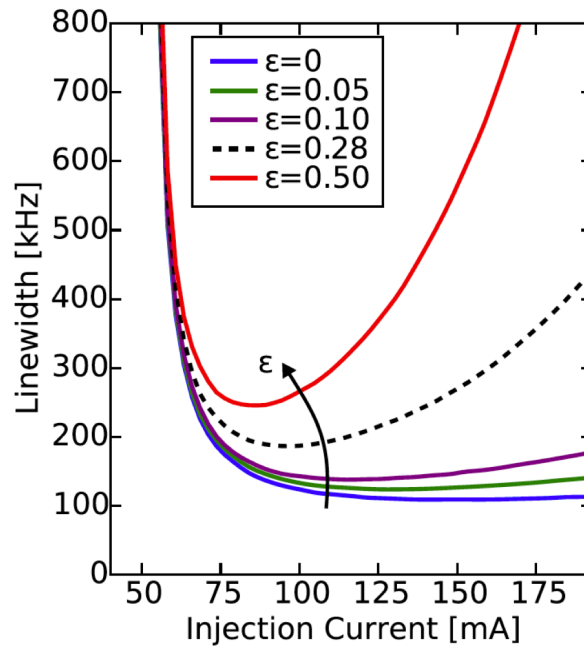


Fig. 3.27 Simulated linewidth as a function of the bias current for different values of gain compression coefficient [218].

3.3.4 Temperature dependence of spectral linewidth

The effect of the temperature on the spectral linewidth of the AR/HR laser device and a commercial QW DFB laser is now investigated, with the temperature being varied from 283 K to 303 K. Fig.3.28(a) displays the spectral linewidth as a function of the normalized bias current for the AR/HR DFB laser measured at 283K, 293K and 303K, respectively. From the pseudo-Voigt profile, a minimum linewidth of 168 kHz is obtained at 283K ($I/I_{th} = 1.3$). When the temperature is raised to 293K, this minimum slightly increases to 177 kHz ($I/I_{th} = 1.4$) and to 178 kHz at 303K ($I/I_{th} = 1.5$). Overall, the variation of the spectral linewidth does not exceed 5%, which proves the very good stability over the temperature range. Such a great thermal stability of QD lasers is attributed to the ultimate carrier confinement as well as to the quality of the QD materials providing maximum gain.

A comparison with a commercial QW DFB laser operating at $1.55 \mu\text{m}$ is also performed. Fig.3.28(b) shows the evolution of the spectral linewidth of the QW DFB laser assuming the same experimental conditions. Results show that the minimum linewidth is now enhanced from 2.5 MHz at 283K to 3.1 MHz at 303K, which corresponds to a variation of about 23% (600 kHz) over the same temperature range. The minimum linewidth at 303 K is found at lower normalized bias current ($I/I_{th} = 2.5$) than the value at 283K ($I/I_{th} = 3.5$), while it is opposite in QD laser. This effect is attributed to the variation of the threshold current which

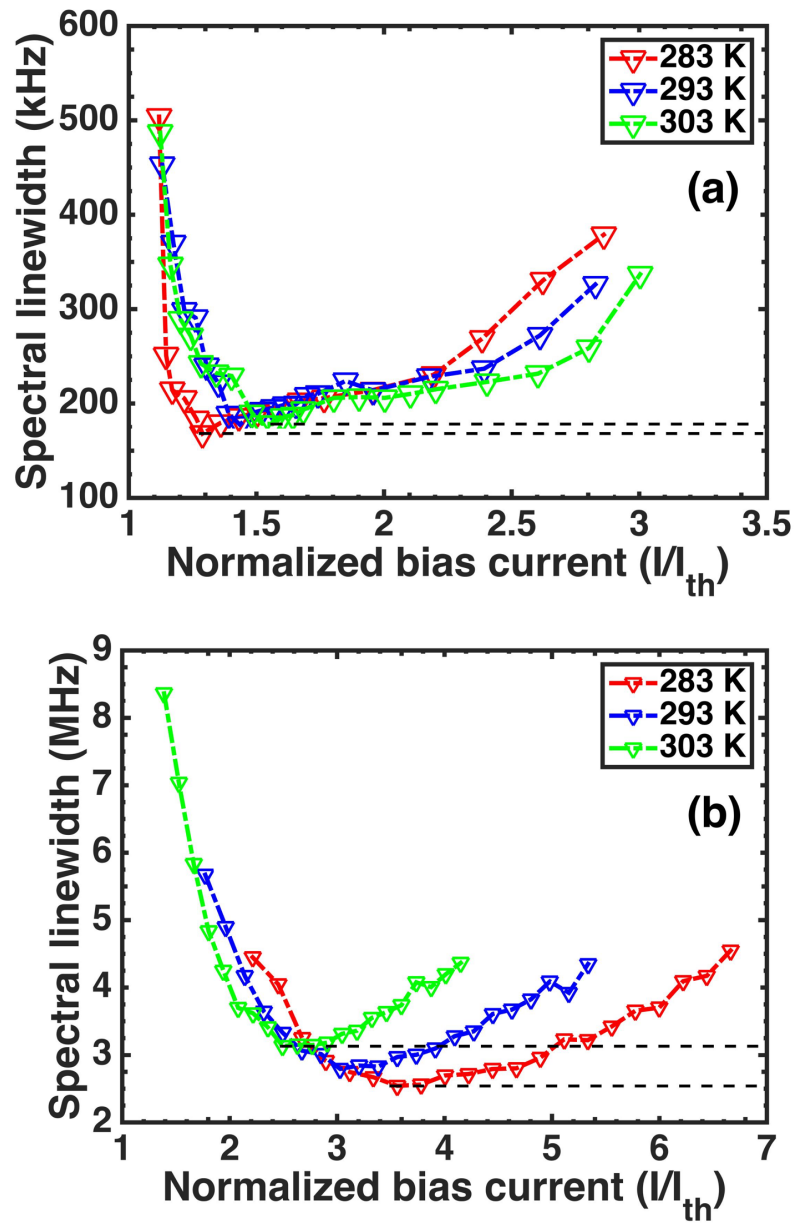


Fig. 3.28 Spectral linewidth of the AR/HR DFB laser (a) and the QW DFB laser (b) as a function of the normalized bias current and measured at 283K, 293K and 303K, respectively. The black dashed lines indicate the minimum linewidth level at 283K and 303K.

is about 61% for the QW laser against 23% for the QD one over the same temperature range. In contrast to QW lasers, the spectral linewidths of QD lasers are found much narrower and rather independent of the temperature, which is very promising for aforementioned applications discussed in the introduction Chapter.

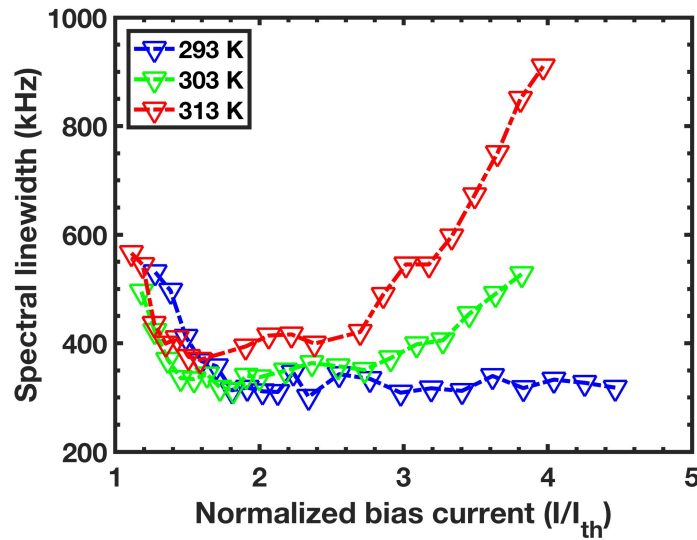


Fig. 3.29 Spectral linewidth of the AR/AR DFB laser as a function of the normalized bias current and measured at 293K, 303K and 313K, respectively.

In order to investigate the temperature dependence of the linewidth rebroadening, the spectral linewidth of the AR/AR laser device is now performed at various temperatures. Fig.3.29 shows the temperature dependence of the linewidth from 293 K to 313 K. At room temperature (293 K), the linewidth is not affected by increasing the injection current hence exhibiting a constant value of about 350 kHz. In addition, at $2 \times I_{th}$, the emission linewidth shows a good thermal stability with an increase not exceeding 410 kHz at 313 K. However, when the injection current is raised to $3.8 \times I_{th}$, a spectral rebroadening is observed leading to a degradation of the emission line up to 850 kHz at 313 K. The temperature dependence of the spectral linewidth results from two effects: first, high temperature reduces the optical power and increases the spectral linewidth according to Eq.3.3. Second, high temperature also increases the escape rate of carriers through thermal activation, to high energy levels leading to an enhanced occupation of high energy states. Thus, the gain spectrum becomes less symmetric and the α_H -factor increases with temperature as well [236]. Despite that, we demonstrate a QD DFB with a stable narrow line between 293 K and 313 K up to $3 \times I_{th}$ and with about 10 mW total output power.

3.4 Experimental analysis of the relative intensity noise

3.4.1 RIN measurement setup

Fig.3.30 shows the experimental setup for the measurement of the RIN.

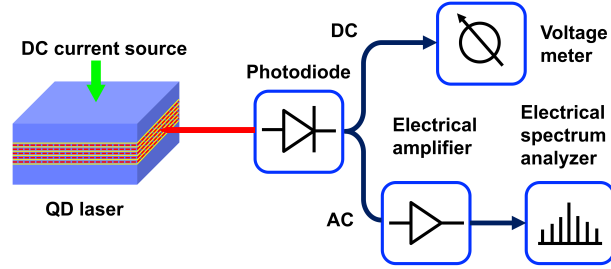


Fig. 3.30 Experimental setup used for investigating the RIN of QD lasers.

The QD laser is pumped by a DC current source, while the device temperature is kept constant at 20 °C using a thermo-electric cooler. The laser emission is coupled into a lensed fiber and then the optical signal is converted into the electrical domain through a low-noise photodiode with a bandwidth of 10 GHz. The DC voltage is measured by a voltage meter through the DC monitor port of the photodiode, while the AC signal is amplified by a broadband amplifier with a typical small-signal gain of 30 dB. In the end, the amplified noise spectrum is measured on an electrical spectrum analyzer (ESA). It is noted that the RIN can also be limited by the shot noise resulting from the random occurrence of the photons. However, the RIN of the laser is usually much above that of the shot noise level, meaning that the measured noise spectrum from the detector reflects the contribution of carriers [296, 157]. The intrinsic laser noise S_{Laser} can be expressed as [296]:

$$S_{Laser} = S_{Total} - S_{Thermal} - S_{Shot} \quad (3.41)$$

where S_{Total} the total noise measured by the ESA, $S_{Thermal} = 4k_B T / R_L$ is the thermal noise, which is independent on the optical power and is determined when the laser is turned off. k_B the Boltzmann constant, T the temperature and R_L the load resistance of the ESA with a value of 50 Ω . S_{Shot} is white noise determined by $S_{Shot} = 2qI_{DC}R_L$ with q the elementary charge, I_{DC} the DC current. Overall, the RIN of the lasers can be recasted as follows [296]:

$$RIN = 10 \log_{10} \left[\frac{(S_{Total} - S_{Thermal}) / (RBW \times G) - S_{Shot}}{P_{DC}} \right] \quad (3.42)$$

where P_{DC} is the electrical DC power, RBW is the resolution bandwidth of the ESA with a value of 200 kHz and G is the gain of the experimental setup including the amplifier, which is measured by the vector network analyzer (VNA).

3.4.2 Analysis of the RIN properties

Fig.3.31 shows the measured RIN spectra at various bias currents of the AR/AR QD DFB laser, which are extracted using Eq.3.42.

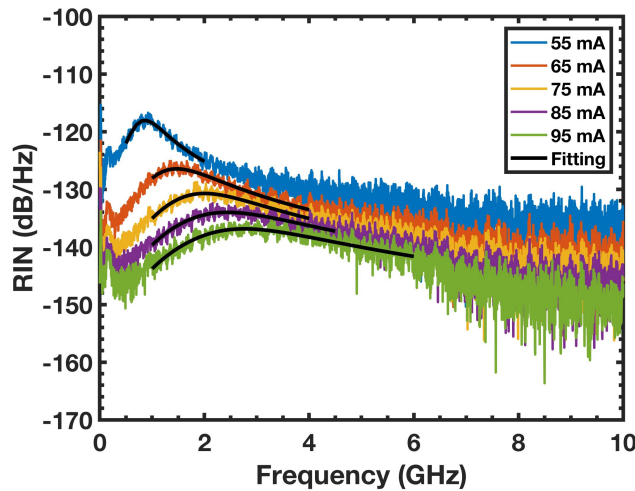


Fig. 3.31 RIN spectra up to 10 GHz for QD lasers at various bias currents. The black lines indicate the curve fitting.

The RIN at low frequencies is relatively high resulting from the bias current noise, thermal noise as well as mode partition noise [296]. This latter noise induced by the share of intensity between the different modes in multimodes lasers [111]. Beyond 1 GHz, the RIN spectrum exhibits a peak with a maximum corresponding the relaxation frequency between photons and electrons in the cavity. The peak frequency increases with the bias current above the threshold. After the peak frequency, the RIN reduces with the increasing frequency and reaches its smallest value. In the meantime, the RIN spectrum decreases with the enhanced bias current and the minimal RIN level is achieved at -155 dB/Hz in the 8-10 GHz range at 95 mA. It is noted that in analog amplitude modulation systems, the single mode laser with a RIN value less than -155 dB/Hz is necessary to avoid feedback reflexions [111]. In order to further reduce the RIN value, we can use a longer cavity length to achieve longer photon lifetime [111].

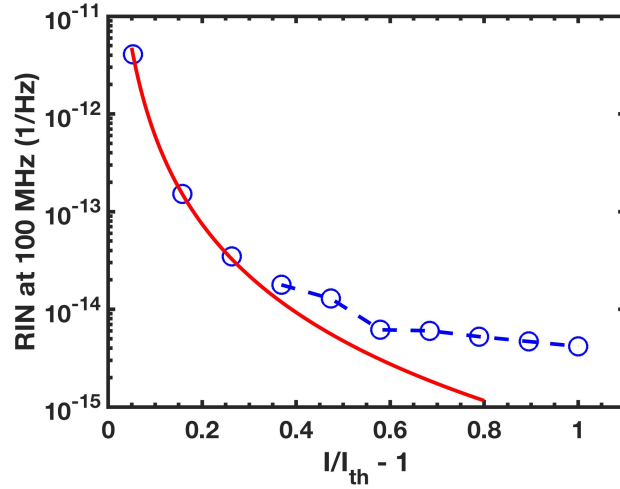


Fig. 3.32 RIN at 100 MHz as a function of $(I/I_{th} - 1)$. The red line indicates the fitting of the dependence of $(I/I_{th} - 1)^{-3}$.

Although deriving the exact expression of RIN is rather complicated, a simple approximation expression of the RIN at low frequency can be expressed as:

$$RIN = \frac{4\beta\tau_p}{n_{pop}(I/I_{th} - 1)^3} \quad (3.43)$$

with β the fraction of spontaneous emission injected into the mode, I_{th} the threshold current, τ_p photon lifetime, n_{pop} the inversion population parameter [111]. This expression shows the RIN decreases with the increase of $(I/I_{th} - 1)^{-3}$ only when the RIN values are less than the value at 30 % above the threshold (with an error less than 10 %). Fig.3.32 presents the RIN values at 100 MHz as a function of the term $(I/I_{th} - 1)$. As shown, the RIN decreases with $(I/I_{th} - 1)^{-3}$ until $0.37 \times (I/I_{th} - 1)$ and then saturates at higher bias currents, indicating that the Eq.3.43 is not valid after the RIN values at 30 % above the threshold. The red line indicates the fitting of the dependence of $(I/I_{th} - 1)^{-3}$, which shows a discrepancy with the RIN values after $0.37 \times (I/I_{th} - 1)$.

In what follows, both the relaxation oscillation frequency (f_{RO}) and damping factor γ are extracted from the curve-fitting of the RIN spectrum through the expression [41]:

$$RIN(\omega) = \frac{a + b\omega^2}{(\omega^2 - \omega_{RO}^2)^2 + \gamma^2\omega^2} \quad (3.44)$$

where ω_{RO} the angular relaxation frequency, ω the angular frequency, a and b coefficients used for the curve-fitting. The corresponding curve fitting for each bias current is also indicated in Fig.3.31 (black lines). Fig.3.33(a) and (b) illustrate the bias current dependence

of the γ and f_{RO} . Both γ and f_{RO} increase with the enhanced bias current, for example at 95 mA ($2 \times I_{th}$), the γ is found as large as 20 GHz along with a f_{RO} of 2.8 GHz. These experimental results is rather qualitatively agree with the simulations indicated in Fig.3.13, reflecting the right trend of bias current dependence of the γ and f_{RO} .

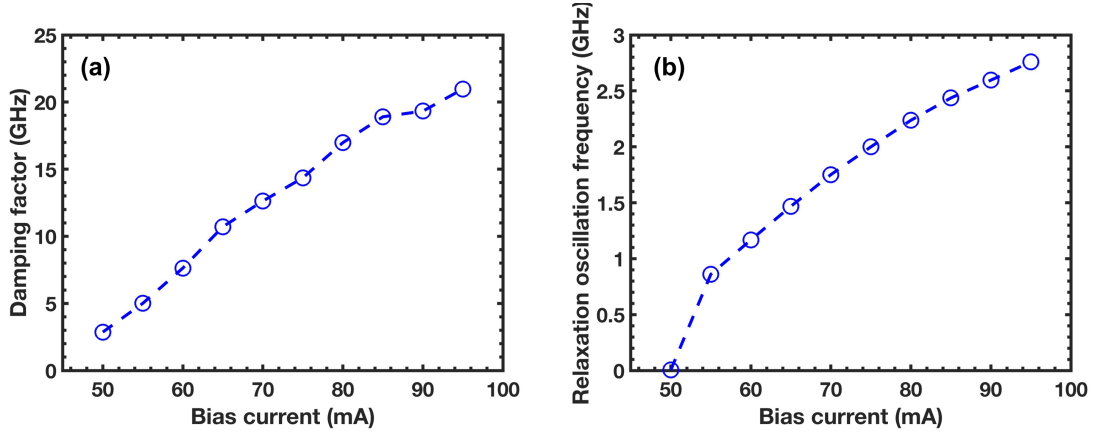


Fig. 3.33 The bias current dependence of the damping factor (a) and relaxation oscillation frequency (b).

Fig.3.34 shows the damping factor as a function of the squared relaxation oscillation frequency. The evolution is linear following the relationship:

$$\gamma = K f_{RO}^2 + \gamma_0 \quad (3.45)$$

with K -factor is the slope and γ_0 is the damping factor offset associate to the inverse of the differential carrier lifetime. From the curve fitting, the K -factor is obtained with a value of 2.4 ns while the γ_0 is 4.3 GHz. Compared with the record modulation bandwidths of 17.5 GHz in InAs/InP QD laser [1], this laser is not good for high speed modulation but excellent for all other low noise related applications.

3.5 Summary

To summarize, the FN, spectral linewidth and RIN characteristics of QD lasers are theoretically investigated from a small-signal analysis of a rate equation model, where both the carrier noise and the spontaneous emission noise are taken into account. Results show that the carrier noise in the GS and the ES significantly increase the amplitude of the RIN, while the contribution of the carrier noise in the RS remains negligible. In addition, it is demonstrated that the ES carrier noise contribution can be suppressed by considering QD lasers with a larger GS-ES energy separation, hence leading to a substantial reduction of the RIN. Last

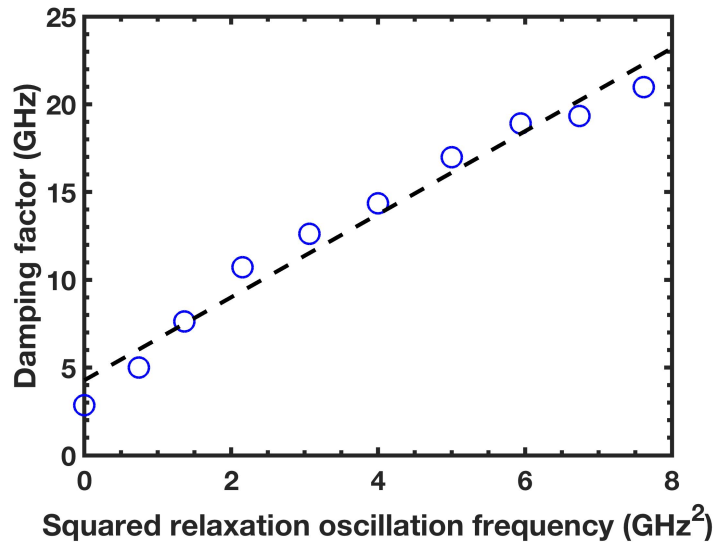


Fig. 3.34 Damping factor versus squared relaxation oscillation frequency.

but not the least, simulations also point out that the carrier noise does not contribute that much to the FN which is determinant for narrow spectral linewidth operation as compared to what exists in QW or bulk lasers. However, it is worthwhile noting that this work does not take into account the stimulated emission and the spontaneous emission noise from ES, meaning that the QD laser emits on the sole GS level. In this case, the highly damped factor yielding from the large gain compression coefficient leads to the low intensity noise in sole GS emitting QD laser [32]. The spontaneous emission noise from the ES is expected to have little impact on the RIN and FN of the GS emission, because it can only slightly perturb carrier fluctuations. In contrast, a recent work showed that the intensity noise of the QD laser was reduced (by 4 dB) when the GS and the ES emit simultaneously, as compared to the case of sole GS or ES emission [210]. This effect has been attributed to the coupling of GS and ES emissions through the finite carrier relaxation time. On the other hand, we believe that the ES emission can hardly affect the FN of GS emission, since the phases of each electric field are uncorrelated.

Second, we experimentally investigated the bias current and temperature dependence of the spectral linewidth of InAs/InP QD DFB lasers. Owing to the low inversion factor, these results show the potential of QDs as a gain medium for narrow spectral linewidth lasers. Using a DFB laser with a low κL and asymmetric facet coatings, a spectral linewidth of 160 kHz (80 kHz intrinsic) is demonstrated. By comparison with QW lasers, we show that the spectral linewidth of QD lasers is rather insensitive to the temperature with minimum values below 200 kHz between 283 K and 303 K. In addition, the numerical simulations based

on differential rate equations nicely reproduces the temperature behavior. Symmetric anti-reflection facet coatings are also used to reduce the LSHB and make the spectral linewidth rather independent of the drive current. However, a linewidth rebroadening is also observed at higher temperature, which may be attributed to the spectral hole burning and to the variations of the α_H with the temperature and bias current. Furthermore, the RIN of the AR/AR DFB laser is also experimentally discussed. A low RIN of less than -155 dB/Hz is measured in the 8-10 GHz range. Both the relaxation oscillation frequency and damping factor are extracted from the curve fitting of the RIN spectrum. By fitting the damping factor versus the squared relaxation oscillation frequency, the K -factor is obtained with a value of 2.4 ns while the γ_0 is 4.3 GHz showing that this laser is not good for high speed modulation but excellent for all other low noise related applications.

Overall, this work is useful for designing and manufacturing ultra-low noise oscillators for high-speed communications, optical frequency combs and radar applications. Moreover, these results also indicate that QD lasers are excellent candidates for narrow linewidth operation which is of paramount importance not only for coherent communication systems but also for high resolution spectroscopy, high purity photonic microwave generation and on-chip atomic clocks.

Chapter 4

Epitaxial QD lasers on silicon: From advanced characterizations to dynamical properties

This chapter at first presents the epitaxial InAs/GaAs quantum dot lasers on silicon studied in this thesis. After a description of their material growth and device fabrication as well as continuous wave behaviors, the chapter focuses on their intensity noise properties. The impact of the p-doping on the relative intensity noise (RIN) properties and subsequently on the modulation properties are investigated. Owing to the p-modulation doped GaAs barrier layer in the active region, the RIN level is found very stable with temperature with a minimum value of -150 dB/Hz. The dynamical features extracted from the RIN spectra show that p-doping between 0 and 30 holes/dot strongly modifies the modulation properties and gain nonlinearities through increased internal losses in the active region and thereby hindering the maximum achievable bandwidth. Furthermore, we report on an ultra-low linewidth enhancement factor (α_H -factor) value of 0.13 rather independent of the temperature range (288 K - 308 K) owing to the low density of threading dislocations and high material gain of the active region. Above the laser threshold, we show that the α_H -factor does not increase extensively with the bias current. In the end, the α_H -factor is also featured through a thermally insensitive method analyzing the residual side-mode dynamics under optical injection locking. The presented results confirm our initial measurements conducted with the amplified spontaneous emission (ASE) i.e. the α_H is as low as 0.15 showing that this method is reliable and compatible with QD lasers on silicon.

4.1 Investigated QD laser devices

4.1.1 Material growth and device fabrication

Laser material of target devices was grown on pieces from a 300 mm on-axis (001) GaP/Si template purchased from NAsP_{III/V}, GmbH. The full laser epitaxial structure and QD growth conditions can be found elsewhere [116]. The epi-layer structure is schematically illustrated in Fig.4.1.

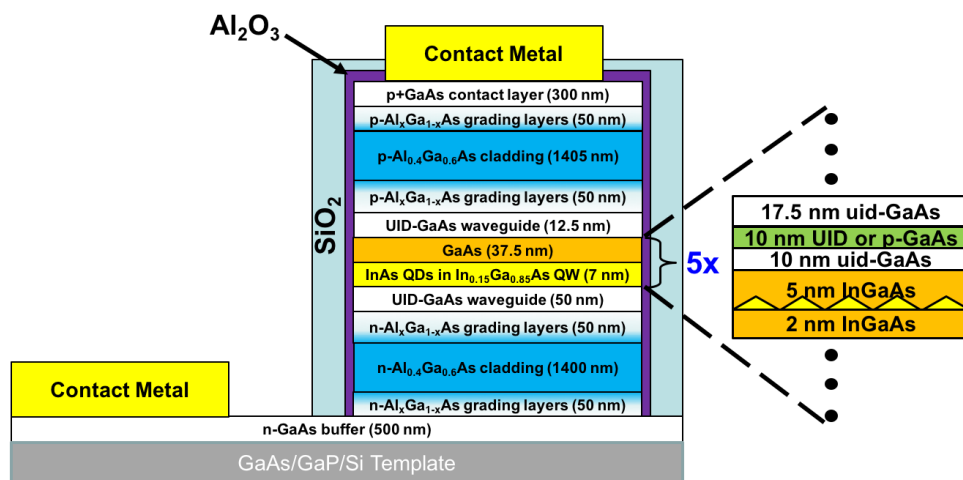


Fig. 4.1 Schematic description of the QD laser epi-layer structure.

First, a buffer was grown to filter dislocations through a combination of four cycles of thermal annealing from 400°C to 700°C and strained InGaAs filter layers. Details are presented in [114]. The laser structure consists of 1400 nm Al_{0.4}Ga_{0.6}As upper (p-type) and lower (n-type) cladding to provide electrical and optical confinement. The active region consists of five periods of p-modulation doped InAs dot-in-a-well layers with 2 nm In_{0.15}Ga_{0.85}As below and 5 nm on top of the dots. The InAs dots were grown at 495°C with a nominal thickness of 2.55 ML at 0.113 ML/s. The dot growth conditions were optimized to minimize inhomogeneous broadening due to dot size fluctuations. To this end, each of the dot conditions was iteratively optimized due to the high degree of coupling between growth conditions. In brief, growth temperature is generally found to be the most critical parameter with a tolerance of < 5 °C about the optimum to achieve narrow photoluminescence simultaneously with high gain. The optimum temperature is strongly coupled to the V/III ratio during growth, so they must be optimized together. Other commonly adopted conditions are the use of As₄ instead of As₂, the addition of growth interruptions [187], and an “In-flush” [279] step where dot inhomogeneity is annealed away through optimized capping layer

thickness and a short anneal at ~ 580 °C. Following the In-flush, growth temperatures should be kept low to minimize further interdiffusion which diminishes, blue-shifts, and broadens the photoluminescence.

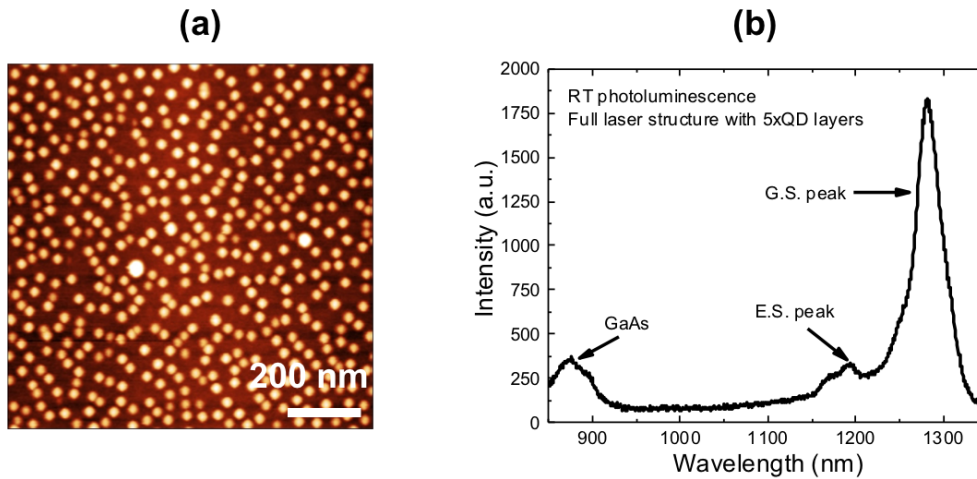


Fig. 4.2 (a) Atomic force microscope image of InAs QDs grown on a GaAs/Si template. Scale bar is 200 nm. (b) Photoluminescence spectrum of the full laser sample.

Fig.4.2(a) shows an atomic force microscope image of an uncapped InAs QDs grown on a GaAs/Si template. The QD density is $4.9 \times 10^{10} \text{ cm}^{-2}$ and the corresponding acceptor/QD ratio is ~ 10 . The optimized growth conditions yielded a photoluminescence full-width-at-half-maximum (FWHM) of < 30 meV. A photoluminescence spectra of the full laser sample revealed a very small FWHM of 29.3 meV from the GS peak as shown in Fig.4.2(b), indicating a highly homogeneous InAs QD size throughout the five QD stacks [117]. Note that the FWHM of room temperature PL from a single stack QD sample was ~ 28 meV [116]. Each dot layer was separated by a 37.5 nm GaAs spacer, which included 10 nm of p-type material at a doping level of $5 \times 10^{17} \text{ cm}^{-3}$ for the p-doped device. As for the undoped one, the p-type layer is absent. The p-doping is used to improve the thermal stability. Indeed, QD lasers suffer from thermal broadening of carriers, especially holes due to their heavier effective mass and consequent tightly spaced energy levels [46]. The thermal broadening decreases the QD ground state gain and increase temperature sensitivity of the threshold current.

The laser sample was processed into narrow ridge-waveguide deep-etched lasers using optical lithography and dry etching. Since the silicon wafer is on-axis (001) orientation without offcuts, Fabry-Perot (FP) cavity was formed by cleaving after thinning the wafer to $\sim 150 \mu\text{m}$. Fig.4.3 shows a facet of a laser. The Fabry-Perot (FP) cavities of the lasers are

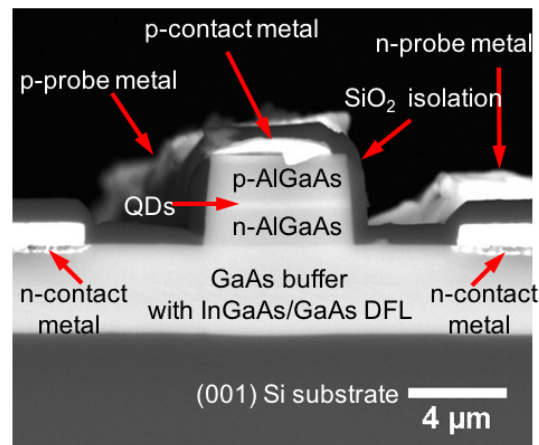


Fig. 4.3 Cross-sectional scanning electron microscope image showing the facet of a fabricated FP QD laser on silicon.

measured at similar length, 1.1 mm for the undoped one and 1.35 mm for the other, with $3.5 \mu\text{m}$ wide ridges deeply etched (through the active region), and two top contacts were used for electrical injection. The facets were formed by cleaving after thinning the silicon substrate to $200 \mu\text{m}$. Dielectric facet coatings were then applied using ion beam deposition of repeated periods of $\text{SiO}_2/\text{Ta}_2\text{O}_5$ to give reflectivities of 60% (front) and 99% (rear).

4.1.2 Light current characteristics and optical spectrum

In what follows, both p-doped and undoped QD lasers are compared. Fig.4.4 depicts the light current characteristics of the undoped (a) and p-doped (b) QD lasers for various temperatures ranging from 288 K to 308 K. The insets show corresponding optical spectra measured at $3 \times I_{th}$.

Devices emit on the sole GS transition close to 1300 nm. The threshold current I_{th} at room temperature (293 K) for the undoped QD laser is 6 mA while that of the p-doped laser is found at 26.5 mA. By varying the temperature from 288 K to 308 K, I_{th} varies from 5.3 mA to 8.3 mA (57% increase) for the undoped laser, while it is only from 26 mA to 28.5 mA (10% increase) for the p-doped one. Compared with the undoped material, the larger threshold current of p-doped QD lasers results from the increase of the optical loss due to high free carrier absorption that results from the large number of holes in the dots [30, 29]. However, the inclusion of the p-type doping mitigates the thermal spread of holes which leads to a rather temperature insensitive threshold current [46, 167, 237].

Fig.4.5 shows the optical spectral envelopes of the QD lasers at $3 \times I_{th}$ and for different temperatures ranging from 288 K to 308 K. With or without doping, the center wavelength is

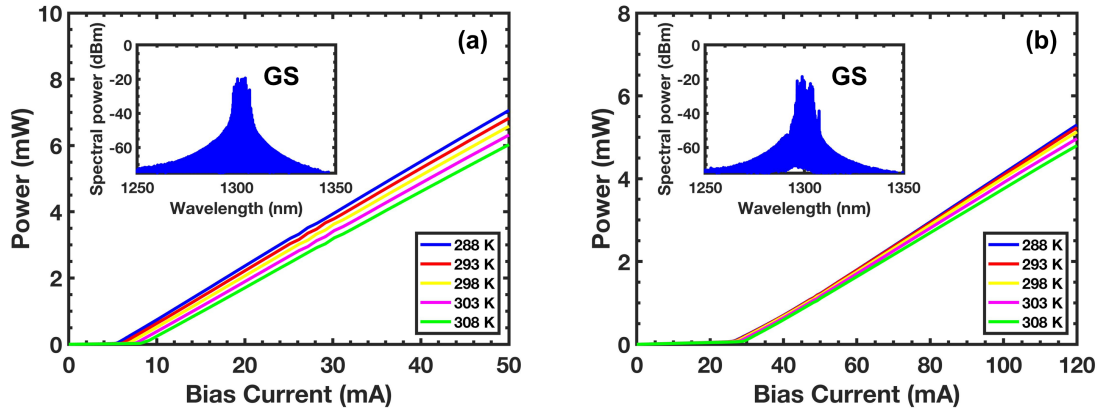


Fig. 4.4 Light-current characteristics of (a) undoped and (b) p-doped QD lasers as a function of temperature varying from 288 K to 308 K with a step of 5 K. The insets show corresponding optical spectra of ground state (GS) emission measured at $3 \times I_{th}$ at 293 K.

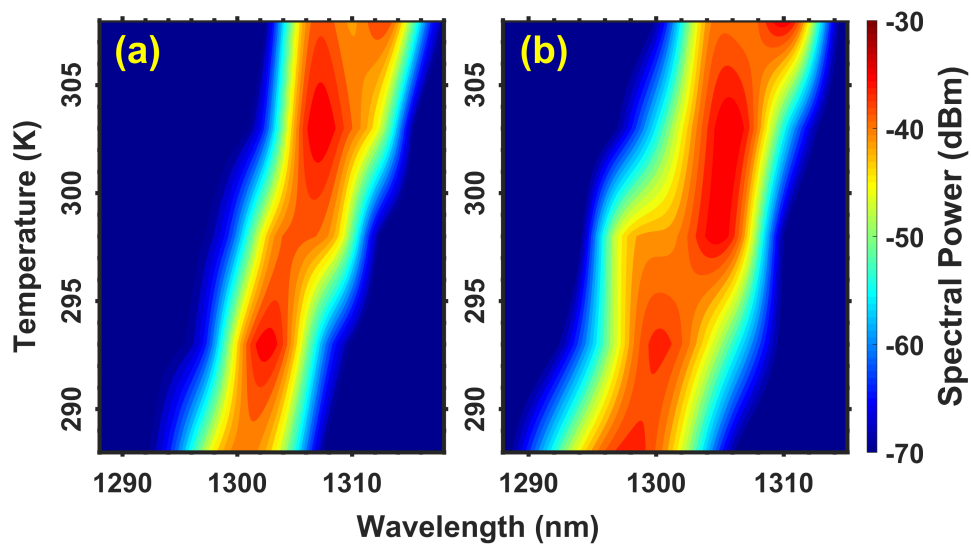


Fig. 4.5 Optical spectral envelopes of (a) undoped and (b) p-doped QD lasers at $3 \times I_{th}$ as a function of temperature.

found evenly red-shifted (~ 10 nm) meaning that defects induced thermal effects is involved well above the laser threshold.

4.2 Intensity noise properties

4.2.1 Effect of the p-doping on the relative intensity noise

In this section, four batches of QD lasers with unintentionally doped (undoped), $0.5 \times 10^{18} \text{cm}^{-3}$, $1 \times 10^{18} \text{cm}^{-3}$ and $1.5 \times 10^{18} \text{cm}^{-3}$ p-type dopant concentration in the active region are compared. These doping concentrations correspond to 0, 10, 20 and 30 extra holes per QD [290], which are tagged as device A, B, C and D, respectively and listed in Table 4.1. It is noted that these four lasers have the same ridge waveguide width of $4 \mu\text{m}$, while the undoped QD laser is 1.1 mm long and the p-doped is 1.35 mm long.

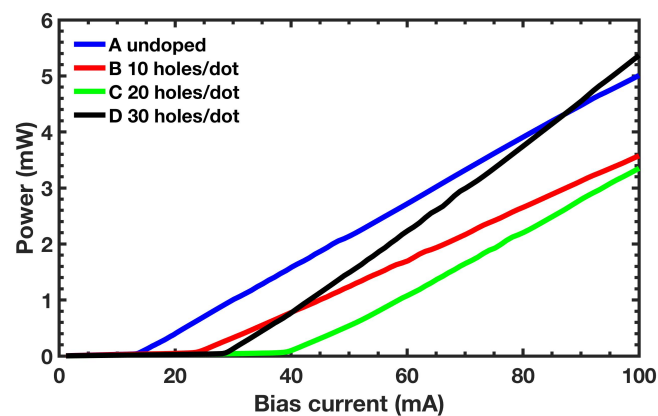


Fig. 4.6 Light-current characteristics of the QD lasers under study.

Fig.4.6 depicts the evolution of light current characteristics of the four QD lasers under study. At room temperature (20°C), the threshold current (I_{th}) for the undoped laser is 13 mA, while it increases from 23 mA (laser B) to 39 mA (laser C) with the increase of the p-doping. The higher threshold of the p-doped lasers is due to the increased optical loss by high free carrier absorption that results from large number holes in the dots [46]. Let us stress that, when p doping increases from 20 to 30 holes/dot, an anomalous behavior is observed in the evolution of the I_{th} , which decreases from 39 mA (laser C) to 29 mA (laser D). Such a behavior is attributed to a slightly higher power reflectivity of the front facet of laser D leading to a decrease of the threshold through a reduction of the transmission losses [46]. All values of the I_{th} and the corresponding threshold current density J_{th} as well as all dynamical parameters are summarized in Table 4.1.

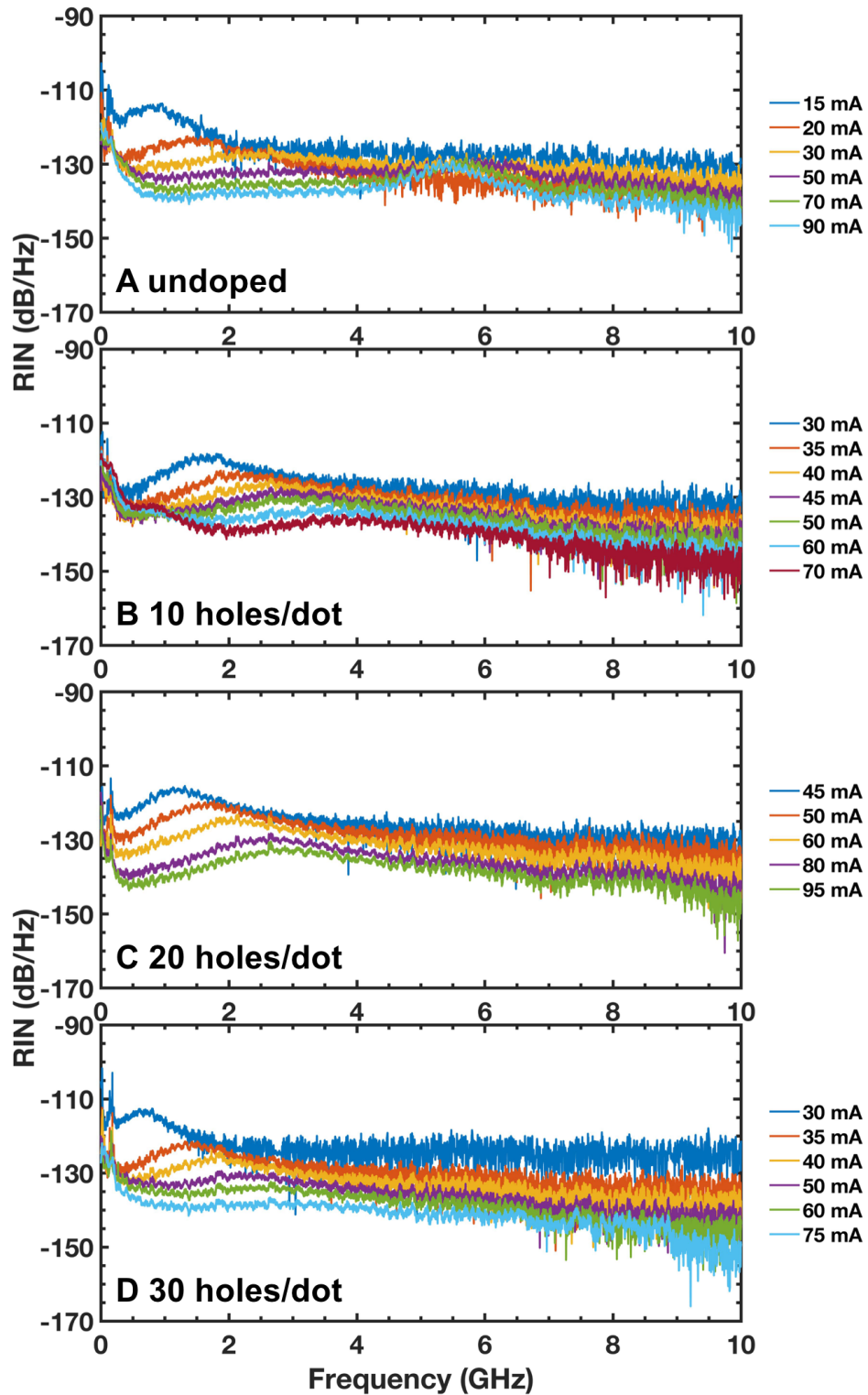


Fig. 4.7 RIN spectra up to 10 GHz for QD lasers A(a), B(b), C(c) and D(d), respectively.

Table 4.1 Static and dynamic characteristics of the undoped and p-doped QD lasers and QW laser.

Device	A	B	C	D	QW
Doping (cm^{-3})	0	0.5×10^{18}	1.0×10^{18}	1.5×10^{18}	0
Holes per QD	0	10	20	30	0
I_{th} (mA)	13	23	39	29	36
J_{th} (A/cm^2)	296	426	722	537	577
K (ns)	4.7	1.7	1.5	2.7	0.9
γ_0 (GHz)	1.5	3.0	5.2	3.3	3.4
$f_{3dB,max}$ (GHz)	1.9	5.2	5.9	3.3	9.9
ϵ_p (mW^{-1})	0.15	0.27	0.40	0.34	0.07
ϵ_S (cm^3)	5.7×10^{-16}	1.0×10^{-15}	1.5×10^{-15}	1.3×10^{-15}	3.3×10^{-17}

Fig.4.7 shows the measured RIN of the tested four QD lasers, which are extracted using Eq.3.42. The RIN spectra are measured at various bias currents depending on their threshold currents. However, for a better comparison, the four RIN spectra are measured for the same coupling power corresponding to the maximal limit of the photodiode (0.72 mW). The RIN at low frequencies is relatively high resulting from the bias current noise, thermal noise as well as mode partition [296], and it reduces with the increasing frequency and saturates at higher bias currents. The minimal RIN level is achieved between -140 dB/Hz and -150 dB/Hz in both undoped and p-doped lasers, which is also in agreement with results in [149, 157].

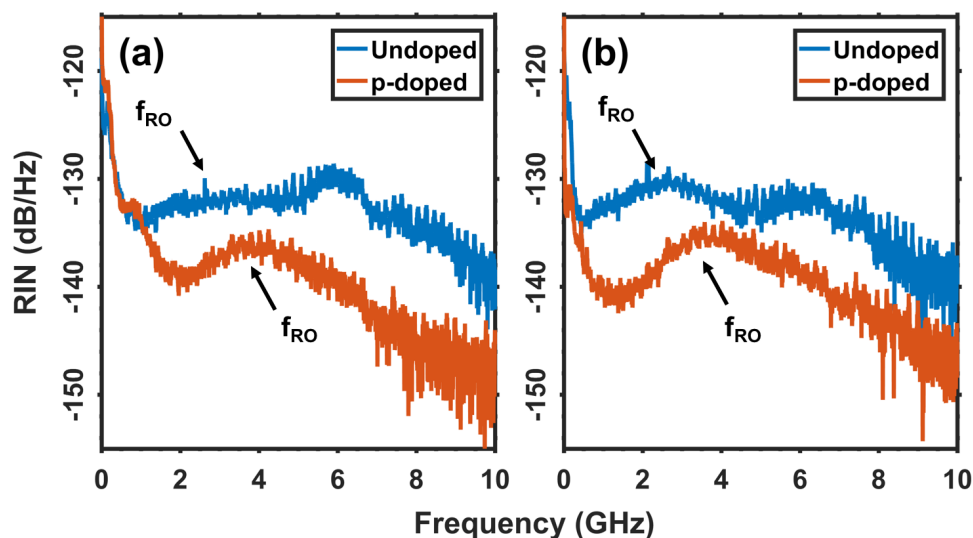


Fig. 4.8 Comparison of the relative intensity noise spectra between the undoped QD laser (Device A) and p-doped QD laser (Device B) biased at $3 \times I_{th}$ for (a) 293 K and (b) 303 K.

Fig.4.8 depicts the comparison of the measured RIN spectra between the undoped (Device A) and p-doped (Device B) lasers at 293 K and 303 K and both lasers biased at $3 \times I_{th}$. At 293 K, a low RIN level of -140 dB/Hz at 10 GHz is demonstrated for the undoped laser, while the laser is overdamped due to the absence of the relaxation oscillation frequency (ROF) peak whatever the bias current. It is worth nothing that the resonance peak at 6 GHz is not the ROF of the laser and rather results from the QD size dispersion induced impurity of longitudinal modes since it appears only at high bias current. In contrast, the p-doped QD laser exhibits a strong ROF peak at around 3.6 GHz due to a smaller damping factor with a reduced RIN level of -150 dB/Hz at 10 GHz. When further increasing the temperature from 293 K to 303 K, the ROF peak pops up again at 2.6 GHz under the same bias level of $3 \times I_{th}$ for the undoped laser, suggesting that the damping of the laser is reduced. On the other hand, the RIN spectrum is rather stable in p-doped laser both in ROF peak and RIN level, indicating that the p-doping does contribute to improve the thermal stability.

4.2.2 Damping factor and relaxation oscillation frequency

In what follows, both the ROF and damping factor are extracted from the curve-fitting of the RIN spectrum according to the Eq.3.41. In comparison with QD lasers, a heterogeneously integrated QW laser has been also investigated that has 7 compressively strained InAlGaAs QWs as the active region and lasing around 1580 nm, other structure details can be found in [157].

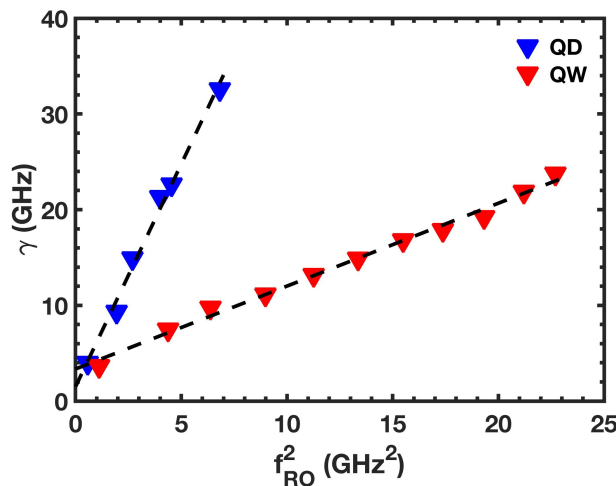


Fig. 4.9 The measured damping factor (γ) as a function of the squared relaxation oscillation frequency (f_{RO}^2) both for QD (Device A) and QW lasers.

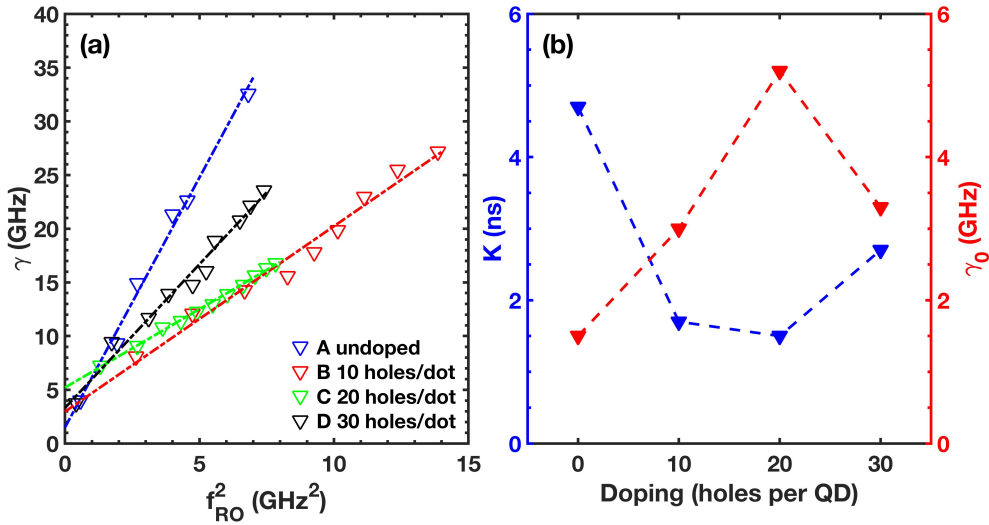


Fig. 4.10 (a) The measured damping factor (γ) as a function of the squared relaxation oscillation frequency (f_{RO}^2) for the QD lasers under study. (b) The K -factor and inverse differential carrier lifetime (γ_0) versus the doping level.

Fig.4.9 depicts the comparison of the measured damping factor γ as a function of squared relaxation frequency f_{RO}^2 between the undoped QD laser (Device A) and QW laser. In both cases, the evolution is linear following the relationship $\gamma = Kf_{RO}^2 + \gamma_0$ with K -factor is the slope and γ_0 is the inverse of the differential carrier lifetime. As QD lasers behave as quasi-class-A oscillators, the damping factor is rising quickly, hence the value is found as large as 33 GHz at $3 \times I_{th}$ with a K -factor of 4.7 ns. Conversely, the damping factor for QW laser increases smoothly up to only 15 GHz at $3 \times I_{th}$. It is noted that the damping factor is relatively high in undoped QD laser which can be useful for isolator-free applications [52]. This feature will be discussed in Chapter 5. Although isolator-free applications remain an important objective, an overdamped laser would of course be somewhat detrimental for direct modulation since the modulation bandwidth would be too much limited. Now, we discuss the effect of the p-doping on the damping factor as well as the modulation bandwidth.

Fig.4.10(a) shows the damping factor as a function of the squared ROF for the four QD lasers, respectively. Fig.4.10(b) depicts the evolution of the K -factor and γ_0 extracted from the curve-fitting as a function of the doping level. The K -factor decreases with the p-doping level from 4.7 ns (laser A) to 1.5 ns (laser C) whereas γ_0 increases from 1.5 GHz to 5.2 GHz. The damping factor offset γ_0 is quite important at low powers where the ROF is small, while for larger resonance frequencies, the K -factor usually describes the damping of the response which can be used to evaluate the maximum 3-dB bandwidth ($f_{3dB,max}$) from the following

equation:

$$f_{3dB,max} = \frac{2\sqrt{2}\pi}{K} \quad (4.1)$$

As expected, the calculated $f_{3dB,max}$ is 1.9 GHz for the undoped laser, which can be further increased to 5.9 GHz for the optimum p-doping level of 20 holes/dot. These results are consistent with the previous works which showed that the p-doping improves the maximum modulation bandwidth [4, 87]. Compared with the record modulation bandwidths of 17.5 GHz in InAs/InP QD laser [1], this modulation bandwidth is not good enough for high speed modulation. We believe that this doping level is not the optimum solution and further work will concentrate on optimizing the doping level [291]. Despite that, a recent result has also shown a 12.5 Gbps error-free transmission with a directly modulated 1.3 μm InAs QD lasers directly grown on silicon. The power penalty is found less than 1 dB after a 12-km transmission distance at 5 Gbps [108]. However, any further increase of the p-doping level to 30 holes/QD leads to a reincrease of the K -factor from 1.5 ns to 2.7 ns hence the $f_{3dB,max}$ decreases from 5.9 GHz to 3.3 GHz, which is due to the increased internal loss [174].

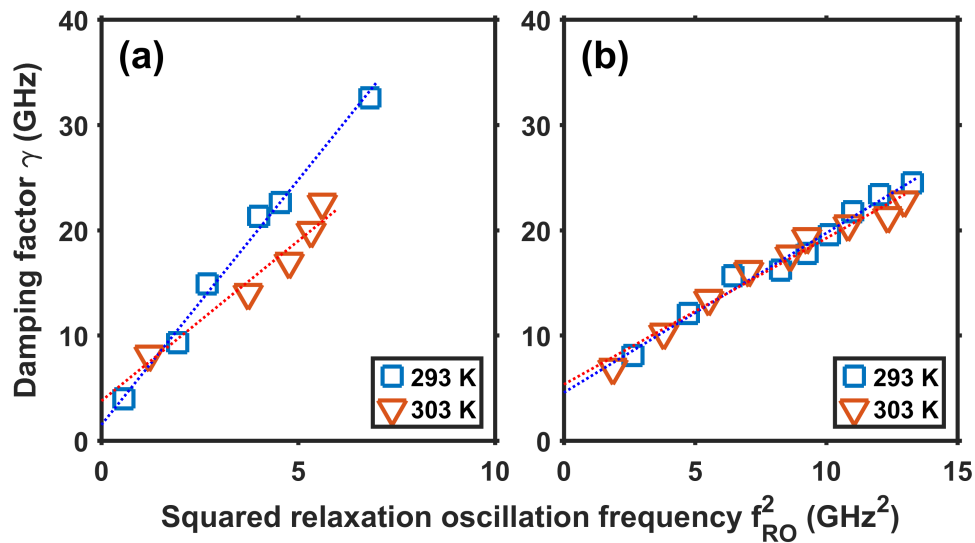


Fig. 4.11 The damping factor as a function of the squared relaxation oscillation frequency for (a) undoped and (b) p-doped QD laser device.

The temperature dependence of the damping factor and ROF is also investigated, Fig.4.11 shows the damping factor as a function of the squared ROF for the undoped (Device A) and p-doped (Device B) lasers at 293 K and 303 K, respectively. For the undoped laser, a damping factor of 33 GHz at $3 \times I_{th}$ is extracted along with a K -factor of 4.6 ns at 293 K. The K -factor is reduced down to 3 ns at 303 K leading to a smaller damping factor of 23 GHz at $3 \times I_{th}$. By comparison, the damping factor of the p-doped laser is found at 25 GHz at $3 \times I_{th}$

with a K-factor of 1.5 ns. Once again, those results prove that the QD laser with p-doping is more stable with temperature not only in terms of the RIN but also for the damping factor. These results confirm that the introduction of p-doping can reduce the damping which is a significant feature influencing the modulation capabilities of epitaxial QD lasers. This effect was explained theoretically by the higher occupation of the QD hole levels leading to strong reduction of the hole scattering rates [167].

4.2.3 Gain compression

Gain compression in semiconductor lasers refers to the decrease of the gain coefficient with optical intensity [104]. This phenomenon is different from gain saturation which corresponds to an equilibrium between the stimulated emission and the refill of the upper lasing level by the pump. Fig.4.12 illustrates the comparison between gain saturation and gain compression. As shown, the gain compression is a depletion of the gain in the upper level.

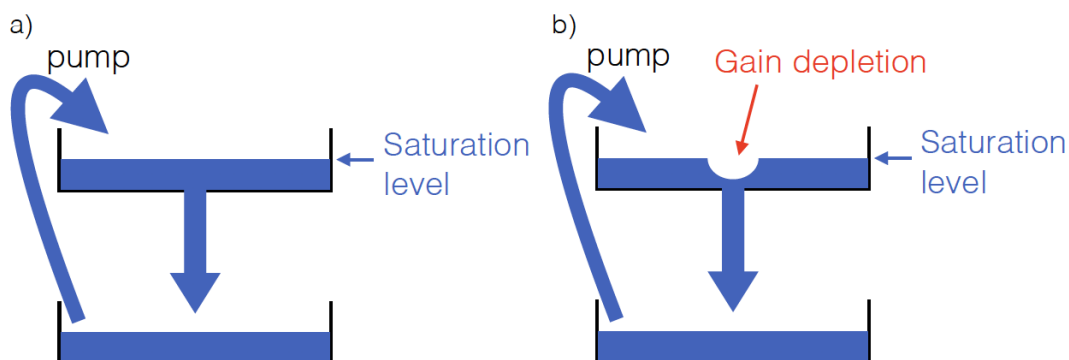


Fig. 4.12 Illustration of gain saturation (a) versus gain compression (b) from [112].

The gain compression originates from gain nonlinearities caused by processes such as carrier heating, spatial and spectral hole burning [73]. Carrier heating effect results from the stimulated emission and the free-carrier absorption hence leading to gain reduction since the gain is dependent on the carrier temperature. Spatial hole burning is due to the existence of two contra-propagating waves in the cavity, which results in an inhomogeneous gain distribution along the cavity. In addition, spectral hole burning attributes to the fast stimulated emission lifetime, which will lead to a carrier depletion in the upper level if it is faster than the intraband relaxation time of the carrier, and hence to a reduction of the gain around the lasing wavelength. Gain compression limits the modulation dynamics of directly

modulated transmitters through adiabatic chirp and is also responsible for the bending of the light-current characteristic curves [70].

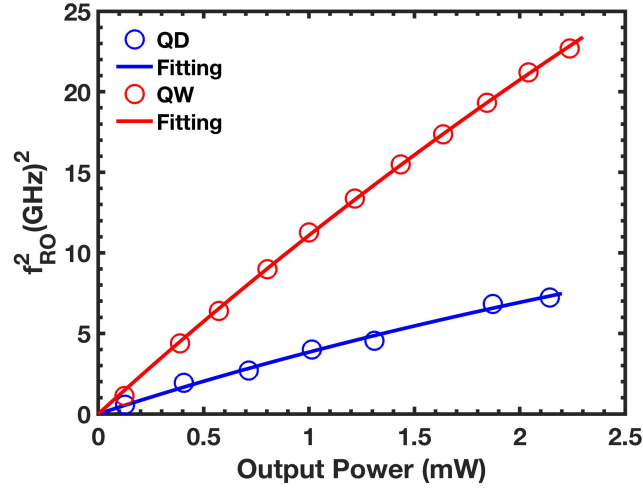


Fig. 4.13 The squared relaxation oscillation frequency (f_{RO}^2) versus the output power both for QD (Device A) and QW lasers.

In Fig.4.13, the square of the measured resonance frequency is plotted as a function of the output power for QD (Device A) and QW lasers. The relaxation oscillation frequency is proportional to the square root of the optical output power, hence the curve-fitting to be used is based on the following expression [73, 243]:

$$f_{RO}^2 = \frac{AP}{1 + \epsilon_P P} \quad (4.2)$$

where ϵ_P denotes the gain compression coefficient related to the output power P indicating that for this pumping level, nonlinear effects start to be significant. A is the modulation efficiency and can be approximated by the initial slope of the curves. By curve-fitting the curves, the gain compression factor is found at 0.15 mW^{-1} for the QD laser which is larger than that of the QW laser for which the gain compression is of 0.07 mW^{-1} . The gain compression factor linked to photon density (S) can then be expressed through the relationship: $\epsilon_S = \epsilon_P P / S$, where $P = h\nu V v_g \alpha_m S$ and V is the cavity volume and $v_g \alpha_m$ is the energy loss through the mirrors. Taking into account the facet reflectivity and modal volume of the laser, ϵ_S is calculated with a value of $5.7 \times 10^{-16} \text{ cm}^3$ for the QD laser against $3.3 \times 10^{-17} \text{ cm}^3$ for the QW one. Those values are in agreement with prior works already published in the literature [73, 41, 243].

Now, we discuss the impact of the doping level on the gain compression effect. The evolution of the squared f_{RO} versus the output power (P) is plotted in Fig.4.14(a) for the four

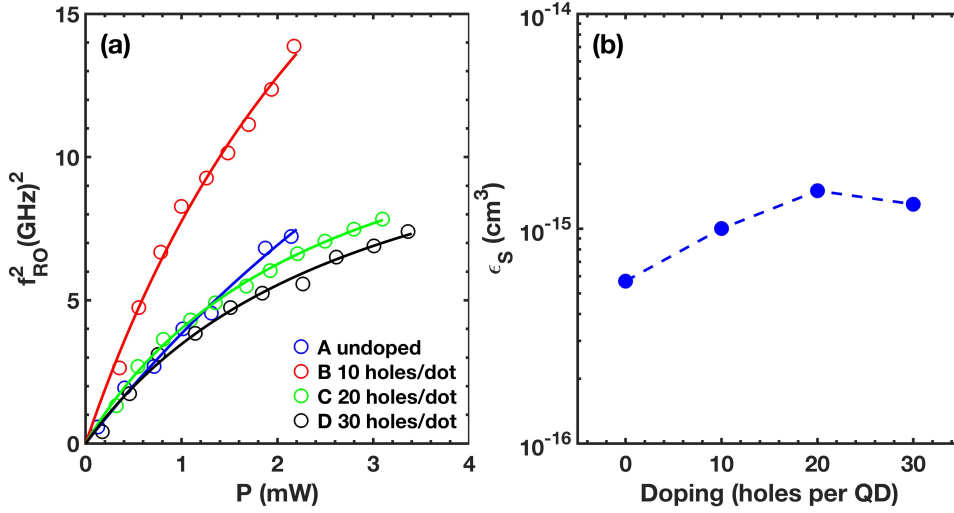


Fig. 4.14 (a) The squared relaxation oscillation frequency (f_{RO}^2) versus the output power (P) for the lasers under study. (b) The extracted gain compression as a function of doping level.

lasers under study. By curve-fitting the curves, ϵ_P is found to increase from 0.15 mW^{-1} for the undoped QD laser A to 0.40 mW^{-1} for the p-doped QD laser C. Fig.4.14(b) displays the calculated ϵ_S as a function of the doping level indicating values in the range from $5.7 \times 10^{-16} \text{ cm}^3$ to $1.5 \times 10^{-15} \text{ cm}^3$ which are in agreement with prior studies [73]. It is noted that ϵ_S related to QD laser D is found a bit lower than that in QD laser C. As aforementioned, this effect is attributed to the possible reduction of the transmission loss nevertheless the ϵ_S is also as large as $1.3 \times 10^{-15} \text{ cm}^3$. To conclude, the results show that the maximum modulation bandwidth can certainly be improved for doping levels between 0 and 20 holes/dot beyond which no real improvements take place due to the joint effects of higher induced internal loss and gain nonlinearities [87, 174].

4.3 Linewidth enhancement factor (α_H -factor)

In this section, we investigate the behavior of the linewidth enhancement factor (α_H -factor) of silicon based QD lasers. The α_H -factor typically describes the coupling between the carrier-induced variation of real and imaginary parts of susceptibility and is defined as [206]

$$\alpha_H = -\frac{4\pi}{\lambda} \frac{dn/dN}{dg/dN} \quad (4.3)$$

where dn and dg are the small index and optical gain variations that occur for a carrier density variation dN . At the system level, a large α_H also results in a frequency chirping under

direct modulation, hence limiting the maximum data rate and transmission distance over a dispersive fiber [131, 129]. The relation between the α_H -factor and the frequency chirp ($\Delta\nu$) can be expressed as:

$$\Delta\nu = -\frac{\alpha}{4\pi} \left(\frac{d}{dt} \ln P + \frac{2\Gamma P \varepsilon}{V_{act} \eta h\nu} \right) \quad (4.4)$$

where P is the output power, Γ is the modal confinement factor, ε is the gain compression factor, V_{act} is the active layer volume, $h\nu$ is the energy per photon and η is the total differential quantum efficiency. As shown in the Eq.4.4, a larger α_H -factor often results in a frequency chirp ($\Delta\nu$) under direct modulation, which typically limits the maximum data rate and transmission distance over a dispersive fiber [131, 129]. Although many studies have suggested near-zero α_H values in QD lasers, most of the experimental observations have actually shown the opposite. Indeed, the strong vertical coupling between the ground state (GS) level and the higher energy levels contributes to drastically increase the α_H -factor [73].

4.3.1 Sub-threshold α_H -factor determination

The α_H -factor is at first extracted from a spectroscopic analysis using amplified spontaneous emission (ASE). The ASE method relies on direct measurements of the differential gain dg and differential refractive index dn as a function of slight changes in the semiconductor laser carrier density in sub-threshold operation. The differential index is measured by tracking the frequency shift of the longitudinal FP mode resonances, while the differential gain is obtained by measuring the net modal gain from the FP modulation depth (gain ripple) in the ASE spectra. The differential gain is equivalent to the variation of net modal gain G_{net} , which can be extracted as [25]:

$$G_{net} = \frac{1}{L} \ln \left(\frac{1}{\sqrt{R_1 R_2}} \frac{\sqrt{x} - 1}{\sqrt{x} + 1} \right) \quad (4.5)$$

with L the cavity length, x the ratio of the peak-to-valley intensity levels, and R_1 and R_2 the front and back facet reflectivity (in intensity), respectively. The differential refractive index dn within the active layer is then related to the modal wavelength λ_m shift $d\lambda$ through $d\lambda/\lambda_m = \Gamma dn/n$ which combined with Eq.4.3 and Eq.4.5 implies that the α_H -factor can be reexpressed as a function of measurable parameters such as:

$$\alpha_H = -\frac{4n\pi}{L\delta\lambda} \frac{d\lambda/dI}{dG_{net}/dI} \quad (4.6)$$

where L is the cavity length, $\delta\lambda$ is the free spectral range. However, it is important to stress that the main weakness of the ASE method results from its poor reliability if thermal effects

are not properly eliminated. Because the change of mode wavelength and the net modal gain require a variation of the bias current I , persistent device heating usually results in a possible underestimation of the α_H -factor. One straightforward method relies on using bias current with continuous-wave operation and eliminating the thermal effects through the inclusion of a thermal correction in Eq.4.6. Following this protocol, the thermal effect induced wavelength red-shift when varying the bias current right above threshold can be subtracted from the wavelength blue-shift measured below threshold. This method can certainly minimize the fitting error theoretically when the thermal correction works under the two assumptions: first, that thermal effects in QD lasers must maintain unchanged below and above threshold; second, the carriers are clamped above threshold. However, in QD lasers, the carrier population is not always clamped because of the carrier filling in the higher energy level which produce a change in the refractive index through the relation:

$$\delta n = \sum_k \delta n_k \quad (4.7)$$

with $k = g, e$ are the indices for GS and ES, respectively.

In order to only account the net carrier-induced frequency shift, thermal effects must be eliminated. To do so, QD devices are biased with a pulse current using the minimal pulse width of $0.1 \mu\text{s}$ [250] which is usually preferred as opposed to the continuous-wave, while the device temperature is carefully monitored and kept constant throughout the measurement. In the experiments, light from the QD lasers is coupled into a $20 \mu\text{m}$ high resolution optical spectrum analyzer via an anti-reflection coated lensed fiber. To eliminate any source of optical feedback from the setup, an isolator is also inserted after the laser. The peak wavelength is then recorded for each duty cycle from 0.1% to 10% in 2% increment. For each sub-threshold bias current, the peak wavelength values are plotted as a function of duty cycle and the extrapolation at 0% duty cycle allows extracting the corresponding values without thermal effects. Finally, a data processing involving a Lorentzian curve-fitting of each FP mode is applied in order to retrieve the peak information in terms of modal wavelength and intensity. Overall, taking into account all the aforementioned elements, the uncertainty of the α_H -factor measurement is of order 0.5% .

Fig.4.15(a) displays one peak wavelength measured for the different sub-threshold currents ranging from 23.5 to 26.5 mA as a function of the duty cycle for the p-doped QD laser ($I_{th} = 26.5$ mA). By decreasing the duty cycle, the peak wavelength redshift is strongly attenuated due to the decrease of the thermal effects. Below 4% duty cycle the red-shift vanishes and the peak wavelength becomes blue-shifted. As such, by extrapolating down to 0% duty cycle (triangle markers), the extracted wavelengths corresponding to the limiting

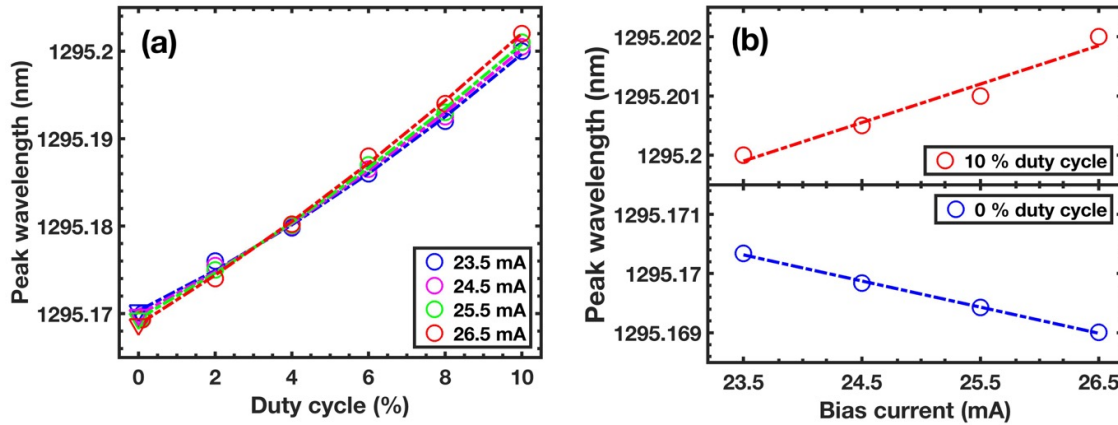


Fig. 4.15 (a) Measured peak wavelength as a function of the duty cycle for different sub-threshold bias currents. (b) Measured peak wavelength as a function of the bias current for two values of the duty cycle.

case for which thermal effects are gone. These values are then used for the determination of the α_H -factor. Fig.4.15(b) shows the peak wavelength as a function of the bias currents for two duty cycles. The wavelength red-shift and blue-shift are clearly evidenced for the cases of 10% and 0% duty cycle. In addition, it is noted that the pulse width of $0.1 \mu\text{s}$ corresponds to the lower bound of the pulsewidth compared with a few microseconds usually used in many studies [250]. Besides, it is also important to stress that going below $0.1 \mu\text{s}$ would result in an extremely low output power and the impossibility to retrieve the gain and then the α_H -factor at the price of a poor accuracy. Therefore, a pulse width of $0.1 \mu\text{s}$ is typically what is recommended to almost eliminate all the thermal effects in the material.

Fig.4.16 displays the spectral dependence of the α_H -factor for the p-doped QD laser. The figure in inset shows the net modal gain for different subthreshold bias currents ranging from $0.88 \times I_{th}$ to I_{th} . The black arrow indicates that the gain is blue-shifted as the bias level increases. At threshold, the net modal gain is about 2.4 cm^{-1} per QD layer. As for the α_H -factor, a variation from 0.13 to 0.29 at 293 K is unveiled over a span of 20 nm. At the gain peak ($\approx 1295 \text{ nm}$), the α_H is of 0.13 which is the lowest value ever reported for any semiconductor laser on silicon. Such a value which is actually even lower than those recently reported on InAs/GaAs QD lasers [99] can be explained by the high quality of the material and the reduced TDD which reduces the inhomogeneous gain broadening and concentrates the oscillator strength at the resonant wavelength.

In order to investigate the influence of thermal effects on the α_H -factor, the pulse width dependence of the measured α_H -factor is also performed on a p-doped QD laser which has 3 QD layers and a 1.5 mm long cavity with a $3 \mu\text{m}$ wide ridge waveguide. As shown in

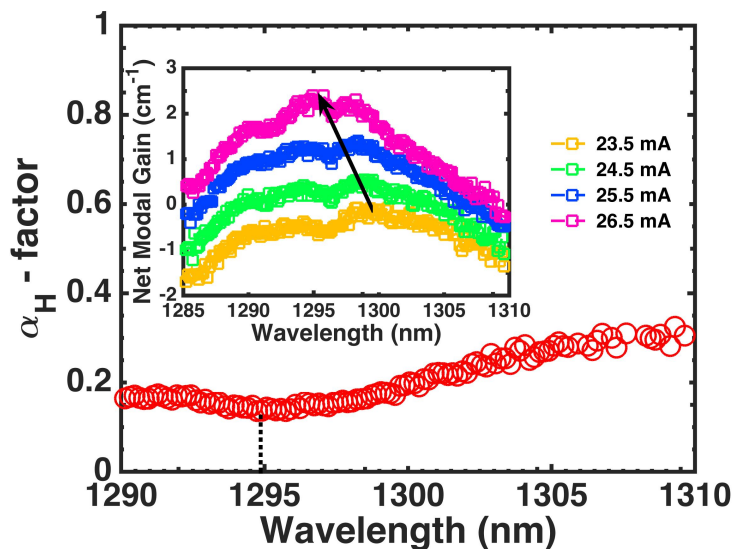


Fig. 4.16 The α_H -factor as a function of the photon wavelength for the p-doped QD laser (293K). The black dotted line indicates the FP gain peak value (1295 nm). The inset indicates the corresponding net modal gain spectra for various subthreshold bias current conditions.

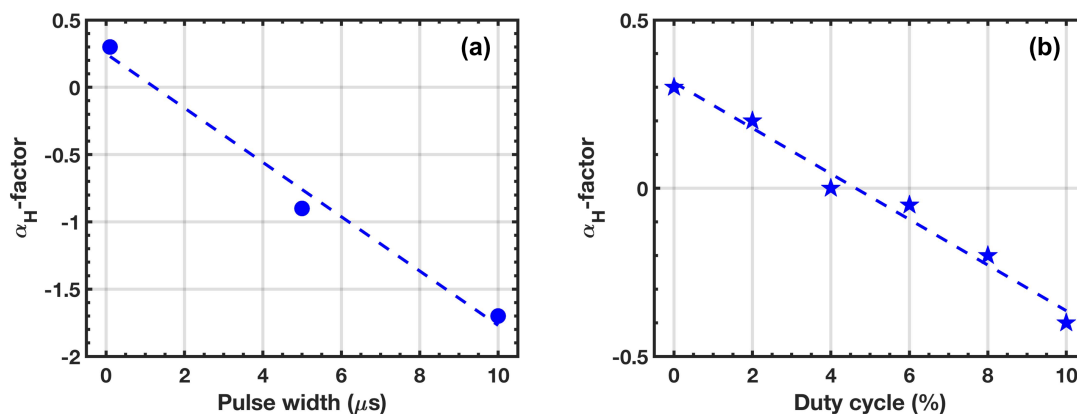


Fig. 4.17 (a) Pulse width dependence of the measured α_H -factor at a fixed duty cycle of 0%. (b) Duty cycle dependence of the measured α_H -factor at a fixed pulse width of 0.1 μs . Note that the linear curve-fitting (dashed lines) are for guiding eyes only.

Fig.4.17(a), this laser has initial α_H -factor of about 0.3 which is found a bit larger than that of 5 QD laser due to the smaller material gain. However, when further increasing the pulse width from 0.1 μs to 5 μs and 10 μs , α_H -factor values extracted at a fixed duty cycle of 0% are found reduced from 0.3 to negative values down to -0.9 at 5 μs and to -1.7 at 10 μs . This effect is attributed to the thermal effect induced wavelength red-shift below threshold which results in the negative α_H -factor values. Fig.4.17(b) also displays the measured α_H -factors extracted at a fixed pulse width of 0.1 μs as a function of different duty cycle ranging from 0 % to 10 % with a step of 2 %. The α_H -factors decrease from 0.3 to -0.35 along with the enhancement of the duty cycle from 0 % to 10 %. Therefore, the α_H -factors can be strongly underestimated if the thermal effects are not completely eliminated from the ASE method. However, it is noted that the laser biased in the pulsed mode also results in a low signal-to-noise ratio and even irregular spectral line shape.

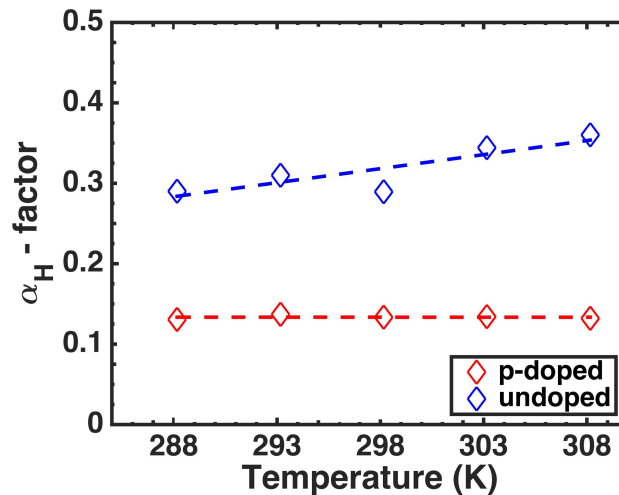


Fig. 4.18 The α_H -factor as a function of temperature for p-doped (red) and undoped (blue) QD lasers. The linear curve-fittings (dashed lines) are for guiding eyes only.

Then, the temperature dependence of the α_H -factor is investigated for both p-doped and undoped QD lasers. Fig.4.18 presents the comparison assuming a temperature range from 288 K to 308 K with a step of 5 K. For each temperature, the α_H values correspond to those taken at the gain peak. Note that the linear curve-fitting (dashed lines) are for guiding eyes only. As expected, the α_H -factor of the undoped slightly increases from 0.29 at 288 K to 0.36 at 308 K, while that of the p-doped device remains constant with a value of 0.13 over the same temperature range. For undoped QD lasers, the increase of the α_H -factor with temperature is due to the increased occupancy in the non-resonant states which reduce the GS differential gain and increases the refraction index variations [42]. On the contrary, for p-doped QD lasers, the refraction index variation is rather constant with temperature because

the Auger recombinations decrease whereas those in the barrier and wetting layer increase. Besides, the α_H -factor of the p-doped QD laser is smaller than that of the undoped QD laser that can be explained by the reduced transparency carrier density [125].

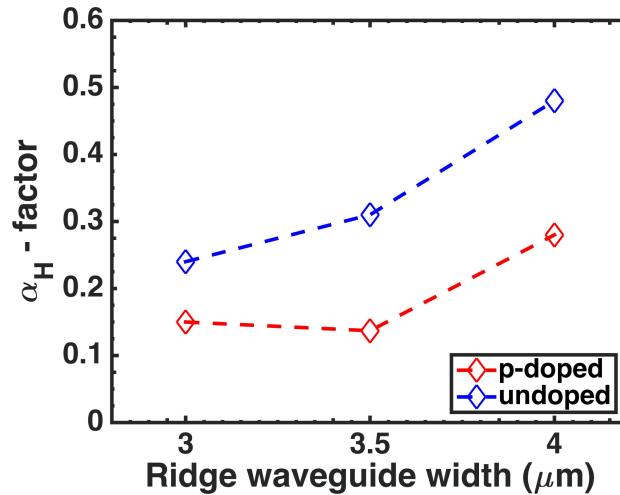


Fig. 4.19 The α_H -factor as a function of the ridge waveguide width for p-doped (red) and undoped (blue) QD lasers (293K).

Lastly, the impact of the ridge waveguide width is also studied. Fig.4.19 depicts the room temperature evolution of the α_H -factor as a function of the ridge width for both p-doped and undoped lasers. As shown, in both situations the α_H -factor clearly increases with the ridge waveguide. While very narrow ridge is usually required to lase in a single spatial mode, any increase of the ridge width affects the injected current density hence the device properties like the modal gain and the α_H -factor [188].

4.3.2 Thermally insensitive determination of the α_H -factor

Although the ASE method is straightforward, it remains sensitive to the thermal effects hence leading to a clear underestimation of the α_H -factor. To address this issue, we optimized the ASE method by using the minimal pulse width of $0.1 \mu\text{s}$ and extraction the α_H -factor at 0 % duty cycle. In order to confirm this measured α_H -factor value by ASE method, the α_H -factor is now investigated with a thermally insensitive method using the residual side-mode dynamics under optical injection locking [274, 53]. Fig.4.20 illustrates the experimental setup where a tunable external cavity laser was used as the master laser and the injected light was coupled into the QD laser (slave laser) through an optical circulator. A polarization controller is inserted to align the polarization of both lasers. The 90 % of the output power was captured by a high resolution optical spectrum analyzer (OSA) and the rest of 10 % was

monitored by a power meter. The temperature of the slave laser was maintained at 293 K throughout the experiment.

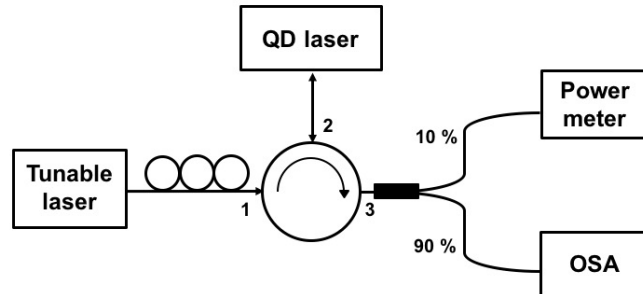


Fig. 4.20 Experimental setup for measuring the α_H -factors.

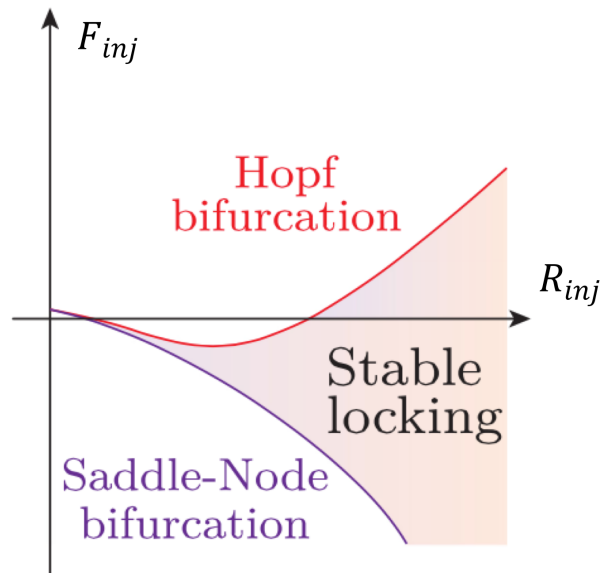


Fig. 4.21 Typical locking map of a laser diode, which includes Saddle-Node bifurcation, Hopf bifurcation and stable locking regime.

The key point of this method is that the optical injection is performed far from the gain peak e.g. to a longitudinal mode around 1315 nm, and the wavelength detuning is operated within the stable locking regime. Optical injection consists in injecting part of the light emitted by a master laser into a slave laser. The frequency detuning (F_{inj}) is defined as the optical frequency difference between the master and slave lasers, while the injection ratio (R_{inj}) is the ratio of the injected signal power (P_{inj}) to the free-running slave laser power (P_0). Fig.4.21 shows the typical locking map of a laser diode. In the particular case when the frequency of the master laser is close enough to the slave laser frequency and the master laser

power is high enough, the slave laser will operate at the master laser frequency. By adjusting the F_{inj} and R_{inj} , we can obtain a stable locking regime where the slave laser operates at the master laser frequency. The boundaries between the stable locking regime and unstable regime correspond to Saddle-Node bifurcation and Hopf bifurcation. Owing to the gain reduction through optical injection, the side modes are deeply suppressed in such way that the residual power of the side modes at the gain peak become governed by the ASE, and therefore the α_H -factor can be extracted as discussed hereinafter.

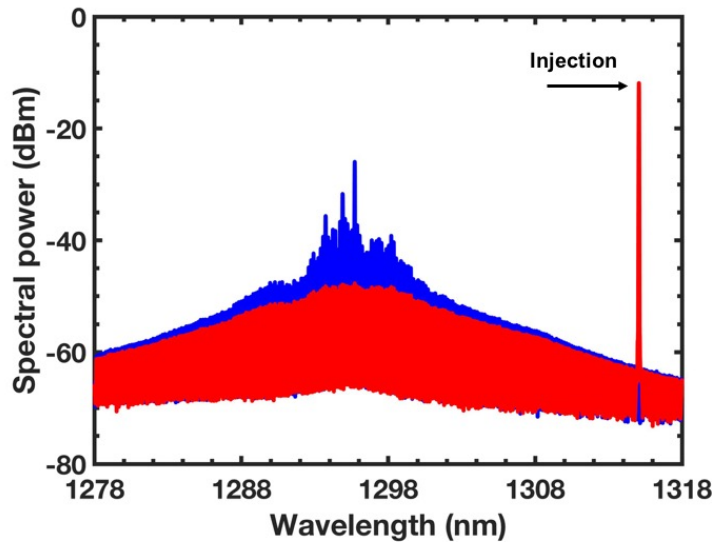


Fig. 4.22 Measured optical spectra for the p-doped QD laser. The blue lines are for the free-running laser (i.e. without optical injection), and the red lines are for the laser that is injection-locked.

Fig.4.22 illustrates the effect of optical injection on the FP cavity modes (blue lines) biased at 27.5 mA right above the threshold. Once the laser is stably-locked, only the mode subject to the optical injection keeps lasing (at 1315 nm) while all side modes are greatly suppressed (red lines). Both the enhanced injection ratio and increased frequency detuning reduce the entire net modal gain compared to that of the free-running laser hence resulting in the suppression of the longitudinal side modes. The optical injection induced gain reduction can be understood through the corpuscular equations of the injection-locked oscillators, which under the steady-state conditions leads to the following expression [274]:

$$\Delta G_{net} = -\frac{2\kappa_c}{v_g} \sqrt{R_{inj}P_0/P_s} \cos\phi \quad (4.8)$$

where the phase ϕ of the laser field is given by:

$$\phi = \sin^{-1} \left(-\frac{2\pi F_{inj}}{\kappa_c \sqrt{R_{inj} P_0 / P_s (1 + \alpha^2)}} \right) - \tan^{-1} \alpha \quad (4.9)$$

with κ_c s the coupling coefficient of the master laser to the slave laser, v_g is the light group velocity and P_s is the intracavity power of the slave laser under optical injection. The above equation shows that the F_{inj} reduces the net modal gain through the phase of the laser field. This gain reduction behavior is similar to that induced by the bias current in the ASE method. Therefore, the Eq.4.6 can be re-expressed as follows:

$$\alpha_H = -\frac{4n\pi}{L\delta\lambda} \frac{d\lambda/d\lambda_m}{dG_{net}/d\lambda_m} \quad (4.10)$$

with λ_m being the injection wavelength of the master laser. Consequently, an enhancement of the wavelength detuning shifts the lasing mode towards the longer wavelength side and reduces the gain to a lower level.

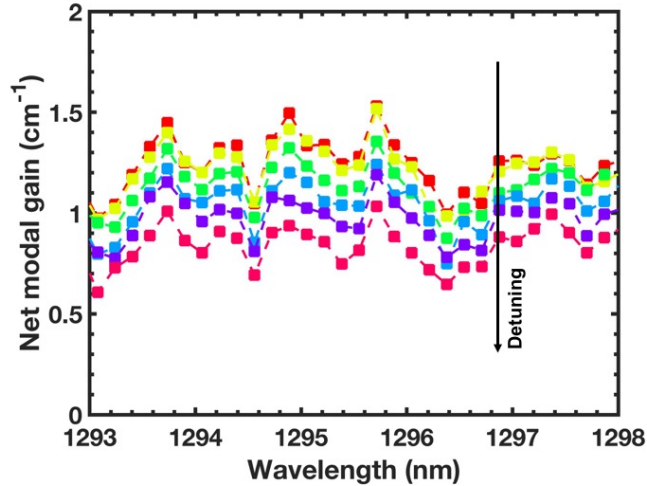


Fig. 4.23 Wavelength variation of the measured net modal gain with detuning of the injected light from shorter to longer wavelength within the stable-locking range.

Fig.4.23 describes the wavelength dependence of the net modal gain spectra for the p-doped QD laser. With the increase of the wavelength detuning, the whole gain spectra fall down gradually. Since this method is based on analyzing the residual side-mode ASE spectra under injection locking (IL), we named it ASE IL.

Fig.4.24(a) reveals the comparison of α_H -factor of the p-doped QD laser measured by ASE and ASE IL methods. In ASE IL method, the laser is biased at 27.5 mA just above the threshold current. The injected light is located at 1315 nm, which is 20 nm away from the gain peak of 1295 nm, while the R_{inj} is fixed at 5 dB. It is noted that this method is not

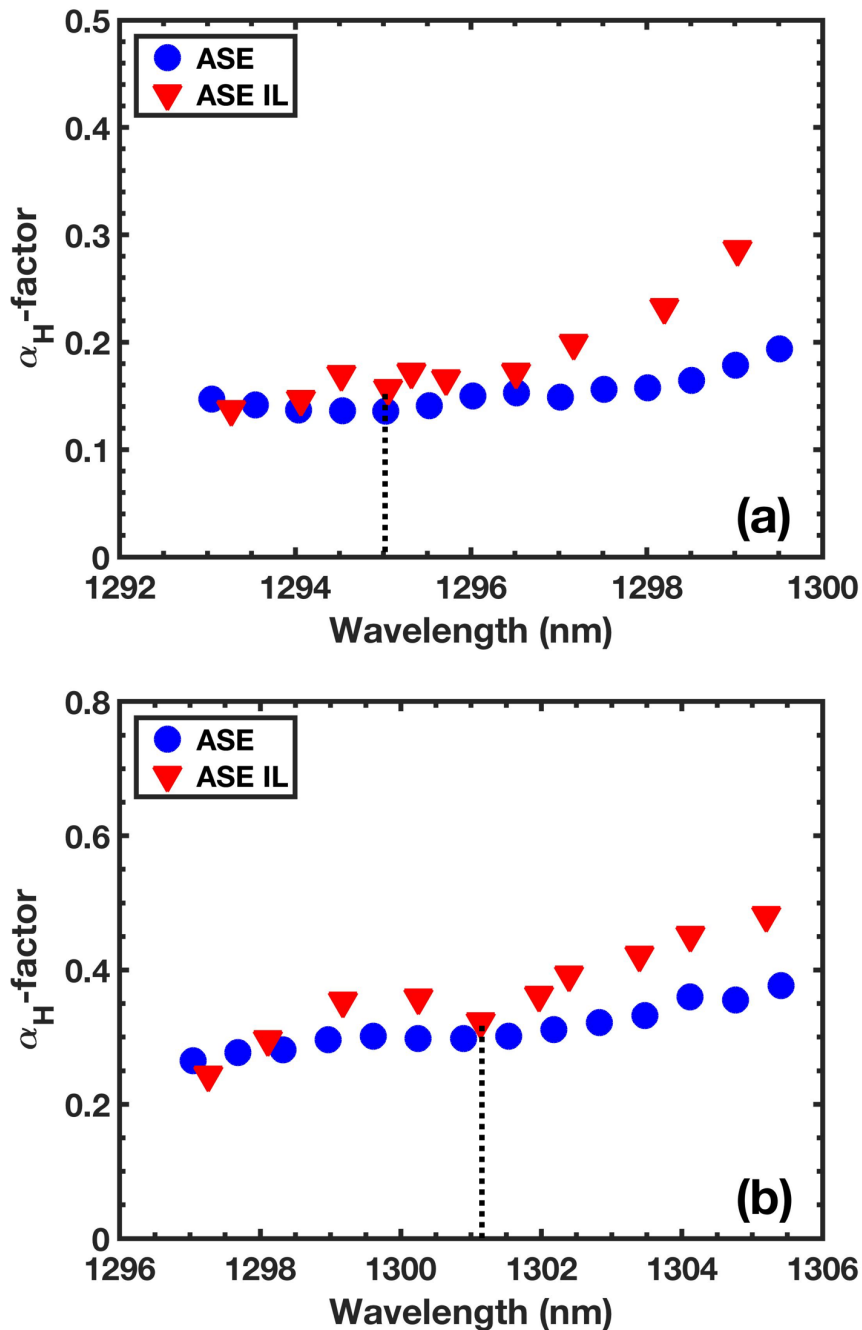


Fig. 4.24 Wavelength dependence of the measured α_H -factor by ASE method and ASE IL method for (a) p-doped QD laser and (b) undoped QD laser. The black dotted lines indicate the FP gain peak value.

sensitive neither to the injection power nor the choice of the injected mode due to the fact that the side modes are non-lasing and operated below threshold [274]. As shown in the Fig.4.24(a), the α_H -factors measured by ASE IL are found in a relatively good agreement with that measured under ASE and increase from about 0.14 at 1293 nm to 0.19 at 1299 nm, even though they are slightly higher. For example, compared with the α_H -factor of 0.13 at 1295 nm measured by ASE method, the α_H -factor measured by ASE IL is found with value of 0.15 with a standard deviation not exceeding 15%. This slight difference is attributed to the fact that ASE IL method relies on a fixed bias current while the ASE method requires a variation of the bias current hence leading to persistent device heating and underestimation of the α_H -factor. Fig.4.24(b) also presents the measured α_H -factor of the undoped QD laser, within the spectral range of 1297 – 1306 nm, the α_H -factor values measured under ASE IL are also consistent with the ASE values. Nevertheless, in both cases, α_H -factors measured from ASE IL are very close to these from ASE method, which means that the ASE method is well optimized only if a pulse width no longer than 0.1 μ s is used and extraction at 0.1 % duty cycle is performed.

4.3.3 Above-threshold α_H -factor determination

Finally, the effective α_H -factor is analyzed above the threshold by considering the effect of higher energy levels. Although, prior studies have shown α_H -factors below the unity in InAs/GaAs QD lasers emitting on the GS transition [99], it is important to remember that this statement remains mostly true at threshold beyond which as the injection current increases, the lower energy states are saturated and the carrier filling into the higher energy levels balloons the α_H -factor to larger values [171]. The above-threshold GS α_H -factor is measured using the injection-locking (IL) technique, which is based on the asymmetry of the stable locking region over a range of detuning on both positive and negative side of the locked mode [160]. By exploiting both negative and positive detuning locking boundaries $\Delta\omega_{min}$ and $\Delta\omega_{max}$ at a fixed bias current, the α_H -factor is retrieved from:

$$\alpha_H = \sqrt{\frac{\Delta\omega_{min}^2}{\Delta\omega_{max}^2} - 1} \quad (4.11)$$

In order to improve the accuracy of the measurement, the locking boundaries are determined by monitoring both the voltage drop out across the junction and the side-mode suppression ratio (SMSR) from the optical spectrum [160].

Fig.4.25 shows the voltage variation of the undoped laser under $1.5 \times I_{th}$ while tuning the master laser. The orange area marks the locking range, with $\Delta\omega_{min}$ and $\Delta\omega_{max}$ the lower

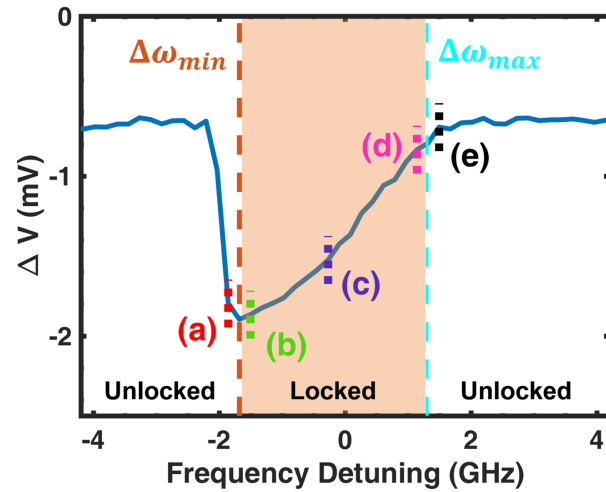


Fig. 4.25 Voltage variation of the undoped laser as a function of the frequency detuning.

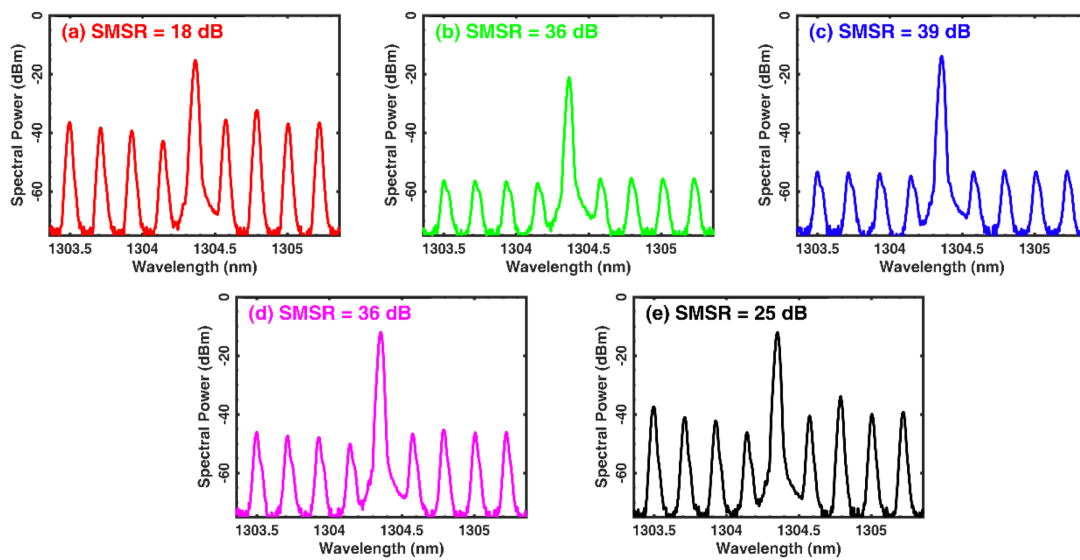


Fig. 4.26 Optical spectra at different frequency detuning marked on Fig. 4.25.

and upper boundaries. The criteria chosen for defining the locking boundaries is to have an SMSR > 35 dB, which is the most restrictive criteria. Within the stable-locking area, this criteria is perfectly fulfilled as illustrated in Fig.4.26 with optical spectra (b), (c) and (d). When exiting the stable-locking area, the SMSR is found to dramatically vary on both sides. On the negative detuning side, the transition from (a) to (b) causes an SMSR variation of nearly 20 dB whereas it is of 10 dB from (d) to (e) on the positive detuning side. Thus, we do confirm that the orange area does correspond to the stable-locking area. We have two proofs for that claim: the drop out of the voltage and the SMSR > 35 dB. As for the error on $\Delta\omega_{min}$ and $\Delta\omega_{max}$ i.e. on the locking bandwidth, the change in the SMSR is so clear that that the accuracy on the frequency detuning is below 80 MHz hence 0.5 pm in wavelength, leading to an estimation error of the α_H -factor not exceeding 10%.

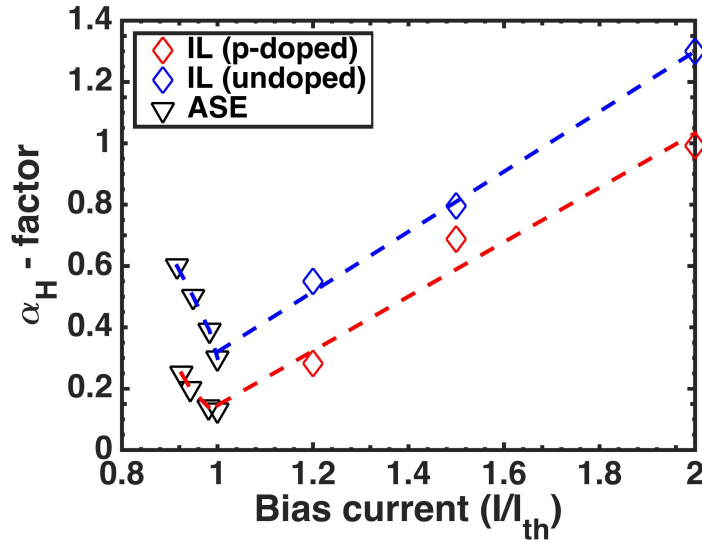


Fig. 4.27 The effective α_H -factor measured as a function of the normalized bias current for p-doped (red) and undoped (blue) QD lasers (293K). The injection ratio is -2 dB.

The GS α_H is displayed as a function of bias current in Fig.4.27 for both undoped and p-doped QD lasers. In the whole experiment, a low injection ratio of -2 dB is chosen. Indeed, for larger injection strengths, the value extracted is no longer that of the QD laser but rather that of the coupled oscillators. For the undoped case, the α_H is found to increase from 0.29 to 1.30 whereas the p-doped one depicts a smoother evolution ranging from 0.13 to about 1 at $I/I_{th} \approx 2$. In both cases, the increase of the effective α_H above threshold remains fundamentally attributed to the plasma effect as well as the carrier filling of the non-lasing states. Nevertheless, it has to be noted that a value of 1.3 at this level of bias current is extremely low compared to prior work with a value as large as 60 [47]. Last but not least, Fig.4.27 shows that the values extracted from the ASE method and decreasing with the bias

current [175] are, close to threshold, in a relative good agreement with those from the IL method which means that the measurements are accurate and stable.

In semiconductor lasers, the differential gain affected by the gain compression effect can be written according to the relationship:

$$g = \frac{g_0}{1 + \epsilon_P P} \quad (4.12)$$

where g_0 is uncompressed differential gain. Therefore, by inserting Eq.4.12 into Eq.4.6, the power dependence of the α_H directly results from the decrease of the differential gain through the gain compression and can be qualitatively approximated by the relationship:

$$\alpha_H(P) = \alpha_0(1 + \epsilon_P P) \quad (4.13)$$

where α_0 describes the α_H -factor at threshold. Eq.4.13 stands for a QW laser for which α_0 remains constant above threshold because the carrier density is clamped.

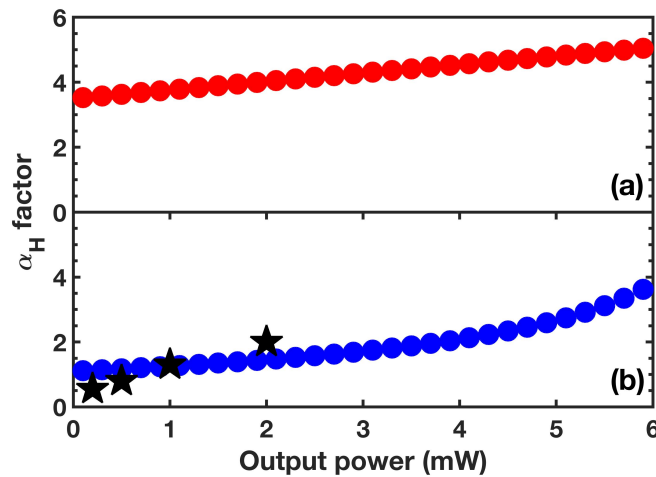


Fig. 4.28 The simulated α_H -factor as a function of the output power for the QW laser (a) and QD laser (b). Superimposed black stars in (b) correspond to experimental data from Fig.4.27.

Thus, Fig.4.28(a) shows that the calculated α_H of the QW laser considering that measured threshold value α_0 of 3.50 and ϵ_P is 0.07 mW^{-1} . As shown, the α_H linearly increases over the range of the output power. However, as compared to QW lasers, the carrier density at the GS is not clamped in QD lasers due to the inhomogeneously gain broadening [75]. In addition, the carrier filling in the ES contributes to increase the α_H of the GS transition hence resulting in an additional dependence with the output power. Indeed, the lasing wavelength can switch from GS to ES with the current injection increases, which means that a carrier accumulation occurs in the ES even though lasing in the GS is still occurring. By considering

gain variation at both GS and ES, the index change at the GS wavelength can be written as:

$$\delta n = \sum_k \alpha_k \delta g_k = \left(\alpha_e \frac{a_e}{a_g} + \alpha_g \right) \delta g \quad (4.14)$$

with $k = g, e$ are the indices of summation for GS and ES, respectively. δ_g and δ_n are the changes of the gain and refractive index at the GS, respectively. a_g and a_e are the differential gains at the ES and at the GS, respectively. α_e is the change of the GS index caused by the ES gain while α_g is related to the GS index change caused by the GS gain variation. The gain saturation in a QD laser can be described by:

$$g_g = g_{max} \left[1 - e^{-\ln(2) \left(\frac{N}{N_{tr}} - 1 \right)} \right] \quad (4.15)$$

with N the carrier density, N_{tr} the transparency carrier density. When the laser operates above threshold, the differential gain for the GS lasing can be simply expressed as a function of the gain compression coefficient, maximum gain g_{max} and gain at threshold g_{th} :

$$a_g = \frac{dg_g}{dN} = \frac{\ln(2)}{N_{tr}} (g_{max} - g_g) \quad (4.16)$$

with $g_g = g_{th}(1 + \epsilon_P P)$ is the uncompressed material gain increasing with the output power. Thus, the a_g can be further expressed as:

$$a_g = a_0 \left(1 - \frac{g_{th}}{g_{max} - g_{th}} \epsilon_P P \right) \quad (4.17)$$

with a_0 the differential gain at threshold. Taking into account all these considerations, it was shown that Eq.4.13 can be reformulated in the case of QD lasers as [73]:

$$\alpha_H(P) = \alpha_g(1 + \epsilon_P P) + \frac{\alpha_1}{1 - \frac{g_{th}}{g_{max} - g_{th}} \epsilon_P P} \quad (4.18)$$

where α_g represents the change of GS index caused by gain variation while α_1 is that induced by ES gain variation. These two coefficients are used as fitting parameters in the simulations. From the theoretical modeling at University of California Santa Barbara, the maximum gain g_{max} is calculated as 24 cm^{-1} and that the gain at threshold g_{th} is 11 cm^{-1} [291]. The ϵ_P is 0.15 mW^{-1} for the undoped QD laser (see Tab.4.1). Fig.4.28(b) shows the calculated power dependence of the α_H -factor (blue dots) for the QD laser. The black star markers correspond to experimental data taken from the Fig.4.27 which have shown that the α_H increases smoothly above the laser's threshold. Therefore, the simulation results qualitatively

agree with the measurements hence indicating that the power dependence of the α_H -factor is essentially ruled out by the gain compression and the carrier filling from the ES. However, according to the Fig.4.28(b), the star marks do not quantitatively agree with the simulation results. This discrepancy is explained by the model itself which does not take into account all the peculiar properties of the QDs (e.g., inhomogeneous broadenings, multiple higher energy levels, etc.). Although the agreement is qualitative rather than quantitative, it does reflect the right trend of the pump current dependence of the α_H -factor. Despite the large gain compression coefficient, Fig.4.28(b) shows that the increase of the α_H -factor is linear until the output power reaches about 4 mW. This effect is attributed to the fact that the switching dynamics towards the ES takes place at a very large bias meaning that the second member of the right-hand side of Eq.4.18 does not impact that much the power dependence of the α_H . This situation is fundamentally different when both gain compression and switching dynamics from GS to ES take place [73].

4.4 Summary

To summarize, these experimental results show that the minimal RIN level below 10 GHz is achieved between - 140 dB/Hz to - 150 dB/Hz in both undoped and p-doped QD lasers and that the p-doping increases the modulation bandwidth with doping level between 0 and 20 holes/dot. However, experiments also show that any further increase of the p-doping enhance the gain compression effect due to the increased internal losses, hence limiting the maximum achievable bandwidth. On the other hand, we demonstrate the ultra-low α_H -factor extracted from the standard ASE method and coupled to the enhanced thermal stability observed in p-doped silicon lasers and mostly results from the low TDD and fewer defects in the active region. Although the ASE method is straightforward, it potentially remains sensitive to the thermal effects hence leading to a clear underestimation of the α_H -factor, in particular, if a pulse width $> 0.1 \mu\text{s}$ is considered. In order to confirm the ASE value, we also investigate the extraction of the α_H -factor with a thermally insensitive method analyzing the residual side-mode dynamics under optical injection locking. The presented results are found in agreement with our initial measurements conducted with the standard ASE method proving that the experimental conditions (pulse width = $0.1 \mu\text{s}$, duty cycle = 0 %) allow to reflect the real value of the α_H -factor. We believe that these results are meaningful for designing future high speed and low noise QD devices to be integrated in future PICs. Last but not least, the high damping factor coupled with the ultra-low α_H -factor in QD laser is also an important feature for isolator-free applications and will be discussed in the next chapter.

Chapter 5

Epitaxial QD lasers on silicon : Analysis of the reflection sensitivity

This chapter systematically investigate the reflection sensitivity of epitaxial InAs/GaAs QD lasers on silicon. Results show that epitaxial QD lasers on silicon are much more resistant to optical feedback than QW lasers. Moreover, the critical feedback level is found to strongly depend on the excited-to-ground-state lasing threshold ratio, which can be considered as an additional figure of merit of the feedback dynamics, thus a laser having a fast switching dynamics with respect to the bias current is more subject to being highly destabilized by parasitic reflections. Furthermore, the impact of the p-doping on the high-speed performance subjected to optical feedback is also discussed. Results show that QD lasers with and without p-doping exhibit a very high degree of resistance to both incoherent and coherent optical feedback. On the top of that, 10 Gbps penalty-free transmissions are demonstrated under external modulation and for different temperatures. This feedback insensitivity mostly results from the low linewidth enhancement factor, the narrow inhomogeneous broadening, the high damping, the absence of off-resonance emission states as well as shorter carrier lifetime.

5.1 Introduction

5.1.1 Principle of optical feedback

The optical feedback is introduced into the semiconductor lasers by reinjecting part of the emitted light of a laser into the laser cavity. Fig.5.1 shows the principle of optical feedback which is performed by aligning a mirror on the laser emission path. The external cavity

round-trip time is defined as :

$$\tau_{ext} = \frac{2n_{ext}L_{ext}}{c} \quad (5.1)$$

with n_{ext} the refractive index of the external cavity, L_{ext} the distance of the laser to the mirror and c the celerity of light. The feedback strength r_{ext} is defined as the ratio between the returned power (P_{return}) and the free-space emitted power (P_{out}) at the coupling facet such as:

$$r_{ext} = \frac{P_{return}}{P_{out}} \quad (5.2)$$

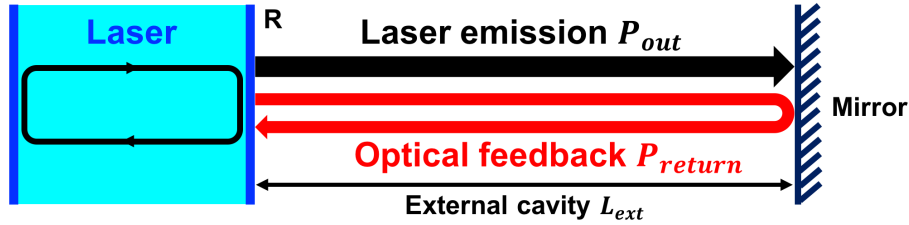


Fig. 5.1 Schematic illustration of a semiconductor laser under optical feedback

Under optical feedback, the dynamics of a semiconductor laser can become unstable and exhibit complex nonlinear dynamics like periodic or chaotic oscillations. According to the Poincaré-Bendixon theorem, a dynamical system can exhibit chaos if and only if three degrees of freedom are involved to destabilize the stability [242].

Arecchi *et al.* proposed a laser classification which depends on the photon lifetime (τ_p), carrier lifetime (τ_c) and polarization lifetime (τ_{pol}), respectively [11]. In class C lasers, τ_p , τ_c and τ_{pol} are of the same order of magnitude ($\tau_c \sim \tau_p \sim \tau_{pol}$) and the system is described by three rate equations with carrier density (N), electric field (E) and the polarization (P). In this case, the laser can easily become chaotic on its own without external control such as NH_3 lasers [281]. Semiconductor lasers are class B lasers where $\tau_c \geq \tau_p \gg \tau_{pol}$. The polarization rate equation can be replaced by its steady-state solution since the polarization response is much faster than the changes of carrier density or electrical field. With only two degrees of freedom, the semiconductor laser can not destabilize by itself hence an additional degree of freedom is always required. To this end, the Q-switching or external control such as optical injection and optical feedback can act as an additional degree of freedom [12]. Let's us note that the two different polarizations arising from a vertical cavity surface emitting laser (VCSEL) can produce chaos without any external perturbations [265]. Finally, for class A laser such as gas laser, both the carrier density and the polarization equations can be replaced

by their steady-state values because of the relationship : $\tau_p \gg \tau_c \sim \tau_{pol}$. On this occasion, two additional degrees of freedom are required to make a chaotic laser [280].

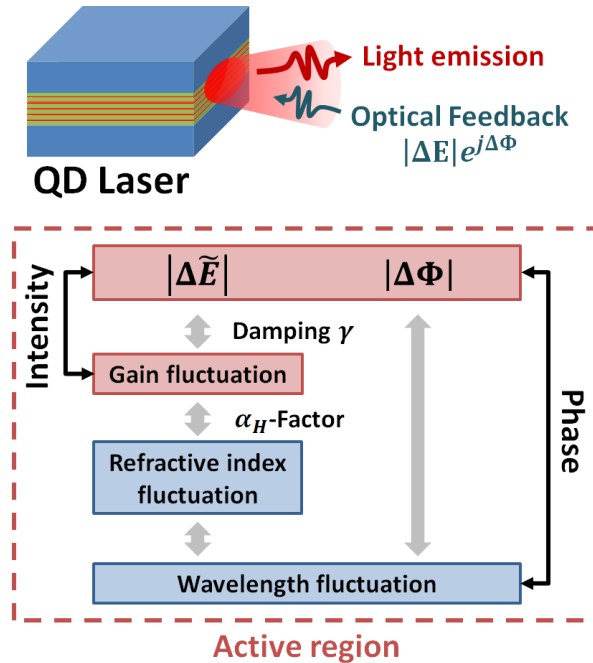


Fig. 5.2 Schematic representation of the physical processes involved in a semiconductor laser under optical feedback.

The physical processes involved in a semiconductor laser under optical feedback are schematically described in Fig.5.2. The phase-amplitude coupling in the active region between the returned light field and the intracavity is represented by field fluctuations both in amplitude and phase (i.e. $|\Delta E|$ and $|\Delta\Phi|$). Optical feedback is coupled into the laser cavity through the output facet and causes a perturbation on the photon density. This perturbation leads to a fluctuation of the carrier density and thus the optical gain. The intensity fluctuation is then modulated by the damping effect and linked to the optical gain, where the gain variation itself impacts on the refractive index through α_H -factor, hence leading to a shift in the lasing wavelength. On the other hand, the phase fluctuation caused by returned field is related to wavelength fluctuation as well. The interaction of the intensity and phase loop essentially makes the dynamics of the laser system under optical feedback very complex and results in the severe complex laser instabilities such as coherence collapse [143, 77, 200].

There are several reasons to explain the question that why semiconductor lasers are so vulnerable to optical feedback. First, the lasers operate with typically high gain and have rather small facet reflectivity (R) which make the laser rather open to the outside world and external optical signals can easily reenter the laser cavity. Second, the external optical

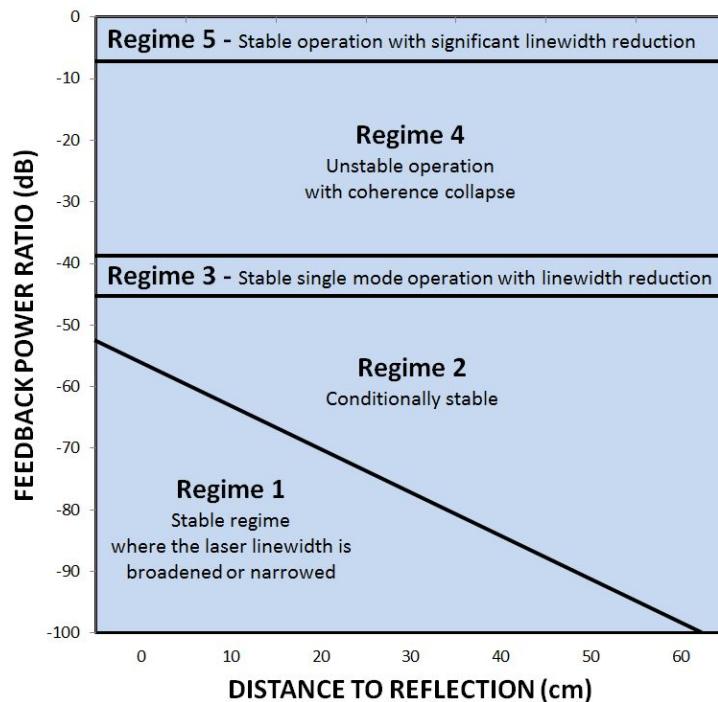


Fig. 5.3 Cartography of optical feedback regimes in a DFB QW laser from [255].

signals can easily disturb the laser when it operates in a state of equilibrium and leading to enhanced noise and even unstable behavior. Various experiments were conducted to further investigate the impact of the optical feedback on the semiconductor laser since 1970 [27]. In 1986, Tkach *et al.* classified the different feedback regimes in a semiconductor distributed feedback (DFB) laser and represented the spectral behavior of the laser as a function of the two feedback parameters : feedback ratio namely feedback strength and the external cavity length [255]. As shown in the Fig.5.3, the identified five distinct feedback regimes successively appear with the increase of the feedback ratio at a fixed external cavity length. The regime one corresponds to the lowest feedback level. The laser is stable with single-mode while the spectral linewidth can be either narrowed or broadened depending on the distance to the reflector which determines the phase of the optical feedback signal. In regime two, mode hopping arises between external cavity modes induced by the feedback phase. In addition, the laser becomes more sensitive to optical feedback for longer external cavity. In regime three, the laser experiences a restabilization and operates on single-mode with the minimal linewidth. The distance to reflection has no effect on the laser dynamics. When further increasing the feedback ratio, the laser enters a regime four where the lasing linewidth is broadened with growing side-modes separated from the main modes by the relaxation oscillation frequency (ROF). The optical feedback induced the undamping of the

relaxation oscillations corresponding to periodic oscillations at ROF (P1) which is regarded as a precursor of the quasi-periodicity route to chaotic oscillations through the so-called coherence collapse regime [143]. The onset of this regime is defined as the critical feedback level which will be introduced in the following parts. Finally in regime five, the laser is highly stable with significant linewidth reduction. This regime is similar to the extended cavity regime where the laser operates as a short active section in a long cavity. In order to achieve this regime, an antireflection coating on the facet subjected to the feedback is required to achieve such high feedback ratio [62, 284, 252].

5.1.2 Lang and Kobayashi equations

The dynamics of a single mode semiconductor laser under optical feedback is described by Lang-Kobayashi rate equations [138]. In this case, only one roundtrip in the external cavity is considered, which suggests a relatively small amount of feedback. The rate equations of the laser subject to optical feedback are expressed as:

$$\frac{d\tilde{E}(t)}{dt} = \left\{ \frac{1}{2}(1 + i\alpha_H) \left[\Gamma G_N(N(t) - N_{tr}) - \frac{1}{\tau_p} \right] + i\omega_0 \right\} \tilde{E}(t) + \kappa \tilde{E}(t - \tau_{ext}) \quad (5.3)$$

$$\frac{dN(t)}{dt} = \frac{\eta_i I}{qV} - \frac{N(t)}{\tau_c} - G_N(N(t) - N_{tr})A^2(t) \quad (5.4)$$

where \tilde{E} the slowly varying complex amplitude of the optical electric field, N the carrier density, τ_c the carrier lifetime and τ_p the photon lifetime. Γ the confinement factor, N_{tr} the transparent carrier density, ω_0 the lasing angular frequency, $G_N = v_g dg/dN$ the linear gain with v_g and g being the group velocity and the optical gain. In Eq.5.3, α_H the linewidth enhancement factor while the second term in the right-hand side is the contribution related to the optical feedback with τ_{ext} the external round trip time in the external cavity. η_i the injection efficiency characterizing the fraction of bias current that generates carriers in the active region. I the injection current, q the electron charge, V the active region volume, A the amplitude of the electric field. κ is the feedback coefficient given by [234]:

$$\kappa = \frac{1}{\tau_{in}} 2C_l \sqrt{r_{ext}} \quad (5.5)$$

where $\tau_{in} = 2n_{int}L_c/c$ the internal round-trip time with n_{int} and L_c being the refractive index and the cavity length of the laser. C_l is the coupling coefficient of the laser's front facet to the

external cavity for a FP laser and is given by [252]:

$$C_l = \frac{1 - R}{2\sqrt{R}} \quad (5.6)$$

with R is the facet reflectivity coupled to the external cavity. In case of a DFB laser, the expression of C_l is more complicated as below [72]:

$$C_l = \frac{2(1 - |\rho_l|^2)\exp(-i\phi_l)(q_0^2 + \kappa_0^2)L^2}{i\kappa_0L(1 + \rho_l^2) - 2\rho_l q_0 L_c} \frac{1}{2qL - \sum_{k=l,r} \frac{(1 - \rho_k^2)\kappa_0 L}{2iq_0L\rho_k + \kappa_0L(1 + \rho_k^2)}} \quad (5.7)$$

with the terms $\rho_k = |\rho_k| \exp(i\phi_k)$ with $k = l, r$ are the complex reflectivities at the left and right facets, respectively (right facet subjected to optical feedback). κ_0 the coupling coefficient of the grating, $q_0 = \alpha_{tot} + i\delta_0$ with α_{tot} the total internal loss and δ_0 the deviation between the lasing and the Bragg wavenumbers.

The dynamics of the electric field amplitude is much lower than the angular frequency ω_0 of the fast optical carrier. In order to eliminate the fast optical carrier component, we assume $\tilde{E}(t) = \tilde{A}(t)\exp(i\omega_0 t)$ with the term $\exp(i\omega_0 t)$ corresponds to the fast lasing oscillations and $\tilde{A}(t)$ is the slow envelop of the complex electric field, which can be further expressed as $\tilde{A}(t) = A(t)\exp(i\Phi(t))$ with $A(t)$ and $\Phi(t)$ being the amplitude and the phase of the field. Under steady-state conditions $\frac{dE}{dt} = \frac{dN}{dt} = 0$, the output power is constant hence $A(t) = A(t - \tau_{ext}) = A_s$, $N(t) = N_s$ and the steady-state phase $\Phi_s = (\omega_s - \omega_0)t$ with ω_s the steady-state angular frequency. Therefore, the steady-state solutions of the Eq.5.3 and Eq.5.4 can be expressed as [200, 256]:

$$A_s^2 = \frac{\eta_i I / qV - N_s / \tau_c}{G_N(N_s - N_{tr})} \quad (5.8)$$

$$\omega_s - \omega_0 = \Delta\omega_s = -\kappa[\alpha_H \cos(\omega_s \tau_{ext}) + \sin(\omega_s \tau_{ext})] \quad (5.9)$$

$$N_s - N_{th} = \Delta N_s = -\frac{2\kappa}{\Gamma G_N} \cos(\omega_s \tau_{ext}) \quad (5.10)$$

5.1.3 Light current characteristic with optical feedback

From the Eq.5.10, the optical feedback has an influence on the threshold gain which related to the threshold current of the laser. Osmundsen *et al.* have derived the expression of the threshold current by taking into account multiple round-trips in the external cavity. For the

limit case of small feedback ratios ($r_{ext} \ll 1$), the threshold current can be expressed as :

$$I_{th} = I_0(1 - 2\kappa\cos(\omega_s\tau_{ext})) \quad (5.11)$$

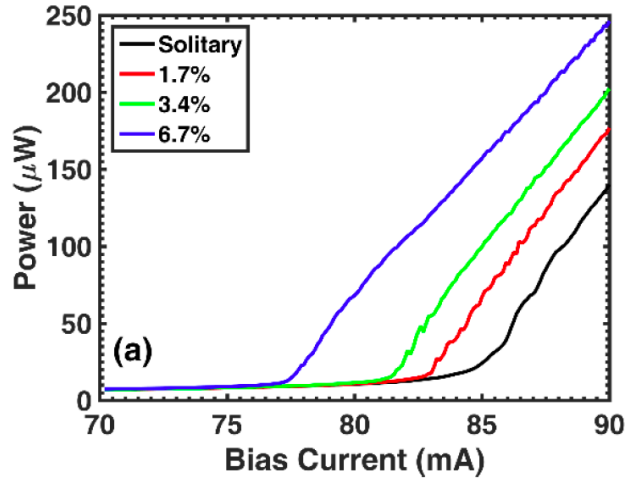


Fig. 5.4 The comparison of the light current characteristics of a QD FP laser between the free-running operation and three different feedback ratio from [98]

Fig.5.4 shows the light current characteristics of a QD FP laser operating in the free-running operation and three different feedback ratio [98]. From Eq.5.10, the laser operates below threshold leading to $N_s - N_{th} < 0$, hence the term $\cos(\omega_s\tau_{ext})$ is positive. Thus, as shown, the carrier density decreases with the increase of the feedback ratio, thus the laser threshold is reduced.

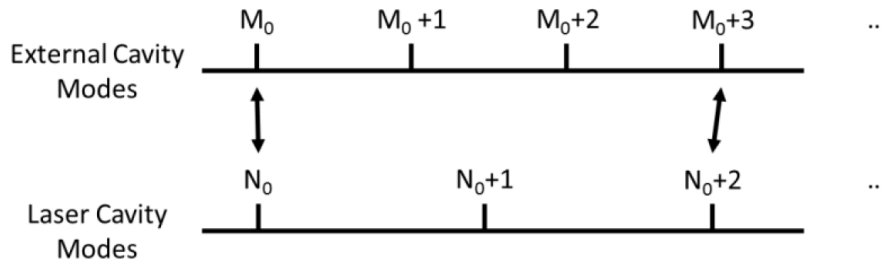


Fig. 5.5 Interaction between the external cavity modes M_i and the laser cavity modes N_i from [138].

In addition, some undulations are sometimes observed in the light-current characteristic curve of a laser under optical feedback (see the red curve in the Fig.5.4). This phenomenon

results from the competition between the laser cavity modes and the external cavity modes [138]. As shown in the Fig.5.5, some laser cavity modes coincide with external cavity modes at a given bias current. Thus, the constructive interferences enhance the output power while the destructive interferences reduce the output power. By increasing the bias current, the refractive index of the laser cavity changes due to carrier density variation and thermal effects. The effective internal cavity length changes with the refractive index leading to a change of laser free spectral range hence laser cavity modes are shifted and the undulations appear in the light-current characteristics.

5.1.4 Phase shift with optical feedback

According to Eq.5.9, the phase condition can be derived as:

$$\Delta\omega_s\tau_{ext} = -C\sin\phi_0 \quad (5.12)$$

with $\Delta\omega_s\tau_{ext}$ the phase difference between the laser cavity field and the delayed field. C the feedback parameter and ϕ_0 the corresponding phase as below:

$$C = \kappa\tau_{ext}\sqrt{1 + \alpha_H^2} = \frac{\tau_{ext}}{\tau_{in}}2C_l\sqrt{1 + \alpha_H^2}\sqrt{r_{ext}} \quad (5.13)$$

$$\phi_0 = \omega_s\tau_{ext} + \arctan(\alpha_H) \quad (5.14)$$

In order to solve the Eq.5.12, it is necessary to calculate the interception between $y = \omega_0\tau_{ext}$ and $y = \omega_s\tau_{ext} + C\sin[\omega_s\tau_{ext} + \arctan(\alpha_H)]$. Fig.5.6 shows the graphical solutions obtained for $C = 0.76$ and $C = 9.50$. If $C < 1$, there is only one stable solution, while various stable or unstable solutions are possible for $C > 1$ [200].

Henry *et al.* also introduced another way to graphically represent the possible oscillations [92]. Based on Eq.5.9 and Eq.5.10, an elliptical orbit can be obtained with expression as:

$$\left(\Delta\omega_s\tau_{ext} - \frac{\alpha_H\tau_{ext}}{2}\Gamma G_N\Delta N_s\right)^2 + \left(\frac{\tau_{ext}}{2}\Gamma G_N\Delta N_s\right)^2 = (\kappa\tau_{ext})^2 \quad (5.15)$$

Fig.5.7 illustrates the carrier density variation versus the phase difference following the Eq.5.15. Their interceptions give the possible solutions of the Eq.5.12 where the stable solutions (external cavity modes) are located on the lower half of the ellipse marked as blacks, the unstable ones are located on the upper half as black circles whereas the red dot at the center is the free-running mode. In Eq.5.15, both α_H -factor and κ determine the ellipse eccentricity. The increase of these two parameters will expand the dimension of the orbit hence more steady-states solutions will be involved and the laser becomes less stable.

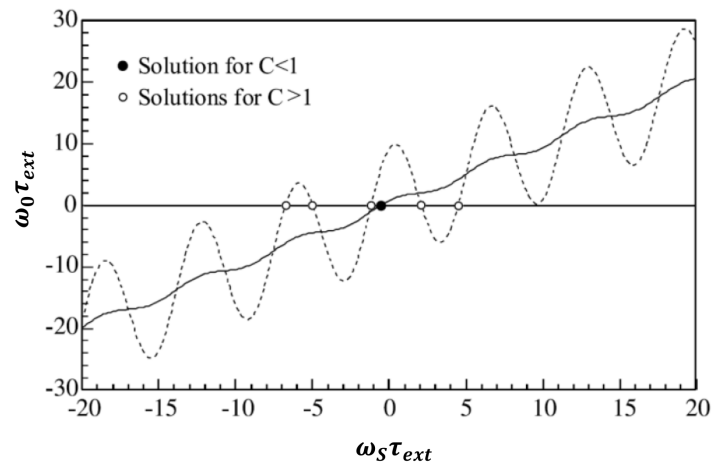


Fig. 5.6 Steady-state solutions with respect to parameter C . Solid and dashed lines are obtained for $C = 0.76$ and $C = 9.50$, respectively. The black circle corresponds to the single solution for $C < 1$ and white circles represent the various solutions for $C > 1$ from [200].

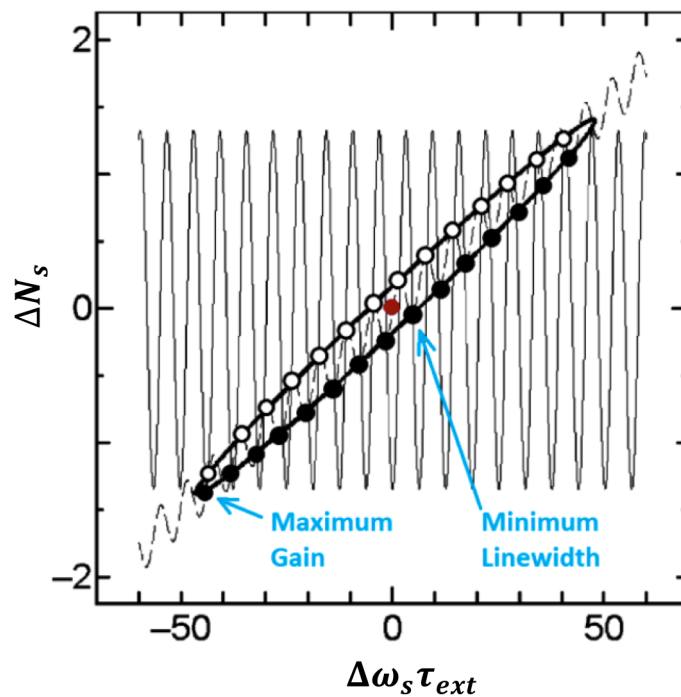


Fig. 5.7 Carrier density variation as a function of the phase difference. Crossing points between solid and dashed sine waves give the locations of the modes. The red dot is the free-running mode [200].

Although the most stable mode is the mode with maximum gain which located on the left hand-side of the ellipse, Levine *et al.* have proved that the laser subject to optical feedback will tend to stabilize on the mode with minimum linewidth, which is the closer one to the free-running mode [144]. This situation corresponds to the feedback regime three. However, these two modes will enter a competitive state and a coherence collapse will occur. The coherence collapse was firstly introduced by Lenstra *et al.* meaning that the feedback terms in the amplitude and the phase of the Lang and Kobayashi equations were interfering hence these equations are no longer linear and a drastic linewidth broadening were obtained [143].

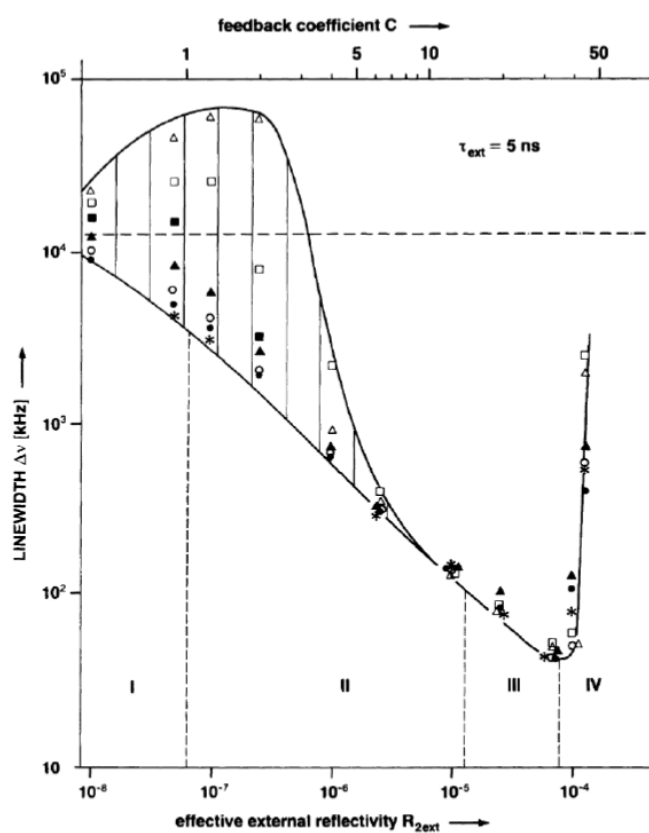


Fig. 5.8 Spectral linewidth as a function of the feedback strength. The markers represent different feedback phase conditions from [211].

The spectral linewidth of the laser under optical feedback can be expressed as below [41]:

$$\Delta\nu = \frac{\Delta\nu_0}{(1 + C\cos\phi_0)^2} \quad (5.16)$$

with $\Delta\nu_0$ the free-running spectral linewidth without optical feedback. Fig.5.8 shows the spectral linewidth behaviour for different values of C namely different feedback regimes

[211]. In regime one ($C < 1$), there is only one solution and the spectral linewidth may be either narrowed or broadened depending on the feedback phase. In regime two with C slightly above unity, the spectral linewidth remains strongly dependent on the feedback phase since there are only a few external cavity modes excited. However when $C > 5$, multiple external cavity modes are involved and the the system is no longer dependent on the feedback phase, hence the laser progressively restabilize to regime three with minimum linewidth mode. When further increasing the feedback ratio, the laser enters the regime four where the spectral linewidth will be dramatically broadened.

5.1.5 Bifurcation diagram representing the laser dynamics

We can also use Runge-Kutta method to solve the Eq.5.3 and Eq.5.4. For a given set of initial conditions such as a given feedback ratio, the numerical time trace of the laser subjected to optical feedback is built by iterations. The final point of the time trace will then be used as the initial condition for the next feedback ratio value. A bifurcation diagram represents the intensity extrema extracted from the time series when excluding the transient part of the trace, as a function of the feedback ratio [242].

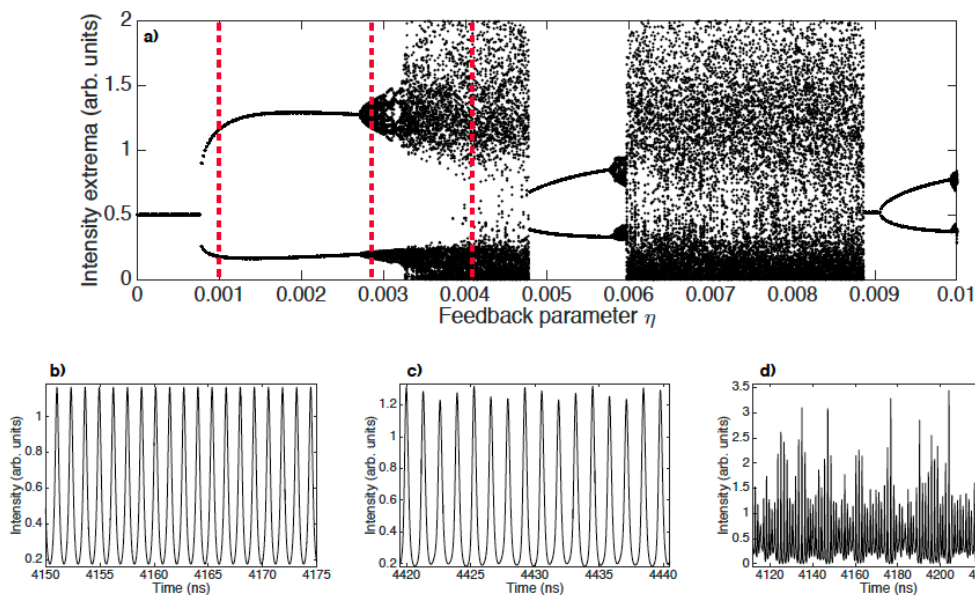


Fig. 5.9 (a) Numerical bifurcation diagram. Corresponding time trace for $\eta = 0.001$ (b), time trace for $\eta = 0.0027$ (c), time trace for $\eta = 0.0042$ (d), from [112].

Fig.5.9(a) displays an example of bifurcation diagram showing a succession of stable and unstable behaviors when increasing the feedback ratio η . As shown, for very low feedback

levels, there is only one line on the bifurcation diagram meaning that the laser is stable. At a critical feedback level of $\eta = 0.0008$, the minimum and maximum of intensity split significantly. This particular point is called Hopf bifurcation showing the transition from the stable regime to the period 1 (P1) regime. The P1 regime corresponds to the time trace of a periodic oscillation at the relaxation oscillation frequency as shown in Fig.5.9(b). When further increasing the feedback ratio, the diagram splits again as another oscillation frequency appears, which is superimposed on the first split as shown in Fig.5.9(c). Along with more and more frequencies are involved, the oscillations become totally aperiodic as Fig.5.9(d). These random pulsations are the chaos instead of noise since they strongly depend on the initial conditions and are purely deterministic. After the chaos regime, the laser restabilizes on an external cavity mode and the cycle starts again. This nonlinear dynamics scenario is called a quasi-periodic route to chaos.

5.1.6 Toward a feedback insensitive semiconductor laser

The integration of optical functions on a microelectronic chip brings many innovative perspectives, along with the possibility to enhance the performance of photonic integrated circuits (PIC)[196]. However, each additional on-chip component can produce a possible source for reflections to any on-chip laser, hence the laser can become unstable and exhibit complex nonlinear dynamics like periodic or chaotic oscillations. Flip-chip or wafer bonding have already reported good performance [219, 251, 227], they remain quite sensitive to not only coherent optical feedback from parasitic back-reflections of the laser emission by the vertical grating couplers and the multiple passive and active interfaces/transitions between the III-V material and silicon [230, 208, 262], but also from possible incoherent feedback originating from amplified spontaneous emission (ASE) noises generated by active building blocks like semiconductor optical amplifiers (SOAs) or active waveguides that are often integrated in the same photonics integrated circuits (PICs) [293]. Fig.5.10 shows the intensity extrema as a function of bias current for a III-V laser integrated on silicon [230]. As shown, even under free-running operation, the strong periodic oscillations are observed at high bias current resulting from the multiple internal reflections between III-V material and silicon. These internal reflections combined with external optical feedback can become highly problematic for the laser stability.

Thus integrated optical isolators are required to maintain the laser functionality. Without isolator, integrated lasers cannot be protected from parasitic reflections by completely suppressing the optical feedback. Integrated isolators are usually classified into three categories: those based on non-linear effects; those based on spatiotemporal modulation; and those based on magneto optic effects [23]. Although on-chip optical isolators with high perfor-

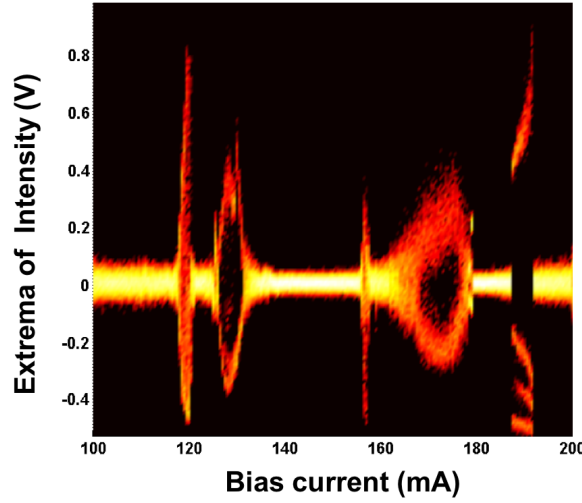


Fig. 5.10 Extrema of intensity as a function of bias current for a III-V laser integrated on silicon under free-running operation [230].

mance have been reported, they still suffer from non negligible insertion loss and remain quite complicate to fabricate [289, 96]. In order to meet the aforementioned requirements, semiconductor lasers monolithically grown, with low-cost, high-yield, energy efficient and much better scalability are still demanded [136]. In addition, the development of feedback insensitive transmitters is a major objective especially for silicon photonics related applications. Recently, the transition to the coherence collapse regime has been investigated in high coherence lasers made with hybrid silicon technology. Owing to the very large quality factor ($Q \approx 10^7$), the frequency noise power spectral density of the III-V/silicon hybrid laser is hardly affected up to a feedback level of -31dB, which is at least 19 dB higher than that of the III-V DFB laser [293, 82]. Another solution relies on the semiconductor Fano lasers, which can strongly suppress dynamic instabilities induced by external optical feedback [217]. However, these technologies are more complex and the laser output power is quite limited.

Now, we introduce the InAs/GaAs quantum dot (QD) technology. In QD lasers, the impact of off-resonance energy states play an important role in the laser dynamics. In particular, prior works showed that a QD laser lasing on the sole GS transition does not exhibit the same dynamical response under optical excitation as that emitting exclusively on the first ES assuming that the two lasers were made with the same materials and come from the same wafer. The GS laser means that the ES threshold current (I_{th}^{ES}) is far from the GS threshold current (I_{th}^{GS}), hence the ratio I_{th}^{ES}/I_{th}^{GS} converges towards infinity, while the ES laser corresponds to $I_{th}^{ES}/I_{th}^{GS} \ll 1$. The effect of this ratio on optical feedback will

be discussed in the following section. Fig.5.11 compares the optical and electrical spectra between the GS and ES lasers for solitary case and under the maximal feedback strength. Under optical feedback, it was shown that InAs/GaAs QD lasers emitting exclusively on the GS transition are much more stable, hence exhibiting chaos-free operation (i.e. no coherence collapse), while those operating on the sole ES transition can display a plethora of dynamic states including broadband chaotic states as shown in Fig.5.11(d) [99, 101, 153]. Such a difference is attributed to the very large damping factor of the GS laser preventing any chaotic oscillations even at the largest feedback ratios.

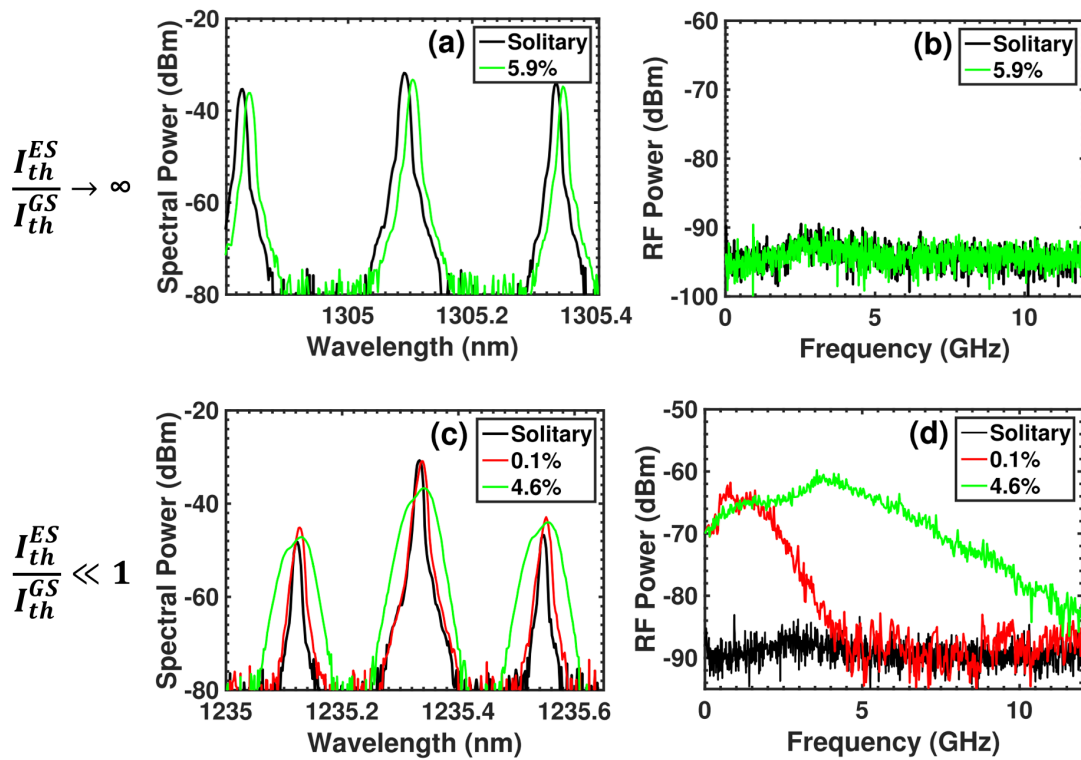


Fig. 5.11 (a) Optical and (b) electrical spectra of the GS laser measured at $3 \times I_{th}$ without feedback (solitary) and for the maximal feedback strength. (c) Optical and (d) electrical spectra of the ES laser measured at $2.5 \times I_{th}$ without feedback (solitary) and for the maximal feedback strength [99].

Overall, InAs/GaAs QD lasers often behave as quasi-class A oscillators hence showing strong damping effects and low linewidth enhancement factor (α_H -factor) [199, 299, 108]. Together, these features do contribute to enhance the laser stability against undesired optical feedback [52, 167]. For instance, a prior work showed that InAs/GaAs QD DFB lasers exhibit low RIN of below -140 dB/Hz even under external optical feedback of -8 dB [176]. Another

work has reported on a 25 Gbps error-free transmission with an integrated InAs/GaAs QD laser transmitter on silicon substrate without optical isolator for core I/O applications [185].

The optical feedback dynamic is usually analyzed through the prism of the critical feedback level r_{crit} which corresponds to the birth of the laser destabilization associated to the first Hopf bifurcation [257]. Indeed, for semiconductor lasers operating under optical feedback, the undamping of the relaxation oscillations is a precursor of the quasi-periodicity route to chaotic oscillations through the fully developed coherence collapse regime [143] whose onset is often related to $r_{ext} = r_{crit}$ [298]. Using Eq.(5.3) and Eq.(5.4) evaluated through small-signal analysis and assuming a long external cavity, the onset of the critical level is given by:

$$r_{crit} = \frac{\tau_{in}^2 \gamma^2}{16C_l^2} \left(\frac{1 + \alpha_H^2}{\alpha_H^4} \right) \quad (5.17)$$

where γ the damping factor. Practically, Eq.5.17 gives the maximum parasitic feedback ratio that can be tolerated for a stable operation of the laser into a communication system. Thus, for $r_{ext} \gg r_{crit}$, the laser operates within coherence collapse regime and the RIN of the laser becomes affected. The noise power (P_{laser}) of the laser received at the photodiode can be expressed as:

$$P_{laser} = R_L M^2 S^2 \Phi^2 RIN B_n \quad (5.18)$$

with R_L the load resistance, M the avalanche factor, S the optical sensitivity of the photodiode, Φ the energy flux applied on the photodiode and B_n the noise bandwidth. From Eq.5.18, the RIN increases the noise power, hence the penalty is enhanced which is disadvantageous for high speed transmission [78].

The Eq.5.17 gives clear insights on how to increase the resistance to optical feedback of a semiconductor QD laser.

1. First, in order to reduce the coupling of the QD laser to the external world, a higher front facet reflectivity is preferred but doing so can also results in a strong reduction of the output power [76]. In this work, the power reflectivity of the front facet is fixed to 60% which is is enough to ensure good optical output power.
2. Second, from the Eq.5.17, a large damping factor increases the optical feedback resistance of the laser which is exactly what happens with QD lasers. Indeed, if the laser dynamics are heavily damped, the gain fluctuation introduced by the photon-density variation can be suppressed. In chapter 4, we have shown that even p-doped QD lasers still exhibit stronger damping than any bulk or QW lasers.
3. Third, decoupling the interaction between the intensity and phase loops is always required by minimizing the α_H -factor. From the Eq.5.17, the small α_H -factor can

induce the high feedback critical level. Semiconductor lasers with bulk and QW active region usually have α_H -factor of $2\sim 5$ [41]. By comparison, low-dimensional nanostructured QD lasers have much lower α_H values near-zero, which is in favor of high feedback resistance [54].

4. Fourth, in QD lasers, the onset of the critical feedback level strongly depends on the excited-to-ground-state ratio, hence a figure of merit showing that a large ratio of the excited-to-ground-state lasing thresholds is more beneficial for maintaining a high degree of stability [100]. This point will be discussed in the following parts.
5. Fifth, from Eq.5.17, we can also increase the cavity photon roundtrip time by using longer cavities to enhance the feedback resistance. In addition, longer cavities have less change of the lasing wavelength for the same amount of phase fluctuation caused by the optical feedback. In this work, using ~ 1 -mm long cavity constitutes a good compromise for maintaining very good feedback resistance and high laser performance.
6. Sixth, from the Eq.3.5, the quality factor (Q -factor) is inversely proportional to the internal loss and the mirror loss. In order to increase the feedback resistance, a high Q -factor is also required through the minimisation of both internal loss and mirror loss [293]. By incorporating the external quality factor (Q_{ext} , see Eq.3.7) into Eq.5.13, C can be rewritten as follows:

$$C = \frac{\omega \tau_{ext}}{Q_{ext}} \sqrt{1 + \alpha_H^2 \sqrt{r_{ext}}} \quad (5.19)$$

with ω the laser resonance frequency. Despite Eq.5.19 being a limiting case of Eq.5.13, it gives a qualitative insight on how Q_{ext} impacts the laser's feedback sensitivity. When the external Q_{ext} factor is large, the C coefficient can be kept to a low value thus providing a relative feedback insensitivity regardless of the feedback strength.

7. Finally, it is noted that the epitaxial defects accelerate Shockley-Read-Hall (SRH) recombination lifetime, which is inversely proportional to the defect density. As for GaAs-based QD laser, the SRH lifetime is usually on the order of 10 ns, which is much longer than spontaneous emission lifetime (~ 1 ns) and hence is negligible. Taking into account the SRH recombination is of paramount importance for epitaxial QD lasers on silicon or germanium. The SRH lifetime τ_{SRH} is incorporated into the carrier equation in order to take into account the SRH non radiative recombinations induced by the epitaxial defects in QD lasers epitaxially grown on silicon. In what follows, the

effective carrier lifetime τ_c' is rewritten such as:

$$\frac{1}{\tau_c'} = \frac{1}{\tau_c} + \frac{1}{\tau_{SRH}} \quad (5.20)$$

By including the effective carrier lifetime in the Eq.5.17, the critical level can be reexpressed as:

$$r_{crit} = \frac{\tau_{in}^2 (K f_{RO}^2 + 1/\tau_c')^2}{16C_l^2} \left(\frac{1 + \alpha_H^2}{\alpha_H^4} \right) \quad (5.21)$$

with K a constant usually refers as the K -factor. f_{RO} the relaxation oscillation frequency.

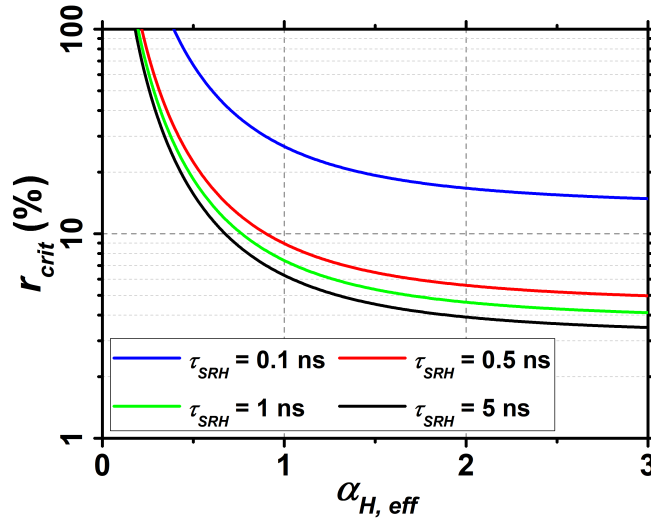


Fig. 5.12 Critical feedback level r_{crit} as a function of the effective α_H -factor for $\tau_{SRH} = 0.1, 0.5, 1$ and 5 ns, respectively.

Fig.5.12 gives the computed values of the critical feedback level as a function of the α_H -factor for different τ_{SRH} of 0.1, 0.5, 1 and 5 ns, respectively. Although the SRH is also expected to affect the α_H -factor, it is assumed here that the dominant contribution of such non radiative contributions in Eq.5.21 remain on the damping factor $K \times f_{RO}^2 + 1/\tau_c'$. Parameters used for the simulations are $\tau_{in} = 23$ ps, $f_{RO} = 3$ GHz, $K = 1$ ns, $C_l = 0.3$, $\tau_c = 1.5$ ns [157]. Besides, it has to be noted that as the simulations are conducted above threshold, the α_H should be most likely considered as an effective parameter which is for QD lasers strongly influenced by nonlinear gain effects and the off-resonance lasing states [54, 73]. Results show that the critical feedback level is strongly affected by the SRH recombinations. Hence for $\alpha_H < 1$, the onset of the instabilities is up-shifted by several order of magnitude. For instance, for $\alpha_H = 1$, r_{crit} increases from 6% to about 27% when the SRH recombination lifetime is

shortened. In a recent paper, it has been shown that the SRH recombination plays a role in the QD lasers on silicon degradation. The bias current accelerates a degradation process that involves the diffusion of defects toward the active region of QD lasers on silicon. As the concentration of defects increases within the active region leading to the increased SRH recombination rate, the threshold current increases and the injection efficiency is reduced [30].

5.2 Experimental optical feedback apparatus

Now, we experimentally analyse the optical feedback dynamics in InAs/GaAs QD Fabry-Perot (FP) lasers epitaxially grown onto silicon. The details on the growth process can be found in the Chapter 4. In the experiment, both coherent and incoherent optical feedback are considered in this section. In the former configuration, as the back-reflection originates from the laser itself, the influence is quantitatively investigated; while for the latter configuration, since the ASE noise is independent of the laser operating conditions, the affection of the feedback is qualitatively studied.

5.2.1 Coherent optical feedback setup

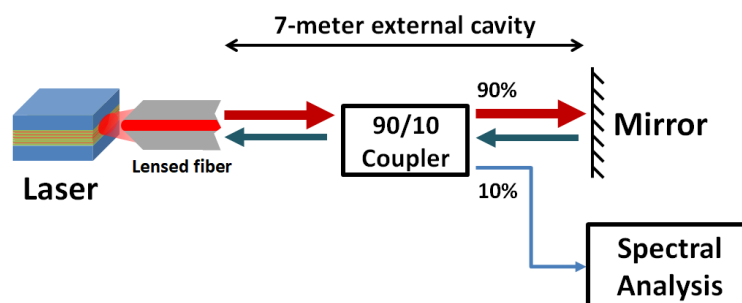


Fig. 5.13 Schematic representation of the setup for coherent optical feedback setup.

The setup to characterize the effects of the coherent optical feedback is schematically represented in Fig.5.13. The emission from the QD laser front facet is coupled with an anti-reflection (AR) coated lens-end fiber, and through the same interface, part of the light is reflected in the fiber back to the laser cavity from a distance of around 7 m away, which corresponds to an external cavity frequency of 14 MHz. Even though a photonic integrated circuit does not experience such long delay optical reflections, this configuration is studied here because it corresponds to the most stringent feedback conditions for the laser. In other words, using a long delay is more pertinent to fully evaluate the potential of the QD laser on

silicon against parasitic reflections. On the feedback path, 90% coupled power is directed to the backreflector (BKR) that consists of a mirror and a variable optical attenuator (VOA). The amount of return power is controlled and quantified by the feedback strength r_{ext} , defined as the ratio between the reflected power and free-space emitting power at the front facet. A polarization controller is inserted in the feedback path to compensate the fiber dispersion in the external cavity and to maximize the effects of the optical feedback namely to have the reflected light in the transverse electric (TE) polarization. As for the feedback phase, since the laser operated within the long-delay configuration where $f_{RO} \gg f_{ext}$ with $f_{ext} = 1/\tau_{ext}$ being the external cavity resonance frequency and f_{RO} being the relaxation oscillation frequency, thus the impact of the phase is negligible [255]. In our work, the achievable range of r_{ext} is from 0% to about 20% and the variation depends on the coupling ratio of the laser emission in the fibre. The losses from the fiber coupling and in the fiber setup are taken into account to accurately calculate r_{ext} , for which the uncertainty is less than 0.1%. The remaining power is then sent to optical and electrical spectrum analyzers to monitor the spectral evolution as r_{ext} varies.

5.2.2 Incoherent optical feedback setup

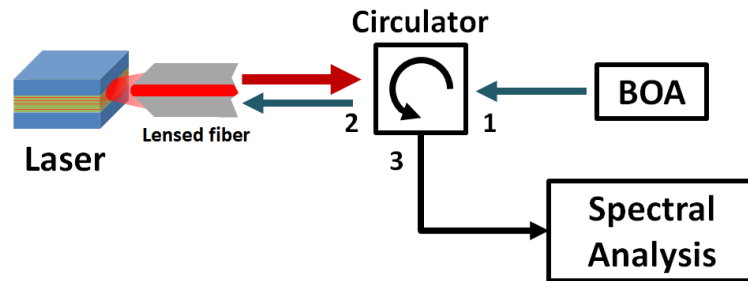


Fig. 5.14 Schematic representation of the setup for incoherent optical feedback setup.

For the incoherent feedback case, the large span of ASE noises interferes with multiple cavity modes and hence can be destructive to the laser performance. To investigate how the QD lasers respond to such incoherent light, we used a booster optical amplifier (BOA) as a source of ASE noise, which is directly injected into the laser cavities through an optical circulator. The corresponding setup is depicted in Fig.5.14. The strength of the ASE injection is controlled through the bias current onto the BOA, and quantified using the ratio (r_{BOA}) between the power from the BOA that has reached the laser facet and the free-space power of the laser, i.e. similar to the definition of r_{ext} . At the end line, the spectral behaviors in both optical and radio-frequency (RF) domain are equally analyzed.

5.2.3 High speed setup with optical feedback

The coherently fed-back laser source is then introduced to a fiberized transmission line that includes a Mach-Zehnder external modulator and a 2 km long single mode fiber coil, as represented in Fig.5.15.

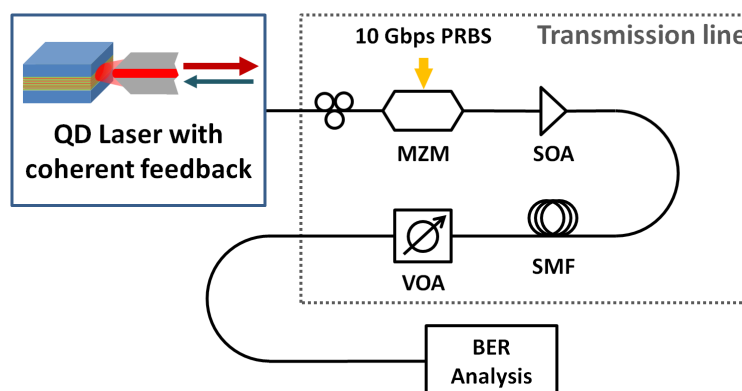


Fig. 5.15 External modulation transmission experiment with optical feedback apparatus. MZM: Mach-Zehnder modulator; SOA: semiconductor optical amplifier; SMF: 2 km long single mode fiber coil; VOA: variable optical attenuator.

The power from the fed-back laser source is amplified by a semiconductor optical amplifier (SOA), and then guided to a Mach-Zehnder modulator (MZM). The modulation format is 10 GHz non-return-to-zero (NRZ) PRBS with a sequence length of $2^{31} - 1$ and the peak-to-peak modulation amplitude V_{pp} is 2V. The output from the MZM is again amplified and injected into a 2 km single-mode fiber (SMF) coil. Alternatively, when it comes to the case of the QW laser, the SOAs are replaced with Erbium-doped fiber amplifiers (EDFA), and the emission is filtered with a bandpass filter of 13 nm before being injected into the MZM. In the end, an error detector (ED) is connected to characterize the bit error rate (BER) and hence the transmission performance. In addition, a high-speed oscilloscope is also used for capturing the eye-diagram.

5.3 Impact of the ES transition on feedback dynamics

5.3.1 Laser static characteristics

The QD lasers studied in this section are from the same bar meaning that the gain media is the same for all devices. The cavity size is 1 mm long in length and $3.5 \mu\text{m}$ in width, with 7 layers of InAs/GaAs QDs in the active region. The threading dislocation density (TDD) of the buffer layer was $3 \times 10^8 \text{cm}^{-2}$ and quantum dot density was $3 \times 10^{10} \text{cm}^{-2}$. Details on

the epitaxial growth process can be found elsewhere [158]. The facets of the 1 mm cavity were coated with 8 pairs and 1 pair of high-reflectivity (HR) films to achieve 95% and 55% reflectivity, respectively.

Typically, QD lasers show three possible regimes of lasing operation, depending on the bias conditions: (I) ground state (GS) lasing; (II) dual state emission showing an interplay dynamic between GS and the first excited state (ES), and (III) first ES lasing [13]. Tab.5.1 presents a list of the main parameters associated to the different QD devices such as, from top to bottom, the ridge width, the threshold currents for each lasing state namely (I_{th}^{GS} and I_{th}^{ES}), the ratio of the ES-to-GS lasing threshold ratio I_{th}^{ES}/I_{th}^{GS} , the peak wavelength for each lasing states namely ($\lambda_{gainpeak}^{GS}$ and $\lambda_{gainpeak}^{ES}$), and the GS-ES energy separation. Although the devices exhibit a different ratio I_{th}^{ES}/I_{th}^{GS} , they all have a similar GS-ES separation of about ~ 40 meV.

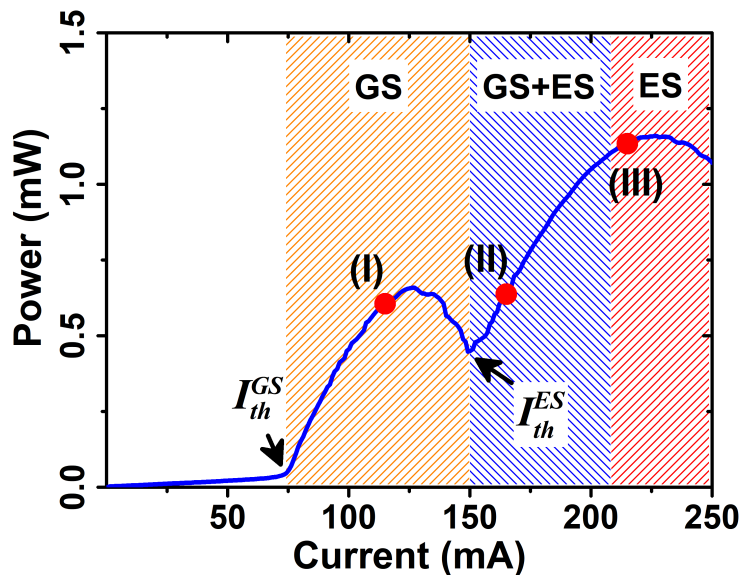


Fig. 5.16 Light-current characteristics of laser #4. The red markers correspond to the optical spectra depicted in Fig.5.17.

Fig.5.16 displays the light-current (LI) characteristics of QD laser #4. The different regimes of operation in QD lasers can be identified with the two thresholds related to the GS and ES transitions respectively. When the ES stimulated emission appears, a decrease of the GS slope efficiency is observed.

Note that the red markers stand for bias levels used for optical spectra measurements as shown in Fig.5.17. At low bias, it is clear that the laser emits on the GS transition, then moves to the dual state-lasing operation, and finally operates solely on the ES lasing state due to the GS quenching.

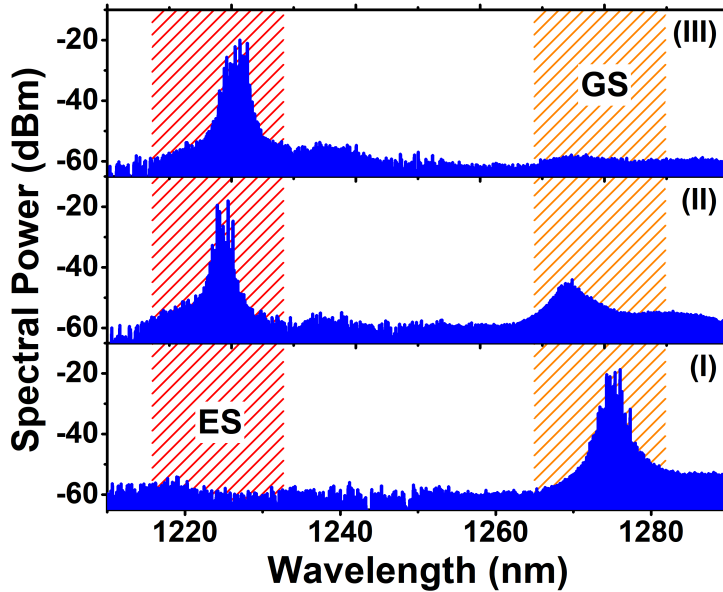


Fig. 5.17 Optical spectra measured for QD laser #4: (I) GS lasing, (II) GS-ES dual state lasing, (III) ES lasing. The bias conditions correspond to the red markers reported in Fig.5.16.

From the Tab.5.1, QD laser samples can be categorized into two groups depending on their ES-to-GS lasing threshold ratio. QD lasers #1 and #2 have a large ES-GS contrast while that of devices #3 and #4 is lower. This difference can be explained from the spectral-hole-burning-induced gain compression. Indeed, although the net gain at the GS is clamped at threshold, the carrier density at the ES keeps growing due to spectral hole burning [73]. Thus, depending on the geometry of the waveguide, the gain compression effect is enhanced, leading to an effective gain compression coefficient, which can influence the onset of ES lasing. Also, it has to be noted that QD lasers with low GS threshold currents exhibit a better ES-GS contrast due to less thermal effects [69]. Possibly, Tab.5.1 shows that the different threshold ratios of GS and ES can also be used as a hint for probing the different internal carrier dynamics among a set of QD lasers.

As all regimes of operation can be observed with those QD lasers, it is possible to analyze the sensitivity to optical feedback and in particular the influence of the ES. One parameter driving the optical feedback dynamics is the α_H -factor. In the specific case of QD lasers, it has been shown that a large inhomogeneous broadening as well as the presence of the off-resonance lasing states contribute to enhance the effective α_H -factor measured above the laser's threshold [73, 273]. As an example, the spectral dependence of the α_H -factor of QD lasers #2 and #3 are extracted from amplified spontaneous emission (ASE) method in the sub-threshold operation [274]. After a proper elimination of the thermal effects (see Chapter4), Fig.5.18 depicts values of about 0.55 and 0.65 respectively at the gain peak which

Table 5.1 Parameters of the InAs/GaAs QD lasers including from top to bottom, the ridge width, the threshold currents, the ES-to-GS lasing threshold ratio, the peak wavelength, and the GS-ES energy separation.

Device	#1	#2	#3	#4
Ridge Width (μm)	3.5	3.5	3	3
I_{th}^{GS} (mA)	46	50	63	74
I_{th}^{ES} (mA)	261	274	169	149
I_{th}^{ES}/I_{th}^{GS}	5.7	5.5	2.7	2
$\lambda_{gainpeak}^{GS}$ (nm)	~ 1280	~ 1280	~ 1270	~ 1270
$\lambda_{gainpeak}^{ES}$ (nm)	~ 1230	~ 1230	~ 1220	~ 1220
GS-ES energy separation (meV)	~ 40	~ 40	~ 40	~ 40

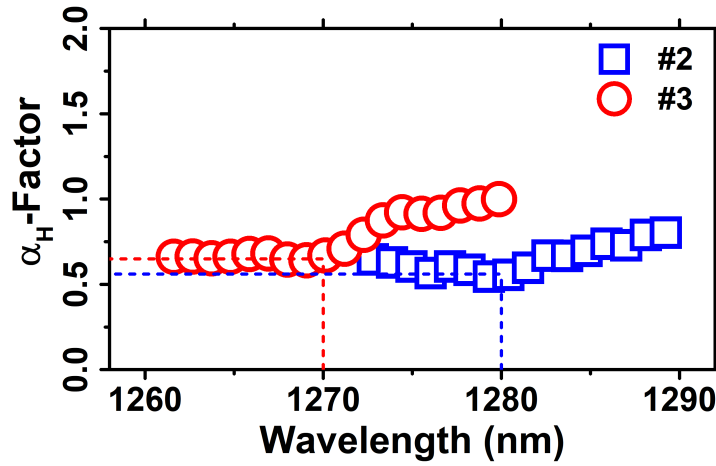


Fig. 5.18 Spectral dependence of the α_H -Factor measured by amplified spontaneous emission (ASE) in QD lasers #2 and #3.

are both smaller than those previously reported on InAs/GaAs QD lasers [99]. Such a low α -factor is an excellent prerequisite for improving the feedback resistant (see Eq.5.17) of QD lasers grown on silicon and results from the large QD size uniformity in the active region [54, 196].

5.3.2 Maximum optical feedback tolerance

To start with, let us investigate the optical feedback dynamics of a QD laser having a high ES-GS contrast.

Fig.5.19(a,b) depicts the optical and radio-frequency (RF) spectra of QD laser #2 in the free-running conditions $r_{ext} = 0$ (black ones) and under $r_{ext} = 20\%$ optical feedback (blue ones) at a bias condition of $2 \times I_{th}$. At this bias level, the laser emits before the occurrence of

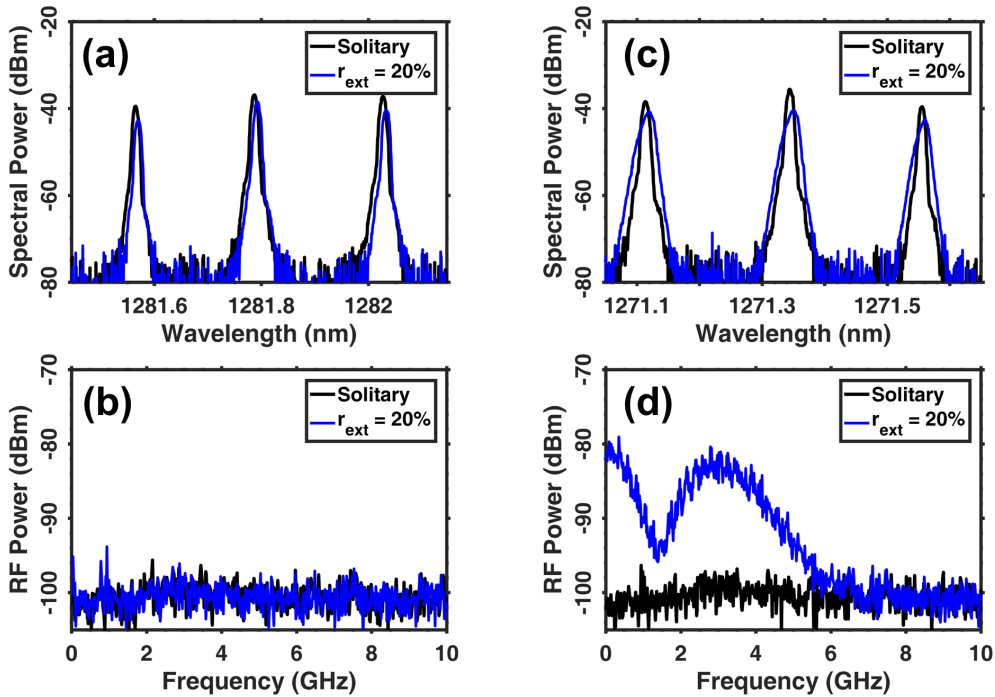


Fig. 5.19 Optical and RF spectra for QD laser #2 (a,b) and #3 (c,d) operating in the free-running $r_{ext} = 0$ (black) condition and under $r_{ext} = 20\%$ optical feedback at $2 \times I_{th}$.

the ES. As noticed, even at a very high value of r_{ext} , the laser stability is maintained. Apart from a slight wavelength shift, no sign of distortion is observed on the FP modes, and the corresponding RF spectrum remains flat without any visible periodic or chaotic oscillations. The QD laser is shown in this case quasi-insensitive to optical feedback taking into account the fact 20% of light reinjected into the laser is already much larger than any typical reflection levels taking place in a transmission system. Such feedback resistance up to 20% is higher than the tolerance level previously reported in GaAs-based QD lasers [199, 102], and is very promising for the conception of isolator-free on-chip optical transmitters. To illustrate the feedback sensitivity of QD laser with a low ES-GS contrast, Fig.5.19(c,d) represents the optical and RF spectra of QD laser #3 taken at $2 \times I_{th}$, i.e. the same bias level as for QD laser #2, namely, below the onset of the ES transition. Compare to Fig.5.19 (a,b), the behavior of this laser is fundamentally different. Without optical feedback, the longitudinal FP modes are not altered. However, at high feedback strength ($r_{ext} = 20\%$), the FP modes are significantly broadened which is the signature of a chaotic behavior as confirmed by the broadband RF spectrum. The low-frequency part below 2 GHz is attributed to partition noise coming from the multimode behavior whereas beyond the magnitude of the chaotic bandwidth is mostly driven by the relaxation oscillation QD frequency [257]. As a conclusion, although the QD lasers

share the same gain medium, it turned out that the responses to optical feedback are found not much alike. As it will be discussed in what follows, this difference is attributed to the ES-to-GS threshold ratio and how fast the ES switching dynamics takes place with respect to the bias current operation.

5.3.3 Dynamical routes

To clarify the optical feedback dynamics of QD laser #3, Fig.5.20 shows the optical and RF mapping spectra as a function of the feedback strength r_{ext} ranging from 0% to 15%. The first column depicts the evolution of the gain peak longitudinal mode whereas the second shows the dynamical route in the RF domain. To cover the different regimes of operation, three different bias currents are considered: $2\times$, $2.85\times$ and $3.75\times I_{th}^{GS}$ respectively. First, Fig.5.20(e) shows that the modal broadening corresponding to the critical level takes place at $r_{ext} = 5.6\%$ which is slightly different than that is observed in Fig.5.20(f) in which the destabilization appears at $r_{ext} = 7\%$. Such difference can be due to the detection path from which only 10% of the lasing beam is coupled into the optical fiber, therefore the amount of optical power transmitted to the spectral analyzers is weaker. Thus, extracting the critical feedback level r_{crit} from the green vertical dashed lines through the optical spectral maps in Figs 5.20(a)(c) and (e) allow to locate the critical levels for QD laser #3 at 2%, 1% and 5.6% respectively. These results indicate that once the ES transition has passed, the resistance to optical feedback increases. However, while approaching the GS-ES dual state lasing regime, the laser stability originally emitting on the GS is affected. In this interplay regime where the laser moves from the GS to the ES, a route to chaos with a higher complexity is observed as compared to the feedback-induced dynamics from the sole lasing states operation.

5.3.4 Impact of the ES-GS contrast

To verify the previous assumptions, similar measurements are now performed onto the other devices with respect to the bias level. Fig.5.21 depicts the extracted r_{crit} as a function of the bias level normalized to the ES threshold current I/I_{th}^{ES} for QD lasers #1, #2, #3, and #4. Overall, the same behavior is observed hence the evolution of r_{crit} strongly depends on the ES-to-GS threshold ratio. For $I/I_{th}^{ES} < 1$, the laser exhibits its higher resistance to optical feedback at low biases because only the GS lasing occurs. As the bias current increases, the critical feedback decreases due to the progressive occurrence of the ES. For instance, in case of QD laser #1, r_{crit} collapses from 12% down to 2.5%. Note that the decrease of the critical feedback level with the bias current is in agreement with a prior work performed on InAs/GaAs QD lasers [99, 74]. Surprisingly, once the ES emission occurs ($I/I_{th}^{ES} > 1$),

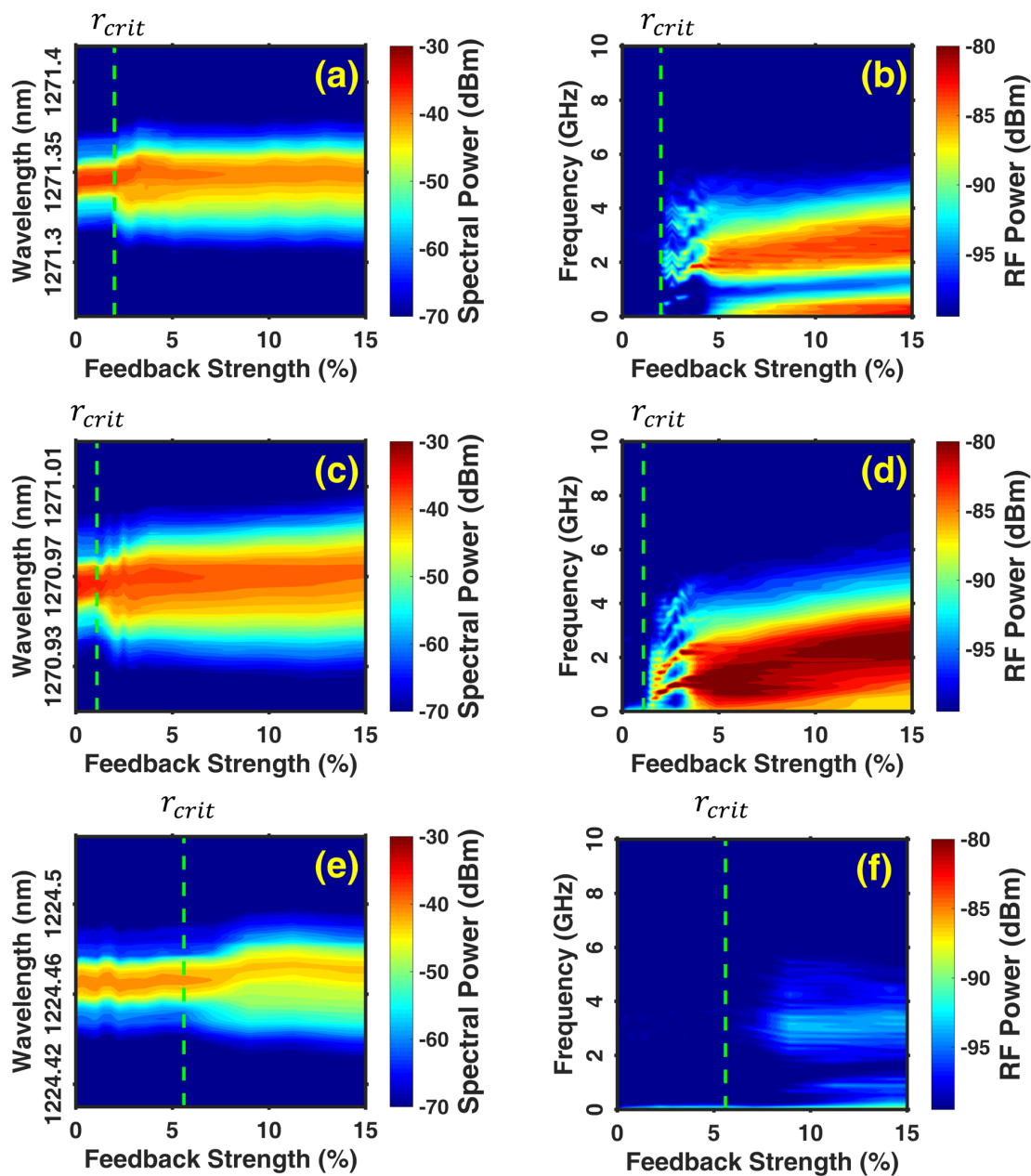


Fig. 5.20 Optical (first column) and RF (second column) spectra mappings of QD laser #3 measured at $2 \times$ ((a),(b)), $2.85 \times$ ((c),(d)) and $3.75 \times I_{th}^{GS}$ ((e),(f)) bias. The green lines mark the critical feedback levels (r_{crit}).

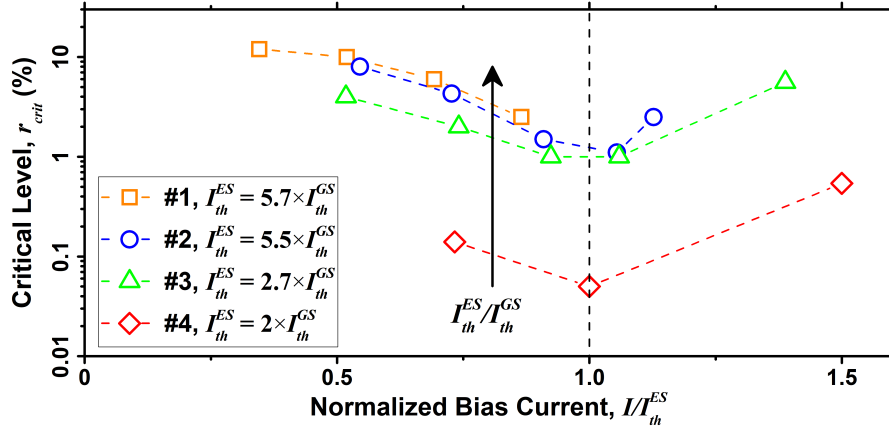


Fig. 5.21 The critical feedback level r_{crit} for QD lasers #1, #2, #3, and #4 (with different ratio I_{th}^{ES}/I_{th}^{GS}) plotted as a function of the ratio of the bias current to the ES lasing threshold I/I_{th}^{ES} .

Fig.5.21 shows a change in the laser dynamics, since the critical feedback level re-increases with the bias current as for single mode lasers and contributes somewhat to restabilize the laser. Fig.5.21 also confirms from the black arrow that a large ratio I_{th}^{ES}/I_{th}^{GS} increases the laser stability. For instance, at $0.7 \times I_{th}^{ES}$, the values for r_{crit} between QD laser #1 and #4 differ by a factor of 60, namely they are respectively of 6% and 0.1%. As shown previously, in the ultimate case for which the QD laser remains on GS transition whatever the bias current ($I_{th}^{ES}/I_{th}^{GS} \rightarrow \infty$), a high stability associated to a chaos-free operation can possibly be observed [101]. We can conclude that this change in the dynamics is most likely related to the carrier filling in the ES which balloons the α_H associated to the GS transition, hence leading to a reduction of the critical feedback level [73, 179]. Then, once the laser operates on the sole ES, the differential gain becomes larger, hence re-increasing the critical feedback level through a reduction of the α_H associated to the ES transition [13, 88, 251]. On the top of that, it is important to stress that, once the laser is on the sole ES transition, any further increase of the pump current also raises the damping accordingly, resulting in the restabilization of the lasers against optical feedback [186, 207]. Although such a higher feedback resistance should also slow down the modulation dynamics, it has been shown that an ES QD laser can, however, exhibit faster speed under direct modulation owing to larger differential gain and less gain nonlinearities [13]. To sum, these experimental results prove that in FP lasers, the ES-GS contrast is of paramount importance for the laser stability, meaning that the ratio of the GS and ES thresholds can be used as a figure of merit to evaluate the reflection sensitivity of such lasers.

5.4 Effect of the p-doping on the reflection sensitivity

5.4.1 Coherent optical feedback

In order to investigate the effect of the p-doping on the optical feedback sensitivity, we compare the dynamics between the undoped and p-doped lasers with doping level of $5 \times 10^{17} \text{ cm}^{-3}$. Compared with the QD lasers in previous section, the TDD is reduced from $3 \times 10^8 \text{ cm}^{-2}$ to $7 \times 10^6 \text{ cm}^{-2}$, which resulting in a record low linewidth enhancement factor as low as 0.13 [54]. Other structure details can be found in chapter 4. From Eq.5.17, compared to QWs, we can expect an improvement of optical feedback resistance in QDs, owing to stronger damping and possibly the smaller α_H . As in a real laser structure, the propagating optical field penetrates into the cladding regions surrounding the active layer, the nominal value of the α_H used in Eq.5.17 should actually be expanded by $1 + \eta$ with $\eta = G\lambda / (2\pi n_e)$ where G is the material gain per unit length, λ the lasing wavelength, and n_e the effective index [206]. Taking into account the for the QD lasers under study, the material gain is about a few hundreds of inverse centimeters, it is found that $\eta < 1$ and the α_H should be pretty constant above threshold [290, 291]. At this point, it is somewhat important to stress that this correcting factor remains minimalist in a sense that it does not incorporate the effects of the gain compression and the higher-energy states which are known to play a key role in the evolution of the α_H with the bias conditions. In order to illustrate this feature, the α_H was measured at $3 \times I_{th}$ at 293 K using optical injection method as presented in Chapter 4. At $3 \times I_{th}$, the α_H -factor is found around 2 for the undoped laser while it is reduced down to 1.3 for the p-doped one. The critical level for the p-doped laser is found more than 4.2 dB above that of the undoped one, and remains above whatever the pumping conditions since the α_H and γ remain unchanged against temperature variations.

To qualify the influence of p-doping on QD lasers subjected to optical feedback, first, the impact of static optical feedback is studied without considering the modulation nor the transmission, hence allowing us to unveil how the optical feedback does affect the spectral properties both in optical and radio-frequency (RF) domains. In order to properly probe the advantages of the QD laser on silicon, a commercial QW FP laser is also used as a reference laser. The room temperature threshold of the QW laser is at 28 mA, while the gain peak wavelength is centered at 1541 nm, with a corresponding α_H -factor of about 2.8. In this section, all lasers dynamic response under feedback is studied at $3 \times I_{th}$.

Fig.5.22 depicts the spectral evolution of both QD and QW lasers along with the increase of r_{ext} at $3 \times I_{th}$. The first row shows the mapping in the optical domain whereas the second is the RF one. As shown in Fig.5.22(a), the QD laser on silicon demonstrates a remarkable stability against optical feedback whatever the feedback strength. Only a slight red-shift of

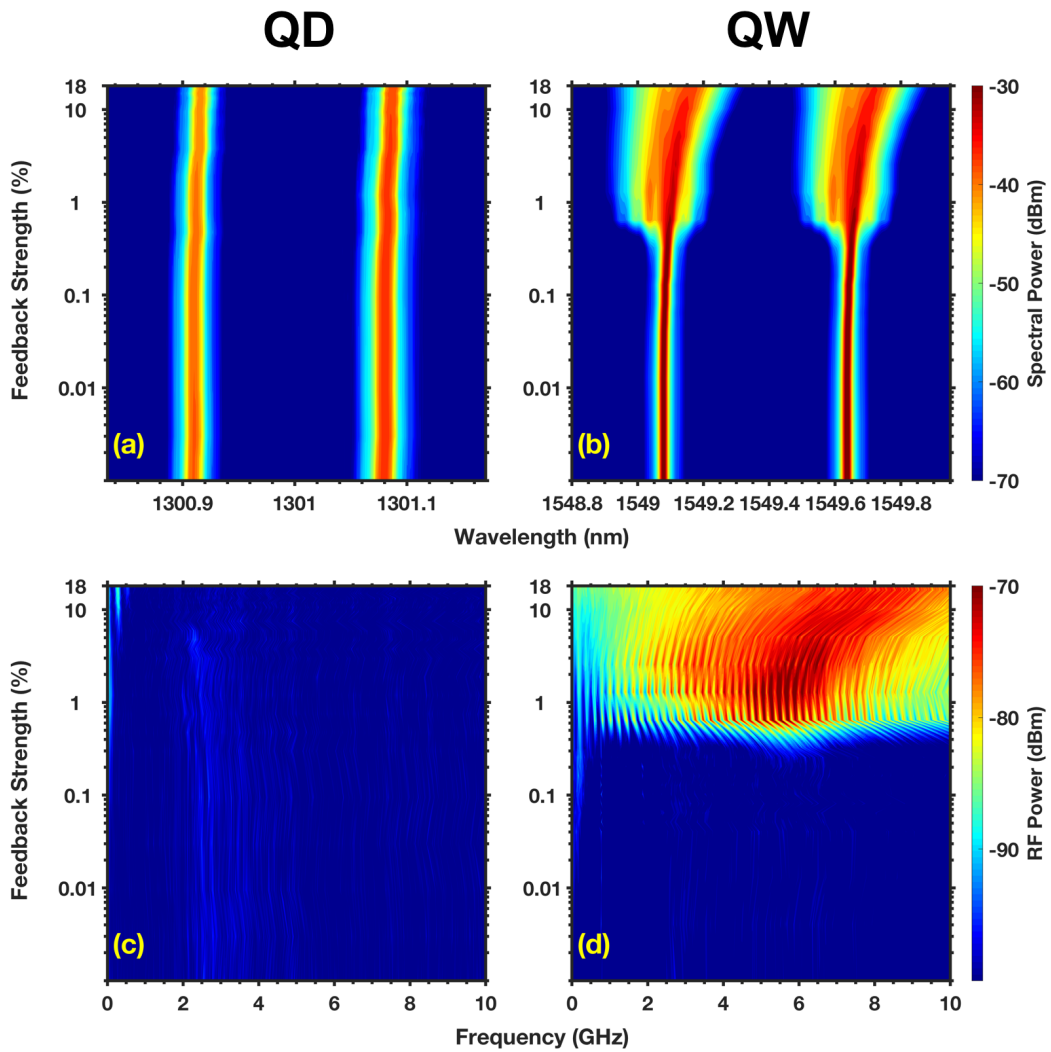


Fig. 5.22 (a) Optical and (c) RF spectral mappings of the p-doped QD laser on silicon as a function of the feedback strength at $3 \times I_{th}$; (b) Optical and (d) RF spectral mappings of the QW laser as a function of the feedback strength at $3 \times I_{th}$. The vertical axis is in logarithmic scale.

the modal wavelength is observed while the RF response in Fig.5.22(c) does not show any sign of nonlinear oscillations. At this stage, the laser displays a chaos-free operation meaning that the coherence collapse state taking place beyond the critical feedback level does not show up in the range of feedback level considered in the experiment. Note that this statement remains perfectly valid even at $6 \times I_{th}$. Compared to [199], the QD lasers on silicon used in this section exhibit a stronger stability against optical feedback because the experiment is performed under the long delay regime which is the most stringent feedback condition [153].

As for the QW laser, the device is not disturbed until 0.3% (i.e. -25 dB) which corresponds to the critical level associated to the onset of the undamping of the relaxation oscillations. A critical feedback level of -25 dB is similar to prior observations made with QW lasers [78]. At higher feedback levels, the laser starts experiencing the route to chaos through coherence collapse with strong broadening of the FP modes (Fig.5.22(b)) and intense chaotic oscillations in the RF domain (Fig.5.22(d)). Any further increase of the feedback strength leads to a more complex chaos (i.e. fully developed coherence collapse) then to a restablization [214]. In this work, these regimes were not all observed due to the induced loss in the long delay experiment.

However, it is worth noting that the front facet reflectivity can contribute to strongly degraded feedback tolerance in QD laser. From Eq.5.17, it is clear that a high output facet reflectivity R reduces the C_l hence leading to a high critical feedback level r_{crit} .

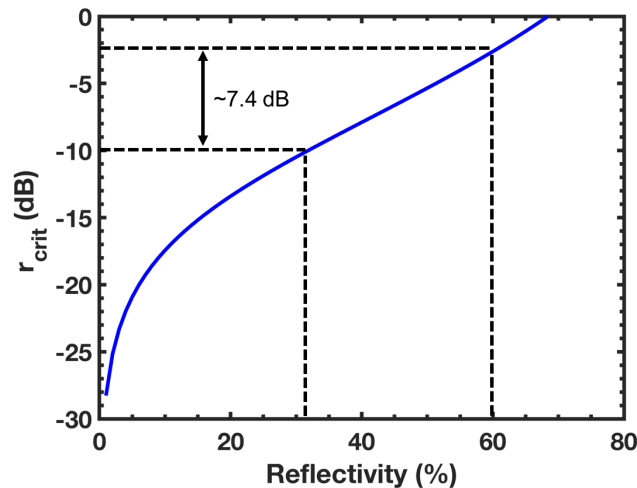


Fig. 5.23 Critical feedback level (r_{crit}) as a function of the reflectivity. The black dotted lines indicate the lasers with facet reflectivity of cleave/99% and 60%/99%.

Fig.5.23 shows the simulated r_{crit} for the p-doped QD laser as a function of R considering the α_H is 1.3 and γ is 25 GHz at $3 \times I_{th}$ as well as τ_{in} is 31.5 ps. As shown, the r_{crit} decreases from -2.6 dB with output facet reflectivity of 60 % to - 10 dB with that of 32 %, which

corresponds to the reflectivity of a cleaved facet. While the rear facets keep a reflectivity of 99 %. Therefore, in order to confirm that the high stability against optical feedback is not total from the high front facet reflectivity, a QD laser with the cleaved output facet while the rear facet having a coating reflectivity of 99% is also performed under optical feedback (cleave/99%). This laser made with the same material as the laser used asymmetric facet coatings of 60%/99%, and the structure (cavity length and ridge width) also keeps the same.

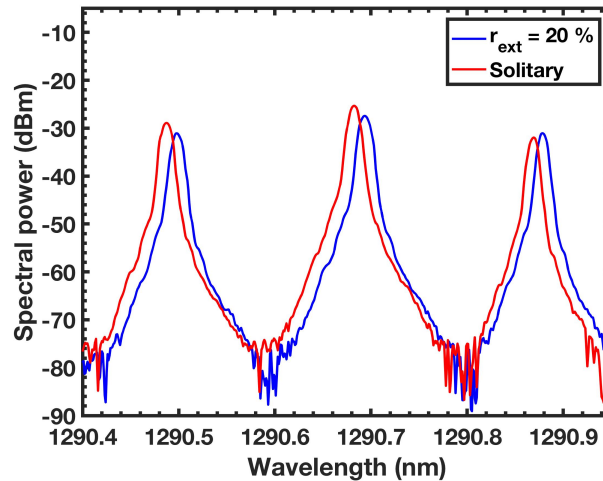


Fig. 5.24 Optical spectra under free-running (red) and 20% (blue) of total reflection.

Fig.5.24 displays the optical spectra under free-running (red) and 20 % of total feedback (blue). The laser remains perfectly stable even under strong optical feedback for which no sign of broadening is observed. Overall, the laser is found totally insensitive to optical perturbations even with cleaved output facet, in this case, the laser cavity is more open to outside world.

Now, the influence of the p-doping on the thermal stability and the optical feedback sensitivity is discussed. In order to properly compare the feedback dynamics between the undoped and p-doped lasers, the range of r_{ext} is fixed from 0% to 16%. The remaining power is then sent to optical and electrical spectrum analyzers to monitor the spectral evolution as r_{ext} varies. Fig.5.25 displays the corresponding feedback dynamics both in the radio-frequency (RF) and optical domains and for two different temperatures (293 K and 303 K). The first column depicts the behaviors of the undoped QD laser and the second for p-doped one. The lower temperature of 293 K is presented in first and third rows whereas the second and fourth rows correspond to 303 K. First, we focus on the upper half of the figure, where the four plots depict the RF spectral maps as a function of r_{ext} . As shown, whatever the feedback strength within the tested range, both lasers remain stable without developing any sign of nonlinear oscillations hence, the RF spectral maps imply that both devices exhibit strong

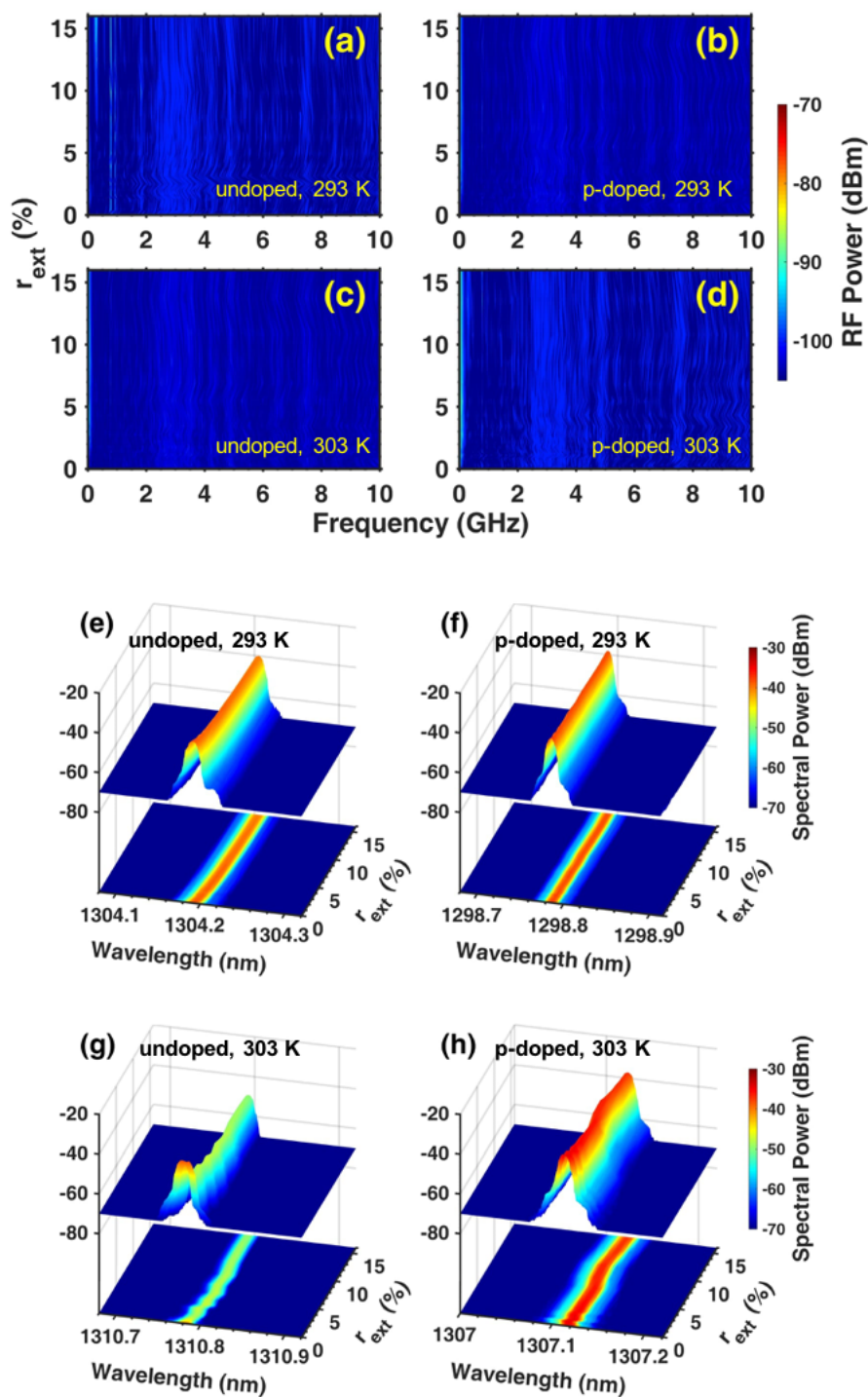


Fig. 5.25 RF and optical spectra for the main longitudinal mode (gain peak) as a function of r_{ext} for the undoped laser at 293 K ((a), (e)) and 303 K ((c), (g)), as well as for the p-doped laser at 293 K ((b), (f)) and 303 K ((d), (h)). The bias current is fixed at $3 \times I_{th}$ for all subplots.

resistance to the back-reflections until the maximum feedback value of $r_{ext}=16\%$ (-8 dB). Such remarkable feature is mainly attributed to the large damping effect which contributes to the suppression undamped relaxation oscillations. Moreover, the α_H -factor is extracted at 2 for undoped laser and even lower at 1.3 for the doped one under the same bias condition of $3 \times I_{th}$. Together, along with the careful optimization of the inhomogeneous broadening related to QD size dispersion[196], these features further enhance the laser stability.

Last but not the least, as mentioned before, the large excited-state to ground state threshold ratio (I_{th}^{ES}/I_{th}^{GS}) lift up the critical feedback level r_{ext} . Here, $I_{th}^{ES}/I_{th}^{GS} > 4.5$ for both devices, the results indicate a r_{ext} beyond -8 dB, while QW lasers typically exhibit a r_{ext} below -25 dB [52]. Nevertheless, although the lasers maintain stable dynamics in the RF domain, they can display distinguishable behaviors in the optical domain. Thus, the lower half of Fig.5.25 records the evolution of the main longitudinal FP mode (gain peak) for both temperatures as a function of the feedback strength. At 293 K, both QD devices remain stable with the increase of r_{ext} namely the FP modes are well preserved without spectral broadening as for the coherence collapse. Only a slight red-shift is observed for the undoped laser when increasing the feedback strength. At 303 K, the two QD lasers behave quite differently. Although both do not show coherence collapse operation, the undoped laser suffers from both intensity and wavelength fluctuations with the increment of r_{ext} whereas the p-doped laser mostly exhibit wavelength fluctuations.

Overall, the results suggest that the undoped laser has a lower tolerance to coherent optical feedback than the p-doped one. Such discrepancy is explained twofold. First, as shown in Fig.4.11 in Chapter 4, when increasing the temperature, the damping factor of the undoped laser exhibits a step down to a level below that of the p-doped one hence leading to a reduction of the laser's feedback insensitivity. In addition, the α_H -factor of the undoped laser was found around 0.30 at 293 K then to increase to 0.34 at 303 K, while it stays constant over temperature for the p-doped case [54]. Therefore, as far as the thermal stability is concerned, the undoped laser is not as good as the one with p-doping leading to a faster destabilization of the laser dynamics in presence of coherent optical feedback.

5.4.2 Incoherent optical feedback

For the incoherent feedback case, Fig.5.26 depicts the RF spectra of both devices in free-running and under incoherent optical feedback with $r_{BOA} = 40\%$. For each laser, the two RF spectra are perfectly overlapped, implying a remarkable insensitivity against ASE noise. The results proves that these QD lasers exhibit a superior resistance to any kind of reflections such as those coming from other on-chip active building blocks.

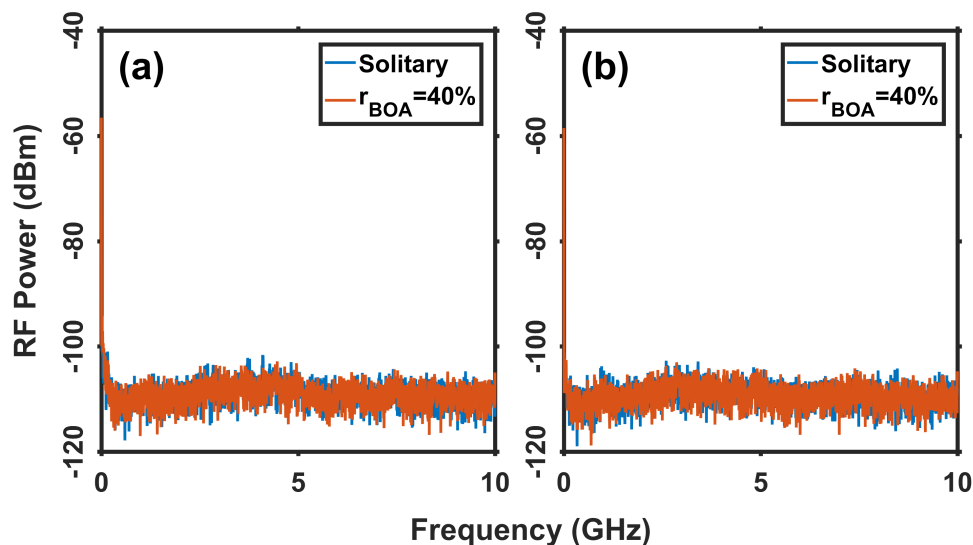


Fig. 5.26 RF spectra in free-running and under 40% incoherent feedback for (a) undoped and (b) p-doped lasers.

5.4.3 High-speed experiments with optical feedback

In the end, high-speed test bed experiments are performed with and without optical feedback. External modulation is preferred rather than direct modulation in order to avoid expanding the phase-space dynamics which would add another degree of freedom resulting in different feedback properties and the impossibility to properly compare the influence of the static optical feedback on the transmission performance.

Fig.5.27-5.30 depict the BER plots in term of received power for both the back-to-back configuration (red and blue colors) and after transmission (black and magenta colors) for four cases: undoped laser at (Fig.5.27) 293 K and (Fig.5.28) 303 K in free-running (square symbols) and under -8 dB maximal feedback (triangle markers); p-doped laser at (Fig.5.29) 293 K and (Fig.5.30) 303 K in free-running and under maximal feedback (-8 dB). For each case, the corresponding eye-diagrams are also presented. Whatever the configuration, BER plots between the free-running and the case for the highest feedback level (-8 dB) overlap each other, hence indicating an excellent stability in both lasers. Moreover, the temperature variation on this stage does not degrade the performances either, at 303 K, a BER in the order of 10^{-12} can still be achieved. This exceptional feature showing no increase of the power penalty with the optical feedback is in line with the initial measurements of the RIN [157]. From Eq.5.18, the noise power received at the photodiode is directly proportional to the RIN. We conclude that the power penalty of the QD lasers under study remains stable because the RIN is not enhanced with the feedback strength. Indeed, it is known that the latter is affected

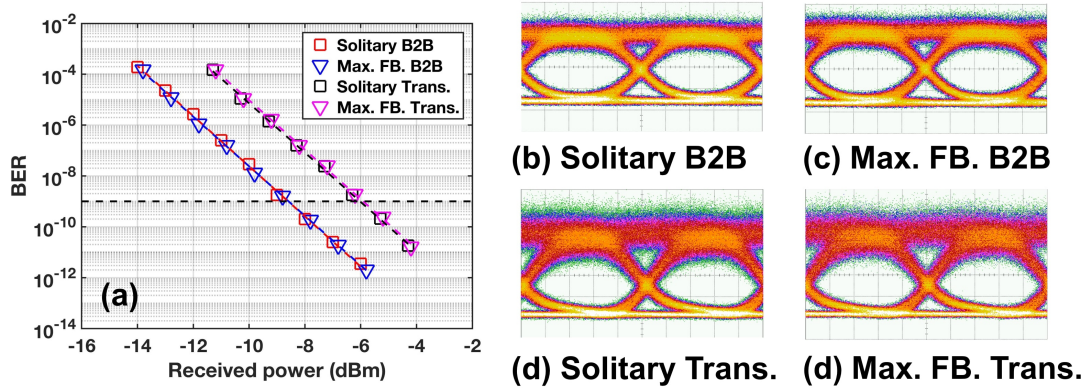


Fig. 5.27 BER plots for back-to-back (B2B) and after transmission (Trans.) with and without feedback (FB) for undoped device at (a) 293 K. (b) Eye diagram of the solitary laser and (c) with maximal feedback in B2B configuration. (d) Eye diagram of the solitary laser and (e) with maximal feedback after transmission. The maximal feedback level is at -8 dB and the bias current is fixed at $3 \times I_{th}$.

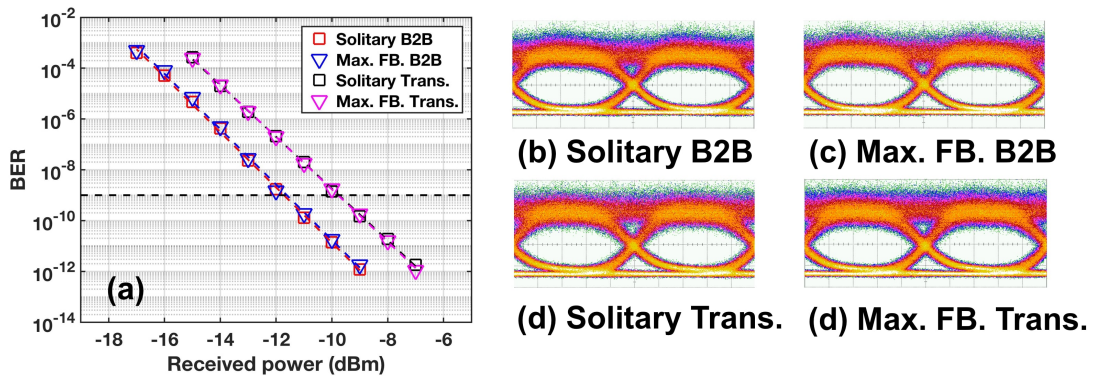


Fig. 5.28 BER plots for back-to-back (B2B) and after transmission (Trans.) with and without feedback (FB) for undoped device at (a) 303 K. (b) Eye diagram of the solitary laser and (c) with maximal feedback in B2B configuration. (d) Eye diagram of the solitary laser and (e) with maximal feedback after transmission. The maximal feedback level is at -8 dB and the bias current is fixed at $3 \times I_{th}$.

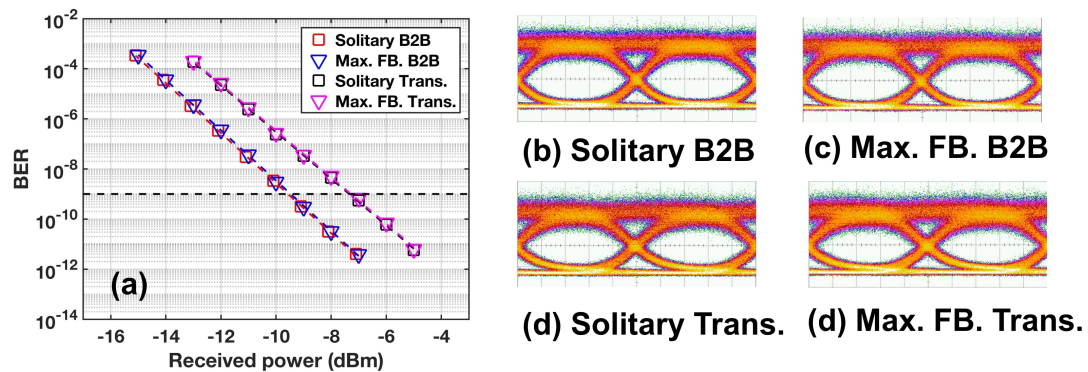


Fig. 5.29 BER plots for back-to-back (B2B) and after transmission (Trans.) with and without feedback (FB) for p-doped device at (a) 293 K. (b) Eye diagram of the solitary laser and (c) with maximal feedback in B2B configuration. (d) Eye diagram of the solitary laser and (e) with maximal feedback after transmission. The maximal feedback level is at -8 dB and the bias current is fixed at $3 \times I_{th}$.

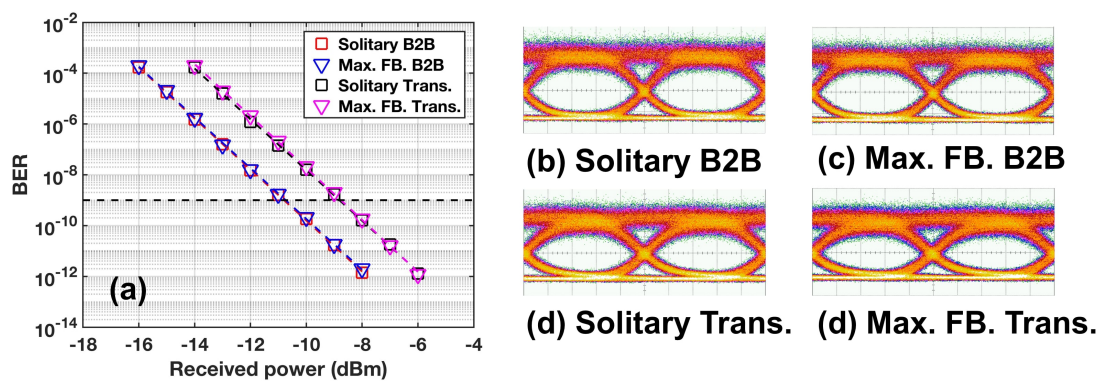


Fig. 5.30 BER plots for back-to-back (B2B) and after transmission (Trans.) with and without feedback (FB) for p-doped device at (a) 303 K. (b) Eye diagram of the solitary laser and (c) with maximal feedback in B2B configuration. (d) Eye diagram of the solitary laser and (e) with maximal feedback after transmission. The maximal feedback level is at -8 dB and the bias current is fixed at $3 \times I_{th}$.

by the optical feedback which is seen as an additional source of spontaneous emission in the laser cavity [276]. As the QD lasers under study do not reach the critical feedback level, both the RIN and the power penalty remain constant which is of first importance in a high-speed communication system [77].

Last but not the least, the results imply that these silicon-based QD lasers can also tolerate temperature fluctuation at least within the range under study. In addition, in all four figures, the power penalties after transmission are about 2 dB at 10^{-9} BER level, which can be attributed to the fiber chromatic dispersion and to residual ASE noises after the propagation through SOA. Let us stress out that, due to limitation in equipment, the amplified signal was not filtered, meaning that residual ASE noise from the SOA should be considered through the fiber coil. On the other hand, looking side by side at Fig.5.27 and Fig.5.28, a shrink of the power penalty is observed. This can be explained by the wavelength difference between the laser emission and the SOA gain spectrum whose centered position is about 1310 nm. As the undoped laser precisely operates around 1310 nm, the ASE noise level involved during the transmission is reduced, hence leading to a decrease in the power penalty. Overall, these results prove that both undoped and p-doped QD lasers directly grown on silicon are insensitive to external reflections. This statement is also confirmed by the eye diagrams, which keep open for B2B and after transmission with optical feedback. Although this exceptional feature remains true within the range of temperature variations, it is however highly promising for high-speed capabilities of such lasers in photonics integrated circuits.

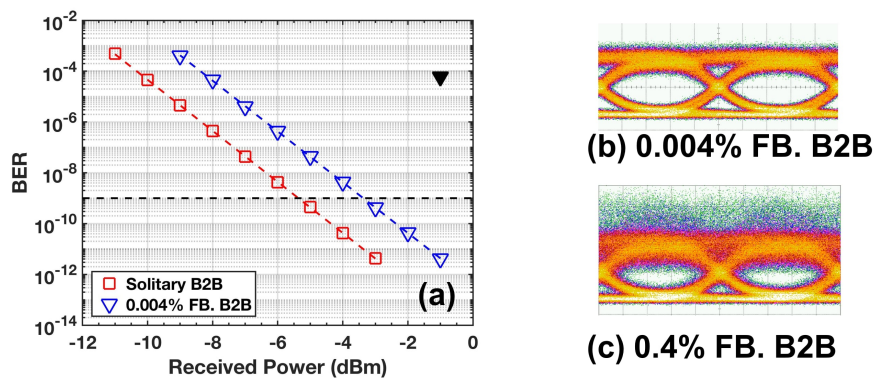


Fig. 5.31 B2B BER curves for solitary QW laser (red) and under 0.004% feedback (blue, eye-diagram in (b)). (c) eye-diagram of the laser under 0.4% feedback, above the critical level. The bias current is fixed at $3 \times I_{th}$.

Similar experiments are then performed for the QW laser. The corresponding BER plots are displayed in Fig.5.31 only for the B2B configuration. Biasing the laser in the stable regime e.g. below the critical feedback level (see in Fig.5.22(b)) with $r_{ext} = 0.004\%$ (i.e. -44

dB), the transmission performance is found already affected with a 2 dB power penalty at $\text{BER} = 10^{-9}$, despite that the eye-diagram remains opened (Fig.5.31(b)). Above the critical feedback level ($r_{ext} = 0.3\%$), the transmission performance is drastically degraded as shown in Fig.5.31(c). Thus, for $r_{ext} = 0.4\%$ (i.e. -24 dB), the laser operates in the coherence collapse regime in which the data transmission is no longer possible as also confirmed by the noisy eye diagram [78]. The corresponding BER value is measured at 6×10^{-5} for a received power of -1 dBm (black triangle marker), which is the power limit of the photodiode in the experiment under study. Nevertheless, this BER value being extremely large, a noise floor is definitely expected at higher received powers.

To sum, these results confirm the great stability of the QD laser on silicon as compared to the QW ones which is a peculiar feature for reflection insensitive transmissions on silicon chips. Such a remarkable feedback resistance results from various contributions. First, the low α_H -factor due to the high QD uniformity combined to the very large ES-to-GS lasing threshold preventing the occurrence of the ES emission [54]. Second, the shorter carrier lifetime due to the higher threading dislocation density (TDD) and epitaxial defects hence resulting in a higher damping [108].

5.5 Summary

In this section, we have experimentally investigated the optical feedback dynamics of QD lasers epitaxially grown on silicon. As opposed to QW lasers, the QD laser under study exhibits a large insensitivity to optical perturbations with about 20% of light back reflected to the facet. Our results also prove that critical feedback level strongly depends on the ES-to-GS lasing threshold ratio meaning that a laser having a fast switching dynamics with respect to the bias current is more subject to be highly destabilized by optical feedback. And then, both epitaxial undoped and p-doped QD lasers are found to exhibit a high tolerance to optical perturbations up to 16% of light back reflected to the front facet. The degree of feedback tolerance of the QD gain medium is highly dependent on the dot size variations, but through careful optimization, it is possible to minimize the inhomogeneous broadening meaning that even epitaxial lasers on silicon can achieve high performance suggesting their capability for isolator-free photonic integration. On the other hand, both device have shown remarkable robustness against ASE noise that could distribute all over a real photonic integrated chip. In the end, the transmission test performed at 10 Gbps demonstrates a power penalty-free operation with both QD lasers even under the strongest optical feedback. However, owing to its much lower α_H -factor, that the p-doped laser has a much higher potential for the two following reasons : First, its critical feedback level is analytically predicted almost 5 dB

higher than that of the undoped case and can be maintained constant with respect to the temperature; Second, the intensity noise, damping and spectral purity are all much better than that of the undoped case especially over temperature variations. To sum, although the price to pay with p-doping is the higher threshold, information displayed in this Chapter show that, overall, the p-doped QD laser performs better even under optical feedback. When p-doping is properly optimized, a higher gain and differential gain along with a reduced the α_H -factor is achieved hence improving high temperature lasing characteristics, reliability of QD lasers on silicon as well as intensity noise feedback properties. The results presented in this Chapter are useful for the realization of future on-chip reflection insensitive and thermo-electrical-cooler-free transmitters for isolator-free transmission in metro, access and data centers optical networks as well as for integrated photonics.

Chapter 6

Conclusions and perspectives

In this thesis, dynamics and nonlinear properties of QD lasers are investigated and analysed.

In the first place, we studied both experimentally and theoretically the frequency noise (FN), spectral linewidth and relative intensity noise (RIN) characteristics of InAs/InP QD DFB lasers. The theoretical simulations are based on a rate equation model including the Langevin noises and the contribution from the off-resonance energy levels. Results show that the carrier noise in the ground state (GS) and the excited state (ES) significantly increase the amplitude of the RIN, while the contribution of the carrier noise in the reservoir (RS) remains negligible. In addition, it is demonstrated that the ES carrier noise contribution can be suppressed by considering QD lasers with a larger GS-ES energy separation, hence leading to a substantial reduction of the RIN. On the other hand, simulations also point out that the carrier noise does not contribute that much to the FN which is determinant for narrow spectral linewidth operation as compared to what exists in quantum well (QW) or bulk lasers. In the measurement, a narrow spectral linewidth of 160 kHz (80 kHz intrinsic linewidth) is demonstrated in AR/HR QD laser owing to a low $n_{sp} \times (1 + \alpha_H^2)$. By comparison with QW lasers, the spectral linewidth is rather insensitive to the temperature with minimum values below 200 kHz between 283 K and 303 K, which also agrees well with simulation. Symmetric AR facet coatings are also used to reduce the longitudinal spatial hole burning and make the spectral linewidth rather independent of the drive current. However, a linewidth rebroadening is also observed at higher temperature, which is attributed to the spectral hole burning and to the variations of the α_H -factor with the temperature and bias current. Furthermore, the RIN of the AR/AR DFB laser is experimentally discussed. A low RIN of less than -150 dB/Hz is measured in the range of 8 to 10 GHz. Both the relaxation oscillation frequency and damping factor are extracted from the curve fitting of the RIN spectrum. By fitting the damping factor versus the squared relaxation oscillation frequency, the K -factor

is obtained with a value of 2.4 ns while the γ_0 is 4.3 GHz, showing that these lasers are not good for high-speed modulation but excellent for all other low noise related applications.

The second part of the thesis investigated the effect of p-doping on the RIN properties and subsequently on the modulation properties of epitaxial InAs/GaAs QD lasers on silicon. Owing to the low threading dislocations density and the p-modulation doped GaAs barrier layer in the active region, the RIN level is found very stable with temperature with a minimum value of -150 dB/Hz. The dynamical features extracted from the RIN spectra show that p-doping between 0 and 30 holes/dot strongly modifies the modulation properties and gain nonlinearities through increased internal losses in the active region and thereby hindering the maximum achievable bandwidth. Moreover, we report an ultra-low α_H -factor of 0.13 that is rather independent of the temperature range (288 K–308 K). Above the laser threshold, the α_H -factor does not increase extensively with the bias current. The below-threshold α_H -factor result was obtained from the amplified spontaneous emission (ASE), extracting the net modal gain change and longitudinal mode wavelength shift with the variation of the subthreshold current. Although this method has been used longly, it can sometimes possibly underestimate its value when thermal effects are not properly eliminated. Thus, we also performed the α_H -factor with a thermally insensitive method that relies on the evaluation of the gain and wavelength changes of the suppressed side modes by optical injection locking. Given that the method is thermally insensitive, the results show values of α_H -factor as low as 0.15, resulting from the low threading dislocation density and high material gain of the active region. Such results also confirm our initial measurements conducted with the ASE method, showing that pulse width of 0.1 μ s and duty cycle of 0 % have to be considered.

The last part of the thesis systematically investigated the influence of optical feedback in epitaxial InAs/GaAs QD lasers on silicon. The boundaries associated to the onset of the critical feedback level corresponding to the first Hopf bifurcation are extracted at different bias conditions with respect to the onset of the first ES transition. Results show that QD lasers directly grown on silicon are much more resistant to optical feedback than QW lasers. However, results also unveil that the onset of the critical feedback level strongly depends on the ES-to-GS contrast, hence a figure of merit showing that a small ratio of the ES-to-GS lasing thresholds is not beneficial for maintaining a high degree of stability. Furthermore, the impact of the p-doping on the high-speed performance subjected to optical feedback is also discussed. Experiments show that these QD lasers exhibit a very high degree of resistance to both incoherent and coherent optical feedbacks. 10 Gbps penalty-free transmissions are also unveiled under external modulation and at different temperatures. Results draw the attention on QD lasers with p-doping which exhibit a better thermal sensitivity, a lower α_H -factor, a higher critical feedback level, and a better spectral stability with less intensity noise.

Overall, We believe these novel results in the thesis are meaningful for designing future high speed and low noise QD devices. As aforementioned, narrow linewidth operation in QD lasers is important not only for coherent communication systems but also for high-resolution spectroscopy, high purity photonic microwave generation and on-chip atomic clocks. Last but not the least, the reflection insensitivity in QD lasers is useful for designing feedback resistant lasers for isolator-free transmission in metro, access, and data center optical networks, future photonics integrated circuits (PICs) on silicon as well as high performance computers.

Future works will be carried out in the following aspects:

1. First of all, the Wavelength Division Multiplexing (WDM) in datacom applications need DFB lasers to control the wavelength. The first InAs/GaAs QD DFB laser on silicon has been successfully demonstrated in 2018 by Wang *et al.* [278]. Although the spectral linewidth of InP-based QD laser has been measured in this thesis, it is worth investigating the spectral linewidth of GaAs-based or even silicon-based QD DFB lasers which are promising for future photonics integrated applications. Moreover, it is worth investigating directly modulated QD DFB lasers on silicon with on-off keying (OOK) format or even more complex with pulse amplitude modulation (PAM), which are important for future high-speed PICs [258]. Last but not the least, the InAs/InP QD single photon emitter is also one possible key component for future long-distance fiber based quantum communication networks [20].
2. Second, the epitaxial QD lasers on silicon in this thesis are operated in the O-band, while C-band silicon-based lasers are desired for long-haul communication owing to their low cost. Despite it is more challenging to directly grow InAs/InP QD laser on silicon due to the larger lattice mismatch between InP and silicon, Zhu *et al.* has successfully achieved InAs/InP QD laser epitaxially grown on silicon with pulsed current pumping [297]. The static and dynamical characteristics as well as nonlinear dynamic of such laser require further investigation.
3. Third, for the reflection sensitivity experiment, it is necessary to study the optical feedback dynamics in QD DFB lasers on silicon and the direct modulation experiments under optical feedback [108]. Compared with the long delay experiment performed in this thesis, the short-delay regimes ($f_{RO} \ll f_{ext}$) under optical feedback need to be explored, which is useful not only for isolator-free application but also for photonic microwave generation [101]. The influence of the SRH recombination on the feedback sensitivity of silicon-based QD laser needs to be performed because it is touted to affect

both the damping factor and the α_H -factor [295]. Next step will involve modeling the nonlinear dynamic including the SRH recombinations.

4. Fourth, the intensity noise and pulse oscillation characteristics of an InAs/GaAs QD laser epitaxially grown on germanium have also been studied during my PhD, this work is in cooperation with ShanghaiTech University, China and Shanghai Institute of Microsystem and Information Technology, China [294]. The laser shows a sub-threshold α_H of 2.5 at the gain peak. The minimum RIN of the laser is around -126 dB/Hz. When the laser is subject to optical feedback, the intensity noise is hardly affected except at the resonance or pulse oscillation peak. We also demonstrate that the laser pumped at high currents is more sensitive to the optical feedback. In addition, we unveil that the free-running Ge-based QDlaser exhibits self-sustained pulse oscillations, emerging from the undamped relaxation oscillations. The pulse oscillations exhibit one period or two periods, depending on the pump currents. The generation of the self-sustained pulse oscillation is qualitatively attributed to the Q-switching mechanism. Finally, we show that both the microwave power and frequency produced by the period-one oscillation increase with the pump currents, while the microwave linewidth is reduced down to about 1.0 MHz. Future work will theoretically investigate the self-sustained pulse oscillation behavior through numerical simulations, which can offer an in-depth insight on the corresponding physical mechanisms.
5. Last but not the least, the development of mid-infrared (MIR) silicon photonic is attractive since silicon is transparent up to approximately 8 and 15 μm hence leading to various applications in biochemical and environmental sensing, medicine, astronomy and MIR communications. On the one hand, quantum cascade lasers (QCL) emitting at wavelengths as short as 2.6 μm has been demonstrated [35]. On the other hand, the first QCL on silicon emitting at 4.8 μm is successfully achieved and operating in pulsed mode at room temperature [241]. Thus, the nonlinear dynamics of semiconductor lasers on silicon could be extended to the MIR range, which reveal novel temporal dynamics. Indeed, the chaotic dynamics have been identified in QCL even though they display a sub-picosecond carrier dynamics and an ultra-large damping factor [113]. To this end, the integrated QCL on silicon can be envisioned for the development of secured communication channels integrated on a PIC.

Chapter 7

Résumé en Français

7.1 Introduction

La photonique sur silicium permet de palier au faible rendement et la consommation énergétique élevée des liens télécoms exploitant les câbles à paires torsadées ou coaxiaux. Cette technologie offre une versatilité exceptionnelle, de nouvelles fonctionnalités et des performances accrues pour les communications à haut-débit, les systèmes d'interconnexions optiques à courte portée et le déploiement de liaisons optiques d'une puce à une autre, d'une carte à une autre, ou d'un rack à un autre (datacom). Le silicium est un matériau semi-conducteur très efficace pour le guidage de la lumière, notamment en raison du fort contraste d'indice avec la silice. Cependant, sa bande interdite indirecte ne permet pas une émission radiative efficace. La réalisation de lasers repose donc sur des technologies hybrides de collage ou de report du matériau actif III-V (« wafer-bonding », « flip-chip ») sur le silicium passif. Cependant, cette intégration hétérogène présente des inconvénients comme par exemple un coût élevé et une évolutivité limitée. Les lasers hybrides sur silicium sont aussi plus sensibles aux réflexions parasites provenant des transitions des différentes interfaces passives/actives. Un moyen permettant de surmonter ces inconvénients consiste à faire croître directement le matériau III-V sur le silicium. Dans ce contexte, les lasers à boîtes quantiques utilisant des atomes semi-conducteurs comme milieu de gain sont des candidats très prometteurs en raison de leur compacité, de leur grande stabilité thermique et d'une tolérance accrue aux défauts structuraux. Certaines applications comme les systèmes cohérents, les futures horloges atomiques intégrées sur puces et les radars où la sensibilité aux bruits de fréquence et d'intensité influe fortement le taux d'erreur binaire requièrent l'utilisation d'émetteurs optiques à très faible bruit. Dans une première partie, cette thèse révèle le potentiel de lasers à boîtes quantiques InAs/InP présentant une largeur de raie spectrale intrinsèque de 80 kHz et un bruit relatif d'intensité inférieur à -150 dB/Hz. A cet effet, il est montré qu'un

faible couplage vertical entre les états liés est plus appropriée pour une réduction du bruit d'intensité notamment grâce à la suppression du bruit de porteurs associée à l'état excité. Dans une deuxième partie, les propriétés dynamiques et non-linéaires des lasers à boîtes quantiques directement épitaxiés sur silicium sont étudiées. Comme susmentionné, les lasers intégrés de manière hétérogène sur le silicium sont plus sensibles aux réflexions parasites. Combinées à une rétroaction optique externe, la stabilité du laser peut s'en trouver fortement affectée. Sachant qu'il n'existe pas à ce jour d'isolateurs optiques intégrés sur puce ayant un taux d'isolation suffisant, le développement d'émetteurs insensibles aux rétroactions est un objectif majeur. Cette thèse présente notamment un résultat de transmission sans erreur à partir d'un laser à boîtes quantique directement épitaxié sur silicium soumis à une modulation externe à 10 Gb/s ainsi qu'à une rétroaction optique maximale de -7 dB. Cette insensibilité aux réflexions résulte de plusieurs propriétés remarquables comme un facteur d'élargissement spectral proche de zéro, un facteur d'amortissement élevé, un fort contraste entre les seuils d'émission des états liés, et une durée de vie des porteurs plus courte. Ces résultats permettent d'envisager le développement de futurs circuits intégrés photoniques sur silicium à haute performance et fonctionnant sans isolateur optique.

7.2 Lasers à boîtes quantiques (QD) InAs/InP à rétroaction distribuée à faible bruit

Dans une première partie, nous étudions la modélisation du bruit relatif d'intensité (RIN), du bruit de fréquence (FN) et de la largeur de raie des lasers à boîtes quantiques. Nous proposons une nouvelle étude numérique du RIN et FN, laquelle incorpore l'ensemble des forces de Langevin (photons et porteurs) dont les bruits de porteurs associés aux niveaux non-résonants de la boîtes comme par exemple celui issu du premier état excité (ES).

La Fig.7.1 illustre le principe de la dynamique des porteurs selon le modèle excitonique de relaxation en cascade. Les paires électrons-trous (excitons) sont directement injectées dans le grand réservoir (RS) à partir des contacts métalliques. Comme le montre la Fig.7.1, la dynamique des porteurs entre RS et les états liés de l'îlot (GS et ES) est contrôlée par les différents temps caractéristiques (relaxation, capture et échappement). Le système d'équations d'évolution décrivant la dynamique du laser s'écrit comme ci-dessous [275]:

$$\frac{dN_{RS}}{dt} = \frac{I}{q} + \frac{N_{ES}}{\tau_{RS}^{ES}} - \frac{N_{RS}}{\tau_{ES}^{RS}}(1 - \rho_{ES}) - \frac{N_{RS}}{\tau_{RS}^{spon}} + F_{RS} \quad (7.1)$$

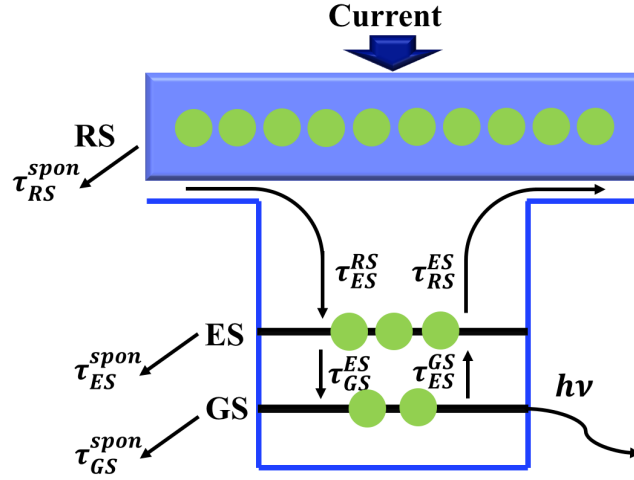


Fig. 7.1 Schéma de principe de la dynamique des porteurs selon le modèle excitonique de relaxation en cascade.

$$\frac{dN_{ES}}{dt} = \left(\frac{N_{RS}}{\tau_{ES}^{RS}} + \frac{N_{GS}}{\tau_{ES}^{GS}} \right) (1 - \rho_{ES}) - \frac{N_{ES}}{\tau_{GS}^{ES}} (1 - \rho_{GS}) - \frac{N_{ES}}{\tau_{RS}^{ES}} - \frac{N_{ES}}{\tau_{ES}^{spon}} + F_{ES} \quad (7.2)$$

$$\frac{dN_{GS}}{dt} = \frac{N_{ES}}{\tau_{GS}^{ES}} (1 - \rho_{GS}) - \frac{N_{GS}}{\tau_{ES}^{GS}} (1 - \rho_{ES}) - \Gamma_p v_g g_{GS} S_{GS} - \frac{N_{GS}}{\tau_{GS}^{spon}} + F_{GS} \quad (7.3)$$

$$\frac{dS_{GS}}{dt} = \left(\Gamma_p v_g g_{GS} - \frac{1}{\tau_p} \right) S_{GS} + \beta_{sp} \frac{N_{GS}}{\tau_{GS}^{spon}} + F_S \quad (7.4)$$

$$\frac{d\phi}{dt} = \frac{1}{2} \Gamma_p v_g (g_{GS} \alpha_{GS} + g_{ES} \kappa_{ES} + g_{RS} \kappa_{RS}) + F_\phi \quad (7.5)$$

Dans les équations 7.1 - 7.5, on note $N_{RS,ES,GS}$ les nombres de porteurs dans les états RS, GS et ES respectivement, S_{GS} le nombre de photons associés à l'émission stimulée sur le niveau GS, ϕ est la phase champ électrique. Les quantités $\tau_{RS,ES,GS}^{spon}$ sont respectivement les taux d'émission spontanée associés à RS, GS et ES, β_{sp} le facteur d'émission spontanée couplé au mode laser, Γ_p le facteur de confinement, v_g la vitesse de groupe, τ_p le temps de vie de photons, $g_{RS,ES,GS}$ le gain du niveau GS, ES, RS et $\rho_{ES,GS}$ les probabilités d'occupation des porteurs sur les niveaux d'énergies ES et GS. $\kappa_{ES,RS}$ sont des coefficients liés aux contributions ES et RS. La modélisation du RIN et FN se fait en deux étapes: la transposition du système dans le domaine des fréquences (analyse petit-signal) et l'introduction des forces de Langevin prenant en compte les bruits de recombinaisons de porteurs $F_{RS,ES,GS}$ et d'émission spontanée F_S pour le nombre de photons et F_ϕ pour la phase. En utilisant une approche petit-signal appliquée aux équations 7.1 - 7.5, le RIN du laser est calculé par la

relation:

$$RIN(\omega) = \frac{|\delta S_{GS}(\omega)|^2}{S_{GS}^2} \quad (7.6)$$

avec $\delta S_{GS}(\omega)$ la variation du nombre de photons sur le niveau GS. Le FN du laser est exprimé par la relation:

$$FN(\omega) = \left| \frac{j\omega\delta\phi(\omega)^2}{2\pi} \right| \quad (7.7)$$

avec $\delta\phi(\omega)$ la variation de la phase. La Fig.7.2(a) montre l'influence du bruit de porteurs $F_{RS,ES,GS}$ dans l'évolution du spectre de RIN (en bleu) à $1.5 \times I_{th}$, $2.5 \times I_{th}$, et $3.5 \times I_{th}$ avec I_{th} le courant de seuil du laser. Les courbes en rouge correspondent au cas où le bruit de porteurs n'est pas pris en compte ($F_{RS,ES,GS} = 0$). Le pic de résonance est associé à la fréquence de relaxation f_R du laser. Lorsque le courant augmente, on observe une augmentation de f_R accompagnée d'une réduction de l'amplitude du pic du au facteur d'amortissement du laser qui devient plus important. Les simulations montrent que l'inclusion du bruit de porteurs $F_{RS,ES,GS}$ rehausse la valeur du RIN en basse-fréquence typiquement avant f_R et ce quelque soit le niveau de courant considéré. Par exemple, à 1 MHz, le RIN augmente de -144 dB/Hz à -134 dB/Hz à $1.5 \times I_{th}$. Cet effet est atténué pour des fréquences proches et supérieures à f_R . Afin de clarifier la contribution des différents niveaux, la Fig.7.2(b) représente le spectre de RIN à $1.5 \times I_{th}$ pour les différents cas $F_{RS,ES,GS}$, $F_{ES,GS}$, F_{GS} et sans bruit de porteurs $F_{RS,ES,GS} = 0$ respectivement. Les simulations montrent que la contribution du bruit de porteurs associé au niveau GS est dominante mais que celle induite par le niveau ES ne peut être négligée. La première augmente l'amplitude du RIN pour toutes les fréquences alors que le deuxième affecte exclusivement la partie basse-fréquence du spectre typiquement avant f_R . Enfin, on observe que bruit de porteurs du grand réservoir F_{RS} n'affecte aucunement le RIN du laser. Puisque F_{GS} et F_{ES} sont les contributions principales, le couplage vertical et donc la différence d'énergie entre les états GS et ES joue un rôle clef.

La Fig.7.3(a) montre l'influence du bruit de porteurs $F_{RS,ES,GS}$ dans l'évolution du spectre de FN (en bleu) à $1.5 \times I_{th}$, $2.5 \times I_{th}$, et $3.5 \times I_{th}$ et les courbes en rouge correspondent au cas où le bruit de porteurs n'est pas pris en compte ($F_{RS,ES,GS} = 0$). Les simulations montrent que le bruit de porteurs a peu de contribution au FN sauf à la fréquence de résonance où le pic est légèrement renforcé. Ceci est compréhensible car la partie haute fréquence du FN est déterminée uniquement par l'émission spontanée du GS alors que la contribution basse fréquence est essentiellement déterminée à la fois par l'émission spontanée et le facteur d'élargissement spectral (α_H) du laser à boîtes quantiques. La largeur de raie totale est donc donnée par $\Delta\nu = 2\pi FN(\omega \ll \omega_R)$. La Fig.7.3(b) présente l'évolution de la largeur de raie

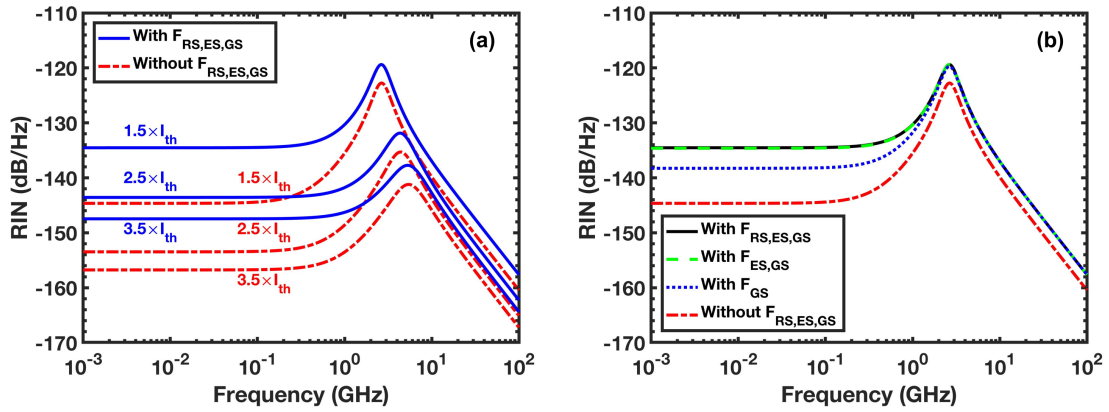


Fig. 7.2 (a) Contribution de $F_{RS,ES,GS}$ aux spectres de RIN à $1.5 \times I_{th}$, $2.5 \times I_{th}$, et $3.5 \times I_{th}$ respectivement; (b) Spectres de RIN à $1.5 \times I_{th}$ pour les cas comprenant $F_{RS,ES,GS}$, $F_{ES,GS}$, F_{GS} et sans bruit de porteurs $F_{RS,ES,GS} = 0$.

calculée en fonction du courant normalisé. La largeur de raie inférieure à 200 kHz est prévue avec lasers à boîtes quantiques.

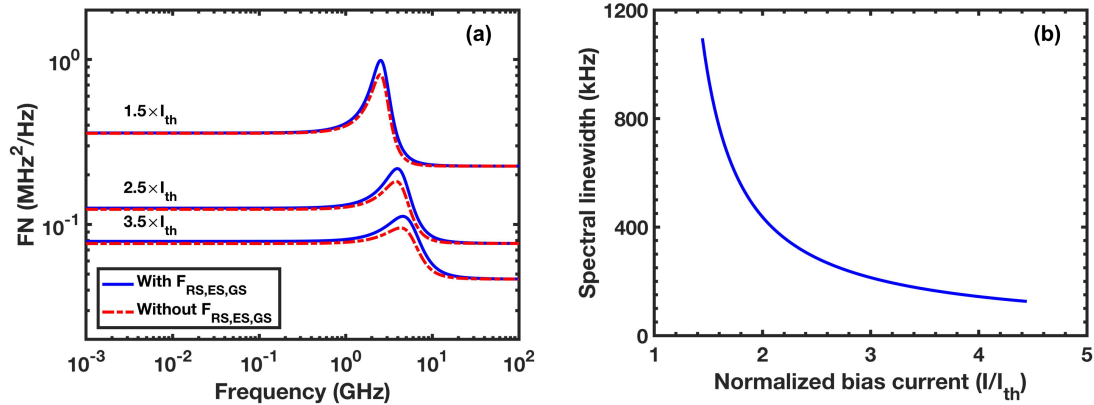


Fig. 7.3 (a) Contribution de $F_{RS,ES,GS}$ aux spectres de FN à $1.5 \times I_{th}$, $2.5 \times I_{th}$, et $3.5 \times I_{th}$ respectivement; (b) Largeur de raie spectrale calculée en fonction du courant normalisé.

Ensuite, nous étudions expérimentalement la largeur de raie et aussi le RIN de lasers à boîtes quantiques InAs/InP émettant à 1520 nm. Les lasers étudiés sont des structures monomodes à réaction distribuée (DFB). Fig.7.4(a) montre la structure du laser et Fig.7.4(b) montre une coupe transversale prise au microscope électronique à balayage (MEB) de la zone active du laser et du réseau de Bragg possédant un coefficient de couplage d'environ 20 cm^{-1} .

Le milieu actif comporte 5 plans de boîtes quantiques InAs dont la croissance a été réalisée par épitaxie par jets moléculaire (MBE) sur substrat InP. Les nanostructures font

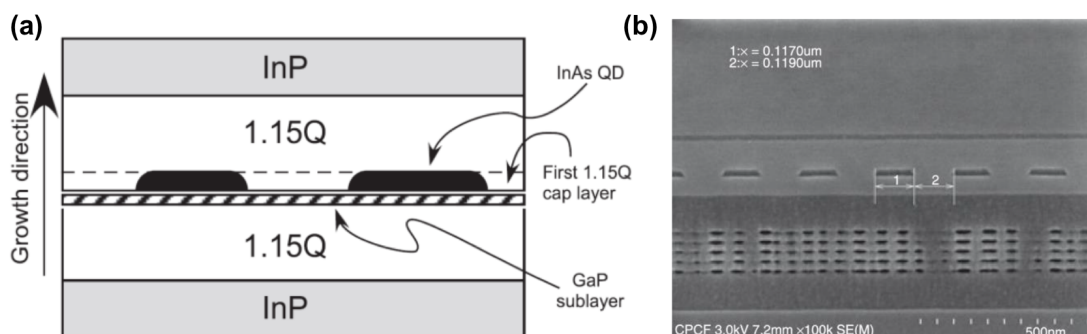


Fig. 7.4 (a) La structure du laser ; (b) Image MEB montrant une coupe transversale de la zone active du laser, le réseau de diffraction ainsi que les plans de boîtes quantiques.

environ $1.6 \text{ nm} \times 50 \text{ nm}$ (hauteur \times largeur), avec une densité d'environ $4 \times 10^{10} \text{ cm}^{-2}$ par plan. Le premier laser étudié possède deux facettes traitées antireflets (AR/AR) tandis que le deuxième est de type AR/HR où HR correspond au revêtement de haute réflectivité appliqué sur la facette arrière. Pour les deux dispositifs, la longueur de la cavité optique est 1 mm, la largeur du ruban est $3 \mu\text{m}$ et la longueur d'onde d'émission est de 1520 nm.

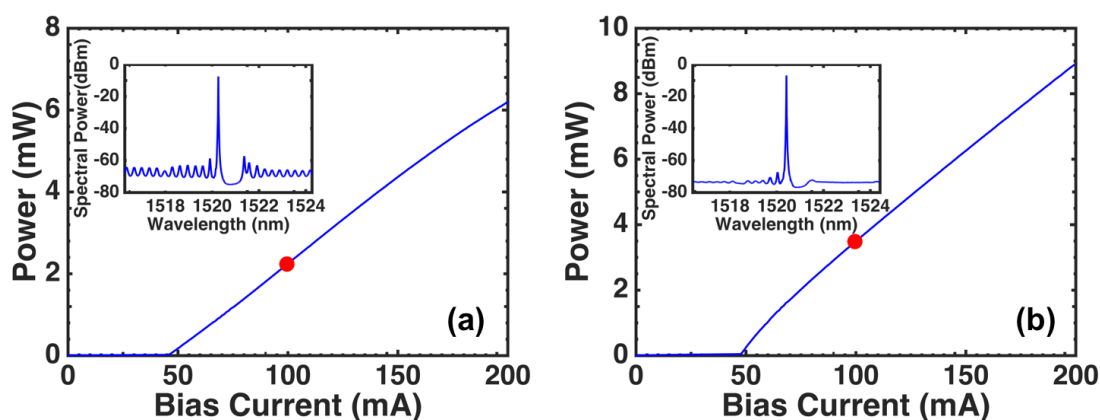


Fig. 7.5 Courbes courant-puissance et spectres optiques à 100 mA pour les lasers DFB InAs/InP AR/HR (a) et AR/AR (b). Les points rouges indiquent les mesures effectuées à $3 \times I_{th}$.

Les Fig.7.5 montrent les caractéristiques courant-puissance et les spectres optique mesurés à 100 mA (marqueurs rouges) pour les deux lasers. A la température de la pièce (293 K), le courant de seuil est de 47.5 mA pour le laser AR/AR et de 49 mA pour le laser AR/HR. Nous utilisons le montage interférométrique pour les mesures de largeur de raie.

La principale source de bruit des diodes lasers est l'émission spontanée de photons dans le mode laser. L'émission spontanée ajoute deux déphasages aléatoires au champ laser: l'un

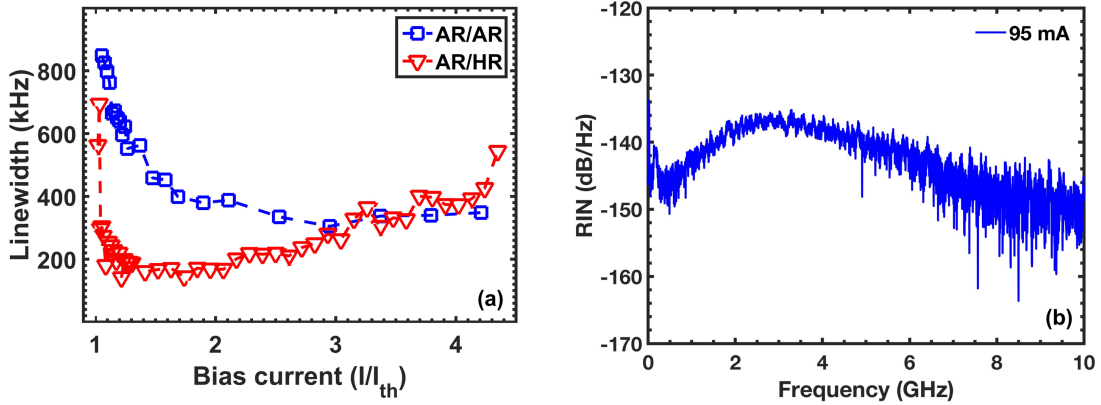


Fig. 7.6 (a) Largeur de raie en fonction du courant de pompe normalisé pour les lasers DFB AR/HR (en rouge) et AR/AR (en bleu). (b) Spectres de RIN mesuré à 95 mA pour le laser AR/AR.

dépend directement de la phase du photon spontané; l'autre est dû à la variation de l'intensité, par l'intermédiaire du couplage phase-amplitude: toute variation de l'intensité du champ provoque une variation du gain optique qui, en modifiant l'indice effectif, modifie la phase du champ. C'est le facteur α_H du laser qui traduit ce couplage. Dans ces conditions la formule de Schawlow-Townes modifiée donnant la largeur de raie spectrale est donnée par la relation [46]:

$$\Delta\nu = \frac{\Gamma_{g_{th}} v_g^2 \alpha_m h\nu}{4\pi P_0} n_{sp} (1 + \alpha_H^2) \quad (7.8)$$

avec $\Gamma_{g_{th}}$ le gain modal de seuil, α_m les pertes de transmissions de la cavité, v_g la vitesse de groupe, $h\nu$ l'énergie du photon, n_{sp} le facteur d'inversion de population, et P_0 la puissance de sortie du laser. La Fig.7.6(a) représente l'évolution de la largeur de raie mesurée pour les deux lasers en fonction du courant de pompe (normalisé par rapport au courant de seuil). Pour le laser DFB AR/HR, une largeur de raie record proche de 150 kHz (largeur de raie spectrale intrinsèque de 80 kHz) est obtenue. En utilisant Eq.7.8, on trouve $n_{sp}(1 + \alpha_H^2) \approx 1.4$ à $P_0 = 1$ mW, valeur environ 16 fois inférieure à celle publiée sur une structure DFB à boîtes quantiques InAs/GaAs ayant une largeur de raie de 800 kHz [46]. Ainsi, la très faible largeur de raie observée s'explique par un facteur d'inversion proche de l'unité et un paramètre $\alpha_H \approx 0.9$. Cependant, la courbe rouge montre l'occurrence d'un ré-élargissement spectral avec le courant de pompe dans le cas du laser DFB AR/HR. Cet effet déjà analysé numériquement [179] est la résultante des non-linéarités spatiales dans la cavité renforcées ici par la forte asymétrie entre les réflectivités et par les interactions porteurs-porteurs dans les nanostructures. La courbe bleu montre que le ré-élargissement disparaît dans le cas du laser DFB AR/AR. Ainsi, l'utilisation des traitements antireflets sur les deux facettes permet

de diminuer fortement les non-linéarités spatiales et de garantir une largeur de raie proche de 300 kHz et relativement indépendante du courant. La Fig.7.6(b) montre le spectre du RIN mesurés à 95 mA pour le laser DFB AR/AR. Le RIN aux basses fréquences est relativement élevé, résultant du bruit de courant, du bruit thermique ainsi que du bruit de partition de mode [296]. Après la fréquence de relaxation, le RIN diminue avec l'augmentation de la fréquence et atteint sa plus petite valeur de -155 dB/Hz dans la gamme de 8-10 GHz. Comparé au laser à puit quantique [93], le laser présente une caractéristique de quasi-classe A avec un amortissement élevé et une planéité améliorée avec un RIN contraint entre -135 dB/Hz et -150 dB/Hz pour toutes les fréquences.

7.3 Insensibilité aux réflexions optiques parasites dans les lasers à boîtes quantiques directement épitaxiés sur silicium

Ensuite, les propriétés dynamiques et non-linéaires des InAs/GaAs lasers à boîtes quantiques directement épitaxiés sur silicium sont étudiées. La Fig.7.7(a) montre l'illustration schématique de la structure épitaxiale du laser. La région active se compose de cinq périodes de couche QD et chacune a été séparée par un espaceur GaAs de 37.5 nm. Le gros plan à gauche de la Fig.7.7(a) représente une période de la région active.

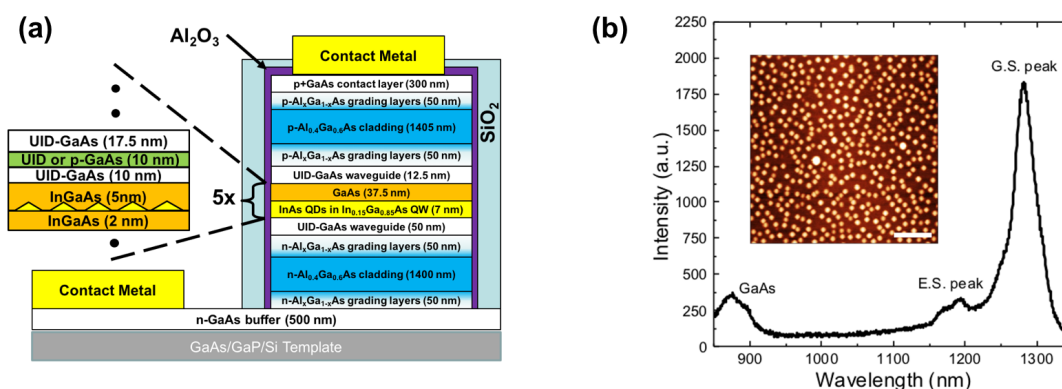


Fig. 7.7 (a) Illustration schématique de la structure épitaxiale du laser. (b) Spectre de photoluminescence de laser complet. L'encart montre une image au microscope à force atomique de boîtes quantiques InAs et la barre d'échelle est de 200 nm.

Comme le montre dans la Fig.7.7(b), un spectre de photoluminescence de l'échantillon laser complet a révélé une très faible pleine largeur à demi-maximum (FWHM) d'environ 30

meV à l'état fondamental (GS), indiquant que la taille des boîtes quantiques est très homogène. L'encart représente une image au microscope à force atomique de boîtes quantiques InAs avec une densité surfacique de $5 \times 10^{10} \text{ cm}^{-2}$. La cavité Fabry-Perot (FP) mesure 1.1 mm de long avec un guide d'onde de $4 \mu\text{m}$ large. La courbe courant-puissance et la spectre optique sont représentés sur la Fig.7.8 (a) et (b). À la température ambiante (293 K), le laser a un courant de seuil I_{th} de 6 mA et un pic de gain autour de 1300 nm.

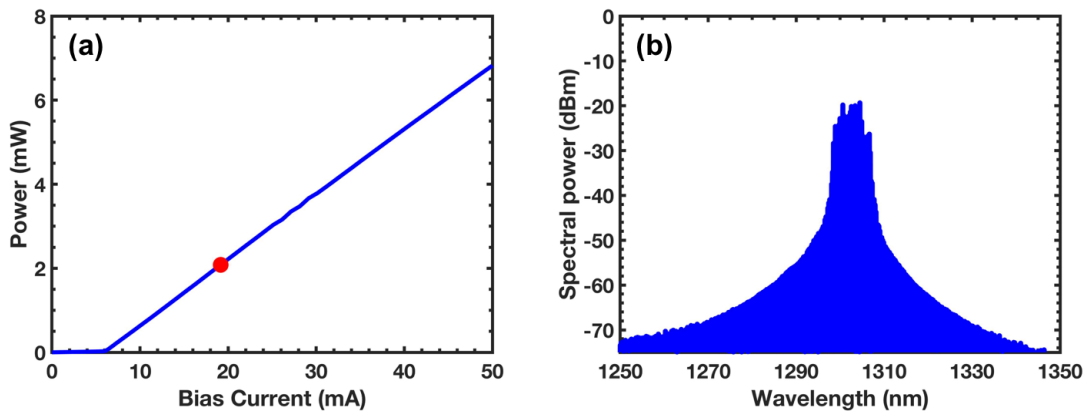


Fig. 7.8 (a) La courbe courant-puissance du laser et le point rouge indique la mesure effectuée à $3 \times I_{th}$. (b) Le spectre optique mesuré à $3 \times I_{th}$.

Le laser à boîtes quantiques est inséré dans une boucle de rétroaction optique externe fibrée pour mesurer les propriétés dynamiques sous rétroaction optique.

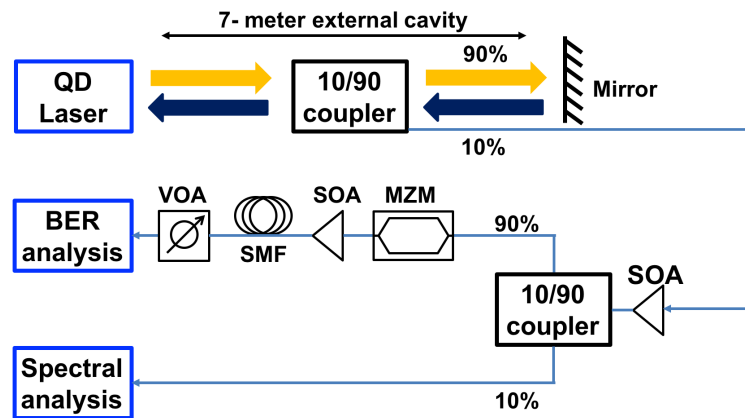


Fig. 7.9 Schéma de la configuration expérimentale de retour optique externe.

Comme le montre la Fig.7.9, l'émission laser est couplée à l'aide d'une fibre lentillée puis divisée par un coupleur 90/10 en deux voies. Dans la première, 90% de la lumière est réfléchiée vers le laser QD à l'aide d'un contre-réflécteur (BKR, backreflector en terme

anglais), composé d'un atténuateur variable et d'un miroir. Un contrôleur de polarisation inséré dans le chemin de retour permet d'ajuster les polarisations des lumières émises et réfléchies afin de maximiser les effets du retour optique. La force de rétroaction (r_{ext}) est définie comme le rapport entre la puissance de sortie de la facette laser soumise au retour optique à la puissance retournée. La longueur de la cavité externe est de 7 mètres, ce qui correspond à une fréquence de cavité externe de 14 MHz. Dans la deuxième voie, isolée du reste de l'installation, la première partie de la lumière est d'abord amplifiée par amplificateur optique à semi-conducteur (SOA) puis modulée par un modulateur Mach-Zehnder à 10 Gb/s et transmise à travers une bobine de fibre mono mode (SMF) de 2 km. Ensuite, le signal est envoyé à l'oscilloscope pour l'analyse du diagramme de l'oeil ou au détecteur d'erreur pour mesurer le taux d'erreur de bit (BER). Enfin, la deuxième partie de la lumière est envoyée vers les analyseurs de spectre électrique et optique (ESA et OSA) pour étudier la dynamique de rétroaction.

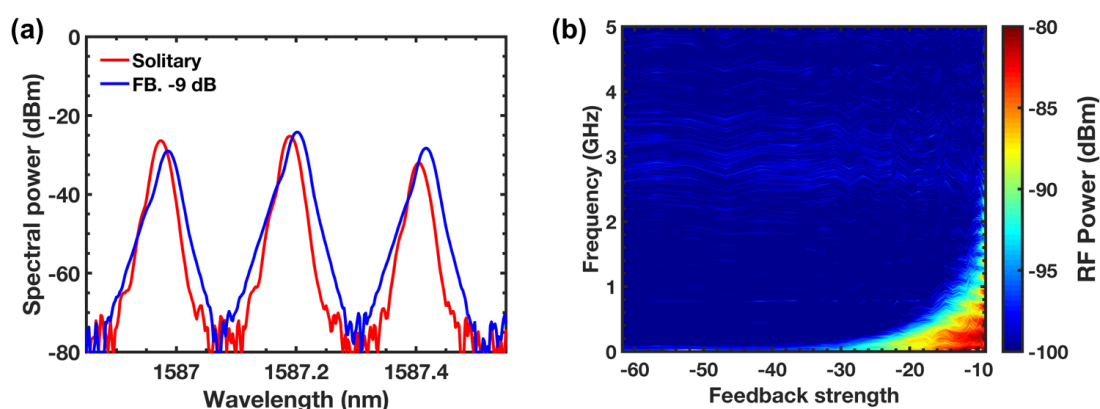


Fig. 7.10 (a) Spectres optique du laser hybride sur silicium mesurés à $3 \times I_{th}$ sans rétroaction (solitaire) et pour la force de rétroaction maximale (-9 dB). (b) Cartographie des spectres électriques du laser hybride mesuré en fonction de r_{ext} .

La dynamique de rétroaction optique du laser hybride sur silicium est d'abord étudiée. Les détails du laser hybride se trouvent dans la littérature [157]. La Fig.7.10(a) compare les spectres optiques enregistrés à $3 \times I_{th}$, sans rétroaction (cas solitaire, par exemple $r_{ext} = 0$) et pour la force de rétroaction maximale ($r_{ext} = -9$ dB). La Fig.7.10(a) montre l'élargissement du mode dans le spectre optique, tandis que la Fig.7.10(b) représente la déstabilisation dans le domaine électrique. En particulier, la Fig.7.10(b) montre que pour environ -30 dB de retour optique, des oscillations quasi périodiques avec un piédestal élevé ont lieu. À la force de rétroaction maximale, on observe un spectre large bande ce qui est une caractéristique des comportements chaotiques. Le seuil du régime chaotique aussi appelé le niveau critique r_{crit}

peut être estimé à partir de:

$$r_{crit} = \frac{\tau_{in}^2 \gamma^2}{16C_l^2} \left(\frac{1 + \alpha_H^2}{\alpha_H^4} \right) \quad (7.9)$$

où γ est le facteur d'amortissement, τ_{in} le temps de retour interne.

$$C_l = \frac{1 - R}{2\sqrt{R}} \quad (7.10)$$

avec C_l le coefficient de couplage de la facette à la cavité externe, avec R la réflectivité de la facette. Ce résultat est en accord avec les travaux antérieurs [157] qui ont montré que le laser hybride sur silicium présente une sensibilité de rétroaction plus élevée en raison de réflexions supplémentaires provenant des différentes interfaces entre les transitions actives/passives et qui deviennent très problématiques pour l'intégration PIC.

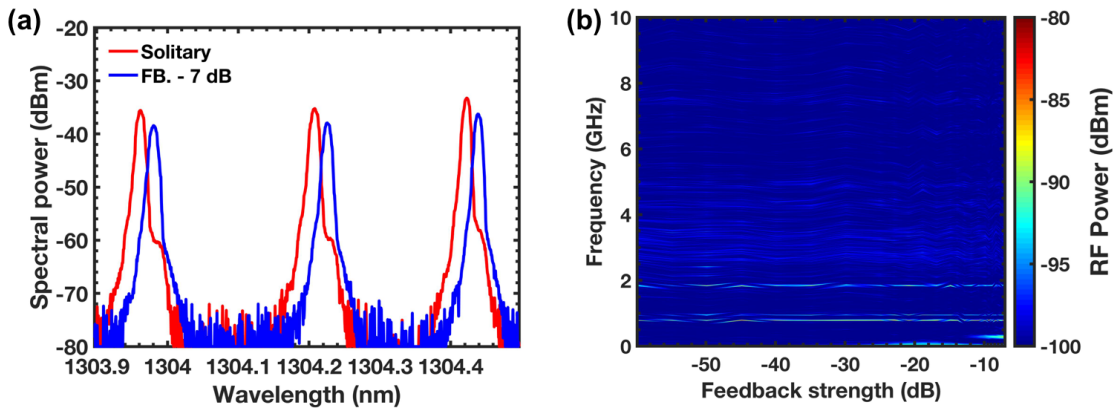


Fig. 7.11 (a) Spectres optique du laser à boîtes quantiques sur silicium mesurés à $3 \times I_{th}$ sans rétroaction (solitaire) et pour la force de rétroaction maximale (- 7 dB). (b) Cartographie des spectres électriques du laser à boîtes quantiques mesuré en fonction de r_{ext} .

Maintenant, les dynamiques de rétroaction des lasers à boîtes quantiques directement épitaxiés sur silicium sont présentés sur la Fig.7.11. On montre que le laser à boîtes quantiques reste stable pour toute la gamme des rétroactions étudiées, seul un petit décalage vers le rouge des modes FP a été observé sans signe d'élargissement spectral. Aucune dynamique complexe (ie. chaos) n'est observée même à la force de rétroaction la plus élevée de - 7 dB comme le prouve la Fig.7.11(b).

Les courbes BER pour les cas sans rétroaction et avec rétroaction sont tracées à la Fig.7.12(a) maximale après transmission de 2 km. La droite horizontale en pointillée de couleur noire correspond au niveau BER de 10^{-9} , qui est classiquement désigné comme la limite sans erreur. Les courbes BER pour ces deux cas se chevauchent parfaitement, ce

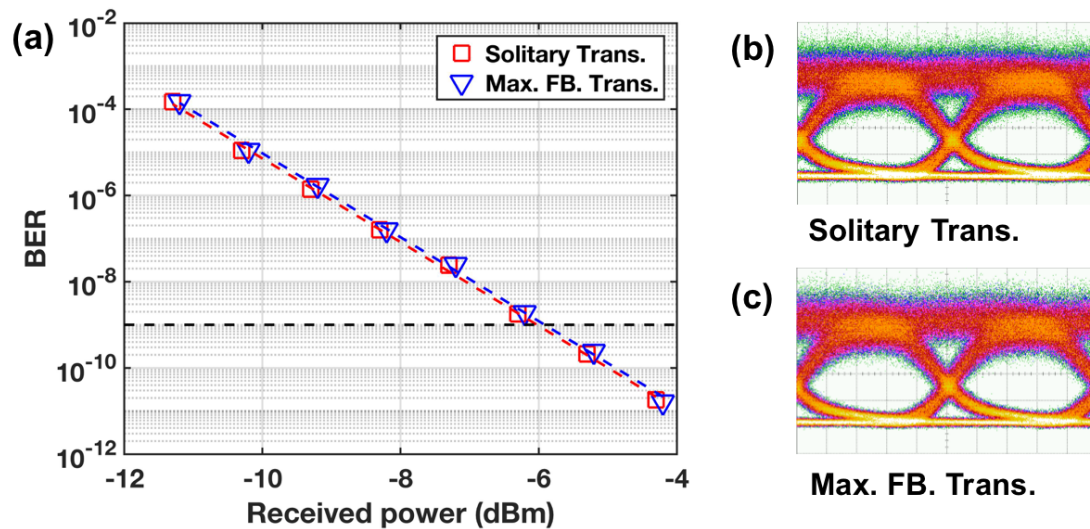


Fig. 7.12 (a) Les courbes BER en fonction de la puissance de réception par le détecteur pour le cas sans rétroaction et la force de rétroaction maximale après la transmission de 2 km. La ligne horizontale pointillée de couleur noire correspond à la limite conventionnelle sans erreur ($BER = 10^{-9}$). Diagramme de l'œil pour le cas sans rétroaction (b) et la force de rétroaction maximale (c).

qui prouve une excellente stabilité du laser à boîtes quantiques sans aucune dégradation des performances. Cette excellente stabilité est également confirmée par les diagrammes de l'œil qui restent ouverts y compris sous rétroaction.

A partir de l'expression du niveau r_{crit} donnée par l'équation 7.9, il est possible d'extraire le facteur d'élargissement spectral (facteur α_H) et le taux d'amortissement lesquels sont des facteurs importants pour déterminer la sensibilité du laser à la rétroaction. Les variations spectrales du facteur α_H sous le seuil pour le laser à boîtes quantiques directement épitaxié sur silicium et le laser hybride sur silicium sont représentées sur la Fig.7.13(a). Le facteur α_H se trouve à environ 3.5 pour le laser hybride et à 0.3 pour le laser à boîtes quantiques. Cette très faible valeur du facteur α_H dans le laser à boîtes quantiques résulte de la faible densité de dislocation de filetage, de la grande uniformité en taille des boîtes quantiques ainsi que de l'émission sur le seul GS avec peu de contribution de l'ES. La Fig.7.13(b) montre le facteur d'amortissement en fonction de la fréquence d'oscillation de relaxation au carré pour ces deux lasers. Un facteur d'amortissement de 15 GHz à $3 \times I_{th}$ est extrait avec un facteur K de 0.9 ns pour le laser à puit quantique. Par comparaison, le facteur d'amortissement du laser à boîtes quantique est plus élevé avec la valeur de 33 GHz à $3 \times I_{th}$. En conclusion, les lasers à boîtes quantiques directement épitaxiés sur silicium présentent une très grande insensibilité aux réflexions optiques. Cette caractéristique unique résulte principalement

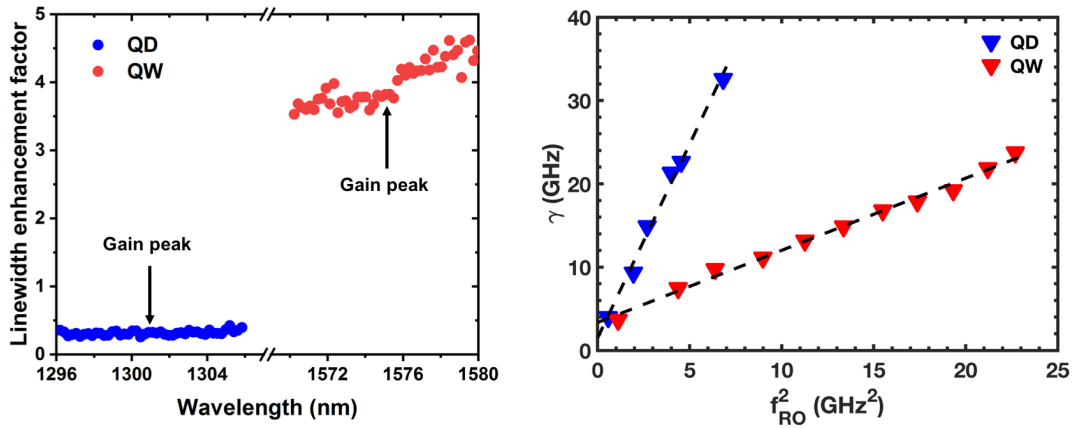


Fig. 7.13 (a) Les variations spectrales du facteur α_H sous-seuil pour le laser à boîtes quantiques et le laser à puit quantique. (b) Le facteur d'amortissement en fonction de la fréquence d'oscillation de relaxation au carré pour le laser à boîtes quantiques et le laser à puit quantique.

comme un facteur d'élargissement spectral proche de zéro, un facteur d'amortissement élevé, et un fort contraste entre les seuils d'émission des états liés (GS/ES).

7.4 Conclusions et perspectives

Cette thèse montre le potentiel de la technologie boîtes quantiques pour la réalisation d'oscillateurs à faible bruit (RIN, FN). La modélisation du bruit des lasers à boîtes quantiques montre que la contribution du bruit de porteurs associée aux niveaux non-résonants des boîtes ne doit pas être négligée. Expérimentalement, une largeur de raie spectrale record d'environ 150 kHz est révélée. Le contrôle des non-linéarités spatiales montre la possibilité de contenir le bruit de phase sur une large gamme de courant. Les sources à boîtes quantiques sont donc très performantes et peuvent être utilisées pour limiter la sensibilité de la réception au bruit de phase de l'oscillateur local dans les systèmes cohérents. Cette thèse aussi présente notamment un résultat de transmission sans erreur à partir d'un laser à boîtes quantique directement épitaxié sur silicium soumis à une modulation externe à 10 Gb/s ainsi qu'à une rétroaction optique maximale de -7 dB. Ces résultats permettent d'envisager le développement de futurs circuits intégrés photoniques sur silicium à haute performance et fonctionnant sans isolateur optique. Nos futurs travaux porteront également sur l'étude des dynamiques sur les lasers monomodes sur silicium et aussi InAs/InP laser à boîtes quantique directement épitaxié sur silicium.

References

- [1] Abdollahinia, A., Banyoudeh, S., Rippien, A., Schnabel, F., Eyal, O., Cestier, I., Kalifa, I., Mentovich, E., Eisenstein, G., and Reithmaier, J. (2018). Temperature stability of static and dynamic properties of 1.55 μm quantum dot lasers. *Optics Express*, 26(5):6056–6066.
- [2] Agrawal, G. P., Duan, G. H., and Gallion, P. (1992). Influence of refractive index nonlinearities on modulation and noise properties of semiconductor lasers. *Electronics Letters*, 28(19):1773–1774.
- [3] Ahmed, M., Yamada, M., and Saito, M. (2001). Numerical modeling of intensity and phase noise in semiconductor lasers. *IEEE Journal of Quantum Electronics*, 37(12):1600–1610.
- [4] Alexander, R. R., Childs, D. T., Agarwal, H., Groom, K. M., Liu, H.-Y., Hopkinson, M., Hogg, R. A., Ishida, M., Yamamoto, T., Sugawara, M., et al. (2007). Systematic study of the effects of modulation p-doping on 1.3- μm quantum-dot lasers. *IEEE Journal of Quantum Electronics*, 43(12):1129–1139.
- [5] Alferov, Z. I., Andreev, V., Garbuzov, D., Zhilyaev, Y. V., Morozov, E., Portnoi, E., and Trofim, V. (1971). Investigation of the influence of the AlAs-GaAs heterostructure parameters on the laser threshold current and the realization of continuous emission at room temperature. *Sov. Phys. Semicond*, 4(9):1573–1575.
- [6] Alghoraibi, I., Rohel, T., Bertru, N., Le Corre, A., Letoublon, A., Caroff, P., Dehaese, O., and Loualiche, S. (2006). Self-assembled InAs quantum dots grown on InP(311)B substrates: Role of buffer layer and amount of InAs deposited. *Journal of Crystal Growth*, 293(2):263–268.
- [7] Allen, C. N., Poole, P., Barrios, P., Marshall, P., Pakulski, G., Raymond, S., and Fafard, S. (2005). External cavity quantum dot tunable laser through 1.55 μm . *Physica E: Low-dimensional Systems and Nanostructures*, 26(1-4):372–376.
- [8] Almeida, V. R., Barrios, C. A., Panepucci, R. R., and Lipson, M. (2004). All-optical control of light on a silicon chip. *Nature*, 431(7012):1081.
- [9] Arakawa, Y., Nakamura, T., Urino, Y., and Fujita, T. (2013). Silicon photonics for next generation system integration platform. *IEEE Communications Magazine*, 51(3):72–77.
- [10] Arakawa, Y. and Sakaki, H. (1982). Multidimensional quantum well laser and temperature dependence of its threshold current. *Applied Physics Letters*, 40(11):939–941.

- [11] Arecchi, F., Lippi, G., Puccioni, G., and Tredicce, J. (1984). Deterministic chaos in laser with injected signal. *Optics Communications*, 51(5):308–314.
- [12] Arecchi, F., Meucci, R., Puccioni, G., and Tredicce, J. (1982). Experimental evidence of subharmonic bifurcations, multistability, and turbulence in a Q-switched gas laser. *Physical Review Letters*, 49(17):1217.
- [13] Arsenijević, D., Schliwa, A., Schmeckebier, H., Stubenrauch, M., Spiegelberg, M., Bimberg, D., Mikhelashvili, V., and Eisenstein, G. (2014). Comparison of dynamic properties of ground-and excited-state emission in p-doped InAs/GaAs quantum-dot lasers. *Applied Physics Letters*, 104(18):181101.
- [14] Asghari, M. and Krishnamoorthy, A. V. (2011). Silicon photonics: Energy-efficient communication. *Nature Photonics*, 5(5):268.
- [15] Asryan, L. and Suris, R. (1996). Inhomogeneous line broadening and the threshold current density of a semiconductor quantum dot laser. *Semiconductor Science and Technology*, 11(4):554.
- [16] Bayer, M. and Forchel, A. (2002). Temperature dependence of the exciton homogeneous linewidth in In_{0.60}Ga_{0.40}As/GaAs self-assembled quantum dots. *Physical Review B*, 65(4):041308.
- [17] Beausoleil, R. G. (2011). Large-scale integrated photonics for high-performance interconnects. *ACM Journal on Emerging Technologies in Computing Systems (JETC)*, 7(2):6.
- [18] Becker, A., Sichkovskiy, V., Bjelica, M., Ripplien, A., Schnabel, F., Kaiser, M., Eyal, O., Witzigmann, B., Eisenstein, G., and Reithmaier, J. (2017). Widely tunable narrow-linewidth 1.5 μm light source based on a monolithically integrated quantum dot laser array. *Applied Physics Letters*, 110(18):181103.
- [19] Bello, F., Lu, Q. Y., Abdullaev, A., Nawrocka, M., and Donegan, J. F. (2014). Linewidth and noise characterization for a partially-slotted, single mode laser. *IEEE Journal of Quantum Electronics*, 50(9):1–5.
- [20] Benyoucef, M. and Reithmaier, J. P. (2018). Telecom wavelength nanophotonic elements for quantum communication. In *2018 IEEE Photonics Society Summer Topical Meeting Series (SUM)*, pages 77–78.
- [21] Bhattacharya, P., Klotzkin, D., Qasaimeh, O., Zhou, W., Krishna, S., and Zhu, D. (2000). High-speed modulation and switching characteristics of In(Ga)As-Al(Ga)As self-organized quantum-dot lasers. *IEEE Journal of Selected Topics in Quantum Electronics*, 6(3):426–438.
- [22] Bhattacharyya, D., Avrutin, E., Bryce, A., Marsh, J., Bimberg, D., Heinrichsdorff, F., Ustinov, V., Zaitsev, S., Ledentsov, N., Kop'ev, P., et al. (1999). Spectral and dynamic properties of InAs-GaAs self-organized quantum-dot lasers. *IEEE Journal of Selected Topics in Quantum Electronics*, 5(3):648–657.

- [23] Bi, L., Hu, J., Jiang, P., Kim, D. H., Dionne, G. F., Kimerling, L. C., and Ross, C. (2011). On-chip optical isolation in monolithically integrated non-reciprocal optical resonators. *Nature Photonics*, 5(12):758.
- [24] Bimberg, D., Grundmann, M., and Ledentsov, N. N. (1999). *Quantum Dot Heterostructures*. John Wiley & Sons.
- [25] Bossert, D. and Gallant, D. (1996). Improved method for gain/index measurements of semiconductor lasers. *Electronics Letters*, 32(4):338–339.
- [26] Brackett, C. A. (1990). Dense wavelength division multiplexing networks: Principles and applications. *IEEE Journal on Selected Areas in Communications*, 8(6):948–964.
- [27] Broom, R., Mohn, E., Risch, C., and Salathe, R. (1970). Microwave self-modulation of a diode laser coupled to an external cavity. *IEEE Journal of Quantum Electronics*, 6(6):328–334.
- [28] Brosson, P., Artigue, C., Fernier, B., Leclerc, D., Jacquet, J., and Benoit, J. (2002). Simple determination of coupling coefficient in DFB waveguide structures. *Electronics Letters*, 24(16):990–991.
- [29] Buffolo, M., Samparisi, F., De Santi, C., Jung, D., Norman, J., Bowers, J. E., Herrick, R. W., Meneghesso, G., Zanoni, E., and Meneghini, M. (2019). Physical origin of the optical degradation of InAs quantum dot lasers. *IEEE Journal of Quantum Electronics*, 55:1–7.
- [30] Buffolo, M., Samparisi, F., Rovere, L., De Santi, C., Jung, D., Norman, J., Bowers, J. E., Herrick, R. W., Meneghesso, G., Zanoni, E., and Meneghini, M. (2020). Investigation of current-driven degradation of 1.3 μm quantum-dot lasers epitaxially grown on silicon. *IEEE Journal of Selected Topics in Quantum Electronics*, 26(2):1–8.
- [31] Camacho-Aguilera, R. E., Cai, Y., Patel, N., Bessette, J. T., Romagnoli, M., Kimerling, L. C., and Michel, J. (2012). An electrically pumped germanium laser. *Optics Express*, 20(10):11316–11320.
- [32] Capua, A., Rozenfeld, L., Mikhelashvili, V., Eisenstein, G., Kuntz, M., Laemmlin, M., and Bimberg, D. (2007). Direct correlation between a highly damped modulation response and ultra low relative intensity noise in an InAs/GaAs quantum dot laser. *Optics Express*, 15(9):5388–5393.
- [33] Carpintero, G., Rouvalis, E., Ławniczuk, K., Fice, M., Renaud, C. C., Leijtens, X. J., Bente, E. A., Chitoui, M., Van Dijk, F., and Seeds, A. J. (2012). 95 GHz millimeter wave signal generation using an arrayed waveguide grating dual wavelength semiconductor laser. *Optics Letters*, 37(17):3657–3659.
- [34] Carroll, J. E., Whiteaway, J., Plumb, D., and Plumb, R. (1998). *Distributed feedback semiconductor lasers*, volume 10. IET.
- [35] Cathabard, O., Teissier, R., Devenson, J., Moreno, J., and Baranov, A. (2010). Quantum cascade lasers emitting near 2.6 μm . *Applied Physics Letters*, 96(14):141110.

- [36] Chen, S., Li, W., Wu, J., Jiang, Q., Tang, M., Shutts, S., Elliott, S. N., Sobiesierski, A., Seeds, A. J., Ross, I., Smowton, P. M., and Liu, H. (2016). Electrically pumped continuous-wave III–V quantum dot lasers on silicon. *Nature Photonics*, 10(5):307.
- [37] Choi, H., Wang, C., and Karam, N. (1991). GaAs-based diode lasers on Si with increased lifetime obtained by using strained ingaas active layer. *Applied Physics Letters*, 59(21):2634–2635.
- [38] Chow, W. W. and Jahnke, F. (2013). On the physics of semiconductor quantum dots for applications in lasers and quantum optics. *Progress in Quantum Electronics*, 37(3):109–184.
- [39] Chow, W. W. and Koch, S. W. (1999). *Semiconductor-laser fundamentals: physics of the gain materials*. Springer Science & Business Media.
- [40] Chow, W. W. and Koch, S. W. (2005). Theory of semiconductor quantum-dot laser dynamics. *IEEE Journal of Quantum Electronics*, 41(4):495–505.
- [41] Coldren, L. A., Corzine, S. W., and Mashanovitch, M. L. (2012). *Diode lasers and photonic integrated circuits*. John Wiley & Sons.
- [42] Cong, D.-Y., Martinez, A., Merghem, K., Ramdane, A., Provost, J.-G., Fischer, M., Krestnikov, I., and Kovsh, A. (2008). Temperature insensitive linewidth enhancement factor of p-type doped InAs/GaAs quantum-dot lasers emitting at 1.3 μm . *Applied Physics Letters*, 92(19):191109.
- [43] Cornet, C., Platz, C., Caroff, P., Even, J., Labbé, C., Folliot, H., Le Corre, A., and Loualiche, S. (2005). Approach to wetting-layer-assisted lateral coupling of InAs/InP quantum dots. *Physical Review B*, 72(3):035342.
- [44] Cornet, C., Schliwa, A., Even, J., Doré, F., Celebi, C., Létoublon, A., Macé, E., Paranthoen, C., Simon, A., Koenraad, P., et al. (2006). Electronic and optical properties of InAs/InP quantum dots on InP(100) and InP(311)B substrates: theory and experiment. *Physical Review B*, 74(3):035312.
- [45] Cox, C. H., Ackerman, E. I., Betts, G. E., and Prince, J. L. (2006). Limits on the performance of RF-over-fiber links and their impact on device design. *IEEE Transactions on Microwave Theory and Techniques*, 54(2):906–920.
- [46] Crowley, M. T., Naderi, N. A., Su, H., Grillot, F., and Lester, L. F. (2012). GaAs-based quantum dot lasers. In *Semiconductors and Semimetals*, volume 86, pages 371–417. Elsevier.
- [47] Dagens, B., Markus, A., Chen, J., Provost, J.-G., Make, D., Le Gouezigou, O., Landreau, J., Fiore, A., and Thedrez, B. (2005). Giant linewidth enhancement factor and purely frequency modulated emission from quantum dot laser. *Electronics Letters*, 41(6):323–324.
- [48] Devaux, F., Sorel, Y., and Kerdiles, J. (1993). Simple measurement of fiber dispersion and of chirp parameter of intensity modulated light emitter. *Journal of Lightwave Technology*, 11(12):1937–1940.

- [49] Dingle, R. and Henry, C. H. (1976). Quantum effects in heterostructure lasers. US Patent 3,982,207.
- [50] Dong, B., Duan, J., Shang, C., Huang, H., Sawadogo, A., Jung, D., Wan, Y., Bowers, J., and Grillot, F. (2019). Influence of the polarization anisotropy on the linewidth enhancement factor and reflection sensitivity of 1.55- μm InP-based InAs quantum dash lasers. *Applied Physics Letters*, 115(9):091101.
- [51] Duan, G.-H., Jany, C., Le Liepvre, A., Accard, A., Lamponi, M., Make, D., Kaspar, P., Levaufre, G., Girard, N., Lelarge, F., et al. (2014). Hybrid III–V on silicon lasers for photonic integrated circuits on silicon. *IEEE Journal of Selected Topics in Quantum Electronics*, 20(4):158–170.
- [52] Duan, J., Huang, H., Dong, B., Jung, D., Norman, J. C., Bowers, J. E., and Grillot, F. (2019a). 1.3- μm reflection insensitive InAs/GaAs quantum dot lasers directly grown on silicon. *IEEE Photonics Technology Letters*, 31(5):345–348.
- [53] Duan, J., Huang, H., Dong, B., Norman, J. C., Zhang, Z., Bowers, J. E., and Grillot, F. (2019b). Dynamic and nonlinear properties of epitaxial quantum dot lasers on silicon for isolator-free integration. *Photonics Research*, 7(11):1222–1228.
- [54] Duan, J., Huang, H., Jung, D., Zhang, Z., Norman, J., Bowers, J., and Grillot, F. (2018a). Semiconductor quantum dot lasers epitaxially grown on silicon with low linewidth enhancement factor. *Applied Physics Letters*, 112(25):251111.
- [55] Duan, J., Huang, H., Lu, Z., Poole, P., Wang, C., and Grillot, F. (2018b). Narrow spectral linewidth in InAs/InP quantum dot distributed feedback lasers. *Applied Physics Letters*, 112(12):121102.
- [56] Duan, J., Wang, X.-G., Zhou, Y.-G., Wang, C., and Grillot, F. (2018c). Carrier-noise-enhanced relative intensity noise of quantum dot lasers. *IEEE Journal of Quantum Electronics*, 54(6):1–7.
- [57] Eisenstein, G. and Bimberg, D. (2017). *Green Photonics and Electronics*. Springer.
- [58] Elbaz, A., El Kurdi, M., Aassime, A., Sauvage, S., Checoury, X., Sagnes, I., Baudot, C., Boeuf, F., and Boucaud, P. (2018). Germanium microlasers on metallic pedestals. *APL Photonics*, 3(10):106102.
- [59] Even, J., Wang, C., and Grillot, F. (2016). From basic physical properties of InAs/InP quantum dots to state-of-the-art lasers for 1.55 μm optical communications: an overview. In *Semiconductor Nanocrystals and Metal Nanoparticles: Physical Properties and Device Applications*, chapter 3. CRC Press.
- [60] Fang, A. W., Park, H., Cohen, O., Jones, R., Paniccia, M. J., and Bowers, J. E. (2006). Electrically pumped hybrid AlGaInAs-silicon evanescent laser. *Optics Express*, 14(20):9203–9210.
- [61] Fiore, A. and Markus, A. (2007). Differential gain and gain compression in quantum-dot lasers. *IEEE Journal of Quantum Electronics*, 43(4):287–294.

- [62] Fleming, M. and Mooradian, A. (1981). Spectral characteristics of external-cavity controlled semiconductor lasers. *IEEE Journal of Quantum Electronics*, 17(1):44–59.
- [63] Gallet, A. (2019). *Hybrid III-V/Si lasers for optical communications*. PhD thesis, Télécom ParisTech.
- [64] Gallet, A., Hassan, K., Jany, C., Card, T., DaFonseca, J., Rebeyrol, V., Shen, A., Provost, J., Van Dijk, F., Girard, N., et al. (2018). Dynamic and noise properties of high-Q hybrid laser. In *2018 IEEE International Semiconductor Laser Conference (ISLC)*, pages 1–2. IEEE.
- [65] Geng, J., Spiegelberg, C., and Jiang, S. (2005). Narrow linewidth fiber laser for 100-km optical frequency domain reflectometry. *IEEE Photonics Technology Letters*, 17(9):1827–1829.
- [66] George, I., Becagli, F., Liu, H., Wu, J., Tang, M., and Beanland, R. (2015). Dislocation filters in GaAs on Si. *Semiconductor Science and Technology*, 30(11):114004.
- [67] Gioannini, M. (2006). Analysis of the optical gain characteristics of semiconductor quantum-dash materials including the band structure modifications due to the wetting layer. *IEEE Journal of Quantum Electronics*, 42(3):331–340.
- [68] Gioannini, M., Dommermuth, M., Drzewietzki, L., Krestnikov, I., Livshits, D., Krakowski, M., and Breuer, S. (2014). Two-state semiconductor laser self-mixing velocimetry exploiting coupled quantum-dot emission-states: experiment, simulation and theory. *Optics Express*, 22(19):23402–23414.
- [69] Gioannini, M. and Montrosset, I. (2007). Numerical analysis of the frequency chirp in quantum-dot semiconductor lasers. *IEEE Journal of Quantum Electronics*, 43(10):941–949.
- [70] Girardin, F., Duan, G.-H., and Gallion, P. (1996). Linewidth rebroadening due to nonlinear gain and index induced by carrier heating in strained quantum-well lasers. *IEEE Photonics Technology Letters*, 8(3):334–336.
- [71] Gong, M., Duan, K., Li, C.-F., Magri, R., Narvaez, G. A., and He, L. (2008). Electronic structure of self-assembled InAs/InP quantum dots: Comparison with self-assembled InAs/GaAs quantum dots. *Physical Review B*, 77(4):045326.
- [72] Grillot, F. (2009). On the effects of an antireflection coating impairment on the sensitivity to optical feedback of AR/HR semiconductor DFB lasers. *IEEE Journal of Quantum Electronics*, 45(6):720–729.
- [73] Grillot, F., Dagens, B., Provost, J.-G., Su, H., and Lester, L. F. (2008a). Gain compression and above-threshold linewidth enhancement factor in 1.3- μm InAs–GaAs quantum-dot lasers. *IEEE Journal of Quantum Electronics*, 44(10):946–951.
- [74] Grillot, F., Naderi, N., Pochet, M., Lin, C.-Y., and Lester, L. (2008b). Variation of the feedback sensitivity in a 1.55 μm InAs/Inp quantum-dash Fabry-Perot semiconductor laser. *Applied Physics Letters*, 93(19):191108.

- [75] Grillot, F., Naderi, N., Wright, J., Raghunathan, R., Crowley, M., and Lester, L. (2011). A dual-mode quantum dot laser operating in the excited state. *Applied Physics Letters*, 99(23):231110.
- [76] Grillot, F., Thedrez, B., and Duan, G.-H. (2004). Feedback sensitivity and coherence collapse threshold of semiconductor DFB lasers with complex structures. *IEEE Journal of Quantum Electronics*, 40(3):231–240.
- [77] Grillot, F., Thedrez, B., Gauthier-Lafaye, O., Martineau, M., Voiriot, V., Lafrayette, J., Gentner, J., and Silvestre, L. (2003). Coherence-collapse threshold of 1.3- μm semiconductor DFB lasers. *IEEE Photonics Technology Letters*, 15(1):9–11.
- [78] Grillot, F., Thedrez, B., Py, J., Gauthier-Lafaye, O., Voiriot, V., and Lafrayette, J. (2002). 2.5-Gb/s transmission characteristics of 1.3- μm DFB lasers with external optical feedback. *IEEE Photonics Technology Letters*, 14(1):101–103.
- [79] Groenert, M. E., Pitera, A. J., Ram, R. J., and Fitzgerald, E. A. (2003). Improved room-temperature continuous wave GaAs/AlGaAs and InGaAs/GaAs/AlGaAs lasers fabricated on Si substrates via relaxed graded $\text{Ge}_x\text{Si}_{1-x}$ buffer layers. *Journal of Vacuum Science & Technology B: Microelectronics and Nanometer Structures Processing, Measurement, and Phenomena*, 21(3):1064–1069.
- [80] Hakki, B. W. and Paoli, T. L. (1973). cw degradation at 300 °K of GaAs double-heterostructure junction lasers. II. Electronic gain. *Journal of Applied Physics*, 44(9):4113–4119.
- [81] Harder, C., Vahala, K., and Yariv, A. (1983). Measurement of the linewidth enhancement factor α of semiconductor lasers. *Applied Physics Letters*, 42(4):328–330.
- [82] Harfouche, M. (2018). *The coherence collapse regime of high-coherence Si/III-V lasers and the use of swept frequency semiconductor lasers for full field 3D imaging*. PhD thesis, California Institute of Technology.
- [83] Hattori, H. T., Seassal, C., Touraille, E., Rojo-Romeo, P., Letartre, X., Hollinger, G., Viktorovitch, P., Di Cioccio, L., Zussy, M., Melhaoui, L. E., et al. (2005). Heterogeneous integration of microdisk lasers on silicon strip waveguides for optical interconnects. *IEEE Photonics Technology Letters*, 18(1):223–225.
- [84] Haug, H. and Koch, S. W. (2009). *Quantum Theory of the Optical and Electronic Properties of Semiconductors: Fifth Edition*. World Scientific Publishing Company.
- [85] Hayau, J.-F., Besnard, P., Dehaese, O., Grillot, F., Piron, R., Loualiche, S., Martinez, A., Merghem, K., and Ramdane, A. (2009). Effect of the wetting layer on intensity noise in quantum dot laser. In *Optical Communication, 2009. ECOC'09. 35th European Conference on*, pages 1–2. IEEE.
- [86] Haysom, J., Aers, G., Raymond, S., and Poole, P. (2000). Study of quantum well intermixing caused by grown-in defects. *Journal of Applied Physics*, 88(5):3090–3092.
- [87] Hein, S., Von Hinten, V., Höfling, S., and Forchel, A. (2008). The impact of p-doping on the static and dynamic properties of 1.5 μm quantum dash lasers on InP. *Applied Physics Letters*, 92(1):011120.

- [88] Heitz, R., Kalburge, A., Xie, Q., Grundmann, M., Chen, P., Hoffmann, A., Madhukar, A., and Bimberg, D. (1998). Excited states and energy relaxation in stacked InAs/GaAs quantum dots. *Physical Review B*, 57(15):9050.
- [89] Helkey, R., Saleh, A. A., Buckwalter, J., and Bowers, J. E. (2019). High-performance photonic integrated circuits on silicon. *IEEE Journal of Selected Topics in Quantum Electronics*, 25(5):1–15.
- [90] Henry, C. (1982). Theory of the linewidth of semiconductor lasers. *IEEE Journal of Quantum Electronics*, 18(2):259–264.
- [91] Henry, C. (1983). Theory of the phase noise and power spectrum of a single mode injection laser. *IEEE Journal of Quantum Electronics*, 19(9):1391–1397.
- [92] Henry, C. and Kazarinov, R. (1986). Instability of semiconductor lasers due to optical feedback from distant reflectors. *IEEE Journal of Quantum Electronics*, 22(2):294–301.
- [93] Herbert, C., Jones, D., Kaszubowska-Anandarajah, A., Kelly, B., Rensing, M., O’Carroll, J., Phelan, R., Anandarajah, P., Perry, P., Barry, L., et al. (2009). Discrete mode lasers for communication applications. *IET optoelectronics*, 3(1):1–17.
- [94] Hoffmann, S. and Hofmann, M. R. (2007). Generation of terahertz radiation with two color semiconductor lasers. *Laser & Photonics Reviews*, 1(1):44–56.
- [95] Homeyer, E., Piron, R., Grillot, F., Dehaese, O., Tavernier, K., Macé, E., Le Corre, A., and Loualiche, S. (2007). First demonstration of a 1.52 μm RT InAs/InP (311)B laser with an active zone based on a single QD layer. *Semiconductor science and technology*, 22(7):827.
- [96] Huang, D., Pintus, P., and Bowers, J. E. (2018a). Towards heterogeneous integration of optical isolators and circulators with lasers on silicon. *Optical Materials Express*, 8(9):2471–2483.
- [97] Huang, D., Tran, M. A., Guo, J., Peters, J., Komljenovic, T., Malik, A., Morton, P. A., and Bowers, J. E. (2019). High-power sub-kHz linewidth lasers fully integrated on silicon. *Optica*, 6(6):745–752.
- [98] Huang, H. (2017). *Optical nonlinearities in quantum dot lasers for high-speed communications*. PhD thesis, Télécom ParisTech.
- [99] Huang, H., Arsenijević, D., Schires, K., Sadeev, T., Bimberg, D., and Grillot, F. (2016a). Multimode optical feedback dynamics of InAs/GaAs quantum-dot lasers emitting on different lasing states. *AIP Advances*, 6(12):125114.
- [100] Huang, H., Duan, J., Jung, D., Liu, A. Y., Zhang, Z., Norman, J., Bowers, J. E., and Grillot, F. (2018b). Analysis of the optical feedback dynamics in InAs/GaAs quantum dot lasers directly grown on silicon. *JOSA B*, 35(11):2780–2787.
- [101] Huang, H., Lin, L.-C., Chen, C.-Y., Arsenijević, D., Bimberg, D., Lin, F.-Y., and Grillot, F. (2018c). Multimode optical feedback dynamics in InAs/GaAs quantum dot lasers emitting exclusively on ground or excited states: transition from short-to long-delay regimes. *Optics Express*, 26(2):1743–1751.

- [102] Huang, H., Schires, K., Lin, L., Chen, C., Arsenijević, D., Sadeev, T., Bimberg, D., Lin, F., and Grillot, F. (2016b). Dynamics of excited-state InAs/GaAs Fabry-Perot quantum-dot lasers under optical feedback. In *CLEO: Science and Innovations*, pages STh4L–6. Optical Society of America.
- [103] Huang, H., Schires, K., Poole, P., and Grillot, F. (2015). Non-degenerate four-wave mixing in an optically injection-locked InAs/InP quantum dot Fabry-Perot laser. *Applied Physics Letters*, 106(14):143501.
- [104] Huang, J. and Casperson, L. W. (1993). Gain and saturation in semiconductor lasers. *Optical & Quantum Electronics*, 25(6):369–390.
- [105] Huffaker, D., Park, G., Zou, Z., Shchekin, O., and Deppe, D. (1998). 1.3 μm room-temperature GaAs-based quantum-dot laser. *Applied Physics Letters*, 73(18):2564–2566.
- [106] Hui, R., Mecozzi, A., D’ottavi, A., and Spano, P. (1990). Novel measurement technique of alpha factor in DFB semiconductor lasers by injection locking. *Electronics Letters*, 26(14):997–998.
- [107] Ilyas, M. and Mouftah, H. T. (2003). *The handbook of optical communication networks*. CRC press.
- [108] Inoue, D., Jung, D., Norman, J., Wan, Y., Nishiyama, N., Arai, S., Gossard, A. C., and Bowers, J. E. (2018). Directly modulated 1.3 μm quantum dot lasers epitaxially grown on silicon. *Optics Express*, 26(6):7022–7033.
- [109] Intel, R. (2017). Intel® silicon photonics 100G PSM4 optical transceiver brief.
- [110] Ishida, M., Hatori, N., Akiyama, T., Otsubo, K., Nakata, Y., Ebe, H., Sugawara, M., and Arakawa, Y. (2004). Photon lifetime dependence of modulation efficiency and K factor in 1.3 μm self-assembled InAs/GaAs quantum-dot lasers: Impact of capture time and maximum modal gain on modulation bandwidth. *Applied Physics Letters*, 85(18):4145–4147.
- [111] Joindot, I. (1992). Measurements of relative intensity noise (RIN) in semiconductor lasers. *Journal de Physique III France*, 2(9):1591–1603.
- [112] Jumpertz, L. (2017). *Nonlinear Photonics in Mid-infrared Quantum Cascade Lasers*. Springer.
- [113] Jumpertz, L., Schires, K., Carras, M., Sciamanna, M., and Grillot, F. (2016). Chaotic light at mid-infrared wavelength. *Light: Science & Applications*, 5(6):e16088.
- [114] Jung, D., Callahan, P. G., Shin, B., Mukherjee, K., Gossard, A. C., and Bowers, J. E. (2017a). Low threading dislocation density GaAs growth on on-axis GaP/Si (001). *Journal of Applied Physics*, 122(22):225703.
- [115] Jung, D., Herrick, R., Norman, J., Turnlund, K., Jan, C., Feng, K., Gossard, A. C., and Bowers, J. E. (2018). Impact of threading dislocation density on the lifetime of InAs quantum dot lasers on Si. *Applied Physics Letters*, 112(15):153507.

- [116] Jung, D., Norman, J., Kennedy, M., Shang, C., Shin, B., Wan, Y., Gossard, A. C., and Bowers, J. E. (2017b). High efficiency low threshold current $1.3 \mu\text{m}$ InAs quantum dot lasers on on-axis (001) GaP/Si. *Applied Physics Letters*, 111(12):122107.
- [117] Jung, D., Zhang, Z., Norman, J., Herrick, R., Kennedy, M., Patel, P., Turnlund, K., Jan, C., Wan, Y., Gossard, A. C., et al. (2017c). Highly reliable low-threshold InAs quantum dot lasers on on-axis (001) Si with 87% injection efficiency. *ACS Photonics*, 5(3):1094–1100.
- [118] Kageyama, T., Nishi, K., Yamaguchi, M., Mochida, R., Maeda, Y., Takemasa, K., Tanaka, Y., Yamamoto, T., Sugawara, M., and Arakawa, Y. (2011). Extremely high temperature (220°C) continuous-wave operation of 1300-nm-range quantum-dot lasers. In *The European Conference on Lasers and Electro-Optics*, page PDA_1. Optical Society of America.
- [119] Kapon, E. (1999). *Semiconductor lasers I: fundamentals*. Academic Press.
- [120] Kechaou, K., Thedrez, B., Grillot, F., Aubin, G., Kazmierski, C., and Erasme, D. (2012). Influence of facet phases on adiabatic chirp behavior of index-coupled distributed-feedback lasers. In *IEEE Photonics Conference 2012*, pages 332–333. IEEE.
- [121] Kelly, B., Phelan, R., Jones, D., Herbert, C., O'carroll, J., Rensing, M., Wendelboe, J., Watts, C., Kaszubowska-Anandarajah, A., Perry, P., et al. (2007). Discrete mode laser diodes with very narrow linewidth emission. *Electronics Letters*, 43(23).
- [122] Khan, M. Z. M., Ng, T. K., and Ooi, B. S. (2014). Self-assembled InAs/InP quantum dots and quantum dashes: Material structures and devices. *Progress in Quantum Electronics*, 38(6):237–313.
- [123] Kihara, K., Soda, H., Ishikawa, H., and Imai, H. (1987). Evaluation of the coupling coefficient of a distributed feedback laser with residual facet reflectivity. *Journal of Applied Physics*, 62(4):1526–1527.
- [124] Kikuchi, K. (2015). Fundamentals of coherent optical fiber communications. *Journal of Lightwave Technology*, 34(1):157–179.
- [125] Kim, J., Su, H., Minin, S., and Chuang, S. L. (2006). Comparison of linewidth enhancement factor between p-doped and undoped quantum-dot lasers. *IEEE Photonics Technology Letters*, 18(9):1022–1024.
- [126] Kirstaedter, N., Ledentsov, N., Grundmann, M., Bimberg, D., Ustinov, V., Ruvimov, S., Maximov, M., Kop'ev, P. S., Alferov, Z. I., Richter, U., et al. (1994). Low threshold, large T_0 injection laser emission from (InGa) as quantum dots. *Electronics Letters*, 30(17):1416–1417.
- [127] Kita, T., Tang, R., and Yamada, H. (2016). Narrow spectral linewidth silicon photonic wavelength tunable laser diode for digital coherent communication system. *IEEE Journal of Selected Topics in Quantum Electronics*, 22(6):23–34.
- [128] Koch, B. R., Norberg, E. J., Kim, B., Hutchinson, J., Shin, J.-H., Fish, G., and Fang, A. (2013). Integrated silicon photonic laser sources for telecom and datacom. In *National Fiber Optic Engineers Conference*, pages PDP5C–8. Optical Society of America.

- [129] Koch, T. L. and Bowers, J. E. (1984). Nature of wavelength chirping in directly modulated semiconductor lasers. *Electronics Letters*, 20(25):1038–1040.
- [130] Koch, T. L., Koren, U., and Miller, B. (1988). High performance tunable 1.5 μm InGaAs/InGaAsP multiple quantum well distributed bragg reflector lasers. *Applied Physics Letters*, 53(12):1036–1038.
- [131] Koch, T. L. and Linke, R. (1986). Effect of nonlinear gain reduction on semiconductor laser wavelength chirping. *Applied Physics Letters*, 48(10):613–615.
- [132] Kotani, J., Van Veldhoven, P., De Vries, T., Smalbrugge, B., Bente, E., Smit, M., and Nötzel, R. (2009). First demonstration of single-layer InAs/InP (100) quantum-dot laser: continuous wave, room temperature, ground state. *Electronics Letters*, 45(25):1317–1318.
- [133] Kovsh, A. (2008). Quantum-dot comb laser with low relative-intensity noise for each mode. *SPIE Newsroom*.
- [134] Kovsh, A., Maleev, N., Zhukov, A., Mikhrin, S., Vasil'ev, A., Semenova, E., Shernyakov, Y. M., Maximov, M., Livshits, D., Ustinov, V., et al. (2003). InAs/InGaAs/GaAs quantum dot lasers of 1.3 μm range with enhanced optical gain. *Journal of Crystal Growth*, 251(1-4):729–736.
- [135] Kroemer, H. (1963). A proposed class of hetero-junction injection lasers. *Proceedings of the IEEE*, 51(12):1782–1783.
- [136] Kwoen, J., Jang, B., Lee, J., Kageyama, T., Watanabe, K., and Arakawa, Y. (2018). All MBE grown InAs/GaAs quantum dot lasers on on-axis Si (001). *Optics Express*, 26(9):11568–11576.
- [137] Kwoen, J., Jang, B., Watanabe, K., and Arakawa, Y. (2019). High-temperature continuous-wave operation of directly grown InAs/GaAs quantum dot lasers on on-axis Si (001). *Optics Express*, 27(3):2681–2688.
- [138] Lang, R. and Kobayashi, K. (1980). External optical feedback effects on semiconductor injection laser properties. *IEEE journal of Quantum Electronics*, 16(3):347–355.
- [139] Ledentsov, N. (2010). Quantum dot laser. *Semiconductor Science and Technology*, 26(1):014001.
- [140] Ledentsov, N., Shchukin, V., Grundmann, M., Kirstaedter, N., Böhrer, J., Schmidt, O., Bimberg, D., Ustinov, V., Egorov, A. Y., Zhukov, A., et al. (1996). Direct formation of vertically coupled quantum dots in Stranski-Krastanow growth. *Physical Review B*, 54(12):8743.
- [141] Lee, A., Jiang, Q., Tang, M., Seeds, A., and Liu, H. (2012). Continuous-wave InAs/GaAs quantum-dot laser diodes monolithically grown on Si substrate with low threshold current densities. *Optics Express*, 20(20):22181–22187.
- [142] Lelarge, F., Dagens, B., Renaudier, J., Brenot, R., Accard, A., van Dijk, F., Make, D., Le Gouezigou, O., Provost, J.-G., Poingt, F., et al. (2007). Recent advances on InAs/InP quantum dash based semiconductor lasers and optical amplifiers operating at 1.55 μm . *IEEE Journal of Selected Topics in Quantum Electronics*, 13(1):111–124.

- [143] Lenstra, D., Verbeek, B., and Den Boef, A. (1985). Coherence collapse in single-mode semiconductor lasers due to optical feedback. *IEEE Journal of Quantum Electronics*, 21(6):674–679.
- [144] Levine, A., Van Tartwijk, G., Lenstra, D., and Erneux, T. (1995). Diode lasers with optical feedback: Stability of the maximum gain mode. *Physical Review A*, 52(5):R3436.
- [145] Li, Q., Ng, K. W., and Lau, K. M. (2015). Growing antiphase-domain-free GaAs thin films out of highly ordered planar nanowire arrays on exact (001) silicon. *Applied Physics Letters*, 106(7):072105.
- [146] Li, S., Gong, Q., Cao, C., Wang, X., Yan, J., Wang, Y., and Wang, H. (2013). The developments of InP-based quantum dot lasers. *Infrared Physics & Technology*, 60:216–224.
- [147] Liang, D. and Bowers, J. E. (2010). Recent progress in lasers on silicon. *Nature Photonics*, 4(8):511.
- [148] Liang, D., Huang, X., Kurczveil, G., Fiorentino, M., and Beausoleil, R. (2016). Integrated finely tunable microring laser on silicon. *Nature Photonics*, 10(11):719.
- [149] Liao, M., Chen, S., Liu, Z., Wang, Y., Ponnampalam, L., Zhou, Z., Wu, J., Tang, M., Shutts, S., Liu, Z., Smowton, P. M., Yu, S., Seeds, A., and Liu, H. (2018). Low-noise 1.3 μm InAs/GaAs quantum dot laser monolithically grown on silicon. *Photonics Research*, 6(11):1062–1066.
- [150] Liao, P. F. and Kelley, P. (2012). *Quantum well lasers*. Elsevier.
- [151] Lin, C.-H., Lin, H.-H., and Lin, F.-Y. (2012a). Four-wave mixing analysis of quantum dot semiconductor lasers for linewidth enhancement factor extraction. *Optics Express*, 20(1):101–110.
- [152] Lin, G., Tang, H.-L., Cheng, H.-C., and Chen, H.-L. (2012b). Analysis of relative intensity noise spectra for uniformly and chirpily stacked InAs-InGaAs-GaAs quantum dot lasers. *Journal of Lightwave Technology*, 30(3):331–336.
- [153] Lin, L.-C., Chen, C.-Y., Huang, H., Arsenijević, D., Bimberg, D., Grillot, F., and Lin, F.-Y. (2018). Comparison of optical feedback dynamics of InAs/GaAs quantum-dot lasers emitting solely on ground or excited states. *Optics Letters*, 43(2):210–213.
- [154] Linder, K., Phillips, J., Qasaimeh, O., Liu, X., Krishna, S., Bhattacharya, P., and Jiang, J. (1999). Self-organized $\text{In}_{0.4}\text{Ga}_{0.6}\text{As}$ quantum-dot lasers grown on Si substrates. *Applied Physics Letters*, 74(10):1355–1357.
- [155] Lingnau, B., Chow, W. W., Schöll, E., and Lüdge, K. (2013). Feedback and injection locking instabilities in quantum-dot lasers: a microscopically based bifurcation analysis. *New Journal of Physics*, 15(9):093031.
- [156] Liu, A. Y. and Bowers, J. (2018). Photonic integration with epitaxial III–V on silicon. *IEEE Journal of Selected Topics in Quantum Electronics*, 24(6):1–12.

- [157] Liu, A. Y., Komljenovic, T., Davenport, M. L., Gossard, A. C., and Bowers, J. E. (2017a). Reflection sensitivity of 1.3 μm quantum dot lasers epitaxially grown on silicon. *Optics Express*, 25(9):9535–9543.
- [158] Liu, A. Y., Peters, J., Huang, X., Jung, D., Norman, J., Lee, M. L., Gossard, A. C., and Bowers, J. E. (2017b). Electrically pumped continuous-wave 1.3 μm quantum-dot lasers epitaxially grown on on-axis (001) GaP/Si. *Optics Letters*, 42(2):338–341.
- [159] Liu, A. Y., Srinivasan, S., Norman, J., Gossard, A. C., and Bowers, J. E. (2015). Quantum dot lasers for silicon photonics. *Photonics Research*, 3(5):B1–B9.
- [160] Liu, G., Jin, X., and Chuang, S.-L. (2001). Measurement of linewidth enhancement factor of semiconductor lasers using an injection-locking technique. *IEEE Photonics Technology Letters*, 13(5):430–432.
- [161] Liu, G., Stintz, A., Li, H., Malloy, K., and Lester, L. (1999). Extremely low room-temperature threshold current density diode lasers using InAs dots in InGaAs quantum well. *Electronics Letters*, 35(14):1163–1165.
- [162] Liu, H., Wang, T., Jiang, Q., Hogg, R., Tutu, F., Pozzi, F., and Seeds, A. (2011). Long-wavelength InAs/GaAs quantum-dot laser diode monolithically grown on Ge substrate. *Nature Photonics*, 5(7):416.
- [163] Liu, S., Wu, X., Jung, D., Norman, J. C., Kennedy, M., Tsang, H. K., Gossard, A. C., and Bowers, J. E. (2019). High-channel-count 20 GHz passively mode-locked quantum dot laser directly grown on Si with 4.1 Tbit/s transmission capacity. *Optica*, 6(2):128–134.
- [164] Lu, Z., Liu, J., Poole, P., Song, C., and Chang, S. (2018). Ultra-narrow linewidth quantum dot coherent comb lasers with self-injection feedback locking. *Optics Express*, 26(9):11909–11914.
- [165] Lu, Z., Poole, P., Liu, J., Barrios, P., Jiao, Z., Pakulski, G., Poitras, D., Goodchild, D., Rioux, B., and SpringThorpe, A. (2011). High-performance 1.52 μm InAs/InP quantum dot distributed feedback laser. *Electronics Letters*, 47(14):818–819.
- [166] Lüdge, K., Schöll, E., Viktorov, E., and Erneux, T. (2011). Analytical approach to modulation properties of quantum dot lasers. *Journal of Applied Physics*, 109(10):103112.
- [167] Lüdge, K. and Schuster, H. G. (2012). *Nonlinear laser dynamics: from quantum dots to cryptography*, volume 5. John Wiley & Sons.
- [168] Malic, E., Bormann, M. J., Hovel, P., Kuntz, M., Bimberg, D., Knorr, A., and Scholl, E. (2007). Coulomb damped relaxation oscillations in semiconductor quantum dot lasers. *IEEE Journal of Selected Topics in Quantum Electronics*, 13(5):1242–1248.
- [169] Marcinkevičius, S. (2008). Dynamics of carrier transfer into In(Ga)As self-assembled quantum dots. In *Self-Assembled Quantum Dots*, pages 129–163. Springer.
- [170] Marcuse, D. (1984). Computer simulation of laser photon fluctuations: Theory of single-cavity laser. *IEEE Journal of Quantum Electronics*, 20(10):1139–1148.

- [171] Marko, I. P., Adams, A. R., Massé, N. F., and Sweeney, S. J. (2014). Effect of non-pinned carrier density above threshold in InAs quantum dot and quantum dash lasers. *IET Optoelectronics*, 8(2):88–93.
- [172] Markus, A., Chen, J., Paranthoen, C., Fiore, A., Platz, C., and Gauthier-Lafaye, O. (2003a). Simultaneous two-state lasing in quantum-dot lasers. *Applied Physics Letters*, 82(12):1818–1820.
- [173] Markus, A., Chen, J. X., Gauthier-Lafaye, O., Provost, J.-G., Paranthoën, C., and Fiore, A. (2003b). Impact of intraband relaxation on the performance of a quantum-dot laser. *IEEE Journal of Selected Topics in Quantum Electronics*, 9(5):1308–1314.
- [174] Martinez, A., Li, Y., Lester, L. F., and Gray, A. L. (2007). Microwave frequency characterization of undoped and p-doped quantum dot lasers. *Applied Physics Letters*, 90(25):251101.
- [175] Martinez, A., Merghem, K., Bouchoule, S., Moreau, G., Ramdane, A., Provost, J. G., Alexandre, F., Grillot, F., Dehaese, O., and Piron, R. (2008). Dynamic properties of InAs/InP(311B) quantum dot Fabry-Perot lasers emitting at 1.52- μm . *Applied Physics Letters*, 93(2):939.
- [176] Matsuda, M., Yasuoka, N., Nishi, K., Takemasa, K., Yamamoto, T., Sugawara, M., and Arakawa, Y. (2018). Low-noise characteristics on 1.3- μm -wavelength quantum-dot DFB lasers under external optical feedback. In *2018 IEEE International Semiconductor Laser Conference (ISLC)*, pages 1–2.
- [177] Matthews, M., Cameron, K., Wyatt, R., and Devlin, W. (1985). Packaged frequency-stable tunable 20 kHz linewidth 1.5 μm InGaAsP external cavity laser. *Electronics Letters*, 21(3):113–115.
- [178] McDaniel, A. and Mahalov, A. (2018). Stochastic differential equation model for spontaneous emission and carrier noise in semiconductor lasers. *IEEE Journal of Quantum Electronics*.
- [179] Melnik, S., Huyet, G., and Uskov, A. V. (2006). The linewidth enhancement factor α of quantum dot semiconductor lasers. *Optics Express*, 14(7):2950–2955.
- [180] Mi, Z., Bhattacharya, P., and Fathpour, S. (2005). High-speed 1.3 μm tunnel injection quantum-dot lasers. *Applied Physics Letters*, 86(15):153109.
- [181] Mi, Z., Bhattacharya, P., Yang, J., and Pipe, K. P. (2005). Room-temperature self-organised $\text{In}_{0.5}\text{Ga}_{0.5}\text{As}$ quantum dot laser on silicon. *Electronics Letters*, 41(13):742–744.
- [182] Mikhrin, S., Kovsh, A., Krestnikov, I., Kozhukhov, A., Livshits, D., Ledentsov, N., Shernyakov, Y. M., Novikov, I., Maximov, M., Ustinov, V., et al. (2005). High power temperature-insensitive 1.3 μm InAs/InGaAs/GaAs quantum dot lasers. *Semiconductor Science and Technology*, 20(5):340.
- [183] Mirin, R., Gossard, A., and Bowers, J. (1996). Room temperature lasing from InGaAs quantum dots. *Electronics Letters*, 32(18):1732–1734.

- [184] Miyamoto, Y., Cao, M., Shingai, Y., Furuya, K., Suematsu, Y., Ravikumar, K., and Arai, S. (1987). Light emission from quantum-box structure by current injection. *Japanese Journal of Applied Physics*, 26(4A):L225.
- [185] Mizutani, K., Yashiki, K., Kurihara, M., Suzuki, Y., Hagihara, Y., Hatori, N., Shimizu, T., Urino, Y., Nakamura, T., Kurata, K., and Arakawa, Y. (2015). Isolator free optical I/O core transmitter by using quantum dot laser. In *2015 IEEE 12th International Conference on Group IV Photonics (GFP)*, pages 177–178. IEEE.
- [186] Mork, J., Tromborg, B., and Mark, J. (1992). Chaos in semiconductor lasers with optical feedback: theory and experiment. *IEEE Journal of Quantum Electronics*, 28(1):93–108.
- [187] Mukhametzhanov, I., Wei, Z., Heitz, R., and Madhukar, A. (1999). Punctuated island growth: An approach to examination and control of quantum dot density, size, and shape evolution. *Applied Physics Letters*, 75(1):85.
- [188] Nagarajan, R. and Bowers, J. E. (1993). Effects of carrier transport on injection efficiency and wavelength chirping in quantum-well lasers. *IEEE Journal of Quantum Electronics*, 29(6):1601–1608.
- [189] Newell, T., Bossert, D., Stintz, A., Fuchs, B., Malloy, K., and Lester, L. (1999). Gain and linewidth enhancement factor in InAs quantum-dot laser diodes. *IEEE Photonics Technology Letters*, 11(12):1527–1529.
- [190] Newman, Z., Maurice, V., Drake, T., Stone, J., Briles, T., Spencer, D., Fredrick, C., Li, Q., Westly, D., Ilic, B., et al. (2018). Photonic integration of an optical atomic clock. *arXiv preprint arXiv:1811.00616*.
- [191] Nielsen, T. R., Gartner, P., and Jahnke, F. (2004). Many-body theory of carrier capture and relaxation in semiconductor quantum-dot lasers. *Physical Review B*, 69(23):235314.
- [192] Nilsson, H. H., Zhang, J.-Z., and Galbraith, I. (2005). Homogeneous broadening in quantum dots due to Auger scattering with wetting layer carriers. *Physical Review B*, 72(20):205331.
- [193] Nishi, K., Takemasa, K., Sugawara, M., and Arakawa, Y. (2017). Development of quantum dot lasers for data-com and silicon photonics applications. *IEEE Journal of Selected Topics in Quantum Electronics*, 23(6):1–7.
- [194] Nishi, K., Yamada, M., Anan, T., Gomyo, A., and Sugou, S. (1998). Long-wavelength lasing from InAs self-assembled quantum dots on (311)b InP. *Applied Physics Letters*, 73(4):526–528.
- [195] Norman, J. (2018). *Quantum Dot Lasers for Silicon Photonics*. PhD thesis, UC Santa Barbara.
- [196] Norman, J. C., Jung, D., Wan, Y., and Bowers, J. E. (2018). Perspective: The future of quantum dot photonic integrated circuits. *APL Photonics*, 3(3):030901.

- [197] Norman, J. C., Jung, D., Zhang, Z., Wan, Y., Liu, S., Shang, C., Herrick, R. W., Chow, W. W., Gossard, A. C., and Bowers, J. E. (2019). A review of high-performance quantum dot lasers on silicon. *IEEE Journal of Quantum Electronics*, 55(2):1–11.
- [198] Nozik, A. J. (2008). Multiple exciton generation in semiconductor quantum dots. *Chemical Physics Letters*, 457(1-3):3–11.
- [199] O’Brien, D., Hegarty, S., Huyet, G., McInerney, J., Kettler, T., Laemmlin, M., Bimberg, D., Ustinov, V., Zhukov, A., Mikhlin, S., et al. (2003). Feedback sensitivity of 1.3 μm InAs/GaAs quantum dot lasers. *Electronics Letters*, 39(25):1.
- [200] Ohtsubo, J. (2012). *Semiconductor Lasers: Stability, Instability and Chaos*, volume 111. Springer.
- [201] Okai, M., Suzuki, M., Taniwatari, T., and Chinone, N. (1994). Corrugation-pitch-modulated distributed feedback lasers with ultranarrow spectral linewidth. *Japanese Journal of Applied Physics*, 33(5R):2563.
- [202] Okoshi, T., Kikuchi, K., and Nakayama, A. (1980). Novel method for high resolution measurement of laser output spectrum. *Electronics Letters*, 16(16):630–631.
- [203] Olesen, H., Tromborg, B., Lassen, H. E., and Pan, X. (1992). Mode instability and linewidth rebroadening in DFB lasers. *Electronics Letters*, 28(5):444.
- [204] Olsson, S. L., Cho, J., Chandrasekhar, S., Chen, X., Winzer, P. J., and Makovejs, S. (2018). Probabilistically shaped PDM 4096-QAM transmission over up to 200 km of fiber using standard intradyne detection. *Optics Express*, 26(4):4522–4530.
- [205] Osborne, S., Blood, P., Smowton, P., Lutti, J., Xin, Y., Stintz, A., Huffaker, D., and Lester, L. F. (2004). State filling in InAs quantum-dot laser structures. *IEEE Journal of Quantum Electronics*, 40(12):1639–1645.
- [206] Osinski, M. and Buus, J. (1987). Linewidth broadening factor in semiconductor lasers—an overview. *IEEE Journal of Quantum Electronics*, 23(1):9–29.
- [207] Otto, C., Globisch, B., Lüdge, K., Schöll, E., and Erneux, T. (2012). Complex dynamics of semiconductor quantum dot lasers subject to delayed optical feedback. *International Journal of Bifurcation and Chaos*, 22(10):1250246.
- [208] Pavesi, L. and Lockwood, D. J. (2011). *Silicon Photonics II: Components and Integration*. Springer.
- [209] Pawlus, R., Breuer, S., and Virte, M. (2017). Relative intensity noise reduction in a dual-state quantum-dot laser by optical feedback. *Optics Letters*, 42(21):4259–4262.
- [210] Pawlus, R., Columbo, L., Bardella, P., Breuer, S., and Gioannini, M. (2018). Intensity noise behavior of an InAs/InGaAs quantum dot laser emitting on ground states and excited states. *Optics Letters*, 43(4):867–870.
- [211] Petermann, K. (2012). *Laser diode modulation and noise*, volume 3. Springer Science & Business Media.

- [212] Platz, C., Paranthoën, C., Caroff, P., Bertru, N., Labbé, C., Even, J., Dehaese, O., Folliot, H., Le Corre, A., Loualiche, S., et al. (2005). Comparison of InAs quantum dot lasers emitting at $1.55\ \mu\text{m}$ under optical and electrical injection. *Semiconductor Science and Technology*, 20(5):459.
- [213] Poole, P., Kaminska, K., Barrios, P., Lu, Z., and Liu, J. (2009). Growth of InAs/InP-based quantum dots for $1.55\ \mu\text{m}$ laser applications. *Journal of Crystal Growth*, 311(6):1482–1486.
- [214] Porte, X., Soriano, M. C., and Fischer, I. (2014). Similarity properties in the dynamics of delayed-feedback semiconductor lasers. *Physical Review A*, 89(2):023822.
- [215] Pourshab, N., Gholami, A., Hekmat, M. J., and Shahriyari, N. (2017). Analysis of narrow linewidth fiber laser using double subring resonators. *JOSA B*, 34(11):2414–2420.
- [216] Provost, J.-G. and Grillot, F. (2011). Measuring the chirp and the linewidth enhancement factor of optoelectronic devices with a Mach–Zehnder interferometer. *IEEE Photonics Journal*, 3(3):476–488.
- [217] Rasmussen, T. S., Yu, Y., and Mork, J. (2019). Suppression of coherence collapse in semiconductor fano lasers. *arXiv preprint arXiv:1906.06923*.
- [218] Redlich, C., Lingnau, B., Huang, H., Raghunathan, R., Schires, K., Poole, P., Grillot, F., and Lüdge, K. (2017). Linewidth rebroadening in quantum dot semiconductor lasers. *IEEE Journal of Selected Topics in Quantum Electronics*, 23(6):1–10.
- [219] Roelkens, G., Liu, L., Liang, D., Jones, R., Fang, A., Koch, B., and Bowers, J. (2010). III-V/silicon photonics for on-chip and intra-chip optical interconnects. *Laser & Photonics Reviews*, 4(6):751–779.
- [220] Roelkens, G., Van Campenhout, J., Brouckaert, J., Van Thourhout, D., Baets, R., Romeo, P. R., Regreny, P., Kazmierczak, A., Seassal, C., Letartre, X., et al. (2007). III-V/Si photonics by die-to-wafer bonding. *Materials Today*, 10(7-8):36–43.
- [221] Röhm, A., Lingnau, B., and Lüdge, K. (2015). Ground-state modulation-enhancement by two-state lasing in quantum-dot laser devices. *Applied Physics Letters*, 106(19):191102.
- [222] Röhm, A., Lingnau, B., and Luedge, K. (2014). Understanding ground-state quenching in quantum-dot lasers. *IEEE Journal of Quantum Electronics*, 51(1):1–11.
- [223] Romeo, P. R., Van Campenhout, J., Regreny, P., Kazmierczak, A., Seassal, C., Letartre, X., Hollinger, G., Van Thourhout, D., Baets, R., Fedeli, J., et al. (2006). Heterogeneous integration of electrically driven microdisk based laser sources for optical interconnects and photonic ICs. *Optics Express*, 14(9):3864–3871.
- [224] Rosencher, E. and Vinter, B. (2002). *Optoelectronics*. Cambridge University Press.
- [225] Salhi, A., Raino, G., Fortunato, L., Tasco, V., Visimberga, G., Martiradonna, L., Todaro, M. T., De Giorgi, M., Cingolani, R., Trampert, A., et al. (2008). Enhanced performances of quantum dot lasers operating at $1.3\ \mu\text{m}$. *IEEE Journal of Selected Topics in Quantum Electronics*, 14(4):1188–1196.

- [226] Sanaee, M. and Zarifkar, A. (2014). Theoretical modeling of relative intensity noise in p-doped 1.3- μm InAs/GaAs quantum dot lasers. *Journal of Lightwave Technology*, 33(1):234–243.
- [227] Santis, C. T., Steger, S. T., Vilenchik, Y., Vasilyev, A., and Yariv, A. (2014). High-coherence semiconductor lasers based on integral high-Q resonators in hybrid Si/III-V platforms. *Proceedings of the National Academy of Sciences*, 111(8):2879–2884.
- [228] Santis, C. T., Vilenchik, Y., Satyan, N., Rakuljic, G., and Yariv, A. (2018). Quantum control of phase fluctuations in semiconductor lasers. *Proceedings of the National Academy of Sciences*, 115(34):E7896–E7904.
- [229] Schatz, R. (1995). Dynamics of spatial hole burning effects in DFB lasers. *IEEE Journal of Quantum Electronics*, 31(11):1981–1993.
- [230] Schires, K., Girard, N., Baili, G., Duan, G.-H., Gomez, S., and Grillot, F. (2016). Dynamics of hybrid III-V silicon semiconductor lasers for integrated photonics. *IEEE Journal of Selected Topics in Quantum Electronics*, 22(6):43–49.
- [231] Schneider, H., Chow, W., and Koch, S. W. (2002). Anomalous carrier-induced dispersion in quantum-dot active media. *Physical Review B*, 66(4):041310.
- [232] Schneider, H. C., Chow, W. W., and Koch, S. W. (2004). Excitation-induced dephasing in semiconductor quantum dots. *Physical Review B*, 70(23):235308.
- [233] Schuh, K., Gartner, P., and Jahnke, F. (2013). Combined influence of carrier-phonon and coulomb scattering on the quantum-dot population dynamics. *Physical Review B*, 87(3):035301.
- [234] Schunk, N. and Petermann, K. (1988). Numerical analysis of the feedback regimes for a single-mode semiconductor laser with external feedback. *IEEE Journal of Quantum Electronics*, 24(7):1242–1247.
- [235] Seimetz, M. (2008). Laser linewidth limitations for optical systems with high-order modulation employing feed forward digital carrier phase estimation. In *OFC/NFOEC 2008-2008 Conference on Optical Fiber Communication/National Fiber Optic Engineers Conference*, pages 1–3. IEEE.
- [236] Septon, T., Becker, A., Gosh, S., Shtendel, G., Sichkovskiy, V., Schnabel, F., Sengül, A., Bjelica, M., Witzigmann, B., Reithmaier, J. P., et al. (2019). Large linewidth reduction in semiconductor lasers based on atom-like gain material. *Optica*, 6(8):1071–1077.
- [237] Shchekin, O. B., Ahn, J., and Deppe, D. G. (2002). High temperature performance of self-organised quantum dot laser with stacked p-doped active region. *Electronics Letters*, 38(14):712–713.
- [238] Siegert, J., Marcinkevičius, S., and Zhao, Q. X. (2005). Carrier dynamics in modulation-doped InAs/GaAs quantum dots. *Physical Review B*, 72(8):085316.
- [239] Smolyakov, G. A. and Osinski, M. (2011). High-speed modulation analysis of strongly injection-locked semiconductor ring lasers. *IEEE Journal of Quantum Electronics*, 47(11):1463–1471.

- [240] Spencer, D. T., Drake, T., Briles, T. C., Stone, J., Sinclair, L. C., Fredrick, C., Li, Q., Westly, D., Ilic, B. R., Bluestone, A., et al. (2018). An optical-frequency synthesizer using integrated photonics. *Nature*, 557(7703):81.
- [241] Spott, A., Peters, J., Davenport, M. L., Stanton, E. J., Merritt, C. D., Bewley, W. W., Vurgaftman, I., Kim, C. S., Meyer, J. R., Kirch, J., et al. (2016). Quantum cascade laser on silicon. *Optica*, 3(5):545–551.
- [242] Strogatz, S. H. and Herbert, D. E. (1996). Nonlinear dynamics and chaos. *Medical Physics-New York-Institute of Physics*, 23(6):993–995.
- [243] Su, H. and Lester, L. F. (2005). Dynamic properties of quantum dot distributed feedback lasers: high speed, linewidth and chirp. *Journal of Physics D: Applied Physics*, 38(13):2112.
- [244] Sugawara, M., Hatori, N., Ebe, H., Ishida, M., Arakawa, Y., Akiyama, T., Otsubo, K., and Nakata, Y. (2005). Modeling room-temperature lasing spectra of 1.3- μm self-assembled InAs/GaAs quantum-dot lasers: Homogeneous broadening of optical gain under current injection. *Journal of Applied Physics*, 97(4):043523.
- [245] Suh, M.-G., Yang, Q.-F., Yang, K. Y., Yi, X., and Vahala, K. J. (2016). Microresonator soliton dual-comb spectroscopy. *Science*, 354(6312):600–603.
- [246] Sun, C., Wade, M. T., Lee, Y., Orcutt, J. S., Alloatti, L., Georgas, M. S., Waterman, A. S., Shainline, J. M., Avizienis, R. R., Lin, S., R. Moss, B., Kumar, R., Pavanello, F., Atabaki, A. H., Cook, H. M., Ou, A. J., Leu, J. C., Chen, Y.-H., Asanovic, K., Ram, R. J., Popovic, M. A., and Stojanovic, V. M. (2015). Single-chip microprocessor that communicates directly using light. *Nature*, 528(7583):534.
- [247] Sun, J., Timurdogan, E., Yaacobi, A., Hosseini, E. S., Leake, G., Coolbaugh, D., and Watts, M. R. (2013). Large-scale optical phased arrays enabled by silicon photonics. In *CLEO: 2013*, pages 1–2. IEEE.
- [248] Takaki, Keishi, KISE, Tomofumi, MARUYAMA, Kazuomi, YAMANAKA, Nobumitsu, FUNABASHI, and Masaki (2003). Reduced linewidth re-broadening by suppressing longitudinal spatial hole burning in high-power 1.55- μm continuous-wave distributed-feedback (CW-DFB) laser diodes. *Quantum Electronics IEEE Journal of*, 39(9):1060–1065.
- [249] Takano, S., Sasaki, T., Yamada, H., Kitamura, M., and Mito, I. (1989). Sub-MHz spectral linewidth in 1.5 μm separate-confinement-heterostructure (SCH) quantum-well DFB LDs. *Electronics Letters*, 25(5):356–357.
- [250] Tan, H., Mi, Z., Bhattacharya, P., and Klotzkin, D. (2008). Dependence of linewidth enhancement factor on duty cycle in InGaAs–GaAs quantum-dot lasers. *IEEE Photonics Technology Letters*, 20(8):593–595.
- [251] Tanabe, K., Watanabe, K., and Arakawa, Y. (2012). III-V/Si hybrid photonic devices by direct fusion bonding. *Scientific Reports*, 2:349.
- [252] Temkin, H., Olsson, N., Abeles, J., Logan, R., and Panish, M. (1986). Reflection noise in index-guided InGaAsP lasers. *IEEE Journal of Quantum Electronics*, 22(2):286–293.

- [253] Thompson, P., Cox, D., and Hastings, J. (1987). Rietveld refinement of Debye–Scherrer synchrotron X-ray data from Al_2O_3 . *Journal of Applied Crystallography*, 20(2):79–83.
- [254] Tien, P. (1977). Integrated optics and new wave phenomena in optical waveguides. *Reviews of Modern Physics*, 49(2):361.
- [255] Tkach, R. and Chraplyvy, A. (1986). Regimes of feedback effects in 1.5- μm distributed feedback lasers. *Journal of Lightwave technology*, 4(11):1655–1661.
- [256] Tromborg, B., Osmundsen, J., and Olesen, H. (1984). Stability analysis for a semiconductor laser in an external cavity. *IEEE Journal of Quantum Electronics*, 20(9):1023–1032.
- [257] Uchida, A. (2012). *Optical communication with chaotic lasers: applications of nonlinear dynamics and synchronization*. John Wiley & Sons.
- [258] Uomi, K., Tsuchiya, T., Aoki, M., Suzuki, M., Nakano, H., and Chinone, N. (2010). Ultrahigh-speed multiquantum well-distributed feedback semiconductor lasers. *Electronics & Communications in Japan*, 75(6):13–23.
- [259] Ustinov, V., Kovsh, A., Zhukov, A., Egorov, A. Y., Ledentsov, N., Lunev, A., Shernyakov, Y. M., Maksimov, M., Tsatsul'nikov, A., Volovik, B., et al. (1998). Low-threshold quantum-dot injection heterolaser emitting at 1.84 μm . *Technical Physics Letters*, 24(1):22–23.
- [260] Van der Ziel, J., Dingle, R., Miller, R. C., Wiegmann, W., and Nordland Jr, W. (1975). Laser oscillation from quantum states in very thin GaAs- $\text{Al}_{0.2}\text{Ga}_{0.8}\text{As}$ multilayer structures. *Applied Physics Letters*, 26(8):463–465.
- [261] Van der Ziel, J., Dupuis, R., Logan, R., and Pinzone, C. (1987). Degradation of GaAs lasers grown by metalorganic chemical vapor deposition on Si substrates. *Applied Physics Letters*, 51(2):89–91.
- [262] Vermeulen, D., De Koninck, Y., Li, Y., Lambert, E., Bogaerts, W., Baets, R., and Roelkens, G. (2012). Reflectionless grating couplers for silicon-on-insulator photonic integrated circuits. *Optics Express*, 20(20):22278–22283.
- [263] Veselinov, K., Grillot, F., Cornet, C., Even, J., Bekiarski, A., Gioannini, M., and Loualiche, S. (2007). Analysis of the double laser emission occurring in 1.55- μm InAs-InP (113)B quantum-dot lasers. *IEEE Journal of Quantum Electronics*, 43(9):810–816.
- [264] Virtanen, H., Uusitalo, T., and Dumitrescu, M. (2017). Simulation studies of DFB laser longitudinal structures for narrow linewidth emission. *Optical and Quantum Electronics*, 49(4):160.
- [265] Virte, M., Panajotov, K., Thienpont, H., and Sciamanna, M. (2013). Deterministic polarization chaos from a laser diode. *Nature Photonics*, 7(1):60.
- [266] Virte, M., Pawlus, R., Sciamanna, M., Panajotov, K., and Breuer, S. (2016). Energy exchange between modes in a multimode two-color quantum dot laser with optical feedback. *Optics Letters*, 41(14):3205–3208.

- [267] Wan, Y., Jung, D., Norman, J., Shang, C., MacFarlane, I., Li, Q., Kennedy, M., Gossard, A. C., Lau, K. M., and Bowers, J. E. (2017a). O-band electrically injected quantum dot micro-ring lasers on on-axis (001) GaP/Si and V-groove Si. *Optics Express*, 25(22):26853–26860.
- [268] Wan, Y., Li, Q., Geng, Y., Shi, B., and Lau, K. M. (2015). InAs/GaAs quantum dots on GaAs-on-V-grooved-Si substrate with high optical quality in the 1.3 μm band. *Applied Physics Letters*, 107(8):081106.
- [269] Wan, Y., Li, Q., Liu, A. Y., Chow, W. W., Gossard, A. C., Bowers, J. E., Hu, E. L., and Lau, K. M. (2016a). Sub-wavelength InAs quantum dot micro-disk lasers epitaxially grown on exact Si (001) substrates. *Applied Physics Letters*, 108(22):221101.
- [270] Wan, Y., Li, Q., Liu, A. Y., Gossard, A. C., Bowers, J. E., Hu, E. L., and Lau, K. M. (2016b). Optically pumped 1.3 μm room-temperature InAs quantum-dot micro-disk lasers directly grown on (001) silicon. *Optics Letters*, 41(7):1664–1667.
- [271] Wan, Y., Norman, J., Li, Q., Kennedy, M., Liang, D., Zhang, C., Huang, D., Zhang, Z., Liu, A. Y., Torres, A., et al. (2017b). 1.3 μm submilliamp threshold quantum dot micro-lasers on Si. *Optica*, 4(8):940–944.
- [272] Wang, C. (2015). Modulation dynamics of InP-based nanostructure laser and quantum cascade laser. *Institut National des Sciences Appliquées de Rennes*.
- [273] Wang, C., Osiński, M., Even, J., and Grillot, F. (2014). Phase-amplitude coupling characteristics in directly modulated quantum dot lasers. *Applied Physics Letters*, 105(22):221114.
- [274] Wang, C., Schires, K., Osiński, M., Poole, P. J., and Grillot, F. (2016a). Thermally insensitive determination of the linewidth broadening factor in nanostructured semiconductor lasers using optical injection locking. *Scientific Reports*, 6:27825.
- [275] Wang, C., Zhuang, J.-P., Grillot, F., and Chan, S.-C. (2016b). Contribution of off-resonant states to the phase noise of quantum dot lasers. *Optics express*, 24(26):29872–29881.
- [276] Wang, J. and Petermann, K. (1991). Noise analysis of semiconductor lasers within the coherence collapse regime. *IEEE Journal of Quantum Electronics*, 27(1):3–9.
- [277] Wang, R., Stintz, A., Varangis, P., Newell, T., Li, H., Malloy, K., and Lester, L. (2001). Room-temperature operation of InAs quantum-dot lasers on InP [001]. *IEEE Photonics Technology Letters*, 13(8):767–769.
- [278] Wang, Y., Chen, S., Yu, Y., Zhou, L., Liu, L., Yang, C., Liao, M., Tang, M., Liu, Z., Wu, J., et al. (2018). Monolithic quantum-dot distributed feedback laser array on silicon. *Optica*, 5(5):528–533.
- [279] Wasilewski, Z. R., Fafard, S., and McCaffrey, J. P. (1999). Size and shape engineering of vertically stacked self-assembled quantum dots. *Journal of Crystal Growth*, 201(5):1131–1135.

- [280] Weiss, C., Godone, A., and Olafsson, A. (1983). Routes to chaotic emission in a cw He-Ne laser. *Physical Review A*, 28(2):892.
- [281] Weiss, C., Klische, W., Ering, P., and Cooper, M. (1985). Instabilities and chaos of a single mode NH_3 ring laser. *Optics communications*, 52(6):405–408.
- [282] Windhorn, T., Metzke, G., Tsauro, B.-Y., and Fan, J. C. (1984). AlGaAs double-heterostructure diode lasers fabricated on a monolithic GaAs/Si substrate. *Applied Physics Letters*, 45(4):309–311.
- [283] Wu, M.-C., Lo, Y.-h., and Wang, S. (1988). Linewidth broadening due to longitudinal spatial hole burning in a long distributed feedback laser. *Applied Physics Letters*, 52(14):1119–1121.
- [284] Wyatt, R. and Devlin, W. (1983). 10 kHz linewidth 1.5 μm InGaAsP external cavity laser with 55 nm tuning range. *Electronics Letters*, 19(3):110–112.
- [285] Xiang, C., Morton, P. A., and Bowers, J. E. (2019). Ultra-narrow linewidth laser based on a semiconductor gain chip and extended Si_3N_4 bragg grating. *Optics Letters*, 44(15):3825–3828.
- [286] Yariv, A. (1989). *Quantum Electronics*. Wiley.
- [287] Yu, Y., Giuliani, G., and Donati, S. (2004). Measurement of the linewidth enhancement factor of semiconductor lasers based on the optical feedback self-mixing effect. *IEEE Photonics Technology Letters*, 16(4):990–992.
- [288] Zhang, C. and Bowers, J. E. (2018). Silicon photonic terabit/s network-on-chip for datacenter interconnection. *Optical Fiber Technology*, 44:2–12.
- [289] Zhang, Y., Du, Q., Wang, C., Fakhru, T., and Bi, L. (2019a). Monolithic integration of broadband optical isolators for polarization-diverse silicon photonics. *Optica*, 6:473–478.
- [290] Zhang, Z., Jung, D., Norman, J., Chow, W. W., and Bowers, J. E. (2019b). Linewidth enhancement factor in InAs/GaAs quantum dot lasers and its implication in isolator-free and narrow linewidth applications. *IEEE Journal of Selected Topics in Quantum Electronics*.
- [291] Zhang, Z., Jung, D., Norman, J. C., Patel, P., Chow, W. W., and Bowers, J. E. (2018). Effects of modulation p doping in InAs quantum dot lasers on silicon. *Applied Physics Letters*, 113(6):061105.
- [292] Zhang, Z., Liu, J., Liu, Y., Guo, J., Yuan, H., Bai, J., and Zhu, N. (2015). 30-GHz directly modulation DFB laser with narrow linewidth. In *Asia Communications and Photonics Conference*, pages AM1B–3. Optical Society of America.
- [293] Zhang, Z., Wang, H., Satyan, N., Rakuljic, G., Santis, C. T., and Yariv, A. (2019c). Coherent and incoherent optical feedback sensitivity of high-coherence Si/III-V hybrid lasers. In *Optical Fiber Communication Conference*, pages W4E–3. Optical Society of America.

- [294] Zhou, Y.-G., Duan, J., Huang, H., Zhao, X.-Y., Cao, C.-F., Gong, Q., Grillot, F., and Wang, C. (2019). Intensity noise and pulse oscillations of an InAs/GaAs quantum dot laser on germanium. *IEEE Journal of Selected Topics in Quantum Electronics*, 25(6):1–10.
- [295] Zhou, Y.-G., Zhao, X.-Y., Cao, C.-F., Gong, Q., and Wang, C. (2018). High optical feedback tolerance of InAs/GaAs quantum dot lasers on germanium. *Optics Express*, 26(21):28131–28139.
- [296] Zhou, Y.-G., Zhou, C., Cao, C.-F., Du, J.-B., Gong, Q., and Wang, C. (2017). Relative intensity noise of InAs quantum dot lasers epitaxially grown on Ge. *Optics Express*, 25(23):28817–28824.
- [297] Zhu, S., Shi, B., Li, Q., and Lau, K. M. (2018). 1.5 μm quantum-dot diode lasers directly grown on CMOS-standard (001) silicon. *Applied Physics Letters*, 113(22):221103.
- [298] Zou, Q. and Azouigui, S. (2012). Analysis of coherence-collapse regime of semiconductor lasers under external optical feedback by perturbation method. *Semiconductor Laser Diode Technology and Applications*, pages 71–86.
- [299] Zubov, F., Maximov, M., Moiseev, E., Savelyev, A., Shernyakov, Y., Livshits, D., Kryzhanovskaya, N., and Zhukov, A. (2015). Observation of zero linewidth enhancement factor at excited state band in quantum dot laser. *Electronics Letters*, 51(21):1686–1688.

Appendix A

Publications

Journal papers

1. **J. Duan**, H. Huang, B. Dong, J. C. Norman, Z. Zhang, J. E. Bowers and F. Grillot, "Dynamic and nonlinear properties of epitaxial quantum dot lasers on silicon for isolator-free integration," *Photonics Research*, Vol. 7, No. 11, (2019).
2. **J. Duan**, H. Huang, B. Dong, D. Jung, J. C. Norman, J. E. Bowers and F. Grillot, "1.3- μm Reflection Insensitive InAs/GaAs Quantum Dot Lasers Directly Grown on Silicon," *IEEE Photonics Technology Letters*, Vol. 31, No. 5, (2019).
3. **J. Duan**, H. Huang, Z. G. Lu, P. Poole, C. Wang and F. Grillot, "Narrow spectral linewidth in InAs/InP quantum dot distributed feedback lasers," *Applied Physics Letters*, 112, 121102, (2018).
4. **J. Duan**, H. Huang, D. Jung, Z. Zhang, J. Norman, J. E. Bowers and F. Grillot, "Semiconductor quantum dot lasers epitaxially grown on silicon with low linewidth enhancement factor," *Applied Physics Letters*, 112, 251111, (2018).
5. **J. Duan**, X. G. Wang, Y. G. Zhou, C. Wang and F. Grillot, "Carrier-Noise Enhanced Relative Intensity Noise of Quantum Dot Lasers," *IEEE Journal of Quantum Electronics*, Vol. 54, No.6, (2018).
6. H. Huang, **J. Duan**, B. Dong, J. Norman, D. Jung, J.E.Bowers and F. Grillot, "Epitaxial quantum dot lasers on silicon with high thermal stability and strong resistance to optical feedback," *APL Photonics* 5, 016103, (2020).
7. Y. Zhou, **J. Duan**, H. Huang, X. Y. Zhao, C. F. Cao, Q. Gong, F. Grillot and C. Wang, "Intensity Noise and Pulse Oscillations of an InAs/GaAs Quantum Dot Laser on

- Germanium," IEEE Journal of Selected Topics in Quantum Electronics, Vol. 25, No. 6, (2019).
8. B. Dong, **J. Duan**, C. Shang, H. Huang, A. B. Sawadogo, D. Jung, Y. Wan, J. E. Bowers and F. Grillot, "Influence of the polarization anisotropy on the linewidth enhancement factor and reflection sensitivity of 1.55 μm InP-based InAs quantum dash lasers," Applied Physics Letters, 115, 091101, (2019).
 9. H. Huang, **J. Duan**, D. Jung, A. Y. Liu, Z. Zhang, J. Norman, J. E. Bowers and F. Grillot, "Analysis of the optical feedback dynamics in InAs/GaAs quantum dots lasers directly grown on silicon," Journal of the Optical Society of America B, Vol. 35, No. 11, (2018).
 10. B. Dong, H. Huang, **J. Duan**, G. Kurczveil, D. Liang, R. G. Beausoleil and F. Grillot, "Frequency comb dynamics of a 1.3 μm hybrid-silicon quantum dot semiconductor laser with optical injection," Optics Letters, Vol. 44, No. 23, (2019).
 11. S. Gomez, H. Huang, **J. Duan**, S. Combri , A. Shen, G. Baili, A. de Rossi, F. Grillot, "High coherence collapse of a hybrid III-V/Si semiconductor laser with a large quality factor," Journal of Physics: Photonics, (accepted).

Conference papers

1. **J. Duan**, H. Huang, B. Dong, J. Norman, Z. Zhang, J. E. Bowers and F. Grillot, "A path to isolator-free integration: suppression of coherence collapse in epitaxial quantum dot lasers on silicon," International Symposium on Physics and Applications of Laser Dynamics (**Oral Presentation**), 20-22 November, Metz, France, (2019).
2. **J. Duan**, H. Huang, B. Dong, D. Jung, Z. Zhang, J. Norman, J. E. Bowers and F. Grillot, "Thermally insensitive determination of the chirp parameter of InAs/GaAs quantum dot lasers epitaxially grown onto silicon," SPIE Photonics West (**Oral Presentation**), 2-7 February, San Francisco, USA, (2019).
3. **J. Duan**, B. Dong, H. Huang, Z. G. Lu, P. J. Poole and F. Grillot, "Thermal dependence of the emission linewidth of 1.52- μm single mode InAs/InP quantum dot lasers," The 31th International Conference on Indium Phosphide and Related Materials (**Oral Presentation**), 19-23 May, Nara, Japan, (2019).

4. **J. Duan**, H. Huang, D. Jung, J. C. Norman, J. E. Bowers and F. Grillot, "Relative intensity noise of silicon-based quantum dot lasers," The 31th International Conference on Indium Phosphide and Related Materials (**Oral Presentation**), 19-23 May, Nara, Japan, (2019).
5. **J. Duan**, H. Huang, K. Schires, P. J. Poole, C. Wang and F. Grillot, "Temperature dependence of spectral linewidth of InAs/InP quantum dot distributed feedback lasers," SPIE Photonics West, (**Oral Presentation**), 27 January–1 February, San Francisco, USA, (2018).
6. **J. Duan**, H. Huang, D. Jung, J. Norman, J. E. Bowers and F. Grillot, "Low linewidth enhancement factor and high optical feedback resistance of p-doped silicon based quantum dot lasers," The Annual Conference of the IEEE Photonics Society (IPC) (**Oral Presentation**), 30 september-04 October, Reston, USA, (2018).
7. **J. Duan**, X. G. Wang, Y. G. Zhou, C. Wang and F. Grillot, "Relative intensity noise properties of quantum dot lasers," SPIE Photonics Asia (**Oral Presentation**), 11-13 October, Beijing, China, (2018).
8. **J. Duan**, X. G. Wang, Y. G. Zhou, C. Wang, F. Grillot, "Contribution des états non-résonants au bruit relatif d'intensité dans les lasers à îlots quantiques," Optique Toulouse (**Oral Presentation**), 03-06 July, Toulouse, France, (2018).
9. **J. Duan**, H. Huang, K. Schires, Z. Lu, P. J. Poole and F. Grillot, "Narrow linewidth quantum dot distributed feedback lasers," The 29th International Conference on Indium Phosphide and Related Materials, (**Oral Presentation**), 14-18 May, Berlin, Germany, (2017).
10. **J. Duan**, H. Huang, K. Schires, P. Poole and F. Grillot, "InAs/InP Quantum Dot Distributed Feedback Lasers With Narrow Spectral Linewidth," International OSA Network of Students (IONS) conference, (**Oral Presentation**), 14-17 June, Paris, France, (2017).
11. **J. Duan**, K. Schires, D. Jung, A. Liu, J. E. Bowers and F. Grillot, "Silicon quantum dot lasers with long delay optical feedback," International Symposium on Physics and Applications of Laser Dynamics, (**Poster Presentation**), 15-17 November, Paris, France, (2017).
12. **J. Duan**, H. Huang, K. Schires, P. Poole, et F. Grillot, "Oscillateurs à boîtes quantiques à très faible largeur de raie pour les systèmes optiques cohérents", 37 èmes Journées

- Nationales D'optique Guidée, (**Poster Presentation**), 04-06 July, Limoges, France, (2017).
13. F. Grillot, **J. Duan**, H. Huang, B. Dong, D. Jung, Z. Zhang, J. Norman and J. E. Bowers, "Linewidth broadening factor and optical feedback sensitivity of silicon based quantum dot lasers," SPIE Photonics West (**Invited Talk**), 2-7 February, San Francisco, USA, (2019).
 14. Y. Zhou, **J. Duan**, H. Huang, C. Cao, Q. Gong, F. Grillot and C. Wang, "Self-sustained pulse oscillations in a quantum dot laser monolithically grown on germanium," CLEO/EUROPE-EQEC, 23-27 June, Munich, Germany, (2019).
 15. F. Grillot, **J. Duan**, H. Huang, B. Dong, J. Norman, Z. Zhang and J. E. Bowers, "1.3 μm high performance epitaxial quantum dot lasers on silicon," 7th International Workshop on Epitaxial Growth and Fundamental Properties of Semiconductor Nanostructures (**Invited Talk**), Kobe, 24-27 September, (2019).
 16. O. Spitz, A. Herdt, **J. Duan**, M. Carras, W. Elsäßer and F. Grillot, "Extensive study of the linewidth enhancement factor of a distributed feedback quantum cascade laser at ultra-low temperature," SPIE Photonics West, 2-7 February, San Francisco, USA, (2019).
 17. B. Dong, A. Sawadogo, **J. Duan**, H. Huang, G. Kurczveil, D. Liang and F. Grillot, "Linewidth enhancement factor and optical injection in a hybrid-silicon quantum dot comb laser," International Conference Group IV Photonics 2019, Singapore, 28-30 August, (2019).
 18. S. Gomez, H. Huang, **J. Duan**, B. Sawadogo, A. Gallet, A. Shen, S. Combrié, G. Baili, A. de Rossi, F. Grillot, "10 Gbps error-free transmission of a high coherent Si/III-V hybrid distributed feedback laser under strong optical feedback," The Annual Conference of the IEEE Photonics Society (IPC), September 29–October 3, San Antonio, USA, (2019).
 19. J. Norman, Z. Zhang, D. Jung, **J. Duan**, H. Huang, F. Grillot and J. Bowers, "Improved Quantum Dot Uniformity and Its Impact on Reflection Sensitivity," European Conference on Integrated Optics (**Invited Talk**), 24-26 April, Ghent, Belgium, (2019).
 20. H. Huang, **J. Duan**, J.G. Provost, Z. Lu, P.J. Poole and F. Grillot, "Failure of the current modulation driven linewidth broadening factor for analyzing the optical linewidth behavior of quantum dot lasers," The 30th International Conference on Indium Phosphide and Related Materials, 29 May-1 June, Boston, USA, (2018).

Appendix B

List of Acronyms

Abbreviation	Phrase
AOM	Acousto-Optical Modulator
ASE	Amplified Spontaneous Emission
BKR	Backreflector
BOA	Booster Optical Amplifier
BER	Bit Error Rate
CBE	Chemical Beam Epitaxy
DFB	Distributed FeedBack laser
DSP	Digital Signal Processing
DBR	Distributed Bragg Reflector
ES	Excited State
ESA	Electrical Spectrum Analyzer
FP	Fabry-Perot
FN	Frequency Noise
FWHM	Full Width at Half Maximum
GS	Ground State
IL	Injection Locking
LSHB	Longitudinal Spatial Hole Burning
MOCVD	Metal-Organic Chemical vapor deposit
MBE	Molecular Beam Epitaxy
MZM	Mach-Zehnder Modulator
OSA	Optical Spectrum Analyzer
NRZ	Non-Return-to-Zero
PD	PhotoDiode
PIC	Photonic Integrated Circuit
PL	Photoluminescence
QW	Quantum Well
QD	Quantum Dot
QDash	Quantum Dash
RS	Reservoir State
RIN	Relative Intensity Noise
RF	Radio-frequency
ROF	Relaxation Oscillation Frequency
SCH	Separate Confinement Heterostructure
SNR	Signal-to-Noise Ratio
SMSR	Side-Mode Suppression Ratio
SRH	Shockley-Read-Hall
SOA	Semiconductor Optical Amplifier
SMF	Single Mode Fiber
TDD	Threading Dislocation Density
VOA	Variable Optical Attenuator
WDM	Wavelength Division Multiplexing

Title : Dynamic and nonlinear properties of quantum dot lasers for photonic integrated circuits on silicon

Keywords : semiconductor lasers, quantum dots, optical feedback, nonlinear dynamics, relative intensity noise, spectral linewidth

Abstract : Silicon photonics have been introduced to overcome low efficiency and high energy consumption of telecom links using twisted pairs or coaxial cables. This technology provides novel functionality and high performance for applications in high speed communication systems, short reach optical interconnects, and the deployment of optical links from chip-to-chip, board-to-board or rack-to-rack (datacom). Silicon is known as a very efficient semiconductor material for waveguiding light in particular owing to the strong index contrast with silica. However, the indirect bandgap of silicon makes light emission from silicon inefficient, and other techniques such as wafer- or flip-chip bonding must be investigated if light emission is to be realized. The drawbacks of such heterogeneous integration concentrate on the high cost and the limited scalability. Lasers heterogeneously integrated on silicon are also more sensitive to optical reflections originating from the transition between passive/active interfaces. The best way to overcome these drawbacks is to move on to direct epitaxial growth of III-V materials on silicon for photonics integration. In this context, quantum dot lasers using semiconductor atoms as a gain medium are ideal because they enable smaller devices, amplification with large thermal stability and high tolerance to epitaxial defects. Ultra-low noise optical transmitters are required not only for the coherent systems but also for future chip-scale atomic clocks and radar related applications be-

cause of the sensitivity to the frequency noise and intensity noise can strongly affect the bit error rates. To this end, the first part of the thesis reports an intrinsic spectral linewidth as low as 80 kHz and a relative intensity noise less than - 150 dB/Hz in InAs/InP quantum dot lasers. In particular, it is shown that a small vertical coupling is more suitable for low intensity noise operation due to the suppression of the carrier noise in the excited state. The second part of the thesis investigates the dynamic and nonlinear properties of epitaxial quantum dot lasers on silicon. As mentioned above, lasers heterogeneously integrated on silicon are more sensitive to parasitic reflections. When combined with external optical feedback, the laser stability can be dramatically affected. As no on-chip optical isolators integrated with lasers and having sufficient isolation ratio exist, the development of feedback insensitive transmitters remains a major objective. This thesis presents an error-free transmission of an epitaxial quantum dot laser on silicon externally modulated at 10 Gb/s and subjected to 100% optical feedback. Such remarkable feedback insensitivity directly results from the near-zero linewidth enhancement factor, the large damping factor, the strong contrast between the ground state and excited states and a shorter carrier lifetime. These results pave the way for future high-performance photonics integrated circuits on silicon operating without optical isolators.



Titre : Propriétés dynamiques et non linéaires des lasers à boîtes quantiques pour circuits intégrés photoniques sur silicium

Mots clés : lasers à semi-conducteurs, boîtes quantiques, rétroaction optique, dynamique non linéaire, bruit relatif d'intensité, largeur de raie spectrale

Résumé : La photonique sur silicium permet de palier au faible rendement et la consommation énergétique élevée des liens télécoms exploitant les câbles à paires torsadées ou les câbles coaxiaux. Cette technologie offre une versatilité exceptionnelle, de nouvelles fonctionnalités et des performances accrues pour les communications à haut-débit, les systèmes d'interconnexions optiques à courte portée et le déploiement de liaisons optiques d'une puce à une autre, d'une carte à une autre, ou d'un rack à un autre (datacom). Le silicium est un matériau semi-conducteur très efficace pour le guidage de la lumière, notamment en raison du fort contraste d'indice avec la silice. Cependant, sa bande interdite indirecte ne permet pas une émission radiative efficace. La réalisation de lasers repose donc sur des technologies hybrides de collage ou de report du matériau actif III-V (wafer-bonding, flip-chip) sur le silicium passif. Cependant, cette intégration hétérogène présente des inconvénients comme par exemple un coût élevé et une évolutivité limitée. Les lasers hybrides sur silicium sont aussi plus sensibles aux réflexions parasites provenant des transitions des différentes interfaces passives/actives. Un moyen permettant de surmonter ces inconvénients consiste à faire croître directement le matériau III-V sur le silicium. Dans ce contexte, les lasers à boîtes quantiques utilisant des atomes semi-conducteurs comme milieu de gain sont des candidats très prometteurs en raison de leur compacité, de leur grande stabilité thermique et d'une tolérance accrue aux défauts structuraux. Certaines applications comme les systèmes cohérents, les futures horloges atomiques intégrées sur puces et les radars où la sensibilité aux bruits de fréquence et d'intensité influence

fortement le taux d'erreur binaire requièrent l'utilisation d'émetteurs optiques à très faible bruit. Dans une première partie, cette thèse révèle le potentiel de lasers à boîtes quantiques InAs/InP présentant une largeur de raie spectrale intrinsèque de 80 kHz et un bruit relatif d'intensité inférieur à -150 dB/Hz. A cet effet, il est montré qu'un faible couplage vertical entre les états liés est plus appropriée pour une réduction du bruit d'intensité notamment grâce à la suppression du bruit de porteurs associée à l'état excité. Dans une deuxième partie, les propriétés dynamiques et non-linéaires des lasers à boîtes quantiques directement épitaxiés sur silicium sont étudiées. Comme susmentionné, les lasers intégrés de manière hétérogène sur le silicium sont plus sensibles aux réflexions parasites. Combinées à une rétroaction optique externe, la stabilité du laser peut s'en trouver fortement affectée. Sachant qu'il n'existe pas à ce jour d'isolateurs optiques intégrés sur puce ayant un taux d'isolation suffisant, le développement d'émetteurs insensibles aux rétroactions est un objectif majeur. Cette thèse présente notamment un résultat de transmission sans erreur à partir d'un laser à boîtes quantique directement épitaxié sur silicium soumis à une modulation externe à 10 Gb/s ainsi qu'à une rétroaction optique maximale de 100%. Cette insensibilité aux réflexions résulte de plusieurs propriétés remarquables comme un facteur d'élargissement spectral proche de zéro, un facteur d'amortissement élevé, un fort contraste entre les seuils d'émission des états liés, et une durée de vie des porteurs plus courte. Ces résultats permettent d'envisager le développement de futurs circuits intégrés photoniques sur silicium à haute performance et fonctionnant sans isolateur optique.

